

**OFFSHORE WIND INTEGRATION  
THROUGH HIGH VOLTAGE DIRECT  
CURRENT SYSTEMS**



MARC CHEAH MAÑE

School of Engineering  
Cardiff University, UK

THESIS SUBMITTED FOR THE DEGREE OF  
DOCTOR OF PHILOSOPHY

Cardiff, June 2017

*To my family*

# CONTENT

<b>CONTENT</b> .....	<b>II</b>
<b>ABSTRACT</b> .....	<b>VI</b>
<b>DECLARATION</b> .....	<b>VII</b>
<b>ACKNOWLEDGEMENTS</b> .....	<b>VIII</b>
<b>LIST ABBREVIATIONS</b> .....	<b>IX</b>
<b>LIST OF TABLES</b> .....	<b>XI</b>
<b>LIST OF FIGURES</b> .....	<b>XIII</b>
<b>CHAPTER 1</b>	
<b>1. INTRODUCTION</b> .....	<b>1</b>
1.1 Offshore Wind Energy .....	1
1.2 HVDC-connected Offshore Wind Power Plants .....	2
1.3 Existing and Future Projects .....	3
1.4 Future Challenges .....	4
1.5 Objectives of the Thesis .....	5
1.6 Thesis Outline .....	5
<b>CHAPTER 2</b>	
<b>2. HVDC-CONNECTED OFFSHORE WIND POWER PLANTS</b> .....	<b>7</b>
2.1 Introduction .....	7
2.2 General Configuration of an HVDC-connected Offshore Wind Power Plant .	7
2.3 HVDC Transmission System Configurations .....	8
2.4 Control of HVDC-connected Wind Power Plants .....	13
2.5 Functional Requirements .....	18
2.6 Summary .....	27
<b>CHAPTER 3</b>	
<b>3. INTERLINKS BETWEEN HVDC-CONNECTED OFFSHORE WIND POWER PLANTS</b> .....	<b>29</b>
3.1 Introduction .....	29
3.2 Interlink Options .....	30
3.3 Case Study .....	32

3.4	Power Loss Analysis .....	32
3.5	Availability Analysis .....	45
3.6	Cost-Benefit Analysis .....	55
3.7	Interlink Cable Capacity.....	57
3.8	Summary .....	62
<b>CHAPTER 4</b>		
<b>4.</b>	<b>INERTIA EMULATION IN OFFSHORE WIND POWER PLANTS .....</b>	<b>64</b>
4.1	Introduction .....	64
4.2	Inertia Response in Variable Speed Wind Turbines .....	65
4.3	Control Strategies for Inertia Emulation .....	70
4.4	Impact of Wind Turbine Recovery Power .....	78
4.5	Integration with VSC-HVDC Transmission Systems.....	82
4.6	Experimental Implementation of Inertia Emulation.....	84
4.7	Simulation and Experimental results.....	89
4.8	Summary .....	94
<b>CHAPTER 5</b>		
<b>5.</b>	<b>ELECTRICAL RESONANCE STABILITY IN HVDC-CONNECTED OFFSHORE WIND POWER PLANTS .....</b>	<b>96</b>
5.1	Introduction .....	96
5.2	Impedance-based Representation of an HVDC-connected OWPP.....	97
5.3	Impedance-based Model of VSCs.....	99
5.4	Stability Analysis of HVDC-connected OWPPs .....	102
5.5	Resonance Characterisation .....	107
5.6	Voltage Stability Analysis.....	111
5.7	Summary .....	120
<b>CHAPTER 6</b>		
<b>6.</b>	<b>CONCLUSIONS.....</b>	<b>121</b>
6.1	General Conclusions .....	121
6.2	Contributions.....	124
6.3	Future Work .....	124

## **APPENDIX A**

### **PUBLICATIONS..... 126**

A.1. Publications Related to this Thesis..... 126

A.2. Other Publications during the PhD..... 126

## **APPENDIX B**

### **DETAILS OF POWER LOSS AND AVAILABILITY ANALYSIS ..... 128**

B.1. Objective Function of OPF Algorithm..... 128

B.2. Variables of OPF Algorithm ..... 129

B.3. Availability Expressions..... 130

B.3.1. AC collector interlink..... 130

B.3.2. AC offshore converter interlink..... 131

B.3.3. DC offshore converter interlink..... 131

B.4. Outage Combinations ..... 132

## **APPENDIX C**

### **MODELLING AND CONTROL OF WIND TURBINE WITH PERMANENT MAGNET SYNCHRONOUS GENERATOR ..... 136**

C.1. Aerodynamic and Mechanical Model ..... 136

C.2. Generator Model..... 137

C.3. Back-to-back Control ..... 138

## **APPENDIX D**

### **LOW ORDER SYSTEM FREQUENCY RESPONSE MODEL.. 139**

## **APPENDIX E**

### **SPECIFICATIONS OF EXPERIMENTAL TEST RIG ..... 140**

## **APPENDIX F**

### **COMPLEX TRANSFER FUNCTIONS..... 143**

## **APPENDIX G**

### **DEMONSTRATION OF POSITIVE-NET-DAMPING STABILITY CRITERIA ..... 145**

G.1. Impedance-based Models..... 145

G.2. Positive-net-Damping Stability Criteria..... 147

G.2.1. Positive-net-damping Criterion from the Gain Margin.....	147
G.2.2. Positive-net-damping Criterion from the Phase Margin .....	149
<b>APPENDIX H</b>	
<b>DETAILS OF CASE STUDIES .....</b>	<b>152</b>
H.1. Case study in Chapter 3.....	152
H.2. Case study in Chapter 4.....	155
H.2.1. Wind Turbine .....	155
H.2.2. HVDC Point-to-point System .....	157
H.2.3. Onshore ac Grid .....	158
H.3. Chapter 5 .....	158
<b>REFERENCES .....</b>	<b>160</b>

## **ABSTRACT**

Offshore wind generation has an important role in the transition to renewable energy. In particular, HVDC-connected Offshore Wind Power Plants (OWPPs) are emerging as an economical solution for long distances from the shore. This thesis was focused on three key areas related to planning, operation and stability issues, which are present technical challenges in the integration of OWPPs through VSC-HVDC transmission systems.

In relation to planning, the installation of interlink cables between OWPPs was analysed to increase the wind power transfer. Different interlink options were compared based on a power loss reduction and an increase of availability. In general, it was recommended to have interlinks close to the wind generation point to provide more flexible active power sharing between OWPPs. Also, a cost-benefit analysis was used to quantify savings from the operation with interlinks and a design procedure was developed to determine the interlink cable capacity.

In terms of operation, inertia emulation was analysed as a potential fast frequency response service from OWPPs. Synthetic inertia and temporary overproduction have been presented as main control strategies to implement inertia emulation and they were compared using MATLAB Simulink. Results showed similar frequency response performance from both strategies, however temporary overproduction was more appropriate in order to comply with system operator's requirements. Emulation of inertia was also demonstrated in a HVDC-connected OWPP employing a hardware-in-the-loop set-up.

The converter control interaction with electrical resonances of the offshore ac grid was analysed. An impedance-based representation of the system was used to identify resonant frequencies and to assess stability. A reformulation of the positive-net-damping criterion was used to evaluate the effect that the offshore HVDC converter control and OWPP configuration have on the stability. As a result, risk of resonance interaction was identified in no-load operation and when a limited number of wind turbines were connected.

# DECLARATION

This work has not been submitted in substance for any other degree or award at this or any other university or place of learning, nor is being submitted concurrently in candidature for any degree or other award.

Signed..... Date.....

## STATEMENT 1

This thesis is being submitted in partial fulfilment of the requirements for the degree of PhD

Signed..... Date.....

## STATEMENT 2

This thesis is the result of my own independent work/investigation, except where otherwise stated, and the thesis has not been edited by a third party beyond what is permitted by Cardiff University's Policy on the Use of Third Party Editors by Research Degree Students. Other sources are acknowledged by explicit references. The views expressed are my own.

Signed..... Date.....

## STATEMENT 3

I hereby give consent for my thesis, if accepted, to be available online in the University's Open Access repository and for inter-library loan, and for the title and summary to be made available to outside organisations.

Signed..... Date.....

# ACKNOWLEDGEMENTS

The completion of this thesis would have not been possible without the support and help of many people. First, I would like to express my gratitude to Dr. Jun Liang for his technical guidance and for always trying to find a practical application to my research. I would also like to thank Prof. Nick Jenkins for his wise advices, which I will remember beyond the research presented in this thesis.

During this journey I had the pleasure to collaborate with other colleagues, who I would like to acknowledge with a special mention. My sincere thanks to Dr. Oluwole Daniel Adeuyi, with whom I have spent many days in the lab and I have learnt, suffered and overcome part of my research with great success. My thanks also go to Dr. Luis Sainz, who helped me to develop and complete an important part of this thesis.

In addition, I would like to acknowledge the financial support of the European Commission through the MEDOW project, which gave me the opportunity to explore and develop my career with different training and dissemination activities. In particular, my special thanks to the other *MEDOWers* for the interesting and useful discussions we shared during this project and also to Cath and Karolina for their patience dealing with all our issues.

I would also like to thank all my colleagues and friends in CIREGS for all the motivation and inspiration I got from them. In particular, my special thanks to Dantas, Tony, Senthoran, Tibin, Gen, Khadijat and Sathsara, with whom I spent most of the lunch and coffee breaks.

Last but not least, my deep gratitude to my family, who always gave me an unconditional support during this journey.

## LIST ABBREVIATIONS

CIGRE	Conseil International des Grands Réseaux Électriques
COPT	Capacity Outage Probability Tables
DFIG	Doubly-Fed Induction Generator
ENTSOE	European Network of Transmission System Operators for Electricity
ETYS	Electricity Ten Year Statement
EWEA	European Wind Energy Association
FRC	Fully Rated Converter
FRT	Fault Ride Through
FSM	Frequency Sensitive Mode
GCP	Grid Connection Point
GIS	Gas Insulated Switch
GSC	Grid Side Converter
HIL	Hardware-in-the-Loop
HQT	Hydro-Québec TransÉnergie
HVAC	High Voltage Alternate Current
HVDC	High Voltage Direct Current
IESO	Independent Electricity System Operator
IGBT	Insulated-Gate Bipolar Transistor
LCC	Line Commutated Converters
LFSM	Limited Frequency Sensitive Mode
MMC	Modular Multilevel Converter
MPPT	Maximum Power Point Tracking
MTDC	Multi-Terminal Direct Current
MTTF	Mean Time To Fail
MTTR	Mean Time To Repair
MVAC	Medium Voltage Alternate Current
NPV	Net Present Value
OFTO	Offshore Transmission Owner
ONS	Operador Nacional do Sistema Eletrico
OPF	Optimal Power Flow
OWPP	Offshore Wind Power Plant
PD	Proportional-Derivative

PI	Proportional-Integral
PLL	Phase Locked Loop
POC	Point of Connection
RL	Resistance-Inductance
RoCoF	Rate of Change of Frequency
SI	Synthetic Inertia
TO	Temporary Overproduction
TSO	Transmission System Operator
UK	United Kingdom
VSC	Voltage Source Converter
WFC	Wind Farm Converter
WPP	Wind Power Plant
WT	Wind Turbine
XLPE	Cross-linked Polyethylene Insulation
PMSG	Permanent Magnet Synchronous Generator

## LIST OF TABLES

Table 1.1: Details of existing HVDC-connected OWPPs projects presented in Figure 1.3 [10], [11], [16].....	4
Table 2.1: Functional requirements in HVDC-connected OWPPs.....	18
Table 3.1: Power loss coefficients of different converters expressed in per-unit [95]–[98]......	35
Table 3.2: Power loss coefficients of single HVDC-connected OWPP in different OPF options expressed in per-unit. ....	39
Table 3.3: COPT for example without interlink. ....	51
Table 3.4: COPT for example with dc offshore converter interlink. ....	51
Table 3.5: COPT for example with ac offshore converter interlink. ....	51
Table 3.6: COPT for example with ac collector platform interlink. ....	52
Table 3.7: Interlink cable costs for a length of 5 km .....	55
Table 3.8: Annual average of undelivered energy and energy losses with their associated savings compared to the base case.....	56
Table 3.9: Results of cost-benefit analysis.....	57
Table 3.10: Sensitivity analysis in relation to the dc breaker cost.....	57
Table 3.11: Results of ac interlink cable capacity selection. ....	59
Table 4.1: Example of HQT requirement of inertia emulation applied for the grid scenario presented in [112]. ....	67
Table 4.2: Specifications for inertia emulation in different system operators .....	68
Table 4.2: Control parameters of Synthetic Inertia strategies.....	73
Table 4.3: Control parameters of Temporary Overproduction strategies .....	73
Table 4.5: RoCoF and maximum frequency deviation for simulations results in Figures 4.6 and 4.7. The minimum values for SI and TO options are highlighted in boldface. ....	77
Table 4.6: Base values for PSCAD model and experimental test rig .....	90

Table 4.7: Frequency deviation and RoCoF from PSCAD simulation results .....	91
Table B.1: Outage combinations of S1-S5 and resulting capacity outage. Capacities of S1-S5 are expressed in per-unit with base power equal to the rated power of an OWPP .....	132
Table E.1: Specifications of wind turbine test rig.....	140
Table E.2: Specifications of VSC test rig .....	141
Table E.3: Specifications of dc network cabinet.....	141
Table E.4: Specifications of real time simulator.....	142
Table E.5: Specifications of grid simulator.....	142
Table H.1: Parameters of Wind Turbines, HVDC converters and transformers. ....	152
Table H.2: Cable parameters.....	153
Table H.3: Cable lengths of wind farm cluster in Figure H.2.....	154
Table H.4: MTTF and MTTR of transmission system components [102], [103]....	155
Table H.5: Parameters of PMSG.....	155
Table H.6: Aerodynamic and mechanical characteristic of WT.....	156
Table H.7: Specifications and control parameters of WT back-to-back converter..	156
Table H.8: Specifications and control parameters of dc cables. ....	157
Table H.9: Specifications and control parameters of HVDC converters. ....	157
Table H.10: Specifications of ac grid model.....	158
Table H.11: Specifications of offshore HVDC converter and HVDC transformer. ....	158
Table H.12: Specifications of WT grid-side converter and WT transformer. ....	159
Table H.13: Specifications of ac export cables and collector transformers.....	159

# LIST OF FIGURES

Figure 1.1: Global wind power capacity and annual additions from 2005 to 2015 [1]. .....	1
Figure 1.2: Cumulative and annual offshore wind installations in Europe from 1993 to 2015 [6].....	2
Figure 1.3 Map of offshore wind farms in the North Sea connected to Germany [16] . .....	3
Figure 2.1: General configuration of an OWPP with two wind farms connected through an HVDC point-to-point link. ....	8
Figure 2.2: OWPP connected through a Point-to-point system. ....	10
Figure 2.3: OWPP connected through an offshore ac grid. ....	11
Figure 2.4: OWPP connected through an offshore dc grid. ....	12
Figure 2.5: General control scheme of a HVDC-connected OWPP .....	13
Figure 2.6: WPP control based on [47].....	14
Figure 2.7: Control scheme for GSCs using vector control .....	16
Figure 2.8: Control scheme for WFCs using amplitude control or vector control. ...	17
Figure 2.9: Active power control functions of OWPP.....	19
Figure 2.10: ENTSOE requirements for voltage at the grid connection point of a dc-connected system [18]. Voltage operational boundaries are function of $Q/P_{\max}$ , where $P_{\max}$ is the maximum active power transmission capacity. The outer envelope represents the maximum values fixed by ENTSOE. The inner envelope is defined by each system operator and it does not have to be a rectangle.....	20
Figure 2.11: National Grid (Great Britain) requirements for reactive power capacity at the interface connection point of a WPP or a DC-connected system [61]. The Q values are expressed as function of the interface point capacity of the OWPP. The dashed area is an optional requirement for active power generation below 0.2 pu. ....	20
Figure 2.12: Voltage limits as function of power factor required by National Grid (Great Britain) in WPPs or DC-connected systems and TenneT (Germany) in offshore-connected systems [34], [61]. TenneT defines the nominal voltage at the onshore	

connection point in 155 kV. National Grid has different voltage levels (380, 220, 110 and 33 kV), but only high voltage is considered for OWPPs. .... 21

Figure 2.13: TenneT (Germany) requirements for reactive power capacity supplied by a generator unit at the grid connection point [34]. .... 21

Figure 2.14: Voltage support during ac fault required by TenneT (Germany) in generating units [34]. .... 22

Figure 2.15: Frequency response characteristic required by EirGrid (Ireland) in WPPs [65]. Points A-E are defined depending on system conditions and location of the OWPP. Deadband frequency range is between B and C. .... 23

Figure 2.16: Frequency response characteristic required by TenneT (Germany) in offshore-connected systems [34]. The power reduction depends on the current available power,  $P_M$ . .... 23

Figure 2.17: ENTSOE requirements for frequency response in DC-connected systems [18]. A Frequency Sensitive Mode (FSM) is defined for under and overfrequency events, whereas a Limited Frequency Sensitive Mode (LFSM) can be defined for a frequency trend or both. The droop gains  $s_1 - s_4$  are at least 0.1%, the maximum deadband is  $\pm 500$  mHz and the maximum insensitivity is 30 mHz. The LFSM is activated for frequency variations higher than 200 mHz. .... 23

Figure 2.18: FRT profile required by ENTSOE at the grid connection point of HVDC-connected power plants [18].  $U_{ret}$  is the retained voltage during an ac fault,  $t_{clear}$  is the fault duration and  $(U_{rec1}, t_{rec1})$  and  $(U_{rec2}, t_{rec2})$  are limits defined during the fault recovery. .... 25

Figure 2.19: FRT requirements for WTs in different countries [84]. .... 26

Figure 3.1: Representation of ac and dc interlinks. .... 29

Figure 3.2: Structure of Chapter 3. .... 30

Figure 3.3: Interlink options between OWPPs. .... 31

Figure 3.4: Case study with two HVDC-connected OWPPs used in power loss and availability analysis. .... 32

Figure 3.5: Model of the case study with enumeration of converters, buses and admittances (interlink cables options are indicated in grey rectangles). .... 34

Figure 3.6: Inputs and outputs of Optimal Power Flow.....	38
Figure 3.7: Total power losses in a single HVDC-connected OWPP for different OPF options and wind generations, <i>POWF</i> .....	40
Figure 3.8: Reactive power supply from offshore converters in a single OWPP for different OPF options and wind generations, <i>POWF</i> .....	40
Figure 3.9: Power loss distribution in a single OWPP for different OPF options. ....	41
Figure 3.10: Percentage distribution of power losses in a single OWPP when optimisation determines reactive power supply and POC voltage (OPF-QV) .....	41
Figure 3.11: Power losses and interlink power flow when one OWPP is generating nominal power and the other is not generating power. ....	44
Figure 3.12: Total power losses for different interlink options and interlink lengths when OWPP1 generates nominal power and OWPP2 does not generate power.....	45
Figure 3.13: Interlink power flows for different interlink options and interlink lengths when OWPP1 generates nominal power and OWPP2 does not generate power.....	45
Figure 3.14: Block diagrams to represent equivalent availability of OWPP transmission system elements. The per-unit quantities are referred to the rated power of an OWPP. ....	47
Figure 3.15: Elements to represent equivalent availability of two OWPPs with interlinks. The per-unit quantities are referred to the rated power of an OWPP .....	50
Figure 3.16: Energy availability for different wind capacity factors when OWPPs generate the same power, transmission system capacity is defined as 100% and interlink capacity for 50% of the OWPP rated power. ....	53
Figure 3.17: Energy availability for different interlink capacities when transmission system capacity is defined as 100% of the OWPP rated power.....	53
Figure 3.18: Energy availability for different transmission system capacities when wind generation from each OWPP is 0.4 pu and interlink capacity is defined as 50% of the OWPP rated power. ....	53
Figure 3.19: Energy availability when failure rates are modified from 0.1 to 10 times the initial value. The discontinuous horizontal dashed lines represent an availability variation of $\pm 1\%$ the initial value.....	54

Figure 3.20: Flow chart to select interlink capacity based on power losses analysis	59
Figure 3.21: Flow chart to select interlink capacity based on availability analysis ...	60
Figure 3.22: Weibull distribution and WT generation used as an example to calculate minimum interlink capacity. ....	61
Figure 3.23: Energy availability for different interlink capacities (a) considering probability of all wind power generations and (b) considering capacity factor of the OWPP. The interlink capacities are expressed in per-unit considering the rated power of an OWPP as a base power. ....	62
Figure 4.1: Inertia Response description.....	65
Figure 4.2: Representation of Inertia Emulation requirements.....	68
Figure 4.3: General scheme of WT controls including inertia emulation.....	69
Figure 4.4: Control scheme of Synthetic Inertia strategy. ....	71
Figure 4.5: Control scheme of Temporary Overproduction strategy. ....	72
Figure 4.6: Comparison of SI strategies considering the same time of overproduction and a maximum power contribution equal to 10% of $P_0$ . ....	75
Figure 4.7: Comparison of TO strategies considering the same time of overproduction and a maximum power contribution equal to 10% of $P_0$ . ....	76
Figure 4.8: Inertia emulation as TO with step function and maximum power contribution equal to 10% of nominal power.....	78
Figure 4.9: Reduction of demand in ac grid with TO strategy.....	78
Figure 4.10: Increase of overproduction time in TO from 6 to 10 s when the demand level is 4 GW.....	79
Figure 4.11: Increase of power rate limit from 0.5 to 3 s when the demand level is 4 GW.....	80
Figure 4.12: Limitation of recovery power with saturation at 2% of $P_0$ when the demand level is 4 GW.....	81
Figure 4.13: Limitation of recovery power with saturation at 2% of $P_0$ and increase of power rate limit from 1 to 3 s when the demand level is 4 GW. ....	82

Figure 4.14: HVDC point-to-point control scheme with artificial frequency coupling between onshore and offshore grids.....	84
Figure 4.15: General diagram of the HIL set-up.....	85
Figure 4.16: Elements represented in the HIL test. The scaled-down components are in black and the emulated elements are in grey. ....	85
Figure 4.17: Wind Turbine test rig.....	86
Figure 4.18: VSC test rig and dc network cabinet .....	87
Figure 4.19: Interior of VSC test rig.....	87
Figure 4.20: Interface of RTDS with VSC test rig.....	88
Figure 4.21: Real time simulator and Grid simulator .....	88
Figure 4.22: Simulation (left side) and experimental (right side) results of the onshore ac grid frequency.....	91
Figure 4.23: Simulation (left column) and experimental (right column) results of the power transfer through HVDC transmission. ....	92
Figure 4.24: Simulation (left column) and experimental (right column) results of the WT rotor speed and efficiency.....	92
Figure 4.25: Simulation (left column) and experimental (right column) results of the DC voltage at WFC and offshore ac frequency deviation. ....	93
Figure 4.26: Simulation results of onshore and offshore frequency and OWPP power variation during activation of inertia emulation.....	94
Figure 5.1: General scheme of an HVDC-connected OWPP. ....	98
Figure 5.2: Impedance-based model of an HVDC-connected OWPP for resonance and stability analysis. ....	99
Figure 5.3: Control structures: (a) Offshore HVDC converter and (b) WT grid side converter.....	101
Figure 5.4: Equivalent impedance-based circuit of an HVDC-connected OWPP with representation of offshore grid circuit.....	102
Figure 5.5: Frequency response with and without simplifications (parameters in Appendix H with $k_p, v = 1, k_i, v = 500$ ).....	108

Figure 5.6: Impedance-based model of an HVDC-connected OWPP with simplified VSC and cable models (indicated in grey rectangles) .....	109
Figure 5.7: Impedance-based model of an HVDC-connected OWPP with aggregation of collector system .....	109
Figure 5.8: Frequency response of OWPP impedance without and with VSC and cable model simplifications (parameters in Appendix H with $k_{p,v} = 1, k_{i,v} = 500$ )..	110
Figure 5.9: Zero-crossing frequencies of $R_{ch}$ when $k_{p,v} = 0.01, k_{i,v} = 2.5$ .....	113
Figure 5.10: Stable area of offshore HVDC converter in no-load operation as function of $k_{p,v}, k_{i,v}$ and $l_{cb}$ (the stable and unstable examples of Figures 5.12 and 5.13 are marked with circles).....	113
Figure 5.11: Root locus of OWPP in no-load operation for variations of export cable length and ac voltage control parameters.....	114
Figure 5.12: Stable example in no-load operation with $k_{p,v} = 0.01, k_{i,v} = 2.5$ and $l_{cb} = 10 \text{ km}$ .....	115
Figure 5.13: Unstable example in no-load operation with $k_{p,v} = 0.01, k_{i,v} = 4.6$ and $l_{cb} = 10 \text{ km}$ .....	116
Figure 5.14: Stable area of offshore HVDC converter as a function of $k_{p,v}$ and $k_{i,v}$ and the number of connected WTs (the stable and unstable examples of Figures 5.16 and 5.17 are marked with a circle). .....	117
Figure 5.15: Root locus of OWPP for variations of ac voltage control parameters and number of WTs. ....	117
Figure 5.16: Stable example when all the WTs are connected ( $N = 80$ ), $k_{p,v} = 1$ and $k_{i,v} = 500$ .....	118
Figure 5.17: Unstable example when 24 WTs are connected, $k_{p,v} = 1$ and $k_{i,v} = 500$ .....	119
Figure 5.18: Instantaneous and RMS voltages at POC when the number of WTs is reduced from 80 to 24 at 1 s. The ac voltage control parameters are $k_{p,v} = 1$ and $k_{i,v} = 500$ .....	119
Figure C.1: Control structure of generator-side VSC. ....	138

Figure C.2: Control structure of grid-side VSC.....	138
Figure D.1: Block diagram of low order system frequency response model.....	139
Figure G.1: Equivalent impedance-based circuit with load subsystem as an impedance. .....	145
Figure G.2: Equivalent impedance-based circuit with source as a Thévenin equivalent and load as Thévenin or Norton equivalents.....	146
Figure G.3: Nyquist trajectories for stable and unstable systems. ....	147
Figure H.1: Equivalent impedance of a string with N WTs.....	154
Figure H.2: Wind farm cluster layout. ....	154

# CHAPTER 1

## INTRODUCTION

### 1.1 OFFSHORE WIND ENERGY

The total wind power capacity has increased more than seven times since 2005, as shown in Figure 1.1. By the end of 2015, wind energy represented 3.7% of the global electricity production and contributed to 15.6% of the renewable energy share [1]. Currently, wind generation is predominately onshore; however, there is an increasing interest in offshore wind generation due to limited onshore site location and less public opposition. Importantly, high-power wind turbines can be installed in the sea and the offshore wind speed is much higher and more uniform than inland [2].

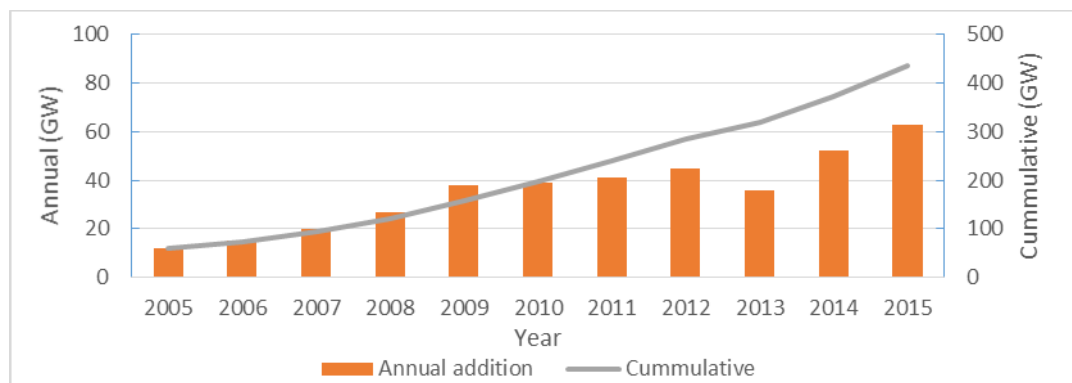


Figure 1.1: Global wind power capacity and annual additions from 2005 to 2015 [1].

In Europe, offshore wind generation has significantly increased during the past decade, as illustrated in Figure 1.2. By the end of 2015, 91% (11 GW) of the global offshore wind capacity was installed in Europe [3]. The European Wind Energy Association (EWEA) expects that the total capacity in Europe will reach 20 GW by 2020 and 66 GW by 2030 [4], [5]. More than two thirds of the total European offshore wind capacity are installed in the North Sea, which is an ideal location for offshore wind generation due to high wind speeds and shallow water [6]. The UK is leading the market with nearly 50% of the total installed capacity in 2015 [6].

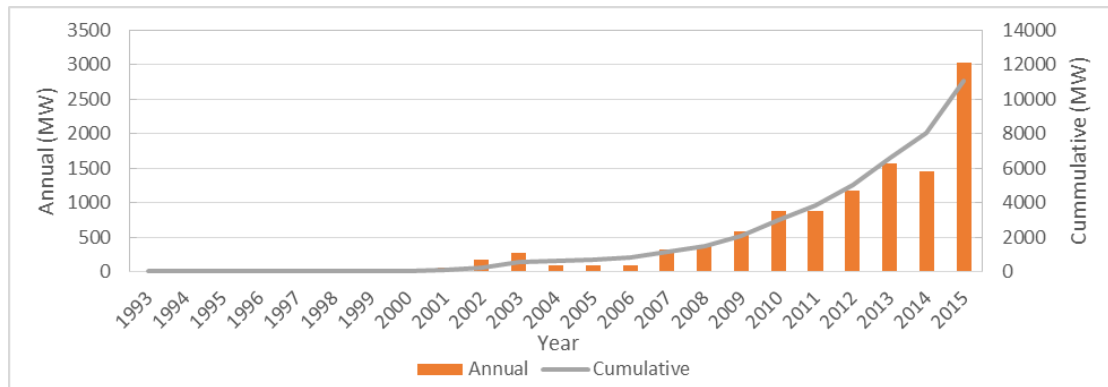


Figure 1.2: Cumulative and annual offshore wind installations in Europe from 1993 to 2015 [6]

## 1.2 HVDC-CONNECTED OFFSHORE WIND POWER PLANTS

Grid integration is one of the main challenges for offshore wind development. Offshore Wind Power Plants (OWPPs) can be connected to the onshore grid through High Voltage Alternate Current (HVAC) or High Voltage Direct Current (HVDC) submarine cables. The ac connection of offshore wind power plants is currently the most common solution, but dc connection provides an economically viable option for long distances (longer than 40 - 100 km [7]). This is because long ac submarine cables generate a considerable amount of reactive power that increases the power losses and requires the installation of reactive compensators. In addition, HVDC connections offer an electrical decoupling between OWPPs and onshore ac grids, which avoids resonance interactions and the propagation of ac faults [8].

HVDC can use two different converter topologies: Line Commutated Converters (LCCs) and Voltage Source Converters (VSCs). Conventional HVDC systems are based on LCC, which allows bulk power transmission for long distances. VSC has been developed recently for HVDC applications and is more suitable than LCC to connect OWPPs. Compared to LCC, VSC provides black start capability and requires a smaller footprint, which reduces the offshore platform cost. Also, VSCs are more robust to onshore ac grid disturbances, since they are based on IGBT valves and do not suffer from commutation failure [8]. VSCs have fast and independent control of active and reactive power, which is beneficial to OWPPs for providing ancillary services to onshore ac grids.

### 1.3 EXISTING AND FUTURE PROJECTS

BorWin1 was the first HVDC link to connect offshore wind farms to shore [9]. Since then, nine HVDC-connected OWPP projects located in the south-eastern part of the North Sea are in operation, under construction or planned, as shown in Figure 1.3 and Table 1.1 [10], [11]. These projects are based on HVDC point-to-point links, but a future offshore grid in the North Sea region with ac and dc interconnections is under discussion [10], [12]. In the UK, the Crown Estate is planning to install up to 25 GW of offshore wind generation and more than 75% of this capacity will be connected through HVDC point-to-point links [13]. In the US, it is anticipated that the Atlantic Wind Connection will integrate up to 6 GW of offshore wind through a Multi-terminal DC Grid (MTDC) [14], [15].

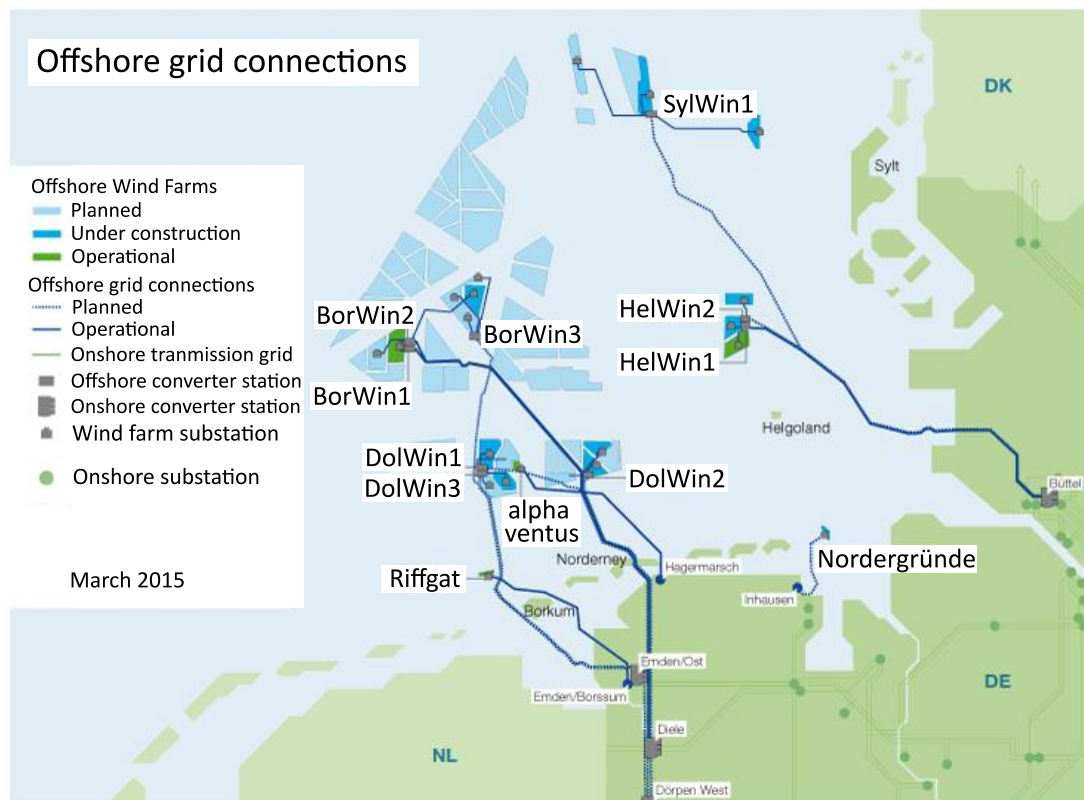


Figure 1.3 Map of offshore wind farms in the North Sea connected to Germany [16].

Table 1.1: Details of existing HVDC-connected OWPPs projects presented in Figure 1.3 [10], [11], [16]

<b>Project</b>	<b>Capacity</b>	<b>Voltage</b>	<b>Cable length</b>	<b>Commissioning year</b>
<i>BorWin1</i>	400 MW	$\pm 150$ kV	200 km	2010
<i>BorWin2</i>	800 MW	$\pm 300$ kV	200 km	2015
<i>DolWin1</i>	800 MW	$\pm 320$ kV	165 km	2015
<i>HelWin1</i>	576 MW	$\pm 250$ kV	130 km	2015
<i>HelWin2</i>	690 MW	$\pm 320$ kV	130 km	2015
<i>SylWin1</i>	864 MW	$\pm 320$ kV	205 km	2015
<i>BorWin3</i>	900 MW	$\pm 320$ kV	200 km	2019
<i>DolWin2</i>	916 MW	$\pm 320$ kV	135 km	2016
<i>DolWin3</i>	900 MW	$\pm 320$ kV	160 km	2018

## 1.4 FUTURE CHALLENGES

The connection of OWPPs through HVDC systems has been demonstrated but it is not a mature technology yet. Offshore HVDC transmission systems have to ensure high reliability due to the long repair time and high cost of offshore maintenance. More complex topologies based on offshore interconnections between OWPPs improve reliability, but increase the cost of the offshore transmission system. The design of the offshore transmission system can be optimised if OWPP and transmission system owners are coordinated [17]. At first, point-to-point HVDC links will be built and at later stages offshore cable connections may be installed between existing OWPPs if it is financially viable. In addition, power flow control and protection strategies are important challenges in interconnected offshore systems, especially for HVDC grids [7].

In future, a large number of synchronous generators are expected to be replaced by asynchronous renewable generation, such as HVDC-connected OWPPs. Therefore, OWPPs must provide ancillary services to onshore grids. A number of these services can be provided by the onshore HVDC converter, *e.g.* voltage support, but other services have to be provided by the Wind Turbines (WTs) and require coordination between HVDC converters and OWPPs, *e.g.* frequency response. The European Union has recently approved a grid code with general requirements for HVDC-connected

systems that was developed by the European Network of Transmission System Operators for Electricity (ENTSOE) [18]. However, a number of requirements, such as inertia response, short-circuit contribution or power oscillation damping, are still under consideration.

Offshore ac and dc grids are isolated systems with high penetration of converters. Poorly damped resonances of an offshore grid can interact with the converter controls until the system becomes unstable. Such resonance interactions caused by WT converters and HVDC converters must be identified during the design process and can be limited by introducing additional damping to the system [19].

## 1.5 OBJECTIVES OF THE THESIS

The research work carried out in this thesis contributes to solve the future challenges for HVDC-connected OWPPs. The aims of this thesis are to investigate interconnection topologies and analyse the operation and stability of OWPPs connected through VSC-HVDC transmission systems. Particular objectives of this thesis include:

- Analyse the contribution of interlink cables between OWPPs to increase availability and reduce power losses of the transmission system.
- Compare wind turbine inertia emulation strategies to provide inertia response from OWPPs.
- Build a hardware-in-the-loop test rig to demonstrate inertia emulation from an OWPP connected through an HVDC point-to-point link.
- Identify instabilities caused by control interactions of VSCs with the resonances of the offshore ac grid. The impact of the offshore HVDC converter is analysed in detailed.

## 1.6 THESIS OUTLINE

The structure of this thesis is as follows:

### *Chapter 2 –HVDC-connected Offshore Wind Power Plants*

This chapter reviews the current research areas for the development of HVDC-connected OWPPs. These research areas include the design of HVDC transmission

system topologies, control structures and functional requirements in an HVDC-connected OWPP.

### *Chapter 3 – Interlinks between HVDC-connected Offshore Wind Power Plants*

This chapter presents a comparative analysis of different topologies with interlink cables between OWPPs. Reduction of power losses and increase of wind energy availability were quantified and discussed in different interlink options. The power losses were analysed using an optimal power flow and the availability was analysed using Capacity Outage Probability Tables (COPTs). Also, a cost-benefit analysis was used to compare the interlink options in terms of operational savings and a design procedure was developed to determine the interlink cable capacity.

### *Chapter 4 – Inertia Emulation in Offshore Wind Power Plants*

This chapter presents the concept and the current developments of inertia emulation in OWPPs. Two main strategies were compared: Synthetic Inertia and Temporary Overproduction. Also, control strategies to limit wind turbine recovery power were described. The implementation of inertia emulation in an HVDC-connected OWPP was demonstrated using a hardware-in-the-loop set-up based on a wind turbine test rig, a VSC test rig, a dc network cabinet, a grid simulator and a real time simulator.

### *Chapter 5 – Electrical Resonance Stability in HVDC-connected Offshore Wind Power Plants*

This chapter analyses the interaction of converter controls with harmonic series resonances of the offshore ac grid. An impedance-based representation of the offshore ac grid and the VSCs was used to identify resonant frequencies and assess stability. A reformulation of the positive-net-damping stability criterion was demonstrated and used to evaluate the effect that the offshore HVDC converter control and the OWPP configuration have on the stability.

### *Chapter 6 – Conclusions*

This chapter outlines the conclusions and contributions of this thesis and describes recommendations for further work.

## **CHAPTER 2**

# **HVDC-CONNECTED OFFSHORE WIND POWER PLANTS**

## **2.1 INTRODUCTION**

The connection of OWPPs through VSC-HVDC links has been demonstrated in real projects but there are still technical challenges that must be addressed, such as the optimal configuration of the transmission system, the control coordination and the provision of ancillary services [11], [20]. The potential topologies to connect an OWPP through an HVDC transmission system are described and discussed. The control of the OWPP and the HVDC converters is presented and the potential control interactions between the converters are highlighted. Also, the functional requirements of the overall system and the onshore and offshore grids are described.

## **2.2 GENERAL CONFIGURATION OF AN HVDC-CONNECTED OFFSHORE WIND POWER PLANT**

Figure 2.1 shows the general configuration of an OWPP connected through an HVDC point-to-point link, where the basic components are indicated. In offshore applications, WTs are based on Doubly-Fed Induction Generators (DFIGs) or generators with Fully Rated Converters (FRCs) [21]. High-power WTs (from 5 MW) use FRCs with Permanent Magnet Synchronous Generators (PMSG) due to their high reliability and efficiency [22]. Offshore WTs generate power at low ac, which is stepped-up with a transformer to a medium ac voltage (33 - 66 kV [20]) collector grid. The most common collector system design consists in a radial grid, where the WTs are connected to different feeders or strings as shown in Figure 2.1 [23]. The wind farms are connected to offshore collector platforms, where transformers step-up the voltage to HVAC (132 – 220 kV [20]). The collector platforms transfer the power to offshore HVDC converters through ac export cables. The offshore HVDC converters operate as rectifiers and deliver the power to the onshore HVDC substation through HVDC transmission cables (up to  $\pm 525$  kV [24]). The onshore HVDC converters operate as

inverters and inject the power to the onshore grid. The early HVDC converters for offshore wind integration were based on 2-level topologies, but current designs use Modular Multilevel Converter (MMC) topologies to reduce the harmonic emission and minimise or eliminate the use of passive filters [11], [23]. Symmetrical monopoles are assumed for each sending end of the HVDC transmission system since this is the arrangement used in the current projects shown in Table 1.1.

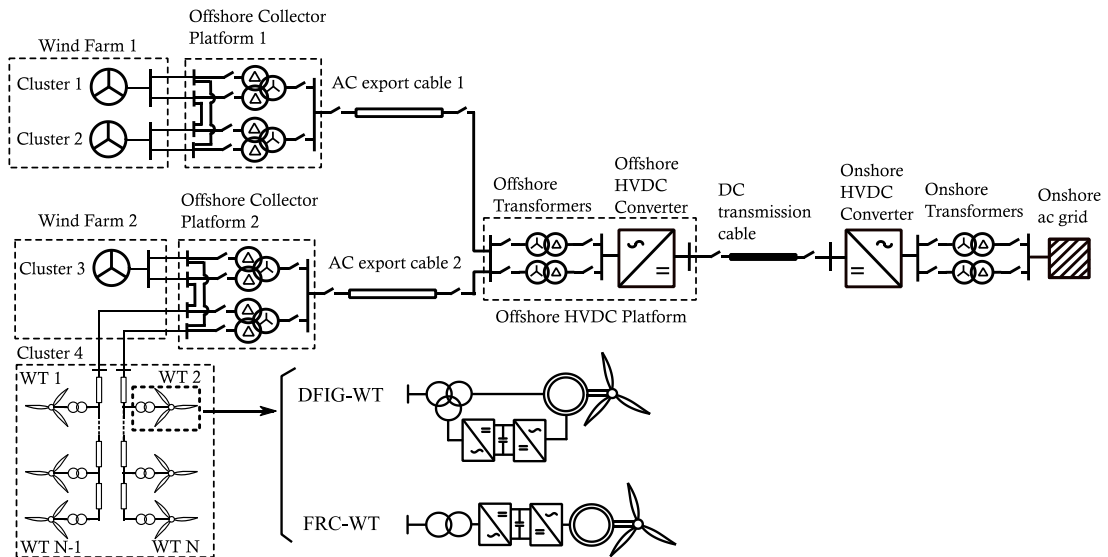


Figure 2.1: General configuration of an OWPP with two wind farms connected through an HVDC point-to-point link.

## 2.3 HVDC TRANSMISSION SYSTEM CONFIGURATIONS

The factors used to choose a transmission system topology for OWPPs are discussed and a number of HVDC transmission options are described.

### 2.3.1 Selection of transmission system configurations

The main objective of the transmission system is to maximise the wind power transfer, which is achieved by reducing the total power losses and energy not supplied [8], [25], [26]. However, a complete evaluation must include an economic assessment and consider regulatory and geographical limitations [17], [27].

Although the components of the transmission system are designed to have minimum power losses, optimal operation of the OWPPs can further reduce the total losses. Even a 0.1% loss reduction of the nominal wind power transfer could represent significant savings [28]. An optimal power flow in an OWPP can be used to determine

the power and voltage set-points of the HVDC converters and the WT converters [29]–[31].

Traditionally, transmission systems were designed on a basis of N-1 or N-2 redundancy, *i.e.* in case of loss of one (N-1) or two assets (N-2), the rest of the system must maintain operation. However, in offshore systems this is not the case due to the high cost of redundant components. As an alternative, two approaches are proposed in [20]:

- The economic value of energy not supplied is compared to costs. For example, the increase of transmission capacity reduces the wind power curtailment, but the initial investment is higher [32]. Therefore, a trade-off between cost of the assets and wind power curtailment defines the optimal transmission capacity.
- A minimum availability of the transmission system is set by the consumer or a governmental institution. For example, in the UK the Offshore Transmission Owners (OFTOs) will be penalised if the availability is less than 98% [33].

An economic assessment based on a cost-benefit analysis is used to select the best transmission system configuration. The costs of the transmission system include the initial investment of the assets and the operation and maintenance costs. The income is mainly from the wind energy generation, but the provision of ancillary services may be rewarded depending on the system operator regulations. Also, the energy savings from the reduction of power losses and power curtailment can be used to compare transmission topologies [8], [25], [26].

The operation and design of the transmission system can be constrained by system operator regulations, *e.g.* in Germany, TenneT requires the grid connection point of OWPPs to be at 155 kV with a continuous operating range between 140-170 kV [34]. If OWPPs are connected to two or more countries, the selection and design of the transmission topology will be more complex due to different regulation requirements and potential incompatibilities between countries [35]. Also, geographical constraints should be considered, such as location of OWPPs, onshore connection and cable routes [27].

Existing HVDC-connected OWPPs are based on point-to-point links, but more complex configurations have additional advantages in terms of power losses reduction and increase of energy availability.

### 2.3.2 Point-to-Point systems

OWPPs can be connected using HVDC point-to-point links. This is the simplest option with the lowest cost. Figure 2.2 shows an example of an OWPP connected through an HVDC point-to-point system.

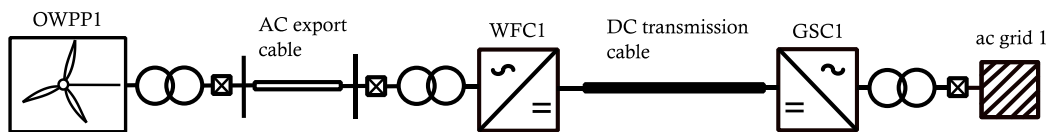
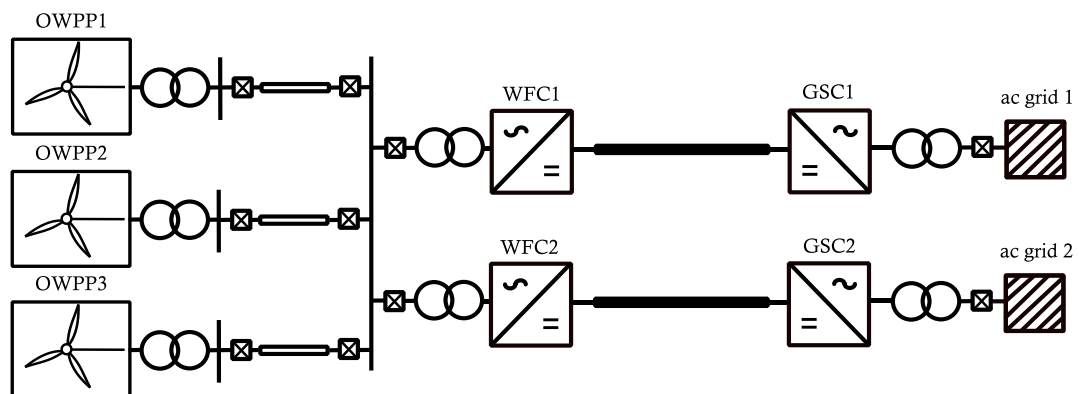


Figure 2.2: OWPP connected through a Point-to-point system.

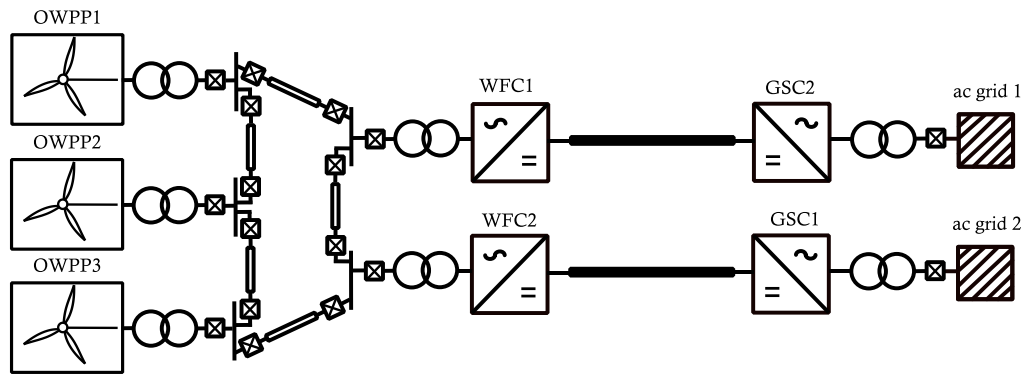
In case of a dc fault, dc breakers are not necessary, since ac breakers at each HVDC converter terminal are used to isolate the dc system. The main disadvantage of this topology is that an outage in the transmission system will cause the power loss of the entire OWPP, because it is assumed that the configuration is based on symmetrical monopoles. All the existing HVDC-connected OWPPs are based on point-to-point configurations [16].

### 2.3.3 Offshore ac interconnections

OWPPs can be interconnected to form an offshore ac grid that delivers wind power to the onshore grid through different dc links. Figure 2.3 shows an example of three OWPPs with two possible ac grid topologies: multi-infeed connection, where the OWPPs are connected to a common ac bus, or meshed ac grid, where the OWPPs are interconnected with ac cables.



(a) Multi-infeed connection



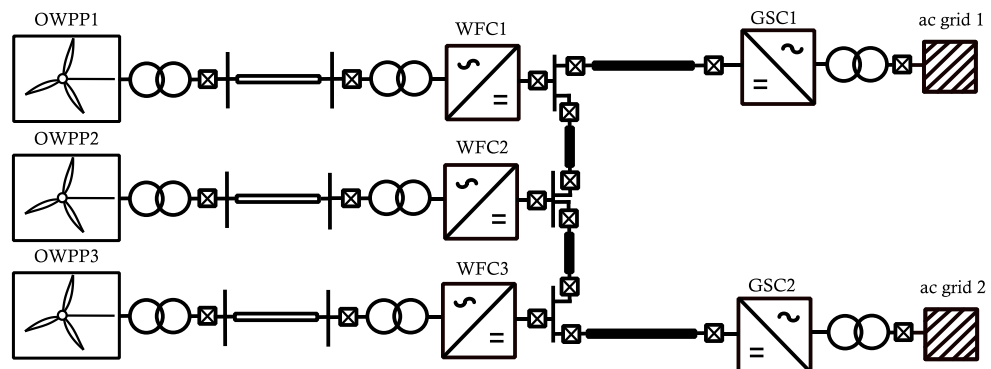
(b) Meshed ac grid

Figure 2.3: OWPP connected through an offshore ac grid.

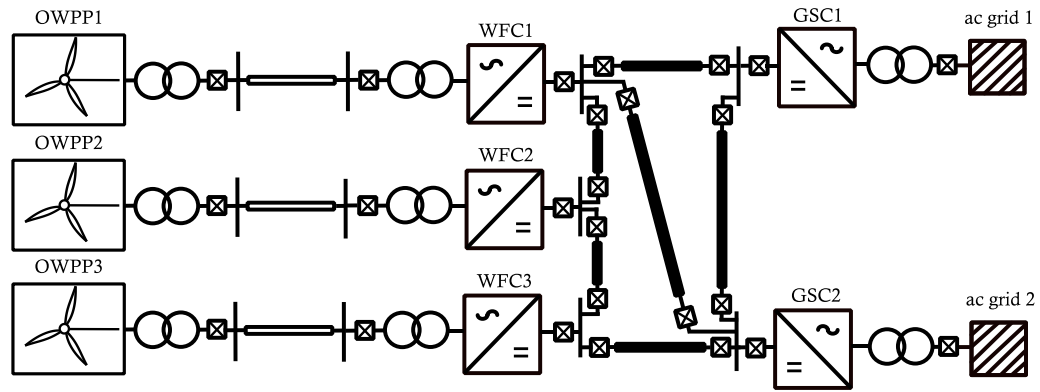
Offshore ac interconnections will increase the availability of the wind power transfer. This is because in case of outage in one of the components, *e.g.* dc transmission cables, ac export cables or HVDC converters, the wind power generation can be exported through the remaining cables or converters. In addition, ac interconnections allow the active power to be shared among the dc links, which can be used to reduce the power losses of the offshore transmission system. Another advantage is that ac breakers can be used to isolate the dc links in case of dc fault, as in the point-to-point configuration. This option has been presented as the Supernode Concept to build part of the future European Supergrid and it has been proposed by National Grid as the integrated strategy to connect the incoming long-distance OWPPs to Great Britain's grid [36], [37].

### 2.3.4 Offshore dc interconnections

As alternative, OWPPs can be interconnected with dc cables to form an offshore dc grid. Figure 2.4 shows an example of three OWPPs with two possible offshore dc grid topologies: multi-terminal dc grid (MTDC) and meshed dc grid.



(a) Multi-terminal dc grid



(b) Meshed dc grid

Figure 2.4: OWPP connected through an offshore dc grid.

Offshore dc interconnections offer the same advantages as the ac interconnections in terms of increasing availability and active power sharing. Meshed dc grids have additional redundancy compared to MTDC grids and they may provide N-1 contingency. However, the total cost of a meshed dc grid is higher due to additional dc cables that increase redundancy. An offshore dc grid requires dc circuit breakers to isolate the dc cables in case of dc fault or HVDC converter outage. DC circuit breakers are not commercially available, which limits the development of an offshore dc grid. AC breakers can be used, but the entire offshore dc grid has to be out of operation after a dc fault [38]. Also, other options based on HVDC converters with fault-blocking capability can be considered as alternative to the dc breakers [39]. Currently only two MTDC grids are in operation: Zhoushan Islands Interconnection and Nan'ao Wind Farm Integration [40], [41].

### 2.3.5 Future designs

In order to decrease the total cost of the offshore transmission system, alternative solutions have been proposed to reduce the size of the offshore HVDC platform or remove it completely. The offshore HVDC converter can be replaced by a diode rectifier, which reduces the converter dimensions and increases the robustness in offshore environments [42]. Other options are based on dc collector systems, where the ac export cables and the ac collector cables are replaced by dc cables. In these configurations, the offshore HVDC converter is replaced by an isolated dc-dc converter, which allows a smaller footprint of the offshore platform due to the use of medium frequency transformers [43]. Also, the offshore platform can be removed and the wind power is transferred to the onshore grid through medium voltage dc cables

[44]. In this case, the WTs are connected to dc feeders at voltages around  $\pm 60$  kV through ac-dc converters. Then, the power is transferred directly to an onshore substation and transformed back to ac voltage through small dc-ac converters connected to each dc feeder or through a large converter in bipolar configuration if the dc feeders are clustered in two groups.

## 2.4 CONTROL OF HVDC-CONNECTED WIND POWER PLANTS

### 2.4.1 General control scheme

Figure 2.5 shows the general control scheme of a HVDC-connected OWPP [11]. The main control blocks are: Grid Side Converter (GSC) control, Wind Farm Converter (WFC) control, Wind Power Plant (WPP) control and WT control. The details of the HVDC converter controls and the WPP control are presented in this section, whereas the WT control is described in Chapter 4 and Appendix C.

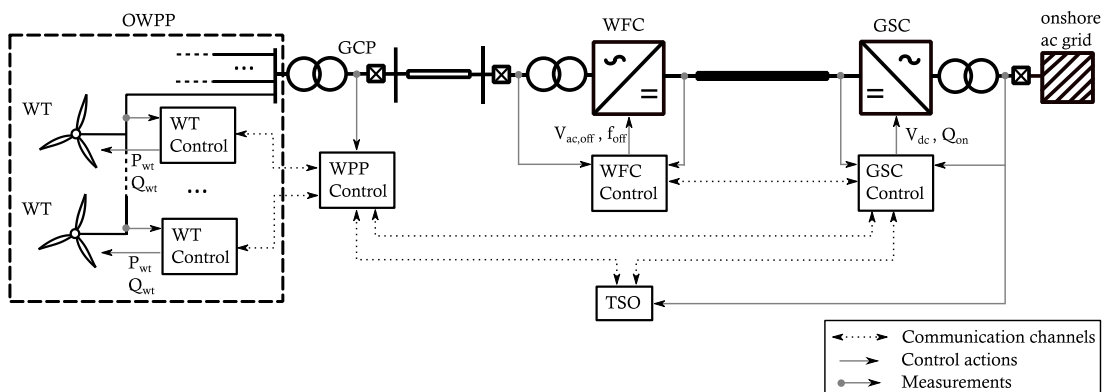


Figure 2.5: General control scheme of a HVDC-connected OWPP

The WFC generates the offshore ac voltage for the WTs, transfers the wind power to the HVDC transmission system and can supply reactive power to the export and collector cables. The GSC controls the dc voltage of the HVDC transmission system and transfers the wind power to the onshore ac grid. The WPP control is responsible for the active and reactive power dispatch of the WTs. The power references are sent from the WPP controller to each WT through communications channels. TSOs have communication with the GSC or the WPP control to request ancillary services for the onshore ac grid. Also, TSOs can request power reductions to the WPP controller for congestion management.

The WTs provide ancillary services to the onshore grid if there is an artificial coupling between the onshore and offshore ac grids. Fast communication between the GSC and the WFC or WPP controller can be used to transfer the variations of onshore frequency and ac voltage to the WTs [45]. Alternatively, artificial coupling can be achieved without fast communication between VSCs [46]. In this case, GSC transfers the variation of onshore frequency or ac voltage as a dc voltage, which is used as a communication signal that is measured by the WFC.

## 2.4.2 Wind Power Plant Control

The WPP control is a centralised controller that defines the active and reactive power scheduling of the WTs based on measurements from the Grid Connection Point (GCP) of the OWPP, the available wind power and the requirements from the TSOs. Figure 2.6 shows an example of the WPP control structure proposed by the Technical University of Denmark (DTU) [47].

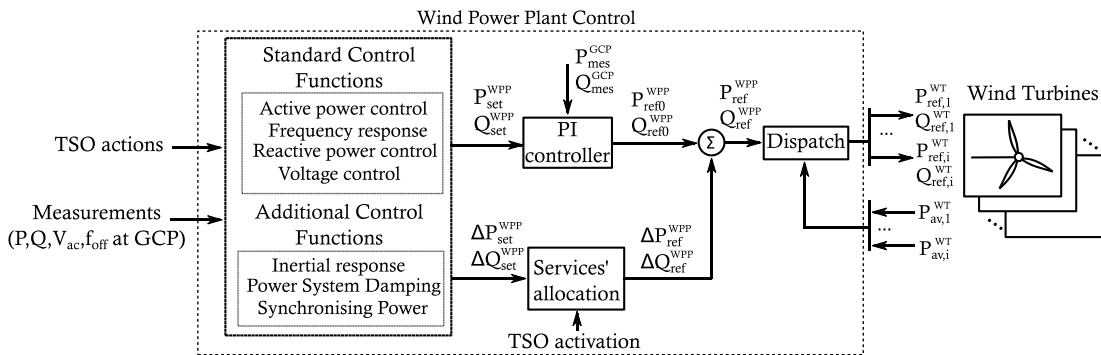


Figure 2.6: WPP control based on [47].

The WPP has a number of control functions that can be activated manually by the TSO or automatically by using measurements at the GCP. According to [47] there are two types of control functions: standard control functions and additional control functions. The standard control functions are services required by TSOs and include active power control, frequency response, reactive power and voltage control. The additional control functions are services expected to be implemented in WPPs and include inertia response, power system damping and synchronising power. Fault Ride Through (FRT) is not included as control function because it is implemented at WT level [47]. The WPP control functions have to be coordinated with the operation of the HVDC transmission system, as explained more in detail in Section 2.5.

The standard control functions provide active and reactive power set-points,  $P_{set}^{WPP}$  and  $Q_{set}^{WPP}$ , that are regulated by a PI controller using power measurements at the GCP,  $P_{mes}^{GCP}$  and  $Q_{mes}^{GCP}$ . The power references from the additional control functions,  $\Delta P_{ref}^{WPP}$  and  $\Delta Q_{ref}^{WPP}$ , are included as feed-forward components after the PI controller outputs,  $P_{ref0}^{WPP}$  and  $Q_{ref0}^{WPP}$  [47]. The PI controller is designed to have a response much slower than the WT control. This allows the additional control functions to operate simultaneously with the standard functions without interaction. The WPP dispatch receives the total active and reactive power references,  $P_{ref}^{WPP}$  and  $Q_{ref}^{WPP}$ , and sends power references to the WTs,  $P_{ref,i}^{WT}$ , according to the available wind power generation of each WT,  $P_{av,i}^{WT}$ .

### 2.4.3 Grid Side HVDC Converter Control

Figure 2.7 shows the general control scheme of a GSC. This VSC is controlled using a vector control strategy, where the  $d$ -axis regulates dc voltage or active power and the  $q$ -axis controls reactive power or ac voltage. The outer loops use PI controllers to compute the ac current references,  $i_d^*$  and  $i_q^*$ , which are fed to the inner loop, as illustrated in Figure 2.7. Also, a Phase Locked Loop (PLL) tracks the phase of the onshore ac voltage, which is used in the vector control to obtain the  $dq$  components.

In an offshore dc grid with several HVDC converters, the GSCs are coordinated using two main options: master-slave control or distributed dc voltage control [48]. In master-slave control, one of the GSCs regulates the dc voltage (master converter) and the others regulate active power (slave converters). The outage of the master converter can cause a blackout in the dc grid, unless another converter takes over the dc voltage regulation. In distributed dc voltage control, a number of GSCs regulate dc voltage and share the active power transfer using a droop control of active power – dc voltage, which is enabled when  $k_{pv}$  or  $k_{vp}$  are non-zero in Figure 2.7. In case of multiple GSCs connected to an onshore ac grid, reactive power and ac voltage regulation can be coordinated with a droop control of reactive power – ac voltage, which is enabled when  $k_{qv}$  or  $k_{vq}$  are non-zero in Figure 2.7.

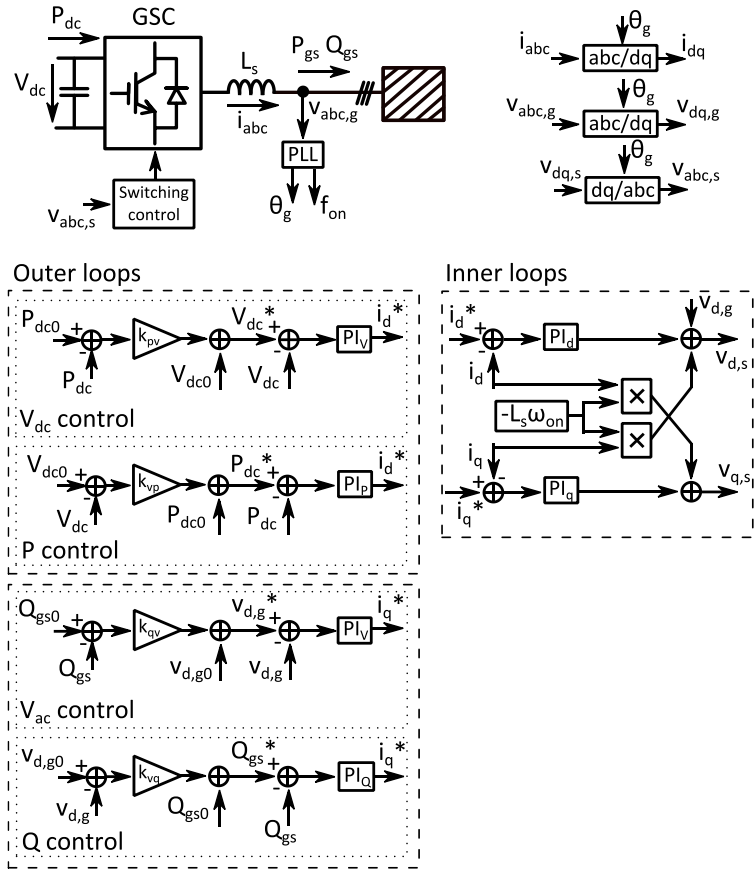


Figure 2.7: Control scheme for GSCs using vector control

## 2.4.4 Wind Farm HVDC Converter Control

Figure 2.8 shows the general control scheme of a WFC. This VSC controls the voltage and frequency of the offshore ac grid. The voltage control can be implemented with an amplitude control or a vector control based on an outer voltage loop and an inner current loop, as illustrated in Figure 2.8 [49]–[52]. If the WFC is an MMC, the high frequency filter (represented as the capacitor  $C_s$  in Figure 2.8) is not necessary and only an outer voltage loop can be used in the vector control [53]. The frequency and phase of the offshore grid are generated by an oscillator.

In case of multiple WFCs connected to an offshore ac grid, the ac voltage control can be coordinated by the converters using a reactive power – ac voltage droop control, which is enabled when  $k_{pf}$  is non-zero [50]. Also, the active power can be shared between the converters using a droop control of active power – frequency, which is enabled when  $k_{qv}$  is non-zero [50], [54].

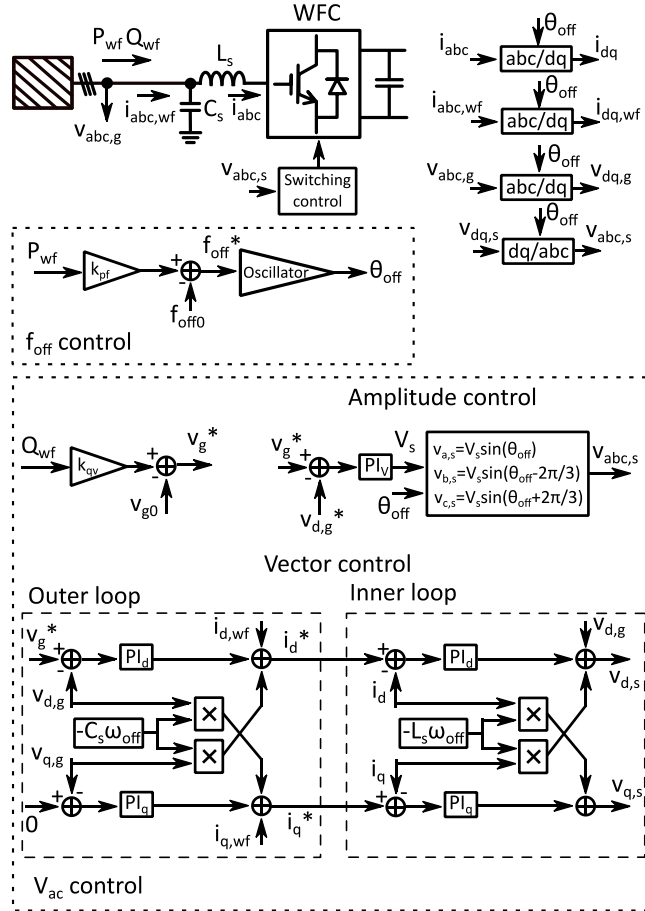


Figure 2.8: Control scheme for WFCs using amplitude control or vector control.

### 2.4.5 Converter Control Interactions

The large number of converters in HVDC-connected OWPPs can cause operational problems due to converter control interactions. OWPPs can become unstable if poorly damped resonances of the offshore ac or dc system interact with the converters. In [55] grid resonances are classified in two main categories: harmonic resonances and near-synchronous resonances.

Harmonic resonances are in the range from hundreds of Hz to few kHz. They are caused by the interaction of electrical resonances with the switching control and the inner current or voltage loop control of the VSCs. In HVDC-connected OWPPs electrical resonances originate from the inductive and capacitive characteristic of cables, transformers and filters of the offshore system [11], [19], [20]. Harmonic instabilities will occur in OWPPs if resonances are excited by the harmonic emission of the converters or during specific operations, such as the offshore grid energisation

or switching operations in the offshore system due to unexpected or planned outages [20], [56].

Near-synchronous resonances are in the range from frequencies below the synchronous frequency  $f_0$  (subsynchronous resonances [57]) to values close to  $2 f_0$  (supersynchronous resonances). They are caused by the interaction of mechanical or electrical resonances with the inner loop control or the outer loop controls of the VSCs, *i.e.* active power control, dc voltage control, reactive power control, ac voltage control and PLL [51], [58], [59]. In HVDC-connected OWPPs mechanical interactions are only possible with WTs based on DFIG, because the stator is directly connected to the offshore ac grid [60].

## 2.5 FUNCTIONAL REQUIREMENTS

The functional requirements of an HVDC-connected OWPP can be classified according to Table 2.1.

Table 2.1: Functional requirements in HVDC-connected OWPPs

<b>Function</b>	<b>Onshore ac grid</b>	<b>Offshore ac grid</b>	<b>Overall system</b>
<i>Active Power Management</i>			x
<i>Reactive Power and Voltage Support</i>	x	x	
<i>Frequency Support</i>	x		
<i>Inertia Response</i>	x		
<i>Fault Ride Through</i>	x	x	
<i>Short Circuit Current Contribution</i>	x	x	
<i>Power Oscillation Damping</i>	x		

The onshore control functions are related to grid code requirements of the onshore grid. The requirements defined for WPPs, dc-connected systems and offshore-connected systems are also applied for HVDC-connected OWPPs. These control functions are provided by the GSC or in coordination with the WFC and the OWPP.

Offshore ac grids connected through HVDC systems are islanded grids with a large number of power converters, which may define different requirements compared to the onshore grids. The offshore control functions are provided by WFCs and WTs. Currently, there are not grid codes for HVDC-connected offshore ac grids and it is assumed that the WTs connected to these islanded systems will follow the grid code requirements of ac-connected OWPPs [20].

### 2.5.1 Active power management

In low-medium wind speeds the OWPP extracts maximum power based on Maximum Power Point Tracking (MPPT) control at each WT and in high wind speeds the OWPP generates the nominal power. The WPP control reduces the active power and limits the rate of change of power when is required by the TSOs. Figure 2.9 illustrates the active power control functions. The wind power can be curtailed to have power reserve for congestion management or frequency response [47]. The power curtailment is achieved with balance control, which is a constant reduction of active power, or delta control (also known as power spinning reserve), which is an active power reduction proportional to the wind generation. In addition, a power ramp rate control is included to limit the increase or decrease of active power.

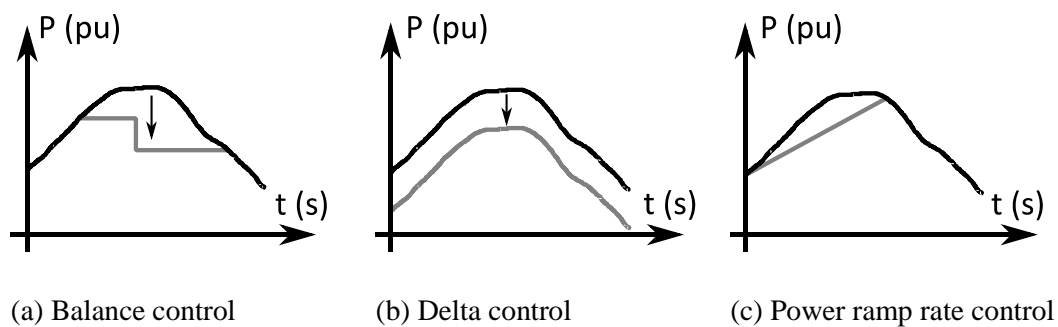


Figure 2.9: Active power control functions of OWPP.

### 2.5.2 Reactive Power Control and Voltage support

In the onshore ac grid, GSCs provide reactive power and ac voltage support based on grid code requirements at the onshore point of connection. The HVDC converter can operate in three different control modes: reactive power control, ac voltage control or power factor control. In Europe, ENTSOE has defined general requirements for dc-connected power park modules in relation to [18]:

- The maximum period of time that the converters must operate in different voltage ranges.
- The reactive power capability as a  $V - Q/P_{\max}$  profile that determines the operational boundaries of the converter as shown in Figure 2.10.
- The voltage transient response.

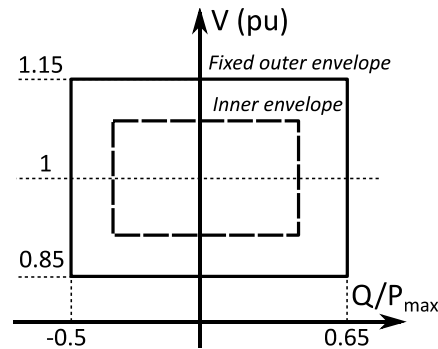


Figure 2.10: ENTSOE requirements for voltage at the grid connection point of a dc-connected system [18]. Voltage operational boundaries are function of  $Q/P_{\max}$ , where  $P_{\max}$  is the maximum active power transmission capacity. The outer envelope represents the maximum values fixed by ENTSOE. The inner envelope is defined by each system operator and it does not have to be a rectangle.

Also, a number of European system operators have more specific regulations. For example, Figure 2.11 shows the reactive power capacity diagram required by National Grid in Great Britain and Figure 2.12 shows the power factor diagram required by TenneT in Germany and National Grid.

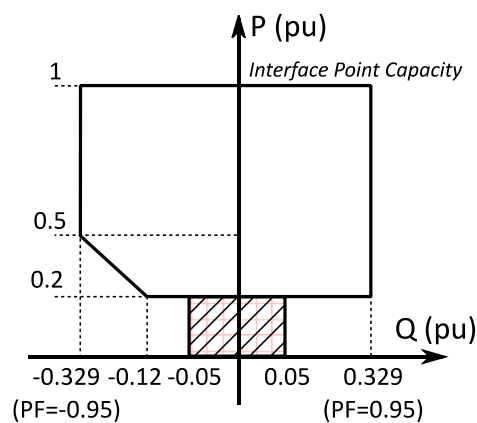


Figure 2.11: National Grid (Great Britain) requirements for reactive power capacity at the interface connection point of a WPP or a DC-connected system [61]. The  $Q$  values are expressed as function of the interface point capacity of the OWPP. The dashed area is an optional requirement for active power generation below 0.2 pu.

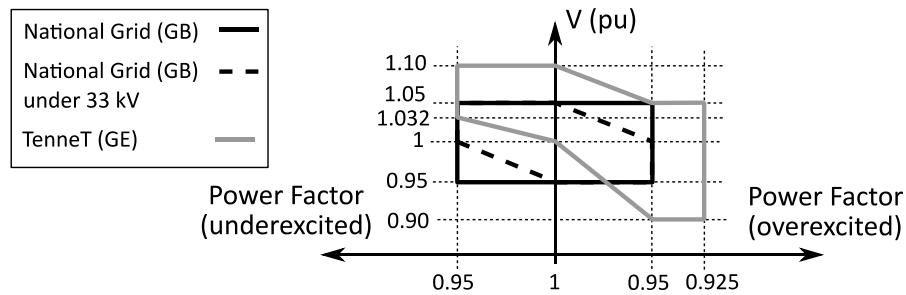


Figure 2.12: Voltage limits as function of power factor required by National Grid (Great Britain) in WPPs or DC-connected systems and TenneT (Germany) in offshore-connected systems [34], [61]. TenneT defines the nominal voltage at the onshore connection point in 155 kV. National Grid has different voltage levels (380, 220, 110 and 33 kV), but only high voltage is considered for OWPPs.

In the offshore ac grid, the voltage is regulated by the WFCs. The WTs can be set to control reactive power, ac voltage or power factor. The minimum requirements in the offshore ac grid are to keep the ac voltage within safe limits and to compensate the reactive power of the medium voltage collector cables and the high voltage export cables. Passive reactive compensators can be installed on the offshore platforms or WTs at the expense of increasing the total installation costs. Also, WFCs and WT grid-side converters can supply reactive power to the offshore ac grid. If all converters supply reactive power, an optimal power flow can be defined to minimise power losses or to reduce the size or number of passive compensation components [29], [49].

Grid codes define requirements for ac-connected OWPPs at the connection point of the offshore ac grid. For example, TenneT defines the PQ-diagram shown in Figure 2.13 for each WT. National Grid does not define specific requirements for each WT, but the reactive power transfer at the offshore grid entry point of OWPPs must be zero.

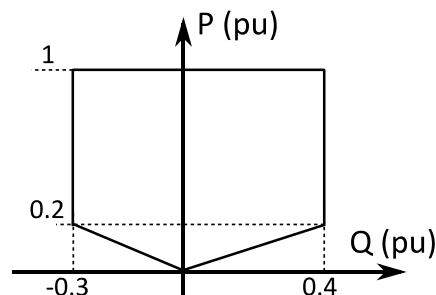


Figure 2.13: TenneT (Germany) requirements for reactive power capacity supplied by a generator unit at the grid connection point [34].

In addition, a number of system operators require WTs to provide voltage control during fault conditions. For example, TenneT defines a reactive power – ac voltage droop characteristic, as shown in Figure 2.14. Also, the reactive power injection from each WT has to be coordinated to prevent ac overvoltage at the terminals located far from the fault [49].

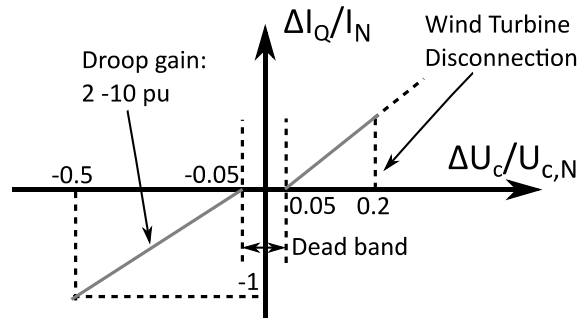


Figure 2.14: Voltage support during ac fault required by TenneT (Germany) in generating units [34].

### 2.5.3 Frequency Support

OWPPs can provide frequency response to the onshore grid as conventional synchronous generators. In case of overfrequency events, WTs reduce the active power output using pitch angle control [62]. If WTs are required to respond to underfrequency events, they must operate in deloaded mode, *i.e.* below maximum power extraction, during normal operation to ensure a power reserve margin. The deloading operation of the WTs is achieved by rotor speed control or pitch angle control [63].

Frequency response can be activated manually by TSOs as a temporary variation of active power, *i.e.* based on balance or delta control. Also, the WTs can respond automatically if they have information about the onshore frequency. This response can be a temporary variation of active power or a droop control that exchanges additional active power according to the onshore frequency variation.

OWPPs connected through HVDC links are decoupled from onshore frequency variations. HVDC converters and the WPP control can be coordinated to transfer the onshore frequency information to the WTs and activate the frequency response. Such frequency coupling between onshore and offshore ac grids can be implemented with fast communications between the VSCs or using the voltage of the HVDC system as an intermediate information signal between the GSC and the WFC [45], [46].

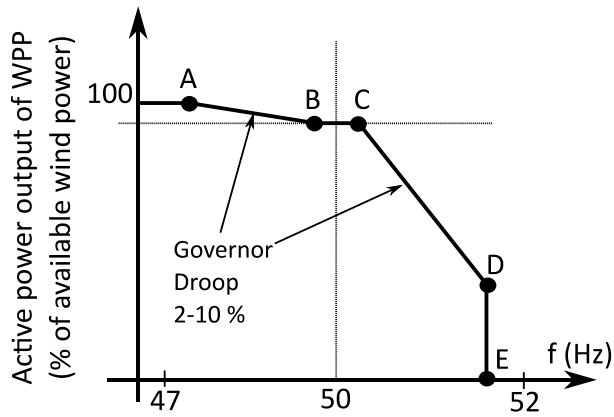


Figure 2.15: Frequency response characteristic required by EirGrid (Ireland) in WPPs [65]. Points A-E are defined depending on system conditions and location of the OWPP. Deadband frequency range is between B and C.

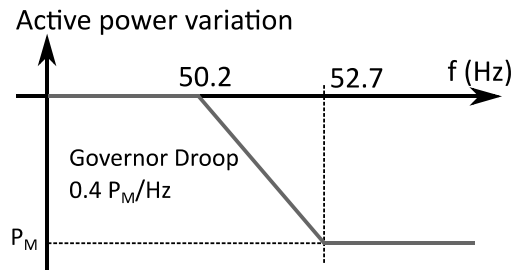


Figure 2.16: Frequency response characteristic required by TenneT (Germany) in offshore-connected systems [34]. The power reduction depends on the current available power,  $P_M$ .

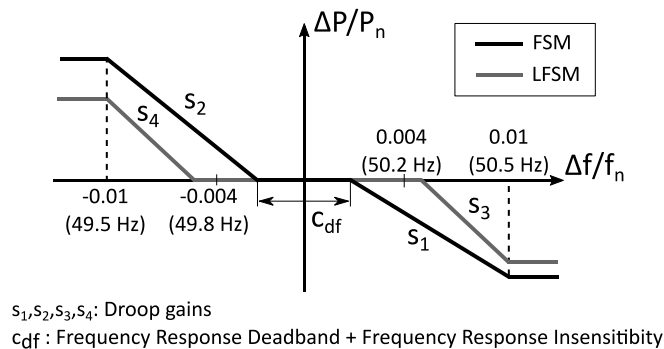


Figure 2.17: ENTSOE requirements for frequency response in DC-connected systems [18]. A Frequency Sensitive Mode (FSM) is defined for under and overfrequency events, whereas a Limited Frequency Sensitive Mode (LFSM) can be defined for a frequency trend or both. The droop gains  $s_1 - s_4$  are at least 0.1%, the maximum deadband is  $\pm 500$  mHz and the maximum insensitivity is 30 mHz. The LFSM is activated for frequency variations higher than 200 mHz.

Grid codes include requirements that define a droop control characteristic and the minimum response times [64]. As example, Figure 2.15 shows the response for under and overfrequency events required by EirGrid in Ireland. A number of system

operators only require response for overfrequency events, *e.g.* TenneT as shown in Figure 2.16. Also, ENTSOE defines the maximum period of time that the converters must operate in different frequency ranges and provides a range of values for parameters of the droop control, as described in Figure 2.17 [18].

### 2.5.4 Inertia Response

Inertia response is a fast frequency response service to limit the frequency variation and the Rate of Change of Frequency (RoCoF) of the onshore ac grid during the first seconds after a power imbalance. This service is activated automatically when the onshore frequency or RoCoF exceed a predefined threshold. OWPPs can provide inertia response through inertia emulation or operating in deloaded mode. Inertia emulation consists on using the kinetic energy stored in WT rotating mass to provide additional power to the onshore grid. Electrostatic energy from dc link capacitors of the HVDC system can be also used to emulate inertia [66]–[70]. The time response to release the energy from dc capacitors is faster than the WT rotating mass. However, the energy extracted from dc capacitors is limited unless large capacitors are utilised [66], [71]. Also, the dc choppers of the HVDC system can be used to absorb power during overfrequency events [72].

The grid codes are starting to introduce inertia response requirements for WPPs. System operators in Canada and Brazil have defined requirements as inertia emulation [73]–[75]. Also, inertia response has been proposed by a number of system operators as a short-term increase of active power. As example, National Grid has introduced a new service called Enhanced Frequency Response to provide support from solar PV, battery storage and WPPs [76], [77]. ENTSOE defines inertia response from dc-connected systems, but the specific requirements have to be agreed between a relevant TSO and the HVDC system owner [18].

### 2.5.5 Fault Ride Through Capability and DC Overvoltage

HVDC-connected OWPPs are required to have FRT capability, *i.e.* they have to remain connected to the onshore or offshore ac grid during temporary ac faults. The grid codes define a voltage-against-time characteristic that represents the minimum voltage that the VSCs have to withstand without disconnection.

In case of onshore ac faults, GSCs have to comply with the onshore grid codes. Figure 2.18 describes the FRT profile required by ENTSOE in HVDC-connected

power plants, where the voltage and time parameters are defined as a range of values at the grid connection point of the GSCs. Also, ENTSOE defines additional requirements, *e.g.* in case of asymmetrical faults or in relation to the post fault active power recovery [18].

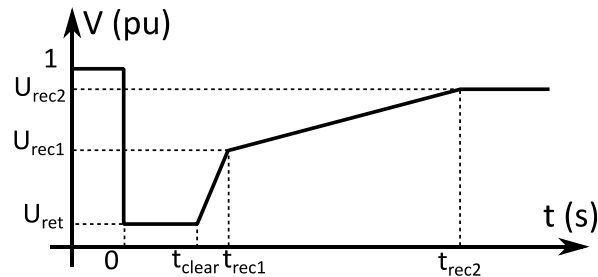


Figure 2.18: FRT profile required by ENTSOE at the grid connection point of HVDC-connected power plants [18].  $U_{ret}$  is the retained voltage during an ac fault,  $t_{clear}$  is the fault duration and  $(U_{rec1}, t_{rec1})$  and  $(U_{rec2}, t_{rec2})$  are limits defined during the fault recovery.

During an onshore ac fault the GSC power capacity is reduced, which will cause a power imbalance in the offshore transmission system if the wind power generation cannot be transferred to the onshore grid. As a consequence, there will be an overvoltage in the dc system. In case of offshore grid topologies with multiple GSCs, the wind power excess can be transferred through the other GSCs if they have available power capacity.

The dc overvoltage can be limited by using dc choppers in the HVDC system that absorb the power excess during an ac fault [78]–[80]. DC choppers are robust, fast and do not affect the OWPP operation. However, the use of a resistor with chopper circuit will have an additional cost and require space in the converter stations. This solution is currently used in existing HVDC-connected OWPPs [81]. In addition, the dc overvoltage can be prevented by reducing the wind power generation [80], [82], [83]. The GSCs connected to the faulty onshore grid and the OWPPs have to be coordinated, since the HVDC system decouples the offshore and onshore ac grids. Fast communications can be used to rapidly deload the WTs, but inherent delays or loss of communication may compromise the effectiveness of this option [83]. As alternative, local measurements of the WTs can be used to activate the power reduction. In this case, the WFCs reduce the ac voltage or increase the frequency of the offshore ac grid according to the dc overvoltage magnitude and this is used as an intermediate signal that is measured by the WTs [80], [82].

In case of offshore ac faults, FRT capability is required for WTs. Each WT follows FRT requirements at the connection point of the collection grid. Figure 2.19 shows a summary of FRT requirements for WTs in various grid codes [84]. Also, WTs have to reduce the wind generation or use a dc chopper to prevent overvoltage in the dc link of the back-to-back converter [85], [86]. WFCs have to remain connected to the offshore ac grid, but FRT requirements are not specified in the grid codes.

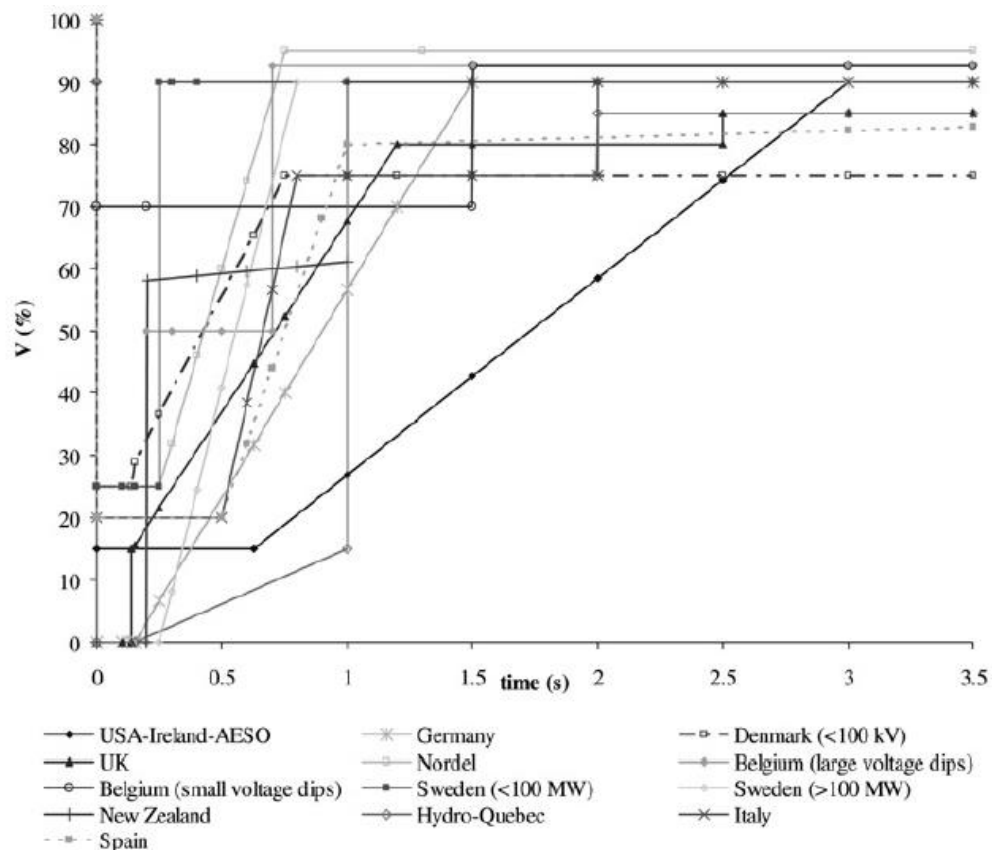


Figure 2.19: FRT requirements for WTs in different countries [84].

### 2.5.6 Short Circuit Current Contribution

During ac faults, the HVDC and WT converters can provide short circuit current, but the contribution is reduced due to the limited overload capacity of VSCs [87]. The injection of reactive short circuit current from VSCs is necessary to avoid maloperation of the ac protection systems and improve the voltage and transient stability of the onshore and offshore ac grids [88].

In case of onshore ac faults, GSCs provide short circuit current. GSCs have general onshore grid code requirements defined by ENTSOE to provide short circuit contribution as a fast fault current [18]. In case of offshore ac faults, WFCs and WTs

provide short circuit current. WFCs do not have grid code requirements, but general recommendations are found in [20]. WFCs should inject full short circuit current during three-phase faults and in case of asymmetrical faults, the converters should reduce the short circuit current contribution to prevent overvoltage in the healthy phases.

The short circuit current contribution of the WTs depends on the WT topology [20]. FRC-WTs can provide limited short circuit current, because the stator of the WT generator is connected to the offshore ac grid through a back-to-back converter. DFIG-WTs can provide high short circuit current, since the stator of the WT generator is directly connected to the offshore ac grid. However, a crowbar circuit in the rotor or a dc chopper in the back-to-back converter are necessary to absorb the short circuit currents and reduce stress on the WT generator. In case of asymmetrical faults, WT grid-side converters can control positive and negative sequence current separately. Negative sequence currents can be suppressed to allow injecting full positive sequence of short circuit current or can be injected to balance the grid voltage [20].

### **2.5.7 Power Oscillation Damping**

Active and reactive power from HVDC-connected OWPPs can be used to damp low frequency power oscillations of the onshore ac grid. Reactive power regulation is provided by the GSCs without contribution from the OWPPs [89], [90]. Active power regulation is provided by the WTs using pitch angle or converter control and must be coordinated with the HVDC converters. Active power might not be sufficient due to the limited short-term overload capability of WT VSCs. A combination of active and reactive power regulation can be used for optimal performance [89].

A number of control strategies have been presented in the literature to provide power oscillation damping from HVDC systems and WPPs, but grid code requirements are still under discussion [89], [91], [92]. For example, ENTSOE defines a power oscillation damping requirement, but the implementation details must be agreed between the owners of HVDC systems or OWPPs and the relevant TSOs [18].

## **2.6 SUMMARY**

In this chapter, three main topics have been discussed: HVDC transmission system configurations, control structures and functional requirements.

Existing HVDC-connected OWPPs use point-to-point links, which represents the simplest option with the lowest cost. More complex topologies with ac and dc interconnections between OWPPs increase redundancy and optimise the wind power transfer, but the initial investment also increases due to the installation of a larger number of components.

The generic control scheme of an HVDC-connected OWPP includes a WPP controller and the control of the onshore and offshore HVDC converters. Communication between control blocks is essential to coordinate the operation of the OWPP and the HVDC system and receive TSO requests.

HVDC-connected OWPPs have general functionalities for active power transfer and specific control functions for onshore and offshore grids. Onshore grid functionalities are mostly related to current and upcoming grid code requirements of TSOs. Offshore grids are islanded systems, where the operation can be optimised without limitations from onshore grid codes.

## CHAPTER 3

# INTERLINKS BETWEEN HVDC-CONNECTED OFFSHORE WIND POWER PLANTS

### 3.1 INTRODUCTION

The first HVDC-connected Offshore Wind Power Plants (OWPPs) were built in Germany and are based on point-to-point links [16]. Offshore cables may be installed between these existing OWPPs in order to increase reliability, minimise power losses, address intermittency of wind and increase trading capability between countries [20], [25], [26], [35], [93]. Such offshore cables are known as interlinks and are illustrated in Figure 3.1 [20]. The increase of reliability employing interlinks was studied in [94] using Dogger Bank offshore wind farms (in the UK) as a case study. However, interlinks increase the cost of the offshore transmission system. Therefore, an economic analysis was undertaken to evaluate the operational savings from reducing power losses and power curtailment when interlinks are installed between OWPPs.

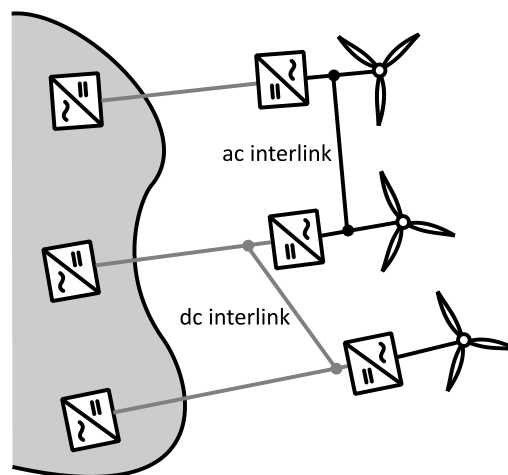


Figure 3.1: Representation of ac and dc interlinks.

This chapter analyses the contribution of three interlink options between two HVDC-connected OWPPs: (i) dc interlink between offshore HVDC converters, (ii) ac interlink between offshore HVDC converters and (iii) ac interlink between collector platforms (see Figure 3.3). The structure of this chapter with the associated sections is illustrated in Figure 3.2. Interlink options are compared in terms of power losses and

reliability and recommendations are proposed to decide the best interlink location. Power losses of the offshore components are reduced with an optimal power and voltage operation defined by the VSCs. Reliability is analysed according to the availability of each transmission system topology and using COPTs. An example of a cost-benefit analysis with real wind speed data is used to evaluate the interlink options and quantify operational savings. In addition, a design procedure is proposed to determine the interlink cable capacity based on power losses and availability requirements.

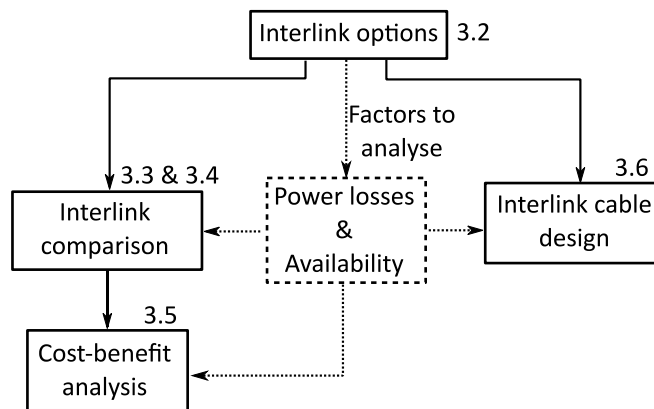


Figure 3.2: Structure of Chapter 3.

## 3.2 INTERLINK OPTIONS

An economic assessment is used to select an optimal interlink option. The objective of this assessment is to minimise the interlink investment cost and maximise the operational savings. The interlink topologies are defined by the following characteristics:

- *Location and length of the cable.* The interlink cables can be installed between HVDC converters or collector platforms. The cable location with the shortest length is preferred for cost reasons.
- *Cable types.* Options with dc and ac cables are compared. The cost and efficiency of the cables depends on their voltage and current ratings. Also, circuit breakers are required to isolate the interlink in case of fault or planned outage. However, dc breakers are not commercially available and they may be more expensive than ac breakers.

An HVDC interlink between onshore converters is not considered in the topology's comparison, because it is mainly used for energy trading between two countries or to increase the transmission capacity between two areas in the same country. Also, interlinks at medium voltage ac (MVAC) between collector platforms are not analysed, because MVAC cables, compared to equivalent HVAC cables, are not suitable for long distance interconnection and large power exchange between OWPPs [20]. Figure 3.3 highlights the interlinks that are analysed in the following sections, which are:

- *dc offshore converter interlink*, which is the HVDC interlink between offshore HVDC converters
- *ac offshore converter interlink*, which is the HVAC interlink between offshore HVDC converters
- *ac collector platform interlink*, which is the HVAC interlink between collector platforms.

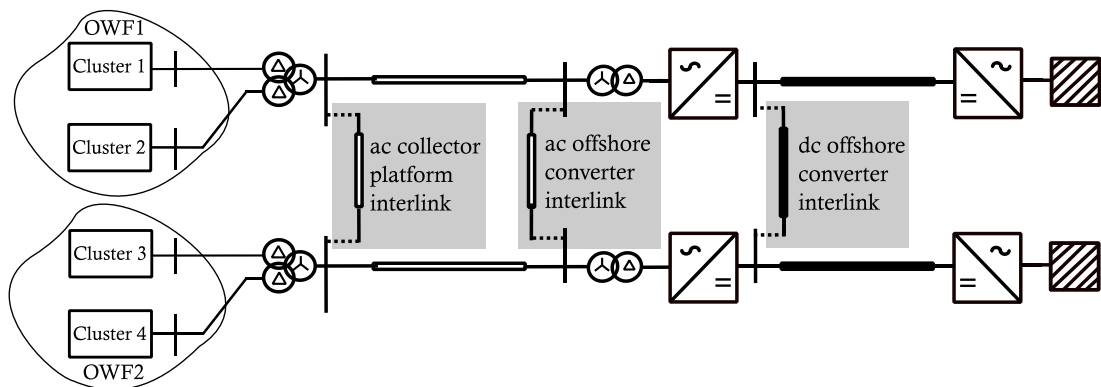


Figure 3.3: Interlink options between OWPPs.

The following factors are analysed to select the appropriate interlink cable:

- *Reduction of power losses*. Interlinks modify the power sharing between transmission systems. This reduces power losses, hence maximises the wind power transfer [20].
- *Increase of energy availability*. Interlinks provide an alternative supply route in case of planned disruption or potential faulted outage of transformers, cables or converters [20]. This reduces the wind power curtailment.

Operational savings will be achieved from a reduction of power losses and increased availability. These two factors are analysed in more detail in the following sections.

### 3.3 CASE STUDY

Two identical 492 MW HVDC-connected OWPPs are considered in this study. Figure 3.5 shows the general scheme of the OWPPs and the transmission system. The OWPPs are based on the layout of the *Fecamp* project [99]. There are 2 wind farm clusters with 41 WTs of 6 MW each one. These clusters are aggregated as single WTs in series with an impedance that has equivalent power losses to the detailed collector grid and the WT transformers [100]. The wind generation is represented as an injection of active power from each cluster.

The wind farms are connected to the collector grid operating at a voltage of 33 kV and the collector transformers step-up the voltage to 220 kV. The export cables have a transmission distance of 10 km and deliver the power to the offshore HVDC platform. The HVDC cables operate at dc voltage of  $\pm 320$  kV and transfer the power generated from the OWPP to the onshore HVDC substation over a transmission distance of 100 km. It is supposed that the HVDC and WT converters supply all the reactive power of the offshore grid and passive elements are not required. More details about the OWPPs specifications are found in Appendix H.

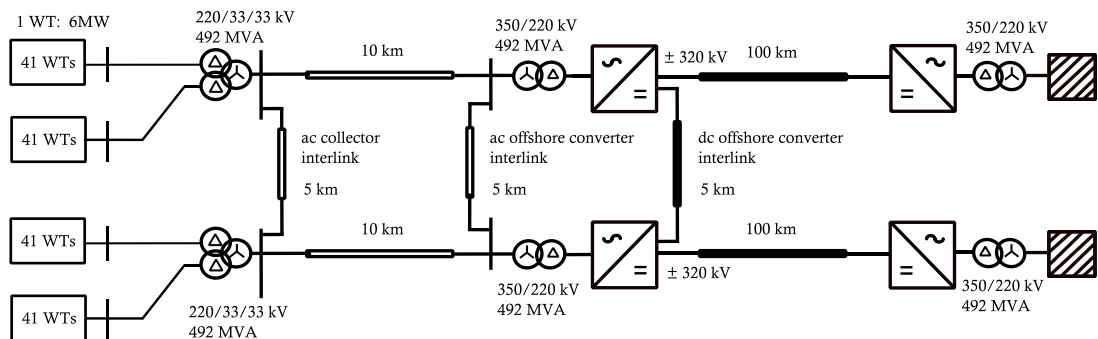


Figure 3.4: Case study with two HVDC-connected OWPPs used in power loss and availability analysis.

### 3.4 POWER LOSS ANALYSIS

An Optimal Power Flow (OPF) algorithm is used to minimise the power losses in HVDC-connected OWPPs. Power loss reduction in the transmission system is quantified when optimal power and voltage are scheduled by the VSCs

### 3.4.1 Possibilities to Reduce Power Losses

VSCs of HVDC-connected OWPPs can control the following magnitudes:

- ac voltage in the offshore ac grid
- dc voltages in the HVDC transmission system.
- reactive power compensation in the offshore ac grid
- active power sharing through the interlinks

If ac and dc voltages are increased the total power losses are reduced. However, power system equipment has voltage limits, which should not be exceeded during normal operation. The ac voltage of the offshore ac grid is controlled by offshore HVDC converters and the dc voltage of the dc links is controlled by onshore HVDC converters.

Offshore HVDC converters and WT grid-side converters supply the necessary reactive power for the components of the offshore ac grid. The reactive power supply can be optimally scheduled to minimise power losses. In a single point-to-point HVDC-connected OWPP, optimal voltages and reactive power supply reduce power losses without using interlinks.

For multiple HVDC-connected OWPPs, interlinks are used to exchange active power and wind power generation is optimally scheduled between the OWPP transmission systems to further reduce the power losses. Offshore HVDC converters control the active power sharing in ac interlinked options and onshore HVDC converters are responsible for the active power sharing in dc interlinked options.

### 3.4.2 Model for Optimal Power Flow Analysis

Figure 3.5 shows the model of the case study in Section 3.3, where the HVDC converters, WTs, buses and admittances are enumerated. The dc cable between buses 3 - 4 and the offshore ac cables between buses 3 - 4 and buses 5 - 6 are the possible interlink options. The offshore and onshore ac grids are represented as admittance matrices, where,

- The ac cables are single  $\pi$  sections with  $\bar{y} = y\angle\varphi = \frac{1}{r+jx_l}$  and  $\bar{y}_c = j\frac{b_c}{2}$
- The transformers are RL circuits with  $\bar{y} = y\angle\varphi = \frac{1}{r+jx_l}$

The offshore dc grid is represented as a conductance matrix, where the dc cables are resistances with  $g = 1/r$ . The HVDC and WT converters are modelled as an injection of active and reactive power with power losses. This representation is sufficient for OPF analysis.

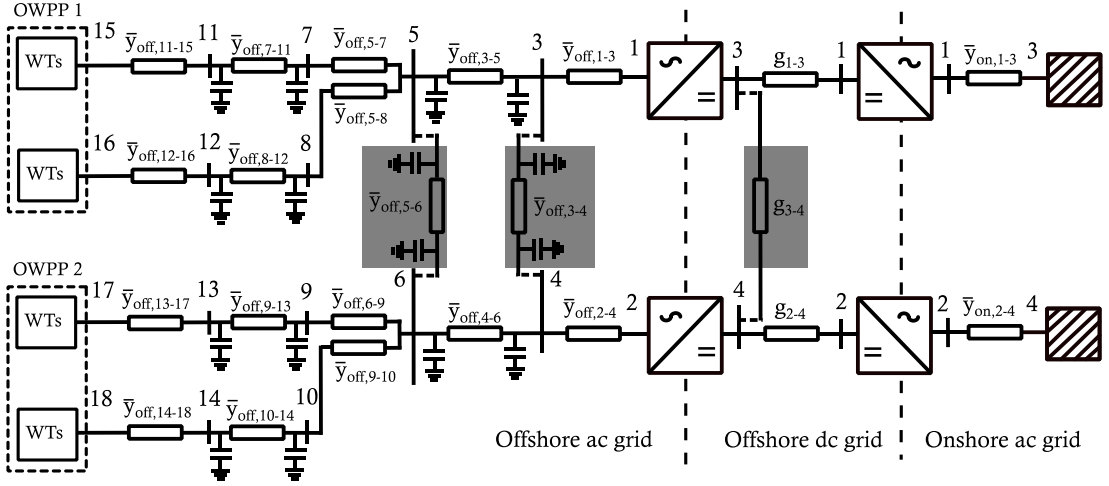


Figure 3.5: Model of the case study with enumeration of converters, buses and admittances (interlink cables options are indicated in grey rectangles).

### 3.4.3 Optimal Power Flow Formulation

The OPF is defined as:

$$\text{Minimize } f(\mathbf{x}, \mathbf{u}) = p_{losses,T} \quad (3.1)$$

$$\text{subject to: } \mathbf{g}(\mathbf{x}, \mathbf{u}) = 0 \text{ and } \mathbf{h}(\mathbf{x}, \mathbf{u}) \leq 0$$

where  $f$  is the objective function,  $\mathbf{x}$  is the vector of state variables,  $\mathbf{u}$  is the vector of control variables to optimise,  $\mathbf{g}$  are the equality constraints and  $\mathbf{h}$  are the inequality constraints of the optimisation problem. More details about the variables are found in Appendix B. The OPF is solved with the interior-point algorithm and using the function *fmincon* from MATLAB.

The objective function of this OPF is to minimise power losses of the transmission system and the VSCs. The expression of the objective function is:

$$p_{losses,T} = p_{loss,ac\_cb} + p_{loss,dc\_cb} + p_{loss,tr} + p_{loss,hvdc\_conv} + p_{loss,wt\_conv} \quad (3.2)$$

where the subscript  $ac\_cb$  represents ac cables,  $dc\_cb$  represents dc cables,  $tr$  represents transformers,  $hvdc\_conv$  represents HVDC converters and  $wt\_conv$  represents WT converters.

The HVDC and WT converter power losses are expressed as:

$$p_{loss,conv} = a + b \cdot i_c + c \cdot i_c^2 \quad (3.3)$$

where  $a$ ,  $b$  and  $c$  are the power loss coefficients that depend on the converter topology and  $i_c$  is the converter current. All these magnitudes are in per-unit considering the rated power and voltage of a converter as base values. The coefficient  $a$  represents constant power losses due to auxiliary equipment (*i.e.* lightning, heating, cooling and control systems), the coefficient  $b$  represents the switching losses of the valves and the coefficient  $c$  represents the conduction losses of the valves. The converter current is formed by the active and reactive power exchange with the ac grid:

$$i_c = \frac{\sqrt{p_c^2 + q_c^2}}{u_c} \quad (3.4)$$

The WT converters are represented as 2-level VSCs and the HVDC converters as MMCs. The power loss coefficients for the WT converters were obtained from [95]. The coefficients for a 2-level VSC-HVDC converter were obtained from [96], but if a multi-level converter topology is considered the power losses are half than in a 2-level VSC [97], [98]. Table 3.1 shows the coefficients used in this study. It is observed that the constant power losses in the MMCs are significantly higher than in the 2-level VSCs. This is because MMC-HVDC substations require more auxiliary equipment than WT 2-level VSCs for the same rated power.

Table 3.1: Power loss coefficients of different converters expressed in per-unit [95]–[98].

Converter	a	b	c
<i>Wind Turbine 2-level VSCs</i>	0.00048	0.0097	0.0048
<i>MMC-HVDC</i>	<i>Offshore converter (rectifier)</i>	0.0042	0.0015
	<i>Onshore converter (inverter)</i>	0.0042	0.0014

More details about the power loss expression of each component are found in Appendix B.

The equality constraints correspond to power flow equations in ac and dc grids. In ac grids, the following equations are defined at each bus for active and reactive power flows:

$$\sum_{j \neq i}^{N_{bus,ac}} p_{i-j} + p_{hvdc\_ac,i} - p_{wt,i} = 0 \text{ for } i = 1, \dots, N_{bus,ac} \quad (3.5)$$

$$\sum_{j \neq i}^{N_{bus,ac}} q_{i-j} + q_{hvdc,i} - q_{wt,i} = 0 \text{ for } i = 1, \dots, N_{bus,ac} \quad (3.6)$$

where  $N_{bus,ac}$  is the number of buses in the ac grids. The active power flow from bus  $i$  to bus  $j$  can be expressed as [159]:

$$p_{i-j} = y_{i-j} v_i v_j \cos(\theta_i - \theta_j - \varphi_{i-j}) \quad (3.7)$$

$$q_{i-j} = y_{i-j} v_i v_j \sin(\theta_i - \theta_j - \varphi_{i-j}) - \frac{b_c}{2} v_i^2 \quad (3.8)$$

where  $b_c = 0$  if the branch between bus  $i$  and  $j$  is a transformer.

In the dc grid, the following equations are defined at each bus for current flows:

$$\sum_{j \neq i}^{N_{bus,dc}} i_{i-j} + i_{hvdc,i} = 0 \text{ for } i = 1, \dots, N_{bus,dc} \quad (3.9)$$

where  $N_{bus,dc}$  is the number of buses in the dc grid. The currents from bus  $i$  to bus  $j$  and the currents from the HVDC converters are expressed as:

$$i_{i-j} = g_{i-j} (v_{dc,i} - v_{dc,j}) \quad (3.10)$$

$$i_{hvdc,i} = \frac{p_{hvdc\_dc,i}}{v_{dc,i}} \quad (3.11)$$

The power flow through the HVDC converters is expressed as:

$$p_{hvdc\_ac} - p_{hvdc\_dc} - p_{loss,hvdc} = 0 \quad (3.12)$$

where the equation for  $p_{loss,hvdc}$  is (3.3).

In addition, more equality constraints are necessary when the OPF does not optimise the powers or voltages of the system. These constraints were used in Section 3.4.4 to analyse the contribution of reactive power and voltage optimisation.

If voltages in the offshore ac grid are not optimised, offshore HVDC converters control POC voltage at 1 pu:

$$v_{off,3} = v_{off,4} = 1 \text{ pu} \quad (3.13)$$

If reactive power supply of the offshore ac grid is not optimised, the reactive power from WTs is equal to zero and offshore HVDC converters supply all reactive power:

$$q_{wt,i} = 0 \text{ for } i = 15, \dots, 18 \quad (3.14)$$

The inequality constraints correspond to voltage and current limits. The ac and dc voltage limits assume a  $\pm 10\%$  deviation from the nominal value:

$$\begin{cases} 0.9 \text{ pu} < v_{off,i} < 1.1 \text{ pu} \text{ for } i = 1, \dots, 18 \\ 0.9 \text{ pu} < v_{on,i} < 1.1 \text{ pu} \text{ for } i = 1, \dots, 4 \\ 0.9 \text{ pu} < v_{dc,i} < 1.1 \text{ pu} \text{ for } i = 1, \dots, 4 \end{cases} \quad (3.15)$$

The current limits are considered in cables, transformers and converters. The current limits in ac cables and transformers are expressed as:

$$\frac{\sqrt{p_{i-j}^2 + q_{i-j}^2}}{v_i} \leq i_{max}, \quad \frac{\sqrt{p_{j-i}^2 + q_{j-i}^2}}{v_j} \leq i_{max} \quad (3.16)$$

$$\text{for } i, j = 1, \dots, N_{bus,ac}$$

The current limits in dc cables are expressed as:

$$g_{i-j}(v_{dc,i} - v_{dc,j}) \leq i_{dc,max} \text{ for } i, j = 1, \dots, N_{bus,dc} \quad (3.17)$$

The current limits in VSCs are expressed as:

$$\frac{\sqrt{p_c^2 + q_c^2}}{v_c} \leq i_{c,max} \quad (3.18)$$

where  $p_c$ ,  $q_c$  and  $v_c$  are the powers and voltage at the ac side of the VSCs.

Figure 3.6 shows the inputs and outputs used in the OPF algorithm. The interlink option is selected as part of the configuration of the system. The optimisation modes are subject to the equality constraints defined by ( 3.13 ) and ( 3.14 ). The voltage and current limits are defined as the inequality constraints in ( 3.15 ) - ( 3.18 ). The control variables represent the reference variables to control the VSCs. The OPF updates the control variables according to the wind power generation.

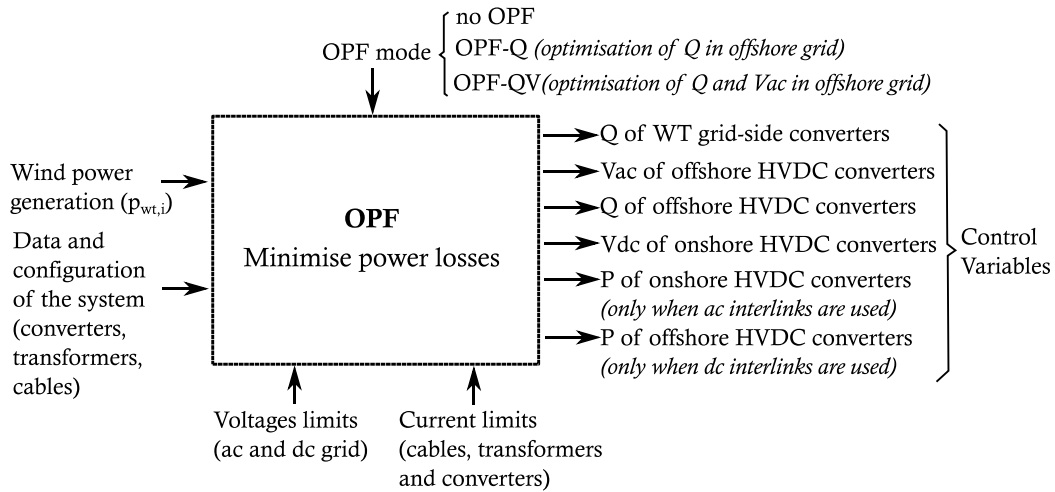


Figure 3.6: Inputs and outputs of Optimal Power Flow.

### 3.4.4 Analysis of a Single Offshore Wind Power Plant

A single HVDC-connected OWPP is analysed to quantify the power loss reduction due to voltage and reactive power optimisation. Three scenarios are studied:

- No OPF: offshore HVDC converters control POC voltage at nominal value and supply all reactive power of the offshore ac grid (*i.e.* power flow is subject to ( 3.13 ) and ( 3.14 )).
- OPF-Q: reactive power supply of the offshore ac grid is optimally shared between offshore HVDC and WT converters to minimise power losses and offshore HVDC converter controls POC voltage at nominal value (*i.e.* power flow is subject to ( 3.13 )).
- OPF-QV: reactive power supply and voltage of the offshore ac grid are optimally scheduled to minimise power losses. Reactive power supply is shared between offshore HVDC and WT converters and the POC voltage is regulated by the offshore HVDC converter assuming a maximum  $\pm 10\%$  deviation from the nominal value.

Figures 3.7 and 3.8 show the total power losses and reactive power results in relation to the wind generation. All the values are expressed in per-unit with base power equal to the rated power of an OWPP, which is 496 MVA. Power losses increase with the wind generation and reach approximately 0.05 pu at nominal power. When the reactive power supply is optimally shared between offshore HVDC and WT converters (OPF-Q) the power losses are reduced by up to 2-3% compared to the case without optimisation. If the reactive power supply and POC voltage set points are optimised (OPF-QV) the power loss reduction is up to 10%.

Without optimisation, the offshore HVDC converters have to provide up to 0.4 pu of reactive power. When reactive power supply is optimised the offshore HVDC converters reduce their power contribution by up to 50% (*i.e.* 0.2 pu), but the WT converters increase their reactive power supply by up to 0.2 pu. If the POC voltage set points are optimised the reactive power supply of the WT converters is reduced by up to 50% (*i.e.* 0.1 pu) compared to the case without optimisation.

The OWPPs are characterised by a power losses vs. wind generation function, which is expressed with a second order polynomial as:

$$P_{loss,OWPP} = a_{loss} + b_{loss} \cdot P_{OWF} + c_{loss} \cdot P_{OWF}^2 \quad (3.19)$$

This expression is obtained from power flow calculations or from real measurements at the offshore and onshore substations. The coefficients of the power losses in Figure 3.7a are obtained in Table 3.2.

Table 3.2: Power loss coefficients of single HVDC-connected OWPP in different OPF options expressed in per-unit.

OPF option	$a_{loss}$	$b_{loss}$	$c_{loss}$
No OPF	0.0103	0.0111	0.0329
OPF-Q	0.0101	0.0126	0.0301
OPF-QV	0.0102	0.0108	0.0275

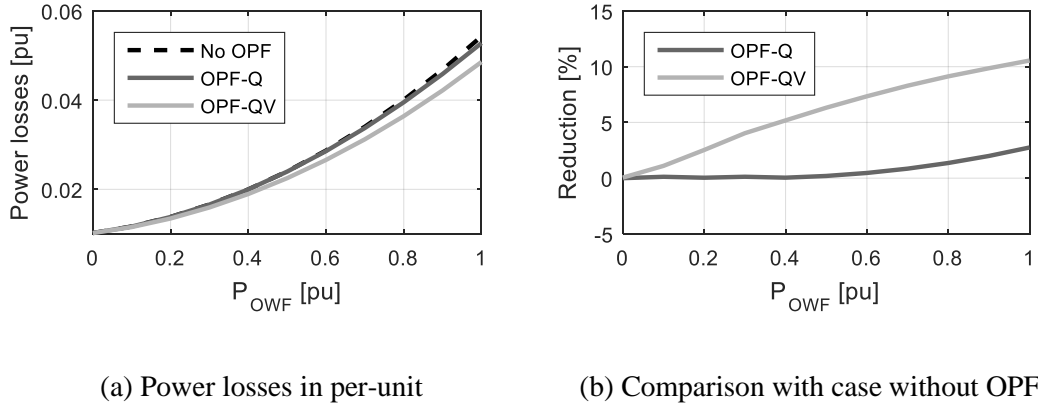


Figure 3.7: Total power losses in a single HVDC-connected OWPP for different OPF options and wind generations,  $P_{OWF}$ .

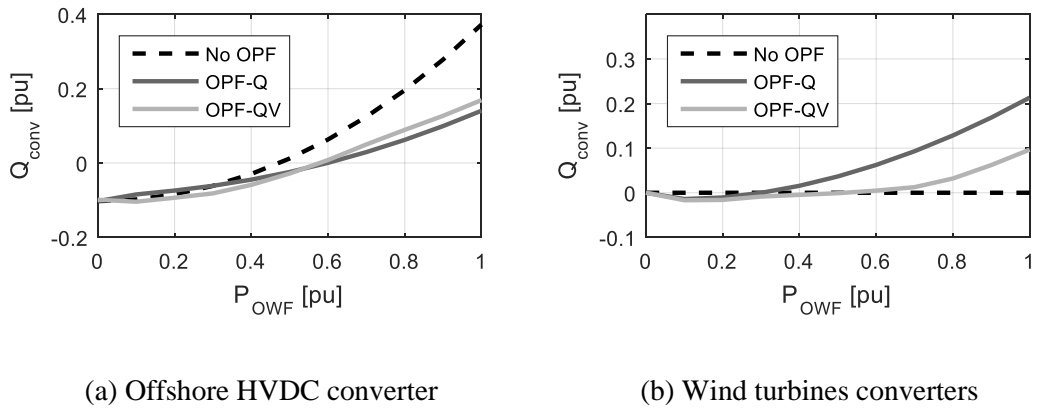
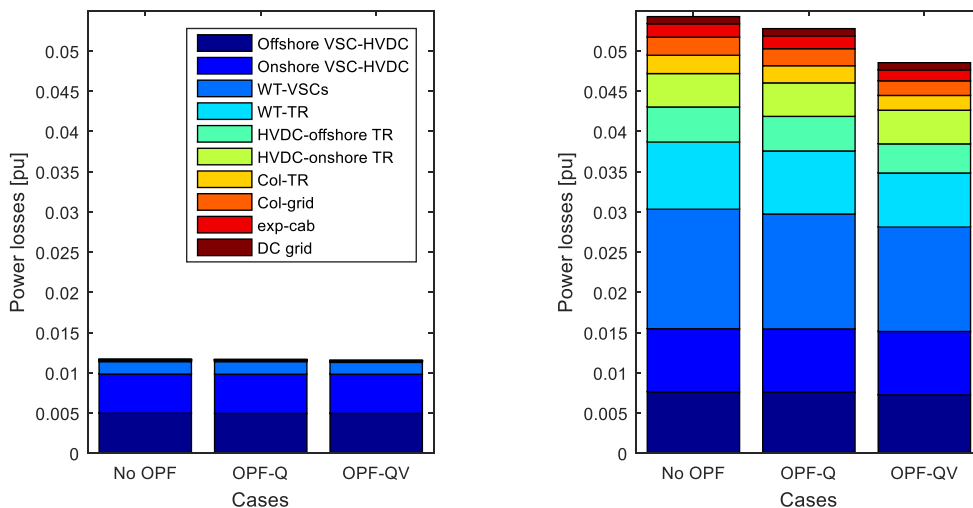


Figure 3.8: Reactive power supply from offshore converters in a single OWPP for different OPF options and wind generations,  $P_{OWF}$ .

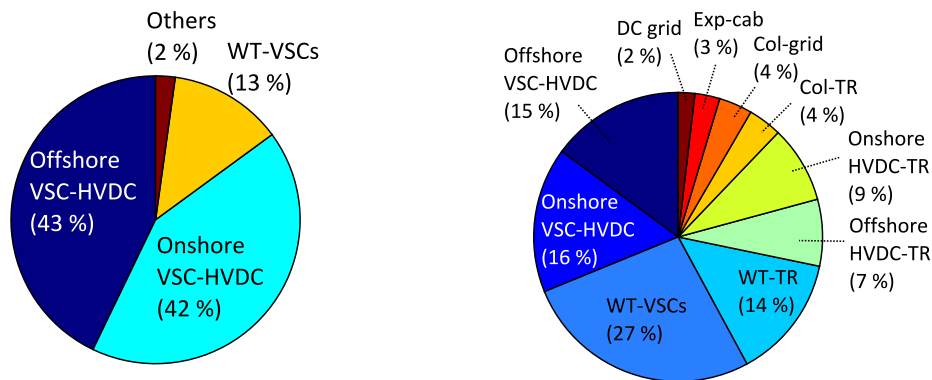
The power loss distribution is analysed in Figures 3.9 and 3.10. Converter power losses account for more than 50% of the total power losses (98% when wind generation is 0.1 pu and 58% when wind generation is 1 pu) due to the constant term of converter power losses (coefficient  $a_{loss}$  in Table 3.1). The transformers account for more than 50% of the non-converter power losses (87% when wind generation is 0.1 pu and 81% when wind generation is 1 pu). The power loss reduction is mainly contributed from decrease of non-converter losses, *i.e.* power losses from cables and transformers, and WT converter losses.



(a) Wind generation at 0.1 pu

(b) Wind generation at 1 pu

Figure 3.9: Power loss distribution in a single OWPP for different OPF options.



(a) Wind generation at 0.1 pu

(b) Wind generation at 1 pu

Figure 3.10: Percentage distribution of power losses in a single OWPP when optimisation determines reactive power supply and POC voltage (OPF-QV)

### 3.4.5 Analysis of interlink contribution

Two HVDC-connected OWPPs are analysed to quantify the power loss reduction when interlink cables are used to share the wind power generation between the OWPP transmission systems. An optimal active power sharing will reduce the power losses of the elements located downstream the interlink cable. The HVDC converters will control the active power transferred through each transmission system based on the control structures described in Sections 2.4.3 and 2.4.4 for multiple converters.

The total power losses of the interlinked OWPPs can be expressed as:

$$P_{loss,intOWPPs} = P_{loss,T1} + P_{loss,T2} + P_{loss,int} \quad (3.20)$$

where  $P_{loss,T1}$  and  $P_{loss,T2}$  are the power losses of the OWPP transmission systems and  $P_{loss,int}$  is the power losses of the interlink. If the interlink cable is short,  $P_{loss,int} \ll P_{loss,T1} + P_{loss,T2}$  and (3.20) is approximated as:

$$P_{loss,intOWPPs} \approx P_{loss,T1} + P_{loss,T2}. \quad (3.21)$$

The power losses of each transmission system can be expressed as:

$$P_{loss,Ti} = P_{loss,i}^{no-opt} + P_{loss,i}^{opt} \quad (3.22)$$

where  $P_{loss,i}^{no-opt}$  are the power losses that cannot be optimised because represent the elements upstream the interlink cable and  $P_{loss,i}^{opt}$  are the power losses that can be optimised with active power sharing because represent the elements located downstream the interlink. If the power losses are characterised by (3.19),  $P_{loss,i}^{no-opt}$  and  $P_{loss,i}^{opt}$  are expressed as:

$$P_{loss,i}^{no-opt} = a_{no-opt} + b_{no-opt} \cdot P_{OWF,i} + c_{no-opt} \cdot P_{OWF,i}^2 \quad (3.23)$$

$$P_{loss,i}^{opt} = a_{opt} + b_{opt} \cdot P_{OWF,i}^{opt} + c_{opt} \cdot P_{OWF,i}^{opt\ 2} \quad (3.24)$$

where  $a_{no-opt}$ ,  $b_{no-opt}$  and  $c_{no-opt}$  are the power loss coefficients of the elements that cannot be optimised;  $a_{opt}$ ,  $b_{opt}$  and  $c_{opt}$  are the power loss coefficients of the elements that can be optimised;  $P_{OWF,i}$  is the wind power generated by each wind farm cluster and  $P_{OWF,i}^{opt}$  is the optimal active power downstream the interlink. If the power losses are neglected, the total wind power generation of the interlinked OWPPs is expressed as:

$$P_{OWF,T} = P_{OWF,1} + P_{OWF,2} \approx P_{OWF,1}^{opt} + P_{OWF,2}^{opt} \quad (3.25)$$

The optimal active powers downstream the interlink,  $P_{OWF,1}^{opt}$  and  $P_{OWF,2}^{opt}$ , can be obtained combining ( 3.21 ) - ( 3.25 ) and applying  $\frac{d P_{loss,intOWPPs}}{d P_{OWF,1}} = 0$

or  $\frac{d P_{loss,intOWPPs}}{d P_{OWF,2}} = 0$ :

$$P_{OWF,1}^{opt} = \frac{b_{opt,2} - b_{opt,1} + 2c_{opt,2}P_{OWF,T}}{2(c_{opt,1} + c_{opt,2})} \quad ( 3.26 )$$

$$P_{OWF,2}^{opt} = \frac{b_{opt,1} - b_{opt,2} + 2c_{opt,1}P_{OWF,T}}{2(c_{opt,1} + c_{opt,2})} \quad ( 3.27 )$$

It is observed that the optimal active powers depend on the transmission system characteristics of the OWPPs (*i.e.* the power loss coefficients of the components) and the total wind power generation,  $P_{OWF,T}$ .

If the two transmission systems are identical, the power loss coefficients are the same and ( 3.26 ) and ( 3.27 ) are equal to:

$$P_{OWF,1}^{opt} = P_{OWF,2}^{opt} = \frac{P_{OWF,T}}{2} \quad ( 3.28 )$$

Therefore, when the interlinked OWPPs are identical the active power is shared equally through each transmission system to minimise power losses. In this case, if the OWPPs generate different powers, the interlink cables will be used to exchange active power between the transmission systems and achieve equal active power sharing. The maximum power loss reduction will occur when one OWPP is generating nominal power and the other is not generating power. This is because in these operational points, the interlinks will exchange the maximum power flow to minimise power losses.

If the power losses upstream the interlink are not negligible, ( 3.25 ) cannot be applied and optimal power sharing defined in ( 3.26 ) - ( 3.28 ) might not represent a valid approximation. This is especially important for long ac export cables and in case of a dc interlink configuration due to the high proportion of the total power losses that could be neglected.

Figure 3.11 compares the interlink options when the HVDC-connected OWPPs are identical and the interlink cable length is 5 km. These results illustrate an operational

point where one OWPP is generating nominal power and the other is not generating power. In these operational conditions, the maximum power loss reduction will be achieved. This is because the interlinks will exchange the maximum power flow to minimise power losses, which is approximately 0.5 pu as shown in Figure 3.11c.

Power losses of the interlinked OWPPs are compared to the case without interlink, where the active power cannot be shared between transmission systems. Also, it is supposed that reactive power supply and POC voltage are optimised in all topologies. The power losses are reduced up to 10% using ac interlinks and up to 5% using the dc interlink compared to the case without intelink, as shown in Figure 3.11b. The ac interlinks reduce twice the power losses compared to the dc interlink, since the ac interlinks are located closer to the sending end of the transmission system and optimise more proportion of the total losses. Also, the power loss reduction using the ac collector platform interlink is higher than using the ac offshore converter interlink, but the difference is small. This is because the ac collector platform interlink further optimises the power losses of the export cables, which represent only up to 3% of the total power losses as shown in Figure 3.10b.

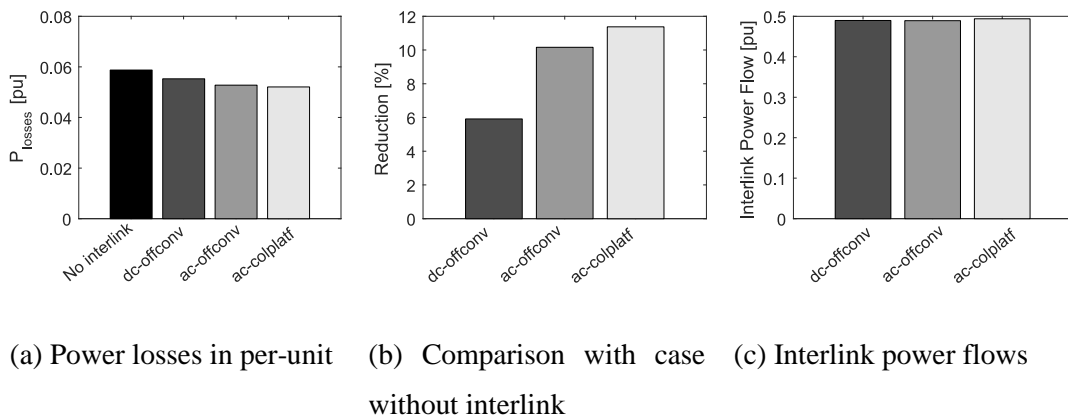


Figure 3.11: Power losses and interlink power flow when one OWPP is generating nominal power and the other is not generating power.

The effect that the interlink length has on the total power losses is analysed in Figures 3.12 and 3.13 when one OWPP is generating nominal power and the other is not generating power. The ac interlinks are the best option to minimise power losses for short lengths (up to 50 - 60 km). The dc interlink is the best option for long lengths since the power loss increase for lengths between 0 and 100 km is not significant, as

shown in Figure 3.12. This is because dc grid power losses represent a small part of the total power losses.

The active power flow through the interlink cables decreases for long distances, as shown in Figure 3.13, due to the increase of power losses of the interlink. Also, in case of ac interlinks, the reactive power supply increases significantly for long distances (*e.g.* up to 0.7 pu at 100 km), affecting negatively the total power losses (*e.g.* up to 4% increase at 100 km).

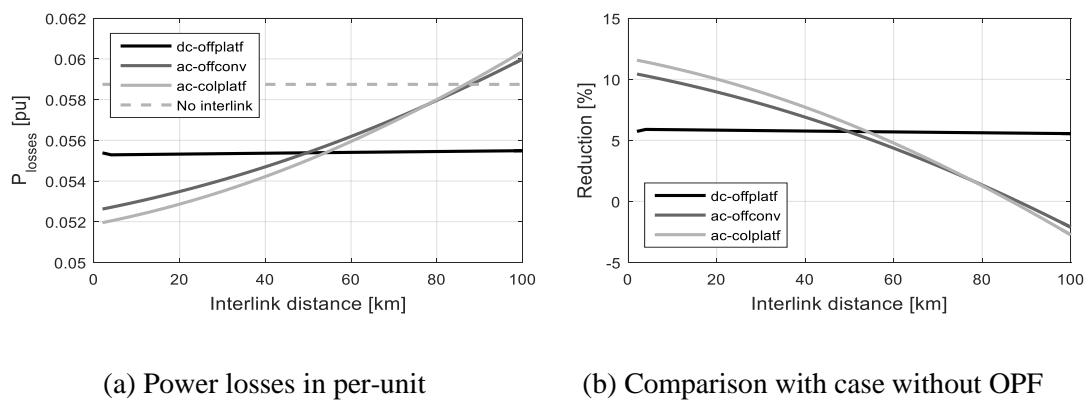


Figure 3.12: Total power losses for different interlink options and interlink lengths when OWPP1 generates nominal power and OWPP2 does not generate power.

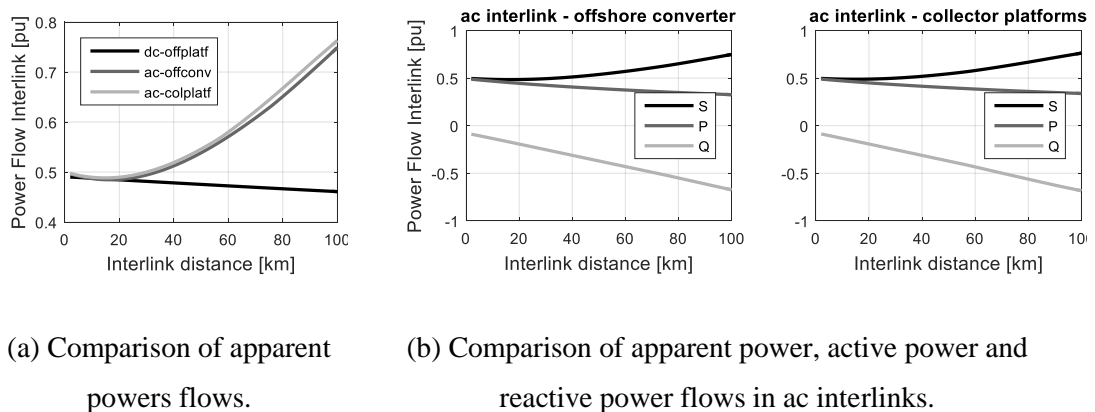


Figure 3.13: Interlink power flows for different interlink options and interlink lengths when OWPP1 generates nominal power and OWPP2 does not generate power.

### 3.5 AVAILABILITY ANALYSIS

The reliability of the interlink options will be analysed in terms of energy availability of the transmission system. Interlink cables increase the total availability of HVDC-connected OWPPs, *i.e.* they reduce the wind power curtailment.

### 3.5.1 Availability representation and methodology

The availability can be studied with analytical or statistical methods [101]. In this chapter, the availability is calculated with an analytical method based on COPTs. The capacity outage of a generation system is the generation capacity that is out of service due to a failure. A COPT is a table that contains all the capacity states of a generation system and the associated probabilities (or availabilities) [101]. The capacity states are introduced in an ascending order of capacity outage magnitude. The total energy availability,  $A_T$ , is expressed as a mean value of availabilities of each capacity state:

$$A_T = \sum_{c_{out}=0\%}^{100\%} A_{c_{out}} (100 - c_{out}) \quad (3.29)$$

where  $c_{out}$  is the capacity outage,  $100 - c_{out}$  is the capacity in service and  $A_{c_{out}}$  is the availability associated to a capacity outage. In case of OWPPs, the capacities are expressed as a percentage of available wind generation or wind capacity factor. The availability associated to a capacity outage is equal to the equivalent availability of a generation system for all the possible outages that result in that capacity.

The equivalent availability of an HVDC-connected OWPP depends on the following components [93], [102]:

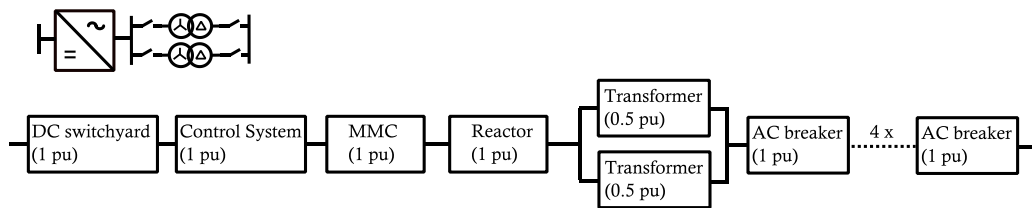
- HVAC breakers, represented as a Gas Insulated Switch (GIS)
- transformers, which are used with the HVDC converters and in the collector platform
- HVDC converters (VSC-MMC), which include the semiconductors, the cooling system and the ventilation system
- converter reactors
- control system of converter, which include the control algorithms and the hardware
- dc switchyard, which includes HV capacitors banks, line reactors, measurement transducers and switchgear
- HVDC breaker, represented as a hybrid dc circuit breaker
- submarine dc and ac cables

The availability of each component,  $A_i$ , is calculated from the failure rate,  $\lambda_{r,i}$ , or mean time to fail,  $MTTF_i = 1/\lambda_{r,i}$ , and the mean time to repair,  $MTTR_i$ , as:

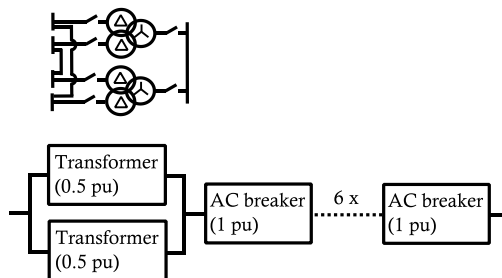
$$A_i = \frac{MTTF_i}{MTTF_i + MTTR_i} = \frac{1}{1 + \lambda_{r,i}MTTR_i} \quad (3.30)$$

The MTTF and MTTR data is in Appendix H and is obtained from [102], [103]. The MTTR values for offshore elements include an additional mean offshore access time depending on the component size [102].

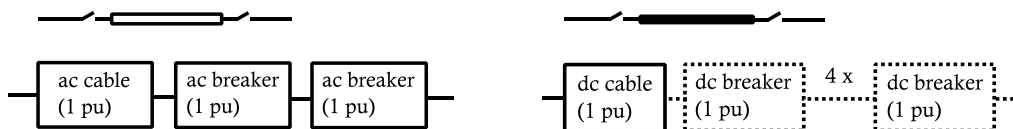
Block diagrams are used to represent the equivalent availability of the elements of an OWPP transmission system, as shown in Figure 3.14. The equivalent availability of each element is a combination of series and parallel components. These combinations are defined according to the consequences that a component failure has on an equivalent element.



(a) Onshore and offshore HVDC platforms



(b) Collector platforms with a ring connected configuration [11]



(c) ac cables

(d) dc cables

Figure 3.14: Block diagrams to represent equivalent availability of OWPP transmission system elements. The per-unit quantities are referred to the rated power of an OWPP.

The equivalent availabilities of the onshore and offshore HVDC converter platforms are:

$$A_{HVDC,1pu} = A_{dcswitch} \cdot A_{CtrlSys} \cdot A_{MMC} \cdot A_{react} \cdot A_{acbrk}^4 \cdot A_{tr}^2 \quad (3.31)$$

$$A_{HVDC,0.5pu} = 2 \cdot A_{dcswitch} \cdot A_{CtrlSys} \cdot A_{MMC} \cdot A_{react} \cdot A_{acbrk}^4 \cdot (1 - A_{tr}) \cdot A_{tr} \quad (3.32)$$

$$A_{HVDC,0pu} = 1 - A_{HVDCconv,1pu} - A_{HVDCconv,0.5pu} \quad (3.33)$$

The equivalent availabilities of the collector platforms are:

$$A_{col,1pu} = A_{acbrk}^6 \cdot A_{tr}^2 \quad (3.34)$$

$$A_{col,0.5pu} = 2 \cdot A_{acbrk}^6 \cdot (1 - A_{tr}) \cdot A_{tr} \quad (3.35)$$

$$A_{col,0pu} = 1 - A_{col,1pu} - A_{col,0.5pu} \quad (3.36)$$

It is supposed that the failure of a GIS produces the failure of all the GISs in the HVDC converter and collector platform [102]. The equivalent availabilities of the ac cables are:

$$A_{ac\_cb,1pu} = A_{acbrk}^2 \cdot A_{ac\_cable} \quad (3.37)$$

$$A_{ac\_cb,0pu} = 1 - A_{ac\_cb,1pu} \quad (3.38)$$

The equivalent availabilities of the dc cables are:

$$A_{dc\_cb,1pu} = \begin{cases} A_{dcbrk}^4 \cdot A_{dc\_cable}, & \text{if topology with dc interlink} \\ A_{dc\_cable}, & \text{if topology with ac interlink} \end{cases} \quad (3.39)$$

$$A_{dc\_cb,0pu} = 1 - A_{dc\_cb,1pu} \quad (3.40)$$

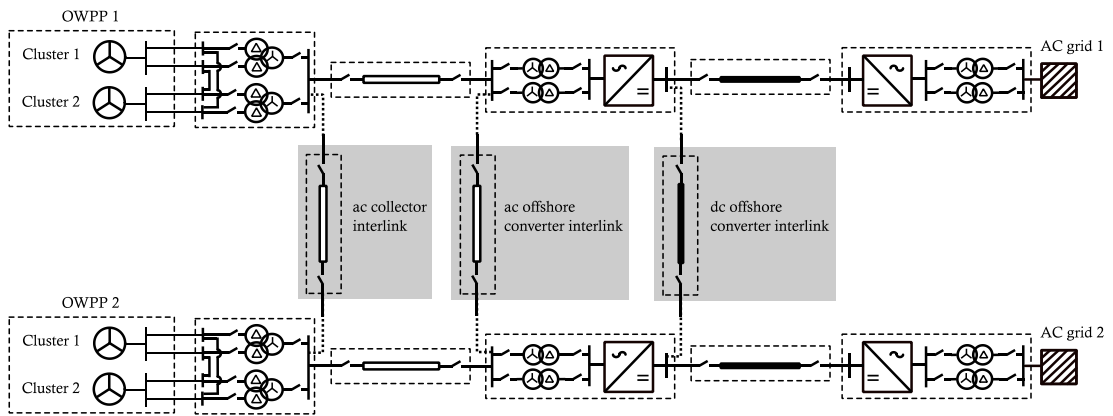
When ac interlinks are used it is assumed that dc breakers are not required since the ac breakers can isolate the dc links in case of HVDC converter or dc link outage. It is assumed that the configuration of the HVDC transmission is a symmetric monopole. In case of a bipolar system, the availability results would be different since there is additional redundancy for failures on the dc cables or the HVDC converters.

### 3.5.2 Analysis of interlink contribution

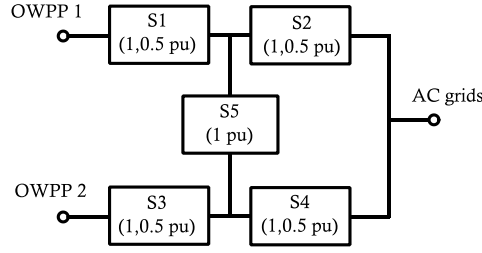
Figure 3.15a shows the detailed representation of two OWPPs with all possible interlink options. A simplified block diagram is shown in Figure 3.15b, where S1 - S5 represent the equivalent availability of different components. S1 and S3 are the equivalent availabilities of components located upstream the interlink, S2 and S4 are the equivalent availabilities of components located downstream the interlink and S5 represents the availability of the interlink cable. S1 - S4 have 3 possible states (1 pu, 0.5 pu and 0 pu) and S5 has 2 possible states (1 pu and 0 pu), which results in a total number of possible states equal to 162 ( $2 \cdot 3^4$ ). This number of states can be reduced to 120 without including states with minimal cut sets, which are the combinations of component failures that cause system failure and represent a 100% of capacity outage. Table B.1 in Appendix B presents the 120 possible combinations. The availability of each state is calculated as:

$$A_{state,i} = A_{S1} \cdot A_{S2} \cdot A_{S3} \cdot A_{S4} \cdot A_{S5} \quad (3.41)$$

If S1 or S3 are unavailable the interlink cannot provide an alternative export route for the wind power generation, which has to be curtailed. If S2 or S4 are unavailable, the interlink can provide an alternative export route, but it is limited to the available capacity of the interlink cable and the elements in S2 and S4. The ac collector platform interlink will provide the highest availability, because it is located at the sending end of the transmission system and can provide redundancy to the largest number of components.



(a) Detailed representation



(b) Simplified representation

Figure 3.15: Elements to represent equivalent availability of two OWPPs with interlinks.

The per-unit quantities are referred to the rated power of an OWPP

The equivalent availabilities of S1 - S5 are calculated as a combination of the availabilities of OWPP transmission system elements presented in Section 3.5.1. As an example, if a dc offshore converter interlink is considered, S1 includes the availabilities of the collector platforms, the ac export cable and the offshore HVDC platform. Therefore, the equivalent availabilities of S1 for all the states (1 pu, 0.5 pu and 0 pu ) are:

$$A_{S1,1pu} = A_{exp\_cb,1pu} \cdot A_{col,1pu} \cdot A_{offHVDC,1pu} \quad (3.42)$$

$$A_{S1,0.5pu} = A_{exp\_cb,1pu} (A_{col,0.5pu} \cdot A_{offHVDC,1pu} + A_{col,1pu} \cdot A_{offHVDC,0.5pu} + A_{col,0.5pu} \cdot A_{offHVDC,0.5pu}) \quad (3.43)$$

$$A_{S1,0pu} = 1 - A_{S1,1pu} - A_{S1,0.5pu} \quad (3.44)$$

More details about the availability expressions for all the interlink options are found in Appendix B.

The availability of each interlink option is analysed considering the specifications of the case study presented in Section 3.3 and the results are shown in Tables 3.3 - 3.6. The wind generation is equal to the typical capacity factor of an OWPP, which is approximately 40% of the OWPP rated power [104]. The transmission system capacity of each OWPP is defined as 100% of the OWPP rated power and the interlink cable is defined as 50% of the OWPP rated power.

The energy availability of each interlink option is calculated with ( 3.29 ) using the COPTs. The availability associated to a capacity outage is calculated as the sum of all the availabilities of those states that have the same capacity outage:

$$A_{c_{out}} = \sum_{i=0}^{N_{out}} A_{state,i} \quad (3.45)$$

where  $N_{out}$  is the total number of states with the same capacity outage. For example, if dc offshore converter interlink is considered, capacity outage equal to 0 % represents 40 states, capacity outage equal to 37.5 % represents 8 states and capacity outage equal to 50 % represents 72 states according to Table B.1 of Appendix B.

It is observed that topologies with interlinks provide availabilities above 98%. The ac interlinks have the highest availability and can reduce the unavailability more than 90% compared to the case without interlink.

Table 3.3: COPT for example without interlink.

Capacity outage (%)	Capacity in service (%)	Availability (%)	Energy Availability (%)
0	100	94.71	97.32
50	50	5.22	
100	0	0.07	

Table 3.4: COPT for example with dc offshore converter interlink.

Capacity outage (%)	Capacity in service (%)	Availability (%)	Energy Availability (%)
0	100	97.36	98.66
37.5	62.5	0.01	
50	50	2.58	
100	0	0.04	

Table 3.5: COPT for example with ac offshore converter interlink.

Capacity outage (%)	Capacity in service (%)	Availability (%)	Energy Availability (%)
0	100	99.54	99.74
37.5	62.5	0.03	
50	50	0.37	
100	0	0.06	

Table 3.6: COPT for example with ac collector platform interlink.

Capacity outage (%)	Capacity in service (%)	Availability (%)	Energy Availability (%)
0	100	99.79	99.87
37.5	62.5	0.03	
50	50	0.11	
100	0	0.07	

### 3.5.3 Sensitivity Analysis

The effect that different factors have on the energy availability is analysed in this section. All capacities are expressed in per-unit considering the rated power of an OWPP as a base value. Figure 3.16 shows the availability variation in terms of wind capacity factor. Availability decreases at high wind capacity factors, because the elements of the OWPP transmission system have a limited power capacity to transfer all wind generation in case of outage. On the other hand, availability is constant when the capacity factor is less than 0.5 pu, because the wind power transfer is not limited by the transmission system capacity in case of outage.

Figures 3.17 and 3.18 show the availability variation in terms of interlink and transmission system capacities. In general, large interlink and transmission system capacities ensure higher energy availability, because in case of outage there is enough capacity to transfer the wind power through an alternative route. However, the availability increases up to a certain interlink or transmission capacity that depends on the wind capacity factor. When the interlink capacity is higher than the wind capacity factor the availability reaches its maximum, as shown in Figure 3.17. In addition, the availability decreases significantly for transmission capacities below the wind capacity factor, *e.g.* from approximately 97% when transmission capacity is 0.4 pu to 25% when capacity is 0.1 pu, as shown in Figure 3.18a. Therefore, it is recommended to select the transmission capacity at least higher than the wind capacity factor in order to avoid an excessive wind power curtailment. The capacity of the transmission system and the interlink must be designed based on a trade-off between the cost of additional capacity to increase energy availability and the total energy savings from the reduction of wind power curtailment.

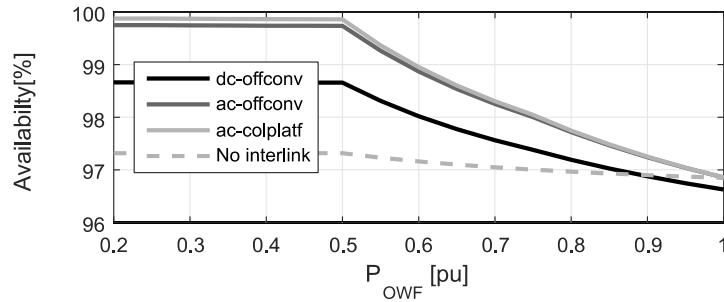
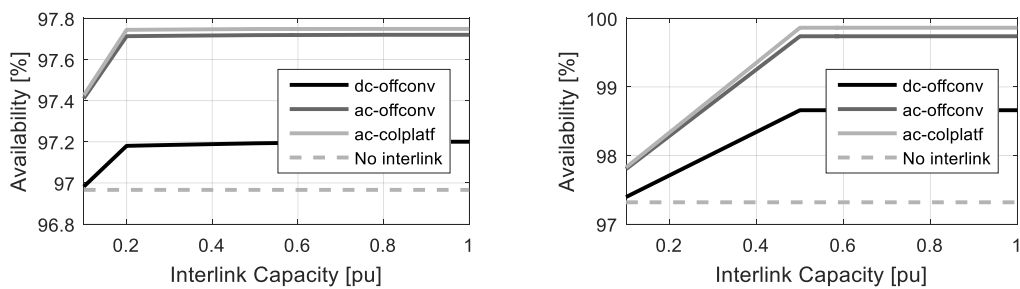
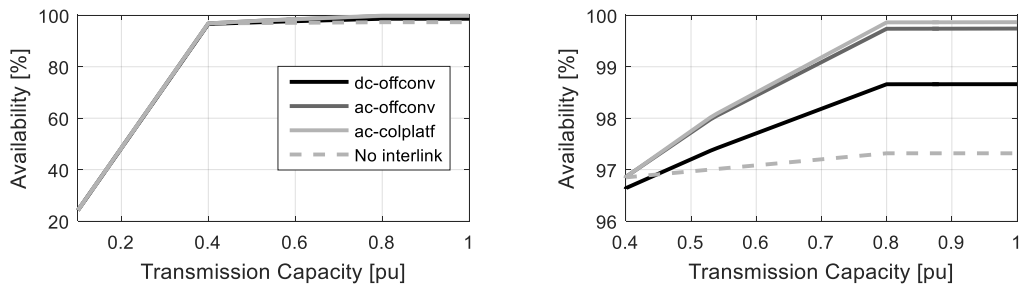


Figure 3.16: Energy availability for different wind capacity factors when OWPPs generate the same power, transmission system capacity is defined as 100% and interlink capacity for 50% of the OWPP rated power.



(a) Wind capacity factor equal to 0.2 pu (b) Wind capacity factor equal to 0.5 pu

Figure 3.17: Energy availability for different interlink capacities when transmission system capacity is defined as 100% of the OWPP rated power.



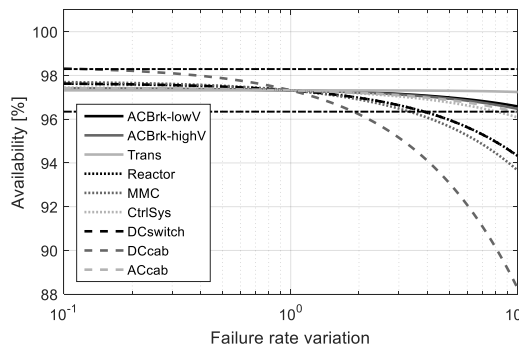
(a) Transmission capacity from 0.1 to 1 pu (b) Transmission capacity from 0.4 to 1 pu

Figure 3.18: Energy availability for different transmission system capacities when wind generation from each OWPP is 0.4 pu and interlink capacity is defined as 50% of the OWPP rated power.

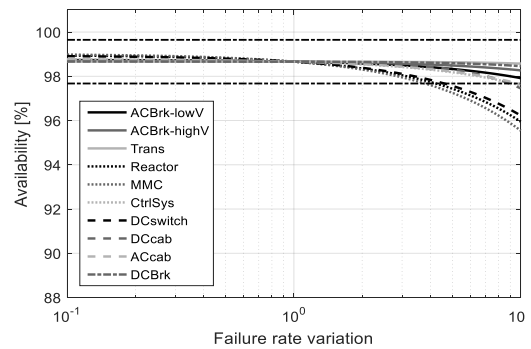
Figure 3.19 shows the availability variation for different failure rates of all the components. The sensitivity analysis with different MTTR values has not been included because the results would provide similar conclusions to evaluate the availability variation. Transformers, ac and dc breakers do not have a significant impact, with availability variations below 1%. The dc cables are the most sensitive

components, with availability variations up to 10% without interlink. The components related to the VSCs (reactors, MMC, control system and dc switchyard) have a significant impact (availability variations between 1 - 4%) in topologies without interlink or with dc interlink.

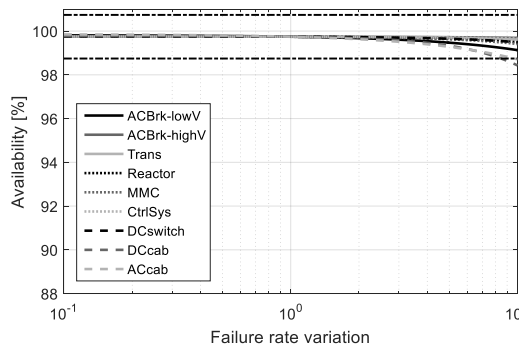
As expected, the topology with ac collector platform interlink is the least sensitive to failure rate variation, with availability difference exceeding 1% only for variation of dc cable failure rate as shown in Figure 3.19d. In general, topologies with ac interlinks are more accurate to calculate energy availability due to a low sensitivity to failure rate variation. Therefore, even with an inaccurate estimation of the failure rate parameters due to lack of information, *e.g.* in case of dc breakers, the availability results are still useful.



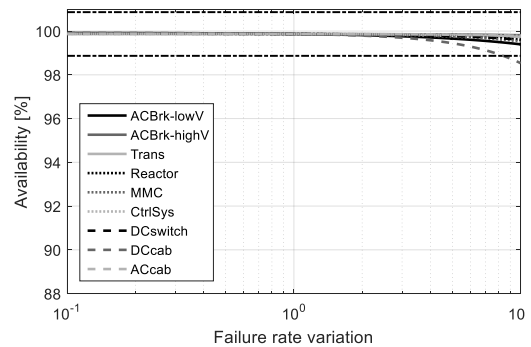
(a) No interlink



(b) DC offshore converter interlink



(c) AC offshore converter interlink



(d) AC collector platform interlink

Figure 3.19: Energy availability when failure rates are modified from 0.1 to 10 times the initial value. The discontinuous horizontal dashed lines represent an availability variation of  $\pm 1\%$  the initial value.

### 3.6 COST-BENEFIT ANALYSIS

An example of a cost-benefit analysis is used to evaluate the profit of the interlink options. The wind generation is based on one year wind speed data from FINO 1 [105] and the effect that the distance between the OWPPs have on the wind speed is represented with the cross-correlation model in [106].

The investment scheme considered in this example is based on the option adopted in the UK [33], where an OFTO has the responsibility to operate and maintain the offshore transmission assets between the OWPPs and the onshore grid. OFTOs own the offshore assets over a period of time and receive an income based on a fixed 20-years transmission tariff that represents the energy cost of offshore wind. Also, OFTOs can be responsible for the design, procurement and construction of the assets (OFTO build licence [33]).

Table 3.7: Interlink cable costs for a length of 5 km

<b>Component</b>	<b>Unit-km price</b>	<b>HVDC-interlink</b>	<b>HVAC-interlinks</b>
<i>ac cables</i> <i>HVAC 3 core cable (aluminium conductor) – 200 MW/220 kV (rating single cable)</i>	£0.355 M/km	-	£1.775 M
<i>ac breaker</i> <i>HVAC GIS switchgear – 220 kV</i>	£2.4 M/unit	-	£4.8 M
<i>dc cables</i> <i>HVDC extruded cables (aluminium conductor) – 600 MW/320 kV (pair of cables)</i>	£0.47 M/km	£2.21 M	-
<i>dc breaker</i> <i>1/6 of a 500 MW and ±320 kV VSC-HVDC [107]</i>	£5.39 M/unit	£21.55 M	-
<i>ac cable installation</i> <i>Single cable, single trench, 3 core</i>	£0.79 M/km	-	£3.95 M
<i>dc cable installation</i> <i>Twin cable, single trench, single core</i>	£ 0.85 M/km	£4.25 M	-
<i>Vessel</i>	£0.25 M/unit	£0.25 M	£0.25 M
<i>Total</i>	-	£28.26 M	£10.78 M

The cost-benefit analysis only considers an investment for the additional interlink cable. Table 3.7 shows the total costs for ac and dc interlink cables with a length of 5 km, where the component costs are from the ETYS 2015 [108]. It is observed that around 75% of the dc interlink costs are from the dc breaker. This component is not commercially available and its cost is estimated as 1/6 of a VSC-HVDC [107].

It is assumed that the OFTO owns the assets for 25 years and that the initial fixed energy cost of offshore wind is £120/ MWh [94], [109]. Therefore, over these 25 years, there will be 20 years of full tariff and 5 years of reduced tariff. This reduced tariff is supposed to decrease 10% each year until the end of the ownership [109]. Table 3.8 shows the annual energy savings at full tariff from the availability increase and power loss reduction when interlinks are used. The ac collector platform interlink provides the highest savings compared to the base case without interlink. It is observed that 90% of the annual savings are from the availability increase.

Table 3.9 shows the results of the cost-benefit analysis considering a standard discount rate of 6% [94]. The ac interlink options have a positive Net Present Value (NPV) for the 25 years investment and the lowest payback period is for the ac collector platform interlink with 4 years.

Table 3.8: Annual average of undelivered energy and energy losses with their associated savings compared to the base case

	<b>Base Case (no interlink)</b>	<b>DC Off. Converter Interlink</b>	<b>AC Off. Converter Interlink</b>	<b>AC Col. Interlink</b>
<i>Annual Undelivered Energy (% of available wind energy)</i>	1.4%	1.1 %	0.68%	0.63%
<i>Savings from availability increase</i>	-	£1.33 M	£2.77 M	£2.95 M
<i>Annual Energy losses (% of wind generation)</i>	5.79%	5.75%	5.72%	5.71%
<i>Savings from power loss reduction</i>	-	£0.16 M	£0.25 M	£0.29 M

Table 3.9: Results of cost-benefit analysis

	<b>DC Off. Converter Interlink</b>	<b>AC Off. Converter Interlink</b>	<b>AC Col. Interlink</b>
<i>Interlink investment</i>	£28.41 M	£10.78 M	£10.78 M
<i>Annual savings (with full tariff)</i>	£1.49 M	£3.02 M	£3.24 M
<i>Payback period</i>	≥ 100 years	5 years	4 years
<i>NPV for 25 years</i>	£-9.84 M	£26.85 M	£29.49 M

The negative NPV in the dc interlink option is mainly caused by the high cost of the dc breaker. Considering that the cost of this component is an estimated value, a sensitivity analysis is shown in Table 3.10 to evaluate the results depending on different dc breaker costs. It is observed that even with a dc breaker cost equal to 0 the payback period is longer than in the ac interlink options.

Table 3.10: Sensitivity analysis in relation to the dc breaker cost

	<b>Cost dc breaker = 0</b>	<b>Cost dc breaker = 25% of initial value</b>	<b>Cost dc breaker = 50% of initial value</b>
<i>Interlink investment</i>	£6.85 M	£12.24 M	£17.63 M
<i>Annual saving (with full tariff)</i>	£1.49 M	£1.49	£1.49
<i>Payback period</i>	6 years	12 years	22 years
<i>NPV for 25 years</i>	£11.71 M	£6.32 M	£0.94 M

### 3.7 INTERLINK CABLE CAPACITY

The interlink cable capacity is determined considering power loss reduction and increase of availability. A minimum interlink capacity is calculated from the power loss analysis,  $S_{in,loss}$ , and another from the availability analysis,  $S_{in,av}$ . The final interlink capacity corresponds to the maximum of  $S_{in,loss}$  and  $S_{in,av}$ .

### 3.7.1 Interlink capacity based on power loss analysis

The interlink capacity is selected as the minimum power exchange to ensure optimal power loss reduction for all operational conditions. If the power losses are neglected, the active power through the interlink cable can be expressed as:

$$P_{int} \approx P_{wf,1} - P_{wf,1}^{opt} = P_{wf,2}^{opt} - P_{wf,2} \quad (3.46)$$

The minimum active power flow through the interlink,  $P_{int,min}$ , corresponds to the maximum difference between the wind farm generation of each OWPP and the optimal power sharing values:

$$P_{int,min} = \max(|P_{wf,1} - P_{wf,1}^{opt}|) = \max(|P_{wf,2} - P_{wf,2}^{opt}|) \quad (3.47)$$

In case of dc interlinks the interlink cable can be selected only based on  $P_{int,min}$  and the nominal dc voltage. In case of ac interlinks, the reactive power compensation of the ac cable has to be included. The reactive power can be expressed as:

$$Q_{comp,int} = U_0^2 \omega C_{int} \quad (3.48)$$

where  $U_0$  is the voltage of the cable and  $C_{int}$  is the equivalent cable capacitance. The reactive power supplied at each side of the interlink cable can be approximated as:

$$Q_{supp,int} = Q_{comp,int} / 2 \quad (3.49)$$

The reactive power compensation of the interlink cable is different at each side of the cable because the voltages are also different, especially for long cables. However, to estimate the minimum interlink capacity it is sufficient to consider that the reactive power supplied at each side of the cable is equal to the worst case scenario, *i.e.*  $U_0 = 1.1$  pu.

Therefore, the minimum ac interlink capacity based on minimum power losses is equal to:

$$S_{int,loss} = \sqrt{P_{int,min}^2 + Q_{supp,int}^2} \quad (3.50)$$

Figure 3.19 shows the design procedure to select the interlink cable capacity based on minimum power losses. As example, the ac interlink cable is selected for the case study presented in Section 3.3. The minimum interlink capacity is calculated based on one year wind generation from real wind speed data in FINO 1 [105]. The effect that the distance between the OWPPs have on the wind speed is represented with the cross-correlation model in [106]. The results are summarised in Table 3.11. It is observed that the reactive power contribution does not modify significantly the interlink capacity because the length is short.

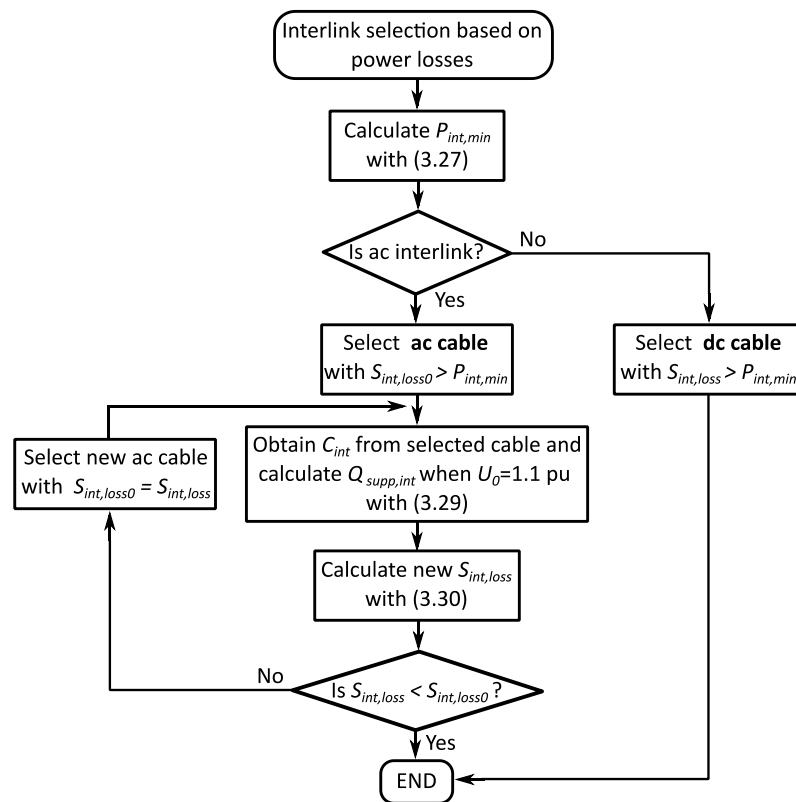


Figure 3.20: Flow chart to select interlink capacity based on power losses analysis

Table 3.11: Results of ac interlink cable capacity selection.

Element	Value
$P_{int,min}$	0.4167 pu (205.01 MW)
$Q_{supp,int}$	0.0262 pu (12.88 Mvar)
$S_{int,loss}$	0.4176 pu (205.46 MVA)
<i>ac cable at 220 kV (data from [110])</i>	XLPE-3 core cable (aluminium conductor); cross section, 500 mm <sup>2</sup> ; maximum current, 540 A; capacitance, 0.14 μF/km and inductance, 0.44 mH/km

### 3.7.2 Interlink capacity based on availability analysis

The maximum availability is reached with a minimum interlink capacity as shown in 3.17. However, this minimum capacity depends on the wind power generation and the transmission system capacity, which increases the complexity of the design process. In order to simplify the design process, it is supposed that the transmission capacity have been already designed in relation to the wind generation and that both OWPPs are close enough to generate the same power.

The availability for all possible wind power generations is considered using a Weibull distribution, which defines the probability of all wind speeds. Therefore, the availability for each interlink capacity  $i$ ,  $A_{T,intcap_i}$ , is calculated as:

$$A_{T,intcap_i} = \int_0^{\infty} A_{Ti}(v_w)p(v_w)dv_w = \sum_{n=0}^N A_{Ti,n}p_n\Delta v_w \quad (3.51)$$

where  $A_{Ti,n}$  is the availability at wind speed  $n$ ,  $p_n$  is the probability to have wind speed  $n$ ,  $N$  is the number of wind speed points considered in the discrete availability calculation and  $\Delta v_w$  is the constant interval between wind speed points.

Alternatively, the availability can be calculated considering a constant wind generation that corresponds to the capacity factor of the OWPP. This option can be used if the Weibull distribution of the OWPP location is not available. Figure 3.21 shows the design procedure to select the interlink cable capacity based on maximum availability

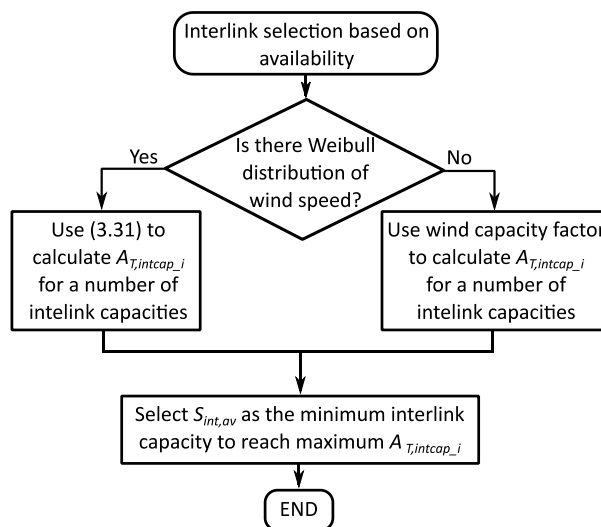


Figure 3.21: Flow chart to select interlink capacity based on availability analysis

As an example, the minimum interlink capacity is calculated for the case study of two OWPPs presented in Section 3.3. Figure 3.22a shows the Weibull distribution from real wind speed data in FINO 1 [105] and Figure 3.22b shows the WT power vs. wind speed curve considering the WT details of Section H.2.1. of Appendix H. The constant interval between wind speed points is equal to 0.1 m/s.

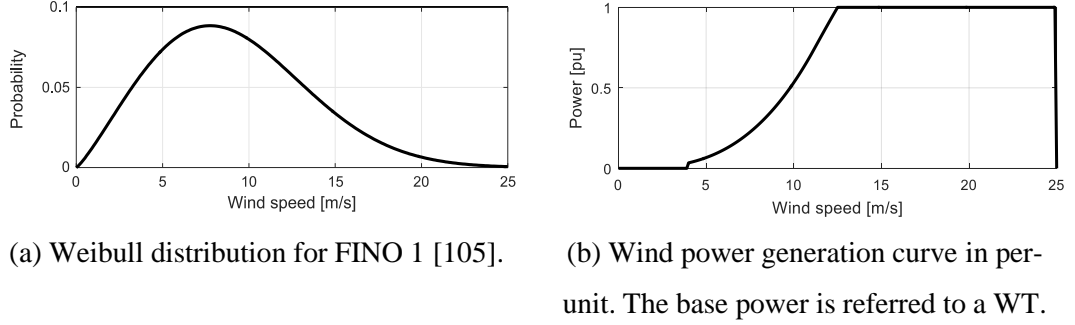


Figure 3.22: Weibull distribution and WT generation used as an example to calculate minimum interlink capacity.

The energy availability considering the probability of wind power generations is shown in Figure 3.23a, where the minimum interlink capacity is equal to 0.5 pu to ensure a maximum availability of approximately 99% for ac interlinks and 98% for the dc interlink. The energy availability considering the capacity factor of the OWPP is shown in Figure 3.23b. The capacity factor is equal to 0.45 pu, which has been calculated as the average generation from the Weibull distribution:

$$P_{OWF,av} = \int_0^{\infty} P_{OWF}(v_w)p(v_w)dv_w = \sum_{n=0}^N P_{OWF,n}p_n\Delta v_w \quad (3.52)$$

where  $P_{OWF,n}$  is the power generation at wind speed  $n$ .

It is observed that the minimum interlink capacity to ensure maximum availability is 0.45 pu, which is slightly lower than the value obtained considering the probability of wind power generations.

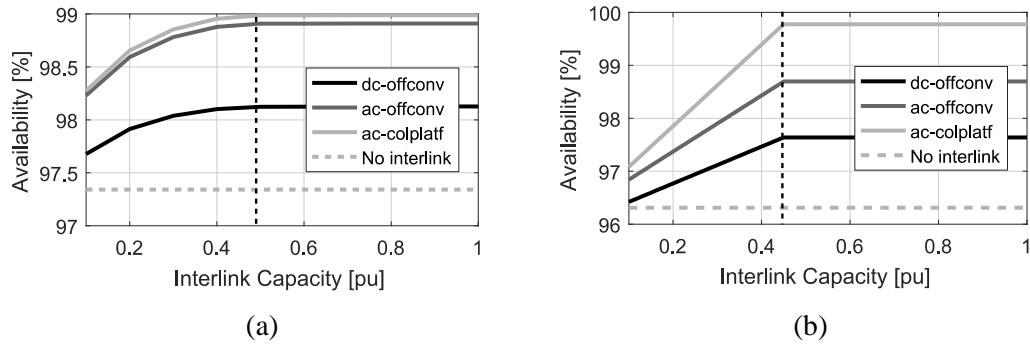


Figure 3.23: Energy availability for different interlink capacities (a) considering probability of all wind power generations and (b) considering capacity factor of the OWPP. The interlink capacities are expressed in per-unit considering the rated power of an OWPP as a base power.

### 3.8 SUMMARY

This chapter compared three interlink options between OWPPs: (i) dc offshore converter interlink, (ii) ac offshore converter interlink and (iii) ac collector platform interlink. A power loss and availability analysis were used to evaluate the benefits of the different interlink options. In general, the ac collector platform interlink is recommended to reduce power losses and increase energy availability for short distances between OWPPs. The dc offshore converter interlink is recommended for long distances between OWPPs to avoid excessive reactive power compensation of long ac cables.

The power losses analysis provided information about the power loss distribution and the power loss reduction when power and voltage set points of the VSCs are optimised. Converter losses represented the largest share of the total power losses, especially at low wind generation, due to their constant losses. An optimal reactive power supply between HVDC and WT converters reduced up to 2 - 3% the power losses and the optimal POC voltage by 7% compared to the case without optimisation. Considering two identical OWPPs, an optimal active power sharing reduced up to 10% the power losses using ac interlinks compared to the case without interlinks. For long distances between OWPPs the dc interlink was the only possible option due to an excessive increase of power losses in the ac interlink topologies.

The availability analysis provided information about the increase of energy availability with interlinks and the sensitivity of the availability to different parameters. The total availability was highly dependent on the wind capacity factor,

the interlink capacity and the transmission capacity. The transmission capacity should be at least higher than the capacity factor of the OWPP in order to avoid an excessive wind power curtailment. The dc cable failure rate was the most sensitive parameter with availability variations up to 10% when interlink was not used. Also, the ac interlink topologies were the least sensitive to failure rate variation.

An example of a cost-benefit analysis was presented using real wind speed data and adopting the investment scheme in the UK. The operational savings were mostly from the availability increase. The ac interlinks provided the shortest payback period even without including the cost of the dc breakers. A design procedure was presented to determine the interlink capacity. The minimum interlink capacity was selected to ensure that the power losses were minimised and the availability was maximised for all operational conditions.

# CHAPTER 4

## INERTIA EMULATION IN OFFSHORE WIND POWER PLANTS

### 4.1 INTRODUCTION

Inertia response is a fast frequency response that limits the frequency deviation during the first several seconds after power imbalance occurs in an ac grid. WTs provide inertia response extracting the kinetic energy stored in their rotating mass. The advantage of using kinetic energy is that WTs do not have to deload and operate below optimal power extraction. Variable speed WTs are not intrinsically sensitive to frequency variations of the grid and they do not provide natural inertia response as conventional synchronous generators do. In addition, large OWPPs connected through HVDC decouple the offshore ac grid from the onshore ac grid. Supplementary control was implemented in WT converters and HVDC converters to emulate inertia response and release kinetic energy stored in the rotating mass of the WTs.

This chapter analyses control strategies for inertia emulation in OWPPs based on existing options in academia and industry. In general, two main strategies have been defined: Synthetic Inertia (SI) and Temporary Overproduction (TO). These strategies are compared according to their implementation and simulation results in MATLAB Simulink. Also, a number of solutions are presented to limit the recovery power of WTs after the kinetic energy has been released. A Hardware-in-the-Loop (HIL) experimental test rig is used to demonstrate the effectiveness of inertia emulation with TO in an HVDC-connected OWPP based on a communication-free control scheme.

## 4.2 INERTIA RESPONSE IN VARIABLE SPEED WIND TURBINES

### 4.2.1 Inertia Emulation Concept

Supplementary control is implemented in the converters of variable speed WTs to emulate inertia response and release the kinetic energy stored in the rotating mass of WTs. The energy initially stored in the rotating mass is expressed as:

$$E_{k0} = \frac{1}{2} J_{wt} \omega_0^2 \quad (4.1)$$

where  $J_{wt}$  is the WT moment of inertia in  $\text{kg}\cdot\text{m}^2$  and  $\omega_0$  is the initial rotor speed in rad/s. The inertia constant is defined as:

$$H = \frac{1}{2} \frac{J_{wt} \omega_0^2}{S_{base}} \quad (4.2)$$

which represents the energy in per-unit, considering the rated power of the generator,  $S_{base}$ .

When the inertia emulation control is activated, WTs increase the power generation using the kinetic energy from the rotating mass and the rotor speed decreases (1-2 in Figure 4.1). The total kinetic energy released by the WTs is expressed as:

$$\Delta E_k = \frac{1}{2} J_{wt} (\omega_0^2 - \omega_f^2) = E_{k0} \left( 1 - \frac{\omega_f^2}{\omega_0^2} \right) \quad (4.3)$$

where  $\omega_f$  is the WT rotor speed in rad/s when the additional power has been exhausted. Once the inertia support has ended, the rotor speed returns back to its initial value. This is referred as recovery period [111]–[114] (2-3 in Figure 4.1).

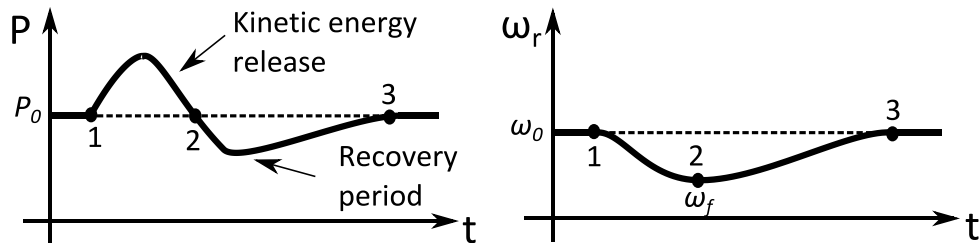


Figure 4.1: Inertia Response description.

WTs consume power during the recovery period to restore the initial kinetic energy. If the WTs are operating at rated wind speed, this additional power is provided by the wind energy excess using pitch angle control. However, if the WTs are operating below rated speed they have to reduce the wind power generation to compensate the recovery power. This further loss of generation will produce a second ac frequency reduction, which is particularly significant for high levels of wind penetration.

The WT inertia response has to be fast enough to reduce the RoCoF and the additional power has to be maintained at least until the minimum frequency is reached. An excess of kinetic energy release may lead to WT stalling due to a rotor speed reduction below the limit specified by manufacturers [114]–[116]. The available kinetic energy depends on wind speed conditions, *i.e.* WTs operating at low wind speeds have a limited amount of kinetic energy. Also, variation and stochastic nature of the wind increase the complexity of determining the kinetic energy that can be released during the inertia response provision [117], [118].

#### 4.2.2 Current Developments in Inertia Emulation

Inertia emulation was presented first time in [119] for DFIG WTs and implemented as a derivative controller. Since then, academia and industry have done important developments to implement and analyse the advantages of inertia emulation in variable-speed WTs. Currently inertia emulation is offered by a number of WT manufacturers and is required by several system operators as an ancillary service. However, inertia emulation is still at a demonstration stage with collaborations between manufacturers and system operators to analyse the impact of such frequency response in real power systems.

WindINERTIA™ control [120] is the inertia emulation service from GE. An increase of 5-10% of the power generation is ensured for short-term under frequency events. The control implementation is described in [121] and simulation and field test results are presented in [122], [123]. Also, ENERCON offers an inertia emulation service with a contribution up to 10% of the nominal power that can be provided for approximately 10 s [124], [125]. In [117] this manufacturer shows a comparison of simulation models and field test measurements for Type 3 and 4 WTs.

Hydro-Québec TransÉnergie (HQT) was the first system operator to request inertia response from WTs. In [73] and [126] HQT defines technical requirements and

validation tests for inertia response. WPPs are required to provide at least the same inertia response as a conventional synchronous generator with inertia constant equal to 3.5 s. For example, this is equivalent to increasing the additional power of the WPPs at least 6% for about 10 s in case of a severe power imbalance as shown in Table 4.1, which considers the grid scenario presented in [112]. Additional requirements were defined as a result of a close collaboration with WT manufacturers (ENERCON and Senvion) [112]. These requirements are going to be included in the grid code as performance guidelines.

Table 4.1: Example of HQT requirement of inertia emulation applied for the grid scenario presented in [112].

Parameter	Value
Synchronous Generation, $S_{SG}$	10 GW
Wind Power Plants with inertia emulation, $S_{WPP}$	2 GW
Minimum frequency for a severe power imbalance, $f_{min}$	58.5 Hz
Frequency threshold for activation of inertia emulation, $f_0$	59.5 Hz
Total kinetic energy released by WPPs in per-unit, $\Delta E_{pu}$	$\Delta E_{pu} = \Delta P_{pu} \cdot \Delta t = 0.6 pu$
Inertia constant of WPPs, $H_{WPP}$	$H_{WPP} = \frac{\Delta E_{pu}}{(1 - \frac{f_{min}^2}{f_0^2})} \frac{S_{WPP}}{S_{SG}} \approx 3.5 s$

Two other system operators have recently introduced inertia response requirements for WPPs: the Independent Electricity System Operator (IESO) [74], located in the Canadian province of Ontario, and the Operador Nacional do Sistema Elétrico (ONS) [75] in Brazil. Table 4.2 compares the inertia response requirements for each system operator and Figure 4.2 shows a representation of these requirements.

In Europe, inertia response is not required from WPPs. However, small synchronous areas, such as Ireland and Great Britain, are considering short-term frequency services that can be provided from non-synchronous generation to limit the RoCoF and the frequency deviation [76], [127]. Also, ENTSOE is starting to address

the impact of a future inertia reduction in Continental Europe and the Nordic synchronous areas [128], [129].

Table 4.2: Specifications for inertia emulation in different system operators

Parameter	HQT [112]	IESO [74]	ONS [75]
Frequency threshold, $f_{th}$	$\leq 0.5$ Hz	0.3 Hz	0.15 Hz
Maximum response delay, $t_{delay}$	1.5 s	1 s	0.5 s
Minimum power contribution, $\Delta P_{IE}$	6% nominal power	10% pre-disturbance power	10% nominal power
Minimum duration, $\Delta t_{IE}$	9 s	10 s	5 s
Maximum recovery power, $\Delta P_{rec}$	20% nominal power	5% pre-disturbance power	-
Maximum time between two consecutive activations, $\Delta t_{cons,act}$	-	2 min	-
Minimum power output for availability of this service	25% nominal power		

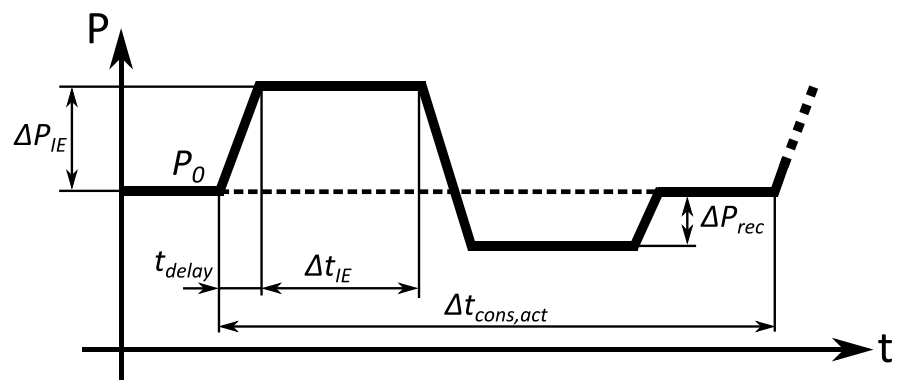


Figure 4.2: Representation of Inertia Emulation requirements.

### 4.2.3 Wind Turbine Control and Implementation of Inertia Emulation

Figure 4.3 shows the general control scheme of a DFIG-WT and a FRC-WT. DFIG-WTs control part of the wind power generation through the rotor of the

induction generator. FRC-WTs control the full wind generation through the stator of the generator. Variable speed WTs are controlled by a back-to-back converter. The grid-side VSC is responsible for regulating the voltage of the dc link between both converters. The generator-side VSC controls the rotor speed of the generator to modify the WT power extraction. More details about WT modelling and VSC controls are found in [86] and in Appendix C. Inertia emulation is implemented as a supplementary control loop in the machine-side VSC, as shown in Figure 4.3. At least, the grid frequency,  $f_g$ , and the optimal power reference,  $P_{opt}$ , are necessary as inputs to provide inertia emulation. A detailed description of inertia emulation control schemes is presented in Section 4.1.

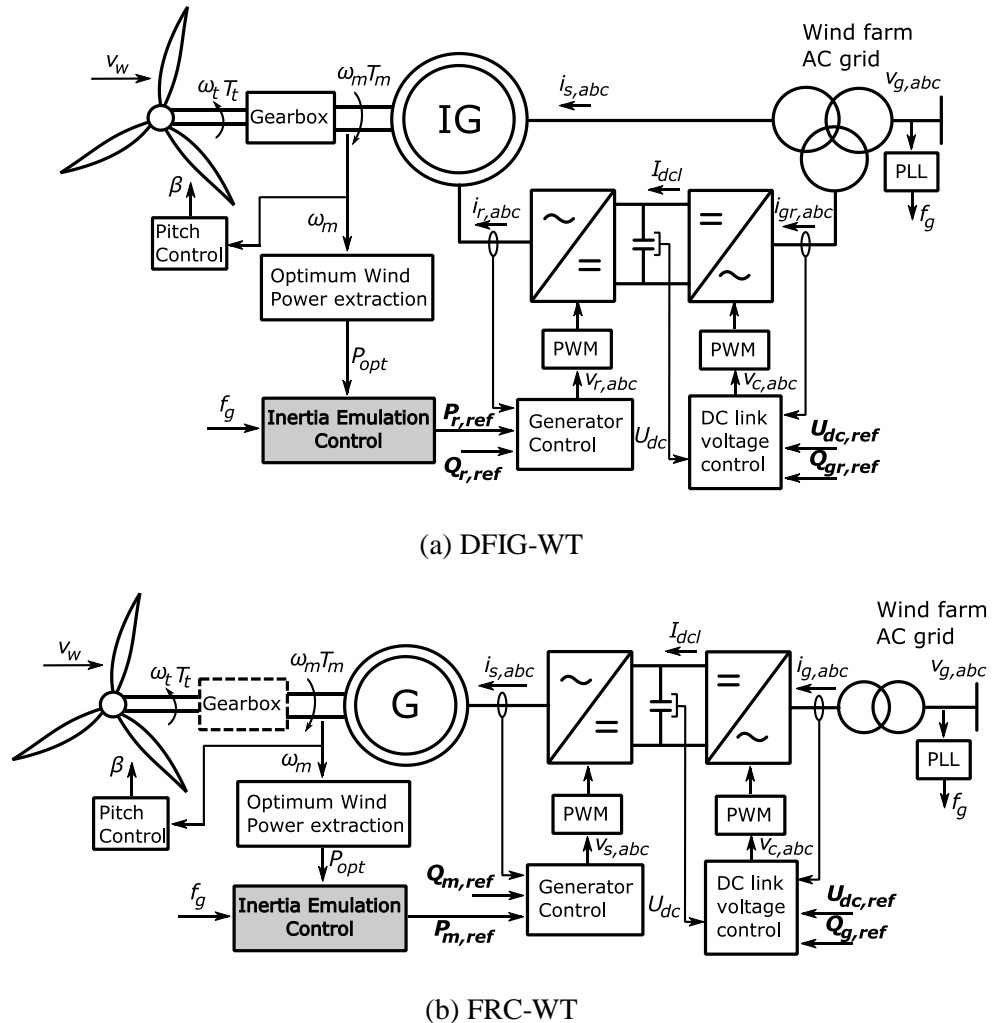


Figure 4.3: General scheme of WT controls including inertia emulation.

Under normal conditions, WTs operating below rated wind speed generate maximum power, based on the optimal power coefficient  $C_p$ . However, when inertia

response is provided, WTs temporarily operate below maximum power extraction. This causes a loss of captured wind energy, which can be expressed as:

$$\begin{aligned} E_{\text{loss,IE}} &= \int_{t_{\text{ini}}}^{t_{\text{end}}} (P_{t,\text{opt}}(t) - P_{t,\text{IE}}(t)) dt = \\ &= \frac{1}{2} \rho \pi r^2 v_w^3 \int_{t_{\text{ini}}}^{t_{\text{end}}} (C_{p,\text{opt}}(t) - C_{p,\text{IE}}(t)) dt \end{aligned} \quad (4.4)$$

Also, the efficiency of captured wind energy is calculated as a power reduction from the optimal  $C_p$ :

$$\eta_{\text{IE}} = \frac{P_{t,\text{opt}} - P_{t,\text{IE}}}{P_{t,\text{opt}}} = 1 - \frac{C_{p,\text{IE}}}{C_{p,\text{opt}}} \quad (4.5)$$

### 4.3 CONTROL STRATEGIES FOR INERTIA EMULATION

A number of strategies have been suggested for inertia emulation in variable speed WTs. In general two main strategies are considered: Synthetic Inertia [111], [121], [130]–[133] and Temporary Overproduction [112]–[114], [131]–[134]. The terms used to define these strategies can be different in other references; *e.g.* SI is also known as inertia coupling [131] or governor-inertia controller [114], whereas TO is also presented as temporary power surge [132], short-term overproduction [113], step response [131] or step over production [114]. In addition, inertia emulation strategies can be implemented as electrical torque or power reference. In this chapter, inertia emulation control with power reference is employed since this option is used by manufacturers and facilitates the consideration of system operator requirements.

#### 4.3.1 Synthetic Inertia

This strategy mimics the inertia response of conventional synchronous generators. Figure 4.4 shows the general implementation of SI, which is based on a PD controller. The derivative controller represents the inertia of the WT generators and can amplify noise from the frequency measurement. A low pass filter is added in the frequency measurement to attenuate this noise. The proportional or droop controller represents the governor action and is used to increase the kinetic energy release and delay the start of recovery period. A washout filter is included in [111], [135] to remove the droop control contribution in steady state and allow the WT recovery. Dead bands are

used in frequency deviation and RoCoF to activate SI based on system operator requirements. In summary, the following options for SI are found in the literature:

- PD controller without washout filter [114], [130], [131], [136]
- PD controller with washout filter [135], [137]
- Proportional controller with washout filter [121], [133], [135]

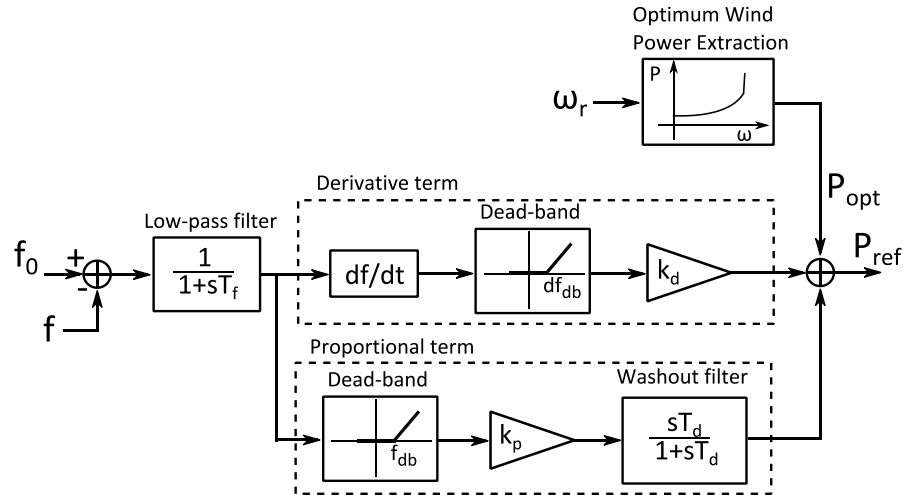


Figure 4.4: Control scheme of Synthetic Inertia strategy.

As explained in Section 4.2.2, the system operators define minimum specifications to set the inertia response performance, such as magnitude of additional power or duration of the energy release. The parameter tuning of SI to comply with these requirements may not be straightforward due to the combination of a low-pass and washout filter.

### 4.3.2 Temporary Overproduction

This strategy provides additional power over a period of time. The additional power is independent of the RoCoF, hence TO does not amplify noise from the frequency measurement. The additional power can be implemented as a step or proportional function [112], [118]. The step function provides a constant maximum contribution independently of the frequency deviation, *i.e.* without considering the imbalance magnitude. The proportional function increases the power in relation to the frequency deviation up to the maximum contribution. For large power imbalances or large proportional gains both strategies have a similar performance, as they provide the maximum power contribution. In [112] a control scheme based on a proportional gain with adjustable sign is proposed to implement the step and proportional functions.

Also, the step function can be implemented with other schemes [114], [118], [138]. In this chapter, the control scheme proposed in Figure 4.5 is used to implement TO as a step function. It is observed that the step function is activated when the frequency crosses a threshold value,  $f_{th}$ , and the rotor speed is higher than a minimum value,  $\omega_{r,min}$ . Also, a rate limiter is added to avoid an excessive mechanical stress in the WT's when TO is activated and deactivated. The additional power,  $\Delta P_{TO}$ , overproduction time,  $\Delta t_{TO}$ , and rate limits can be defined based on system operator requirements. This definition facilitates the introduction of inertia emulation as a WT ancillary service as shown in [112]. However, it should be noted that  $\Delta P_{TO}$  is constant and independent of the frequency deviation, which can generate an overreaction if the power imbalance is small and there is an excess of additional power.

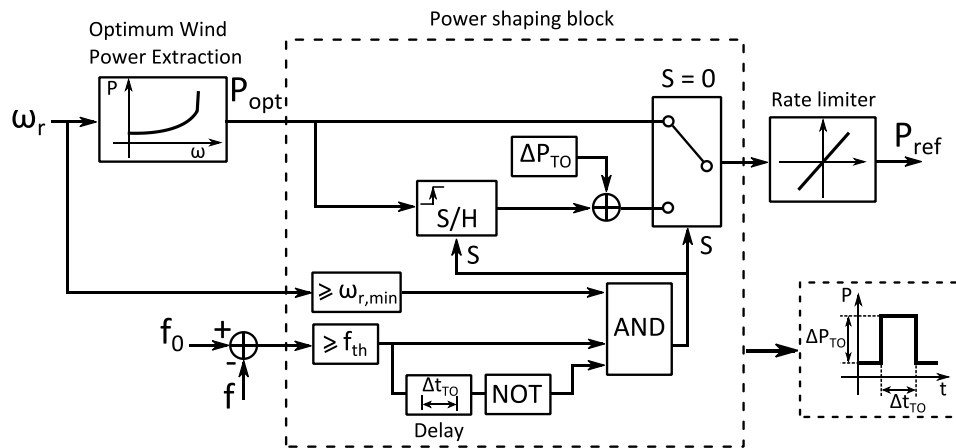


Figure 4.5: Control scheme of Temporary Overproduction strategy.

### 4.3.3 Comparison of Inertia Emulation Strategies

The two control strategies are tested in a simulation model developed in MATLAB Simulink that includes a 1.2 GW offshore wind farm connected to a 5 GW ac grid. An under-frequency event is represented with an imbalance equal to 7.5% of the ac grid demand, *i.e.* a 375 MW load. The offshore wind farm is modelled as an aggregation of 6 MW type 4 WT's. WT's are represented with an aerodynamic model and an inertia emulation control, but the back-to-back converter and the WT generator dynamics are not included, because their dynamics do not affect the inertia response. The ac grid is represented as a low order system frequency response model as described in Appendix D. The details of the WT's and the ac grid model can be found in Appendix H.

The control strategies are evaluated and compared based on maximum frequency deviation,  $\Delta f_{max}$ , and RoCoF of the ac grid. The maximum RoCoF is measured for the first second after the imbalance and with a sampling time of 0.5 s [18], [139]. WTs are operating below the rated speed, *e.g.* at 0.6 pu, to analyse the impact of the WT recovery power. SI and TO are designed to release kinetic energy for 6 s with a maximum power contribution equal to 10% of the pre-disturbance power,  $P_0$ . The control parameters for the inertia emulation strategies are in Tables 4.3 and 4.4.

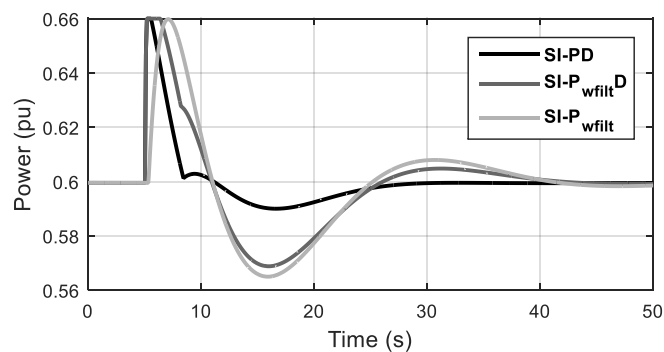
Table 4.3: Control parameters of Synthetic Inertia strategies

Parameters	PD (no washout filt.)	PD (with washout filt.)	P (with washout filt.)
Derivative gain, $k_d$	0.3	0.3	-
Proportional gain, $k_p$	0.04	0.14	0.202
Time constant of first order filter, $T_f$	0.1 s		
Time constant of washout filter, $T_d$	-	6 s	4.5 s
Dead band frequency, $f_{db}$	0.1 Hz		
Dead band RoCoF, $df_{db}$	0.1 Hz/s		
Maximum power contribution, $\Delta P_{TO}$	0.06 pu		

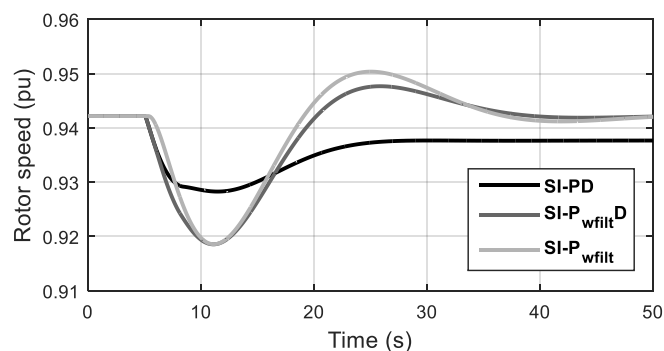
Table 4.4: Control parameters of Temporary Overproduction strategies

Parameters	Step function	Proportional function 1	Proportional function 2
Maximum power contribution, $\Delta P_{TO}$	0.06 pu		
Overproduction time, $\Delta t_{TO}$	6 s		
Threshold frequency, $f_{th}$	0.1 Hz		
Rate Limiter	$\pm \Delta P_{TO} / 0.5$ s		
Proportional gain during energy release, $k_p$	-	0.15	0.3
Proportional gain during recovery, $k_{rec}$	-	-0.01	

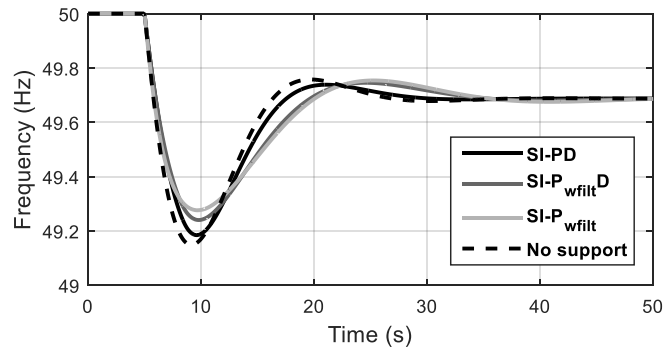
In Figure 4.6 the SI strategies are compared. The PD controller with a washout filter has the lowest RoCoF and the P controller has the lowest  $\Delta f_{max}$ , as shown in Table 4.5. The PD controllers can reduce the RoCoF significantly due to the fast response of the derivative controller. If the proportional action of the PD controller does not use washout filter, a limited amount of kinetic energy can be released, as shown in Figure 4.6b, where the rotor speed reduction is smaller than in the other SI options. As concluded in [135], the proportional controller with a washout filter can be designed to provide better frequency containment than the PD controllers, but the power increase is not fast enough to reduce the RoCoF significantly. The recovery time and power in the PD controller without washout filter are smaller than in the other SI options. This is because the kinetic energy release is smaller and the proportional action does not allow the rotor speed to return back to the initial value, as shown in Figure 4.6b.



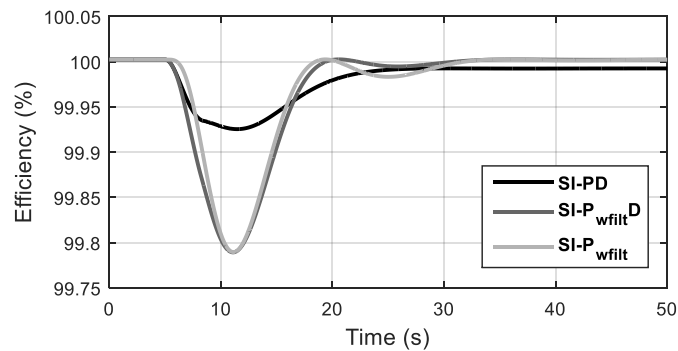
(a) Wind power generation.



(b) Wind turbine rotor speed.



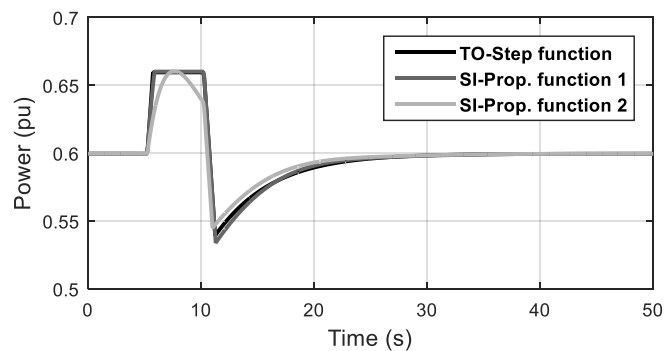
(c) Frequency of AC system.



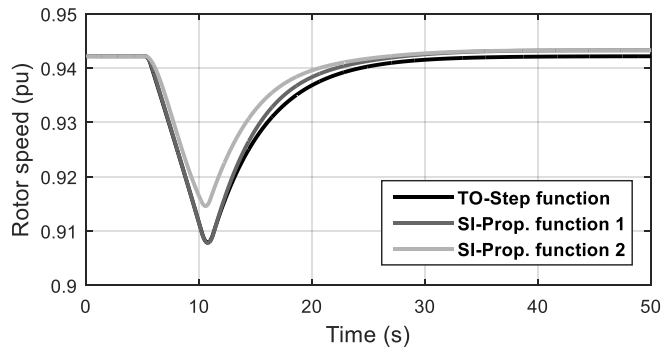
(d) Efficiency of captured wind energy, based on (4.5)

Figure 4.6: Comparison of SI strategies considering the same time of overproduction and a maximum power contribution equal to 10% of  $P_0$ .

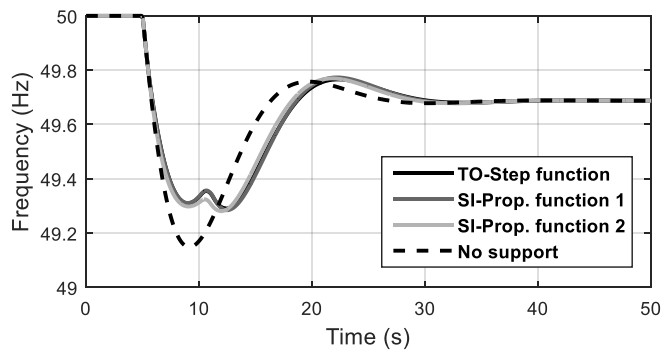
In Figure 4.7 the TO strategies are compared. The step function and proportional function 1 provide similar RoCoF and  $\Delta f_{max}$ , as shown in Table 4.5, because the additional power is equal to the maximum contribution and the initial power increase is approximately the same. If the gain of the proportional function is small enough, the power contribution does not saturate and the inertia support decreases, as shown in Figure 4.7 for proportional function 2.



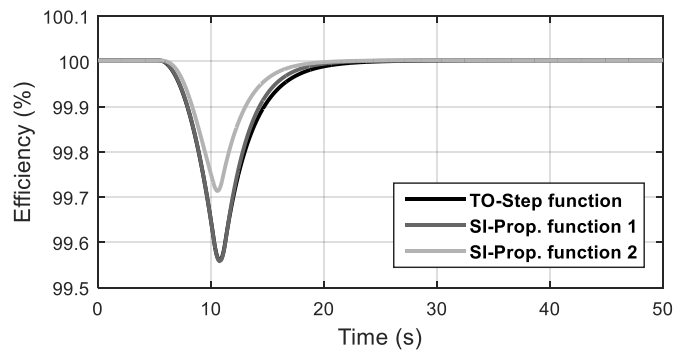
(a) Wind power generation.



(b) Wind turbine rotor speed.



(c) Frequency of AC system.



(d) Efficiency of captured wind energy, based on ( 4.5 )

Figure 4.7: Comparison of TO strategies considering the same time of overproduction and a maximum power contribution equal to 10% of  $P_0$ .

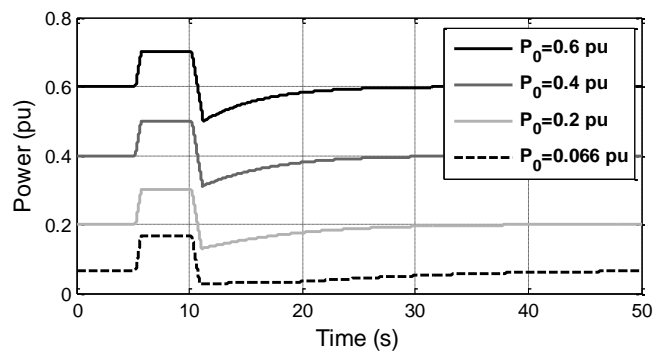
The  $\Delta f_{max}$  in TO is lower than in SI, because the power contribution in TO is higher during the overproduction period. SI with derivative controller provides the lowest RoCoF, but TO can reduce the RoCoF if the rate limiter is decreased. The recovery period is shorter in TO than in SI, but the recovery power is higher, which affects the ac grid with a second frequency dip at  $t=10-15$  s. In Figures 4.6d and 4.7d the efficiency of captured wind energy is calculated based on the deviation from the

optimal  $C_p$  in ( 4.5 ). As mentioned in [132], the loss of captured wind energy during inertia response is not significant, because the efficiency reduction is less than 0.5%.

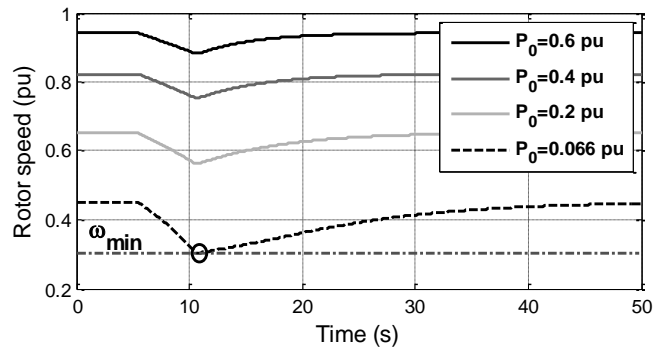
Table 4.5: RoCoF and maximum frequency deviation for simulations results in Figures 4.6 and 4.7. The minimum values for SI and TO options are highlighted in boldface.

Case		Maximum RoCoF (Hz/s)	$\Delta f_{max}$ (Hz)
No support		0.386	0.85
SI	PD (no washout filter)	0.319	0.82
	PD (with washout filter)	<b>0.317</b>	0.76
	P (with washout filter)	0.366	<b>0.72</b>
TO	Step function	<b>0.346</b>	<b>0.69</b>
	Proportional function 1	0.349	0.69
	Proportional function 2	0.366	0.70

It is important to define the minimum power output for availability of inertia emulation. This minimum power depends on the reduction of rotor speed during the provision of inertia emulation. The rotor speed must be above the minimum value defined by the manufacturers to avoid WT stalling. In this case study, the minimum rotor speed is 0.304 pu according to the WT data from Appendix H. Figure 4.8 shows the provision of inertia emulation for different power generations when the maximum power contribution is 0.1 pu (10% of nominal power). Inertia emulation is implemented as TO with step function, because this is the strategy with the highest rotor speed reduction during inertia response. It is observed that the minimum power output to ensure that inertia emulation is available is 0.066 pu.



(a) Wind power generation.



(b) Wind turbine rotor speed.

Figure 4.8: Inertia emulation as TO with step function and maximum power contribution equal to 10% of nominal power.

#### 4.4 IMPACT OF WIND TURBINE RECOVERY POWER

The WT recovery power can generate a second frequency dip larger than the initial frequency reduction caused by the imbalance. This is especially significant in TO, where the overproduction deactivation produces an initial high power acceleration to recover the rotor speed.

Also, in case of a high wind penetration scenario this situation is more likely to occur. For example, in small ac systems, such as Ireland or Great Britain, low demand scenarios can significantly increase the wind penetration level. Figure 4.9 shows the effect of the recovery power when TO is designed as a step function and different demand levels are considered. It is observed that when demand decreases, the inertia response improves the frequency containment of the first frequency reduction, but the second dip is larger.

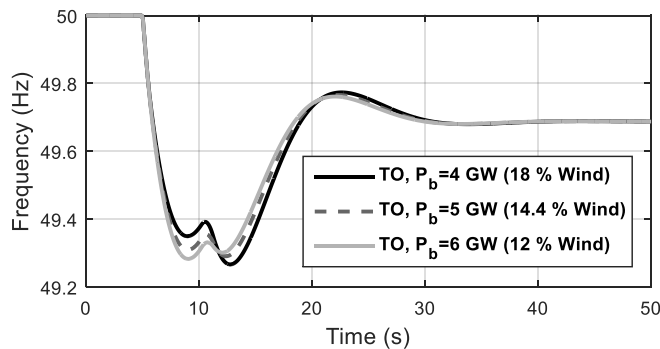


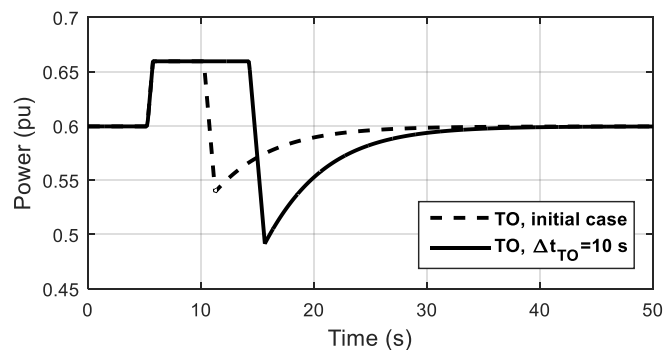
Figure 4.9: Reduction of demand in ac grid with TO strategy

This problem has been identified by HQT in [112] and three solutions are presented to reduce the impact of the WT recovery power in the case of TO:

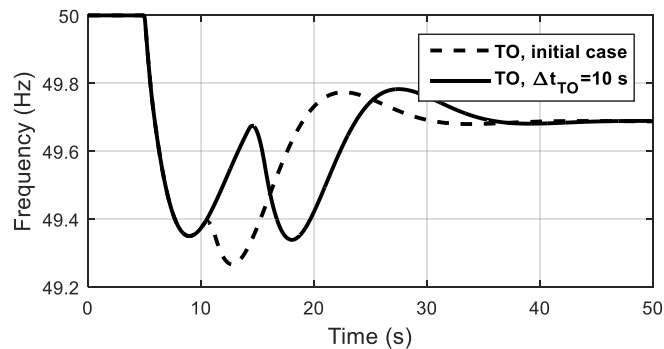
- Increase of overproduction time
- Delay the transition to the recovery phase
- Limit the recovery power

In case of SI, the increase of overproduction time and delay of the transition to the recovery phase are equivalent. These solutions can be applied modifying the control of each WT or coordinating the inertia emulation of the WTs to obtain a desired aggregated inertia response from a WPP [63], [136], [140]. In this section the control modification in individual WTs is presented.

The increase of overproduction time delays the recovery period until the frequency is restored and the second frequency dip is compensated by the primary response of the synchronous generation. If there is a high wind penetration and the synchronous generation is limited the second frequency dip might not be compensated. Figure 4.10 shows an example, where the overproduction time is increased from 6 s to 10 s.



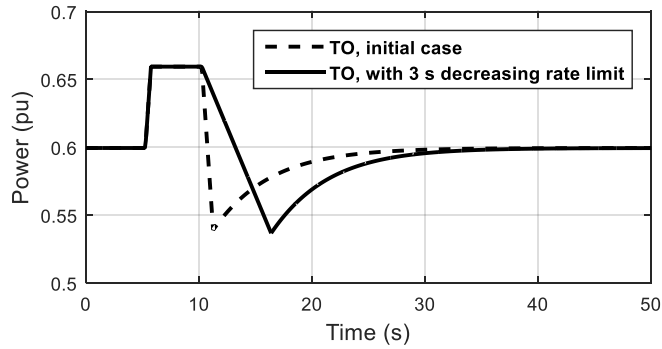
(a) Wind power generation.



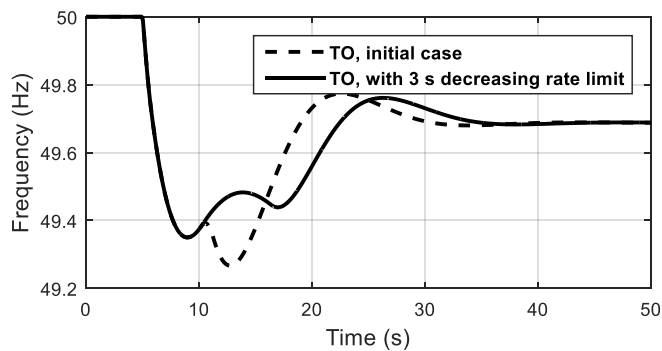
(b) Frequency of AC system.

Figure 4.10: Increase of overproduction time in TO from 6 to 10 s when the demand level is 4 GW.

In addition, the recovery period can be delayed if the transition time to the recovery phase increases. This option can be implemented increasing the power rate limit in Figure 4.5 only when the power is reduced. Figure 4.11 shows an example where the power rate limit is increased from 1 to 3 s.



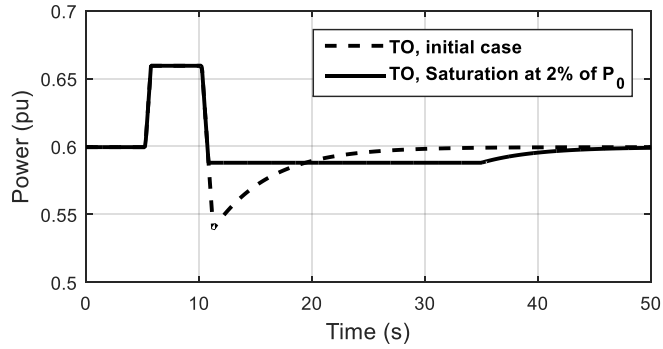
(a) Wind power generation.



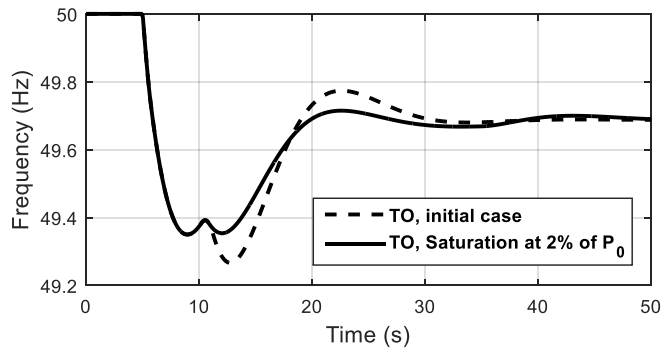
(b) Frequency of AC system.

Figure 4.11: Increase of power rate limit from 0.5 to 3 s when the demand level is 4 GW.

The limitation of the recovery power can directly attenuate the second frequency dip. This solution extends the recovery time and increases the period of suboptimal operation of the WTs. However, as mentioned in Section 4.3.3 the loss of captured wind energy during inertia response is not significant. The recovery power limitation can be implemented using a saturation block when the recovery period starts. Figure 4.12 shows an example where the recovery power is saturated at 2% of the pre-contingency power.



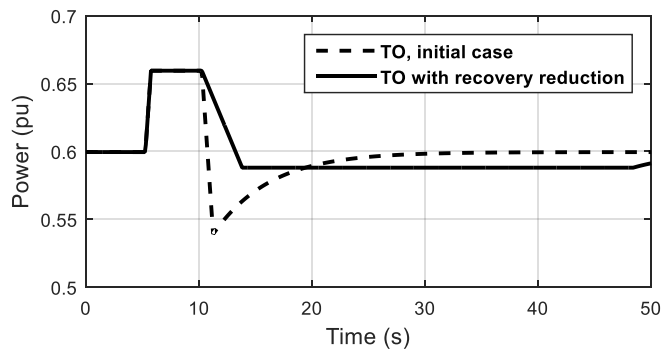
(a) Wind power generation.



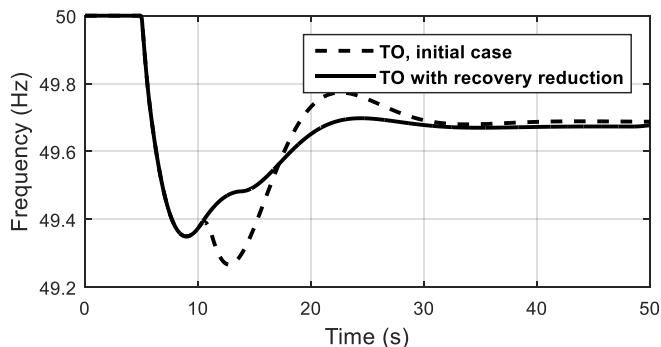
(b) Frequency of AC system.

Figure 4.12: Limitation of recovery power with saturation at 2% of  $P_0$  when the demand level is 4 GW.

A combination of these factors can be used to define the WT recovery for TO [112], [118]. Figure 4.13 shows an example where the second frequency dip is delayed increasing the power rate limit and attenuated limiting the recovery power.



(a) Wind power generation.



(b) Frequency of AC system.

Figure 4.13: Limitation of recovery power with saturation at 2% of  $P_0$  and increase of power rate limit from 1 to 3 s when the demand level is 4 GW.

## 4.5 INTEGRATION WITH VSC-HVDC TRANSMISSION SYSTEMS

HVDC transmission systems decouple offshore grids from onshore ac grids. If inertia response from OWPPs is required, the information of frequency deviations has to be transferred from the onshore grid to the OWPP.

Fibre optic links embedded within ac and dc cables can be used for fast communication between the VSCs [45], [62], [141]. Figure 4.14a shows the control scheme for an OWPP connected through an HVDC point-to-point system using communications. The frequency is measured with a PLL in the onshore HVDC converter and it is transferred directly to the WTs to activate inertia emulation [45]. Another option is to transmit the onshore frequency signal to the offshore HVDC converter, which will modify the offshore frequency and activate inertia emulation as in ac-connected OWPPs [62]. A loss of communication or occasional long delays may challenge the effectiveness of this option.

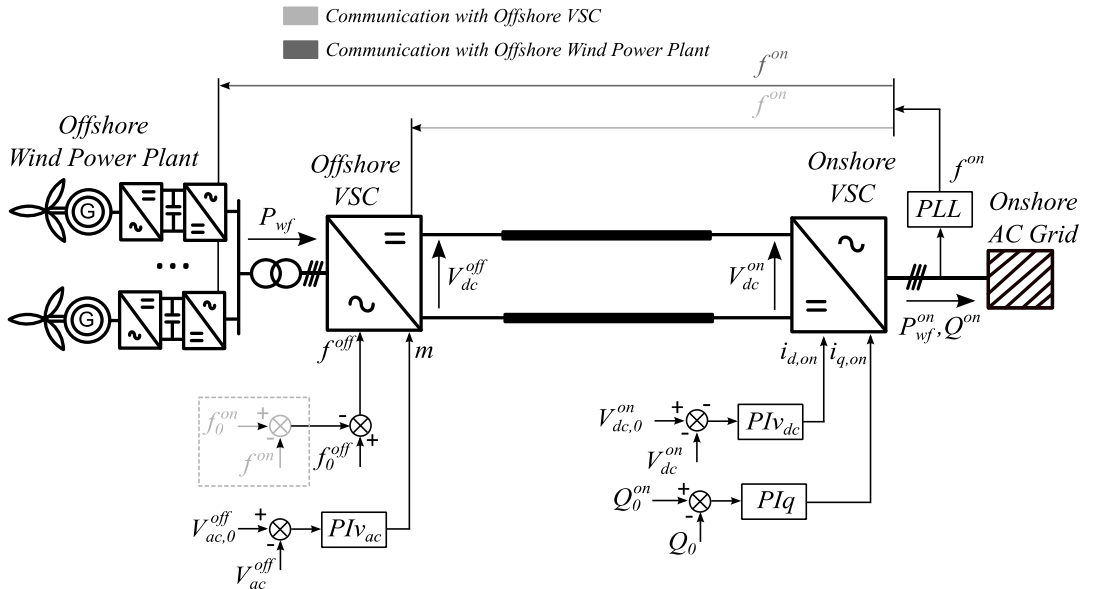
Alternatively, a communication-free control scheme can be implemented relying on local measurements of the HVDC converters. In this case, the voltage of the HVDC link is used as an intermediate signal to transfer the onshore frequency variations to the offshore HVDC converter [45], [46], [67], [69], [142], as show in Figure 4.14b. In the onshore HVDC converter, the dc voltage is modified with a  $f - V_{dc}$  droop control using onshore frequency measurement. In the offshore HVDC converter the dc voltage measurement is used to modify the offshore frequency with a  $V_{dc} - f$  droop control.

Therefore, the offshore frequency can be expressed in relation to the onshore frequency as:

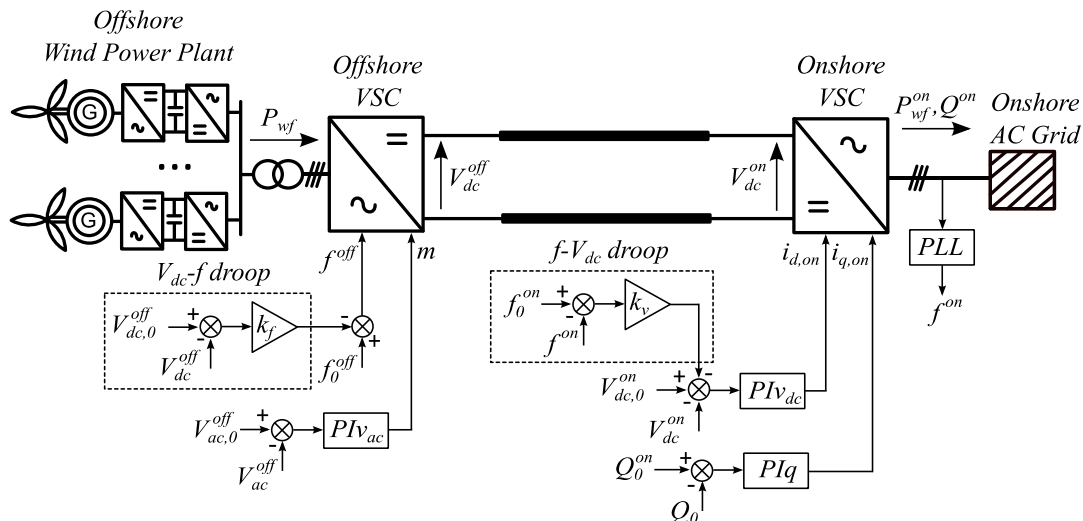
$$f^{off} = f_0^{off} + k_v k_f (f^{on} - f_0^{on}) \quad (4.6)$$

where  $f_0^{off}$  and  $f_0^{on}$  are the reference frequencies,  $f^{off}$  and  $f^{on}$  are the measured frequencies and  $k_v$  and  $k_f$  are the droop gains. If the offshore frequency replicates the same onshore frequency variations,  $f_0^{on} = f_0^{off}$  and the droop gains are defined such that  $k_v k_f = 1$ .

This alternative is robust against loss of communication since it relies on local control actions. However, the measurement accuracy is subjected to noise and converter control delay. Also, potential interactions may exist with the protection schemes, as the dc voltage variations during ac or dc faults can be detected as a power imbalance in the onshore ac grid [46]. The parameter selection of the droop gains should ensure that the dc voltage variations are inside safe operational limits during the largest disturbances on the onshore ac grid. The dc voltage limits are usually defined at  $\pm 10\%$  of the nominal value [45], [62], but in real applications they depend on the insulation levels of dc cables and the HVDC converter modulation.



(a) Option with fast communication to transfer onshore frequency signal to the offshore HVDC converter (light grey) or the OWPP (dark grey).



(b) Option without communications to transfer onshore frequency signal to the offshore HVDC converter using dc voltage as intermediate signal.

Figure 4.14: HVDC point-to-point control scheme with artificial frequency coupling between onshore and offshore grids.

The connection of OWPPs to MTDC grids increases the options to provide inertia response from WTs, but the control implementation is more complex as well. Coordinated control strategies of the MTDC grid without relying on communications are analysed in [143]–[145]. Also, the authors in [141] proposed a control scheme with fast communication to avoid potential interactions between the onshore converters and incorrect operation of inertia response from WTs. In [146] the PhD candidate in collaboration with the main author developed an alternative coordinated control for MTDC systems to transfer the WT recovery power to undisturbed ac grids and allow correct operation of MTDC grids during multiple power imbalances.

## 4.6 EXPERIMENTAL IMPLEMENTATION OF INERTIA EMULATION

Inertia Emulation from HVDC-connected OWPPs is tested in an experimental rig. The experiment considers an OWPP connected through an HVDC point-to-point system. In [146] a similar experiment is presented for a MTDC system using the same experimental rig, but the test was focused on the coordinated control scheme of the MTDC grid.

### 4.6.1 Description of Hardware-in-the-Loop Set-up

Figure 4.15 shows the general diagram of the HIL set-up. The main components are: WT test rig, VSC test rig, dc Network cabinet, real time simulator and grid simulator. The WT test rig, VSC test rig and dc Network cabinet represent scaled-down elements of a simulated system. The real time simulator represents a model of the onshore ac grid, which is interfaced to the VSC test rig with a grid simulator.

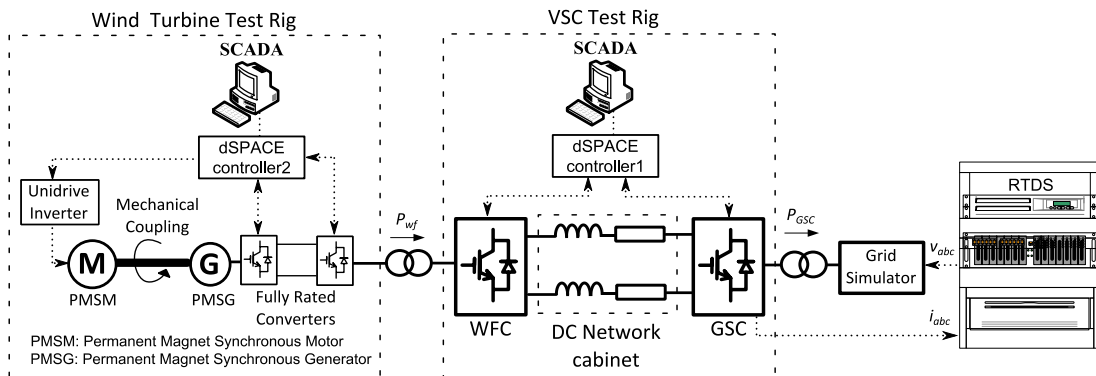


Figure 4.15: General diagram of the HIL set-up

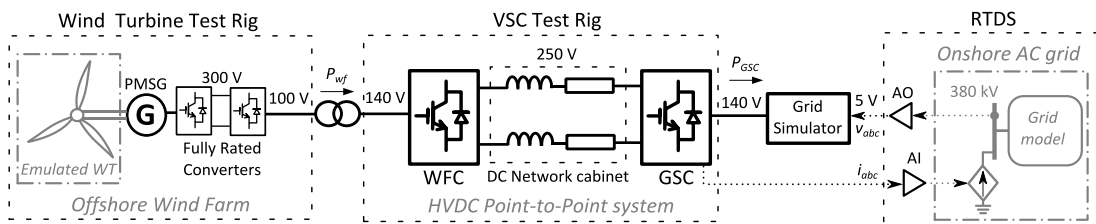


Figure 4.16: Elements represented in the HIL test. The scaled-down components are in black and the emulated elements are in grey.

### 4.6.2 Wind Turbine Test Rig

The WT test rig represents an OWPP as an aggregation of PMSG-WTs. This test rig is formed by two permanent magnet synchronous machines, a back-to-back converter, a variable-speed motor drive (Unidrive inverter) and an embedded computer (dSPACE), as shown in Figure 4.17. The electrical machines are coupled through a shaft. The motor absorbs power from the laboratory supply and the generator injects this power to the VSC test rig. The generator is a scaled-down representation of a real PMSG and the motor emulates the aerodynamic and mechanical response of a real WT. The Unidrive inverter controls the speed of the motor, whereas the dSPACE controls the back-to-back VSCs and supervises the operation of the test rig. An autotransformer is necessary to step up the output voltage from the back-to-back

converter to the VSC test rig (100/140 V). The technical specifications of the test rig are in Appendix E.

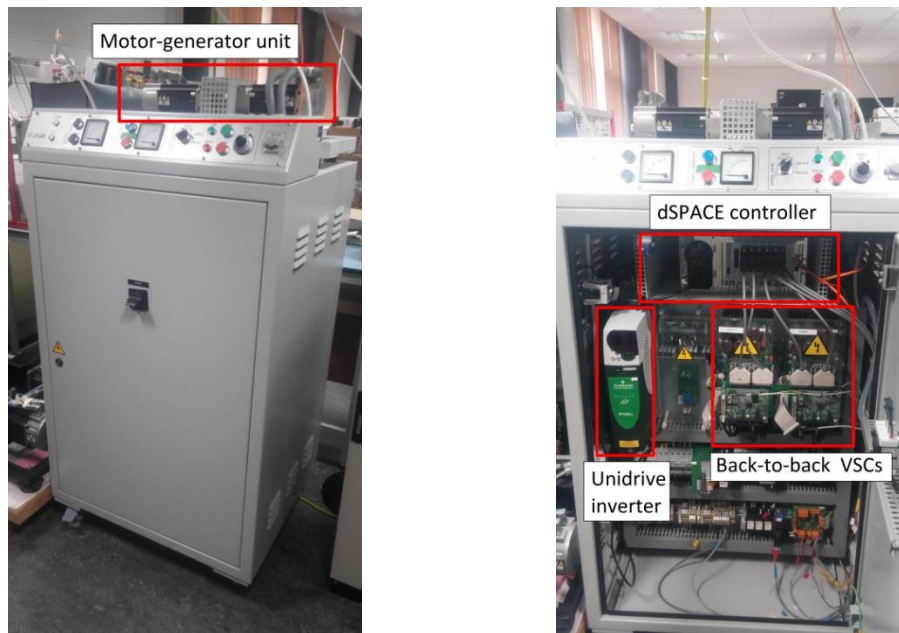


Figure 4.17: Wind Turbine test rig

### 4.6.3 VSC Test Rig and DC Network Cabinet

The VSC test rig represents the HVDC converters. This test rig formed by three 2-level VSCs, an embedded computer (dSPACE), ac inductors and dc inductors, as shown in Figure 4.19. The dSPACE controls the VSCs and monitors the test rig operation. Only two VSCs (WFC and GSC) are used in the experiment to test an HVDC point-to-point system. WFC absorbs power from the WT test rig and GSC injects this power to the grid simulator.

The VSCs are interconnected through the dc network cabinet, which is used as a scaled-down representation of dc cables. This cabinet includes dc inductors, dc capacitors and distributed  $\pi$  models to represent dc cables, as shown in Figure 4.18. More technical specifications about the VSC test rig and the dc network cabinet are found in Appendix E. In this experiment, the dc cables are represented with the dc inductors.

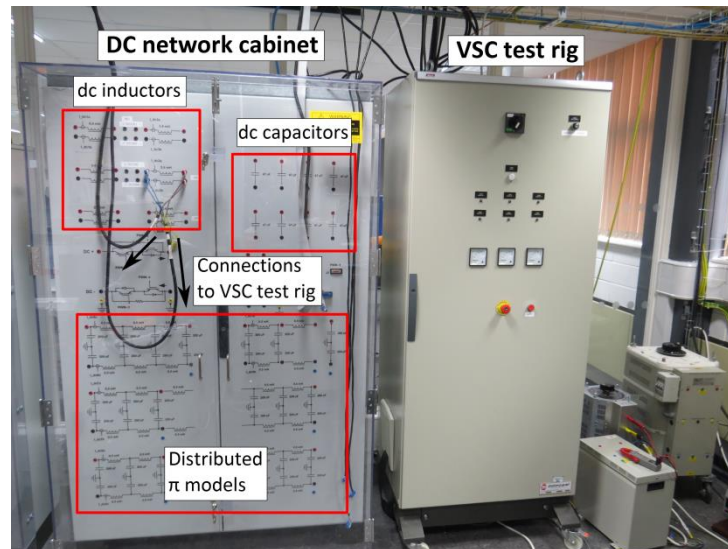


Figure 4.18: VSC test rig and dc network cabinet

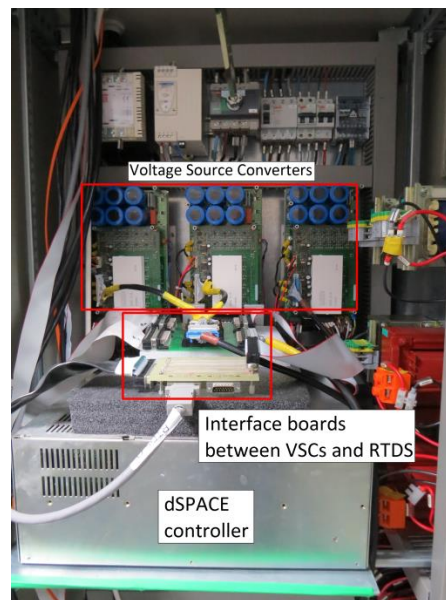


Figure 4.19: Interior of VSC test rig

#### 4.6.4 Real Time Simulator and Grid Simulator

The real time simulator (RTDS) models the onshore ac grid as a low order system frequency response model. RSCAD software is used to build the models for RTDS. The real time simulator provides the voltage of the onshore ac system as an analog output signal, and receives the current measurement from GSC as an analog input, as shown in Figures 4.15, 4.16 and 4.20. A phase difference exists between the actual VSC test rig current and the RTDS measurement,  $i_{abc}$ , due to a transmission signal delay. A lead-lag compensator is used in RTDS to eliminate the phase difference in

the current measurement (-4.96 degrees). The current output of the lead-lag filter,  $i_{abc, response}$ , is the input signal to a controllable source in RSCAD model.

The grid simulator interfaces the RTDS to the VSC test rig. It receives the voltage signals from the RTDS and generates the necessary output voltage for GSC, as shown in Figure 4.20a. This grid simulator is a four-quadrant power amplifier that absorbs the power from the GSC and injects it back to the laboratory supply. Figure 4.21 shows a picture of the real time simulator and the grid simulator and their technical specifications are found in Appendix E.

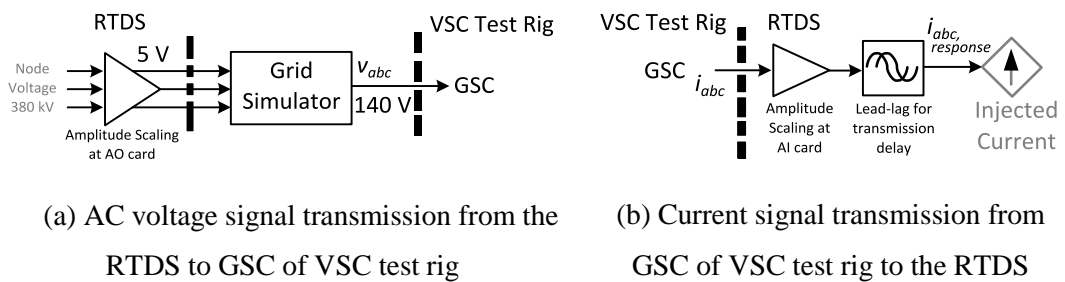


Figure 4.20: Interface of RTDS with VSC test rig

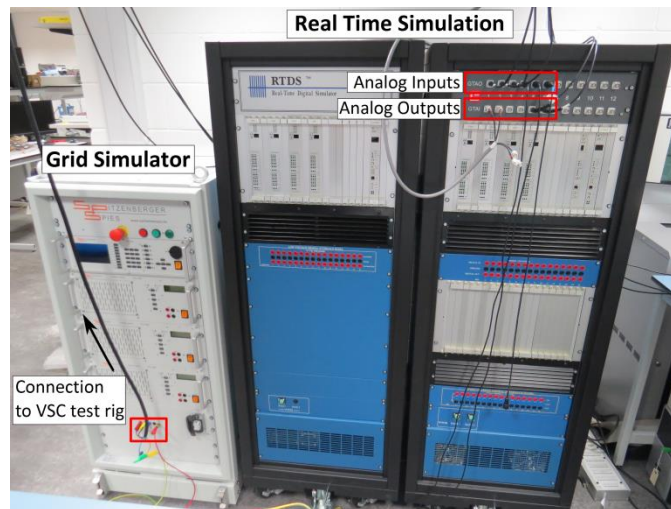


Figure 4.21: Real time simulator and Grid simulator

#### 4.6.5 Contributions to the implementation of the Hardware-in-the-Loop Set-up

This HIL set-up was implemented in collaboration with Dr. Oluwole Daniel Adeuyi from Cardiff University. The PhD candidate was responsible for the following tasks:

- Implementing converter controls of the WT test rig, including an inertia emulation control, and the aerodynamic and mechanical model of a real WT in the dSPACE controller [147].
- Implementing ac voltage control in the WFC, which is necessary to connect the WT test rig to the VSC test rig.
- Defining scaling gains to interface RTDS to VSC test rig.
- Implementing lead-lag controller to compensate phase delay in current measurement.

## 4.7 SIMULATION AND EXPERIMENTAL RESULTS

The case study to implement inertia emulation from an HVDC-connected OWPP is the same as in Section 4.3.3, but the WT generator and VSC dynamics are considered. Inertia emulation of WTs is implemented as TO, based on the step function presented in Figure 4.5 and with the parameters in Table 4.4. A communication-free control scheme is used to artificially couple the offshore and onshore frequencies. The droop gains,  $k_v$  and  $k_f$ , are defined as:

$$k_v = \frac{\Delta V_{dc,max}}{\Delta f_{on,max}} ; k_f = \frac{\Delta f_{off,max}}{\Delta V_{dc,max}} \quad (4.7)$$

where  $\Delta f_{on,max}$  and  $\Delta f_{off,max}$  are the maximum frequency deviations on the onshore and offshore grids and  $\Delta V_{dc,max}$ , is the maximum dc voltage deviation in the HVDC transmission system. In this case,  $\Delta V_{dc,max} = 0.1 pu$  and  $\Delta f_{on,max} = \Delta f_{off,max} = 0.8 Hz$ , which results as  $k_v = 0.125 Hz^{-1}$  and  $k_f = 8 Hz$ . More details of the other controllers are found in Appendix H.

The experimental results are compared against PSCAD simulations. These results are expressed in per-unit according to the base values in Table 4.6. The dynamic response of the experimental test rig and PSCAD model depends on the dc cable and VSC parameters. The test rig cable inductance and resistance and the dc capacitors and ac inductors of the VSCs were scaled-down in order to have equal per-unit values as the PSCAD model and to achieve an equivalent dynamic response between the experimental rig and PSCAD model.

Table 4.6: Base values for PSCAD model and experimental test rig

Parameter	PSCAD model	Experimental test rig
Power, $P_b$	1.2 GW	700 W
Voltage HVDC transmission, $V_{hvdc,b}$	640 kV	250 V
Impedance HVDC transmission, $Z_{dc,b} = V_{hvdc,b}^2/P_b$	341.3 $\Omega$	89.29 $\Omega$
AC voltage, $V_{ac,b}$	380 kV	140 V
AC impedance, $Z_{ac,b} = V_{ac,b}^2/P_b$	120.3 $\Omega$	28 $\Omega$
Wind Turbine rotor speed, $\omega_{r,b}$	148.5 rpm	2010 rpm

Three cases were studied:

- No IE: no inertia emulation from OWPP.
- IE: inertia emulation without WT recovery power limitation.
- IE-R: inertia emulation with WT recovery power limitation. This is achieved by saturating the recovery power at 4% of pre-disturbance power and increasing the transition delay to the recovery phase from 0.5 to 3 s.

The imbalance occurs at 2 s and is modelled as a connection of a resistive load. Figures 4.22 - 4.26 show the simulation and experimental results of the onshore and offshore ac grid frequencies, powers at each HVDC terminal, dc voltage at WFC, WT rotor speed and WT efficiency. In general, there is good agreement between the simulation and experimental results. The no-load power losses of the VSCs produce an offset difference about 0.075 pu between the active power through the GSC and WFC, as shown in Figure 4.23b. This is because the VSC operating power is 700 W, which is about 14 times less than the rated power of 10 kW.

#### 4.7.1 Rate of Change of Frequency and Frequency Deviation

Table 4.7 shows the RoCoF and maximum frequency deviation results associated to the frequencies in Figure 4.22. As mentioned in Section 4.3.3, the RoCoF is measured for the first second after the imbalance and with a sampling time of 0.5 s. The inertia response from WTs reduces the maximum frequency deviation 16.9% and the RoCoF 6%. The sudden decrease of WT power when the inertia emulation is deactivated generates a second drop in the onshore ac frequency, as shown in Figure 4.22 when WT recovery period is not limited.

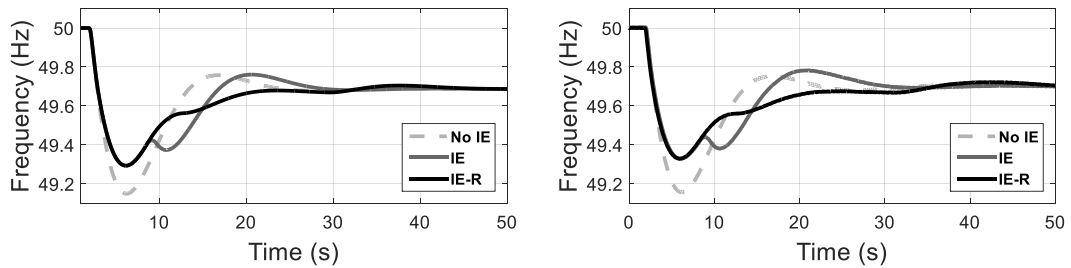


Figure 4.22: Simulation (left side) and experimental (right side) results of the onshore ac grid frequency

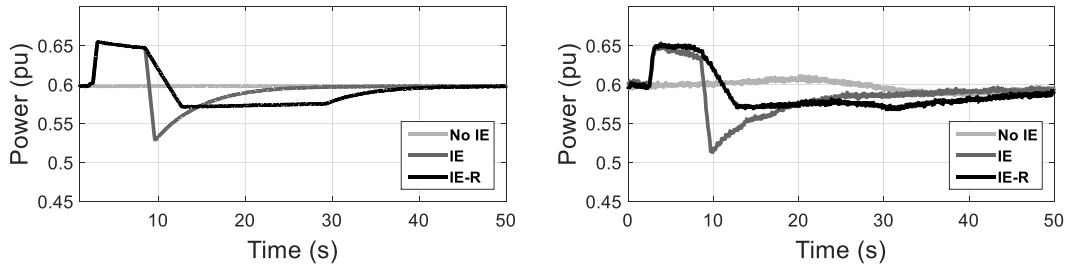
Table 4.7: Frequency deviation and RoCoF from PSCAD simulation results

Case	Maximum RoCoF (Hz/s)	$\Delta f_{max}$ (Hz)
No IE	0.352	0.851
IE	0.331	0.707
IE-R	0.331	0.707

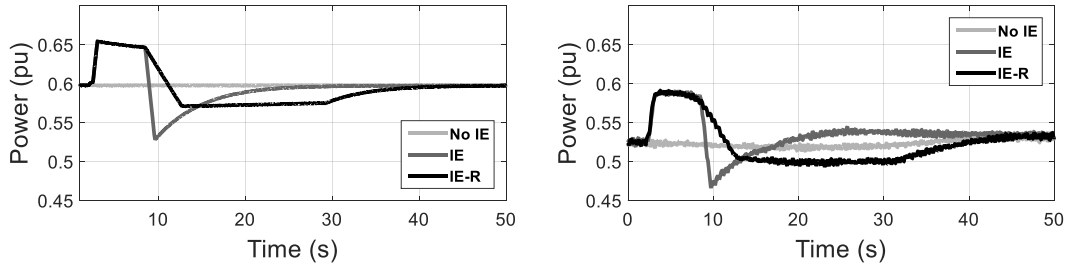
## 4.7.2 Wind Turbine Recovery Power

The impact of the WT recovery period on the frequency can be limited when the WT recovery power is saturated and the transition to the recovery phase is delayed. Figure 4.23 shows that the wind power generation without recovery limitation decreases down to 12.5% of the pre-disturbance power and with recovery limitation the reduction is saturated at 4%. As a consequence, the second frequency drop is attenuated, but the WTs need more time to recover the kinetic energy from the rotating mass. This is shown in Figure 4.24a, where the rotor speed without recovery limitation returns back to the pre-disturbance speed approximately at 30 s and with recovery limitation this time is extended to 50 s. The recovery phase delay shifts the second frequency drop from 11 s to 14 s. Also, this delay increases the inertia response period from 6 s to 9 s. As a result, more kinetic energy is extracted from the rotating mass and the minimum rotor speed slightly reduces from 0.9 pu to 0.89 pu, as shown in Figure 4.24a.

The recovery limitation decreases the efficiency of the WTs, *i.e.* increases the loss of captured wind energy, due to a longer recovery period and a higher rotor speed reduction. However, the efficiency reduction is not significant as shown in Figure 4.24b. The efficiency in the experimental results is lower than in the simulation results due to large power losses of the experimental test rig.

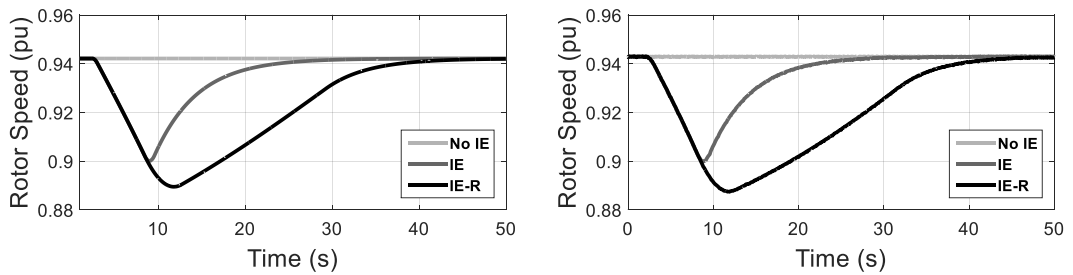


(a) Active power through WFC

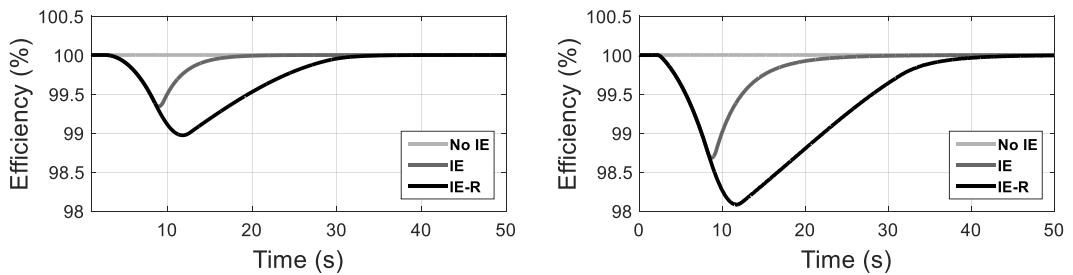


(b) Active power through GSC

Figure 4.23: Simulation (left column) and experimental (right column) results of the power transfer through HVDC transmission.



(a) WT rotor speed

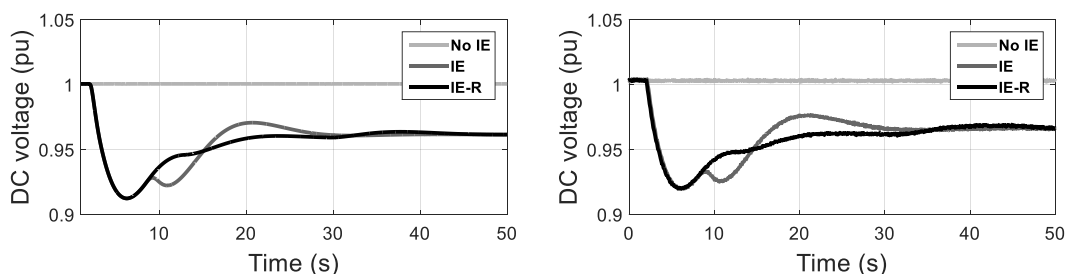


(b) WT efficiency

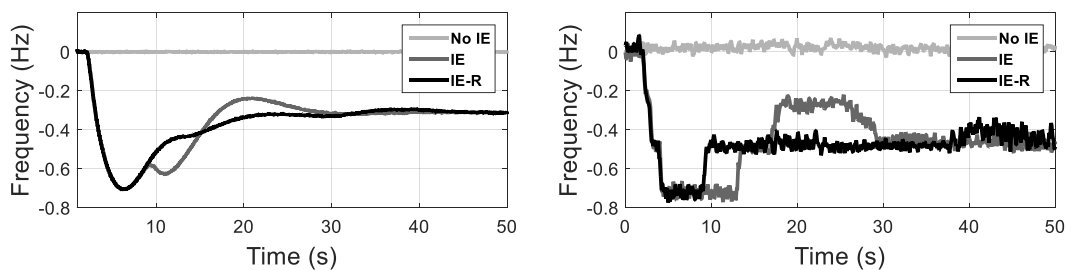
Figure 4.24: Simulation (left column) and experimental (right column) results of the WT rotor speed and efficiency

### 4.7.3 DC voltage and Offshore Frequency Variation

Figure 4.25 shows the dc voltage and offshore ac frequency variations due to the additional  $f - V_{dc}$  droop implemented in the GSC and the  $f - V_{dc}$  droop implemented in the WFC. Therefore, an artificial coupling between the offshore and onshore grids is defined to allow the OWPP to provide inertia response. It is observed that the offshore ac frequency variation is the same as in the onshore grid since the droop gains were defined such that  $k_v k_f = 1$ . Also, the dc voltage deviations are about 0.08 pu, which is within permissible limits, assuming dc voltage limits of  $\pm 10\%$  on the HVDC transmission system.



(a) DC voltage at WFC



(b) Offshore ac frequency deviation

Figure 4.25: Simulation (left column) and experimental (right column) results of the DC voltage at WFC and offshore ac frequency deviation.

### 4.7.4 Response Times

The inertia emulation from OWPP is not activated instantaneously as shown in Figure 4.26, where the onshore and offshore frequencies and the OWPP power variation are illustrated during the activation of inertia emulation. It is observed that the offshore ac frequency starts to decrease 100 ms after the imbalance. This delay is affected by the response delay of the converter controls and the length of the dc cables. The WTs detect the frequency deviation and start to increase their power with a delay

of 400 ms. This delay is caused by the frequency threshold in the inertia emulation control and the response delay of the converter controls. Considering that the maximum power contribution is designed to be reached in 500 ms, the total activation time is equal to 1 s.

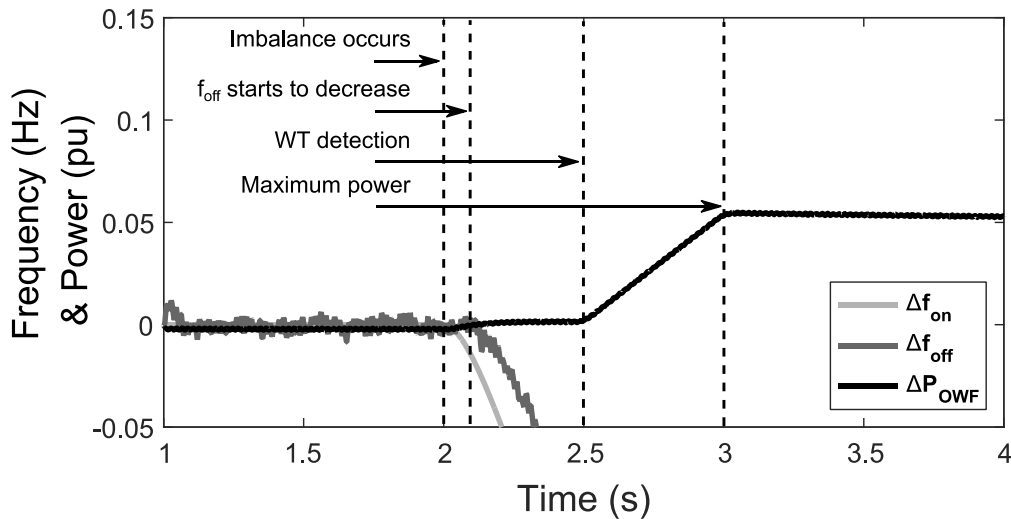


Figure 4.26: Simulation results of onshore and offshore frequency and OWPP power variation during activation of inertia emulation.

## 4.8 SUMMARY

This chapter analysed two strategies for inertia emulation in OWPPs: Synthetic Inertia (SI) and Temporary Overproduction (TO). SI mimics inertia response of synchronous generators using different combinations of PD controllers and TO injects additional power using a step or proportional function. Considering system operator's requirements for WT inertial emulation, the parameter tuning of TO is more appropriate than in SI. Also, TO is more robust against frequency measurement noise than SI, but it provides a fix additional power independently of the frequency deviation, unless a proportional function is used.

A number of SI and TO control implementations were simulated in MATLAB Simulink and compared in terms of maximum frequency deviation, RoCoF and loss of captured wind energy during inertia response provision. The SI implemented as a PD or P controller with washout filter and the TO had a similar performance in terms of RoCoF and maximum frequency deviation. Also, the impact of recovery power on

the frequency response was reduced by delaying the recovery period and limiting the recovery power.

A HIL experimental test rig was used to demonstrate inertia emulation with TO in an OWPP connected through an HVDC point-to-point link. A communication-free strategy was chosen to define an artificial coupling between the onshore and offshore frequencies. The experimental results showed good agreement with an equivalent PSCAD simulation model. The maximum power contribution from inertia emulation was activated in 1 s and the frequency coupling between onshore and offshore grids introduced a 100 ms delay.

## CHAPTER 5

# ELECTRICAL RESONANCE STABILITY IN HVDC-CONNECTED OFFSHORE WIND POWER PLANTS

### 5.1 INTRODUCTION

Harmonic instabilities have been reported in practical installations such as BorWin1, which was the first HVDC-connected OWPP [19], [148]. More recently, electrical interactions between offshore HVDC converters and series resonances have been identified in DolWin1 and highlighted by CIGRE Working Groups as potential causes of instability during the energisation of the offshore ac grid [11], [20], [81]. In HVDC-connected OWPPs, the long export ac cables and the power transformers located on the offshore HVDC substation cause series resonances in the frequency range of 100 ~ 1000 Hz [11], [20], [149], *i.e.* at harmonic frequencies. Moreover, the offshore grid is a poorly damped system without a rotating mass or resistive load [19], [20]. The typical control of an offshore HVDC converter could further reduce the total damping at the resonant frequencies until the system becomes unstable [51].

The state space eigenvalue analysis provides information about all the oscillation modes of the system and the contribution of the different state variables. However, a detailed information for all elements is required and high-order dynamic models for large systems can exceed the computation limits of the solvers. As alternative, frequency domain methods can be used to analyse stability with less compute-intensive effort. Methods based on the impedance characterization of the system represent the frequency response of the grid and converters from their connection point. The impedance frequency response can be obtained from real measurements, *i.e.* without detailed data of the elements. Therefore, manufacturers and system operators can provide the impedance frequency response without compromising their intellectual property [19]. However, the impedance representation of the system analyses stability from the connection point of the grid and converters, which might

not consider all the oscillation modes of the system, and does not provide information about the contribution of the state variables.

This chapter analyses and discusses the impact that harmonic series resonances have on the voltage stability of HVDC-connected OWPPs. An impedance-based representation is used to identify resonances and to assess stability considering the effect of the offshore converters. A reformulation of the positive-net-damping criterion [150] is used to determine the resonance stability of an OWPP. This alternative approach evaluates the net-damping for electrical series resonances and provides a clear relation between electrical resonances of the OWPP and stability. Analytical expressions of the harmonic series resonances are obtained and the total damping of the OWPP is used to characterise conditions of stability. The effect that the HVDC converter control parameters and the OWPP configuration have on stability is shown using examples. Root locus analysis and time-domain simulations in PSCAD/EMTDC are used to validate the stability conditions.

## **5.2 IMPEDANCE-BASED REPRESENTATION OF AN HVDC-CONNECTED OWPP**

An impedance-based representation is suitable for the modelling of converters of an HVDC-connected OWPP whenever detailed design information is not available. Such a converter representation offers advantages as it can easily be combined with the equivalent impedance of the offshore ac grid to characterise resonant frequencies. It is also possible to consider the effect of the converter controllers. Moreover, the stability assessment methods for impedance-based representations are simple and less computational intensive compared to other traditional methods such as eigenvalue analysis [19], [151].

The configuration of an HVDC-connected OWPP is shown in Figure 5.1. Type 4 WTs are considered in this configuration, since this is the preferred topology for high rated power offshore WTs to increase reliability. If Type 3 WTs were considered, near-synchronous resonances would be originated due to interactions with the WT generator.

The WTs are connected to strings of the collector system through step-up transformers from low to medium voltage. Each WT grid side VSC has a coupling

reactor and a high frequency filter represented as an equivalent capacitor. The strings are connected to a collector substation, where transformers step-up from medium to high voltage. The collector transformer in Figure 5.1 is an equivalent representation of 4 transformers that are connected in parallel in normal operation [20]. Export cables send the generated power to an offshore HVDC substation, where a VSC-based MMC operates as a rectifier and delivers the power to the dc transmission system. The dc transmission system and the onshore HVDC converters are not represented in this study, because the offshore ac grid dynamics are not transferred to the dc system.

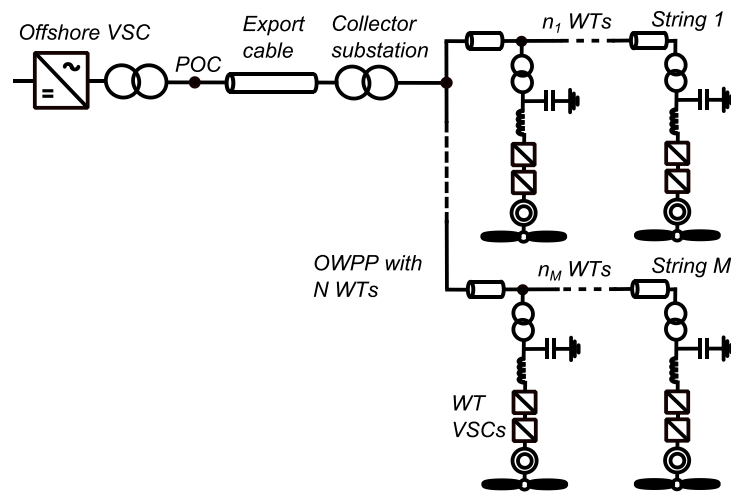


Figure 5.1: General scheme of an HVDC-connected OWPP.

Figure 5.2 shows an impedance-based model of the HVDC-connected OWPP suitable for the analysis of electrical resonances and stability. The ac cables of the export and collector system are modelled as single  $\pi$  sections with lumped parameters and the transformers are modelled as RL equivalents. These models are accurate enough to characterise the harmonic resonances that are responsible for stability issues [20]. The VSCs are represented by equivalent circuits, which include the frequency response of the controller. The offshore VSC is represented by a Thévenin equivalent as it controls the ac voltage of the offshore grid [51], [152]; however, Norton equivalents are used to represent the WT VSCs since they control current [152], [153].

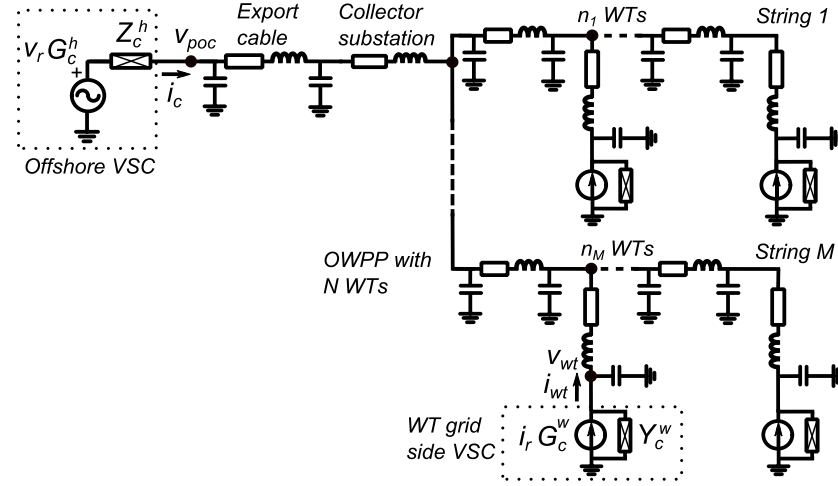


Figure 5.2: Impedance-based model of an HVDC-connected OWPP for resonance and stability analysis.

### 5.3 IMPEDANCE-BASED MODEL OF VSCS

The VSC models are represented in a synchronous  $dq$  frame and in the Laplace  $s$  domain, where complex space vectors are denoted with boldface letters for voltages and currents as  $\mathbf{v} = v_d + jv_q$  and  $\mathbf{i} = i_d + ji_q$ . More details about complex space vectors and transfer functions are found in Appendix F.

#### 5.3.1 Offshore VSC Model

The offshore VSC controls the ac voltage of the offshore grid. Figure 5.3(a) describes the control structure of this converter. If the VSC uses an MMC topology, high frequency filters are not required and only a voltage control loop is considered [53], [154]. Additionally, the internal MMC dynamics can be neglected if a circulating current control is implemented [154]. The control action based on a PI controller is expressed as:

$$\mathbf{v}_{\text{vsc}}^h = F_{PI,v}(\mathbf{v}_r - \mathbf{v}_{\text{poc}}) \quad (5.1)$$

$$F_{PI,v} = k_{p,v} + \frac{k_{i,v}}{s} \quad (5.2)$$

where  $\mathbf{v}_{\text{vsc}}^h$  is the reference voltage for the offshore converter,  $\mathbf{v}_r$  is the control reference voltage at the Point of Connection (POC),  $\mathbf{v}_{\text{poc}}$  is the voltage measured at the POC and  $F_{PI,v}$  is the PI controller for the voltage control loop.

The dynamics across the equivalent coupling inductance of the offshore converter are expressed as:

$$\mathbf{v}_{\text{vsc}}^h = \mathbf{v}_{\text{poc}} + \mathbf{i}_c (R_f^h + sL_f^h + j\omega_1 L_f^h) \quad (5.3)$$

where  $\mathbf{i}_c$  is the current from the HVDC converter,  $L_f^h$  is the coupling inductance,  $R_f^h$  is the equivalent resistance of the coupling inductance and  $\omega_1 = 2\pi f_1$  rad/s ( $f_1 = 50$  Hz).

A Thévenin equivalent of the offshore VSC (see Figure 5.2) is obtained by combining (5.1) and (5.3):

$$\mathbf{v}_{\text{poc}} = \mathbf{v}_r \cdot G_c^h - \mathbf{i}_c \cdot Z_c^h \quad (5.4)$$

$$G_c^h = \frac{F_{PI,v}}{1 + F_{PI,v}}; Z_c^h = \frac{R_f^h + sL_f^h + j\omega_1 L_f^h}{1 + F_{PI,v}} \quad (5.5)$$

where  $G_c^h$  is the voltage source transfer function and  $Z_c^h$  is the input-impedance of the converter.

### 5.3.2 Wind Turbine VSC Model

Each WT is equipped with a back-to-back converter, but only the grid side VSC is represented in this study, because the generator side VSC is decoupled from the ac voltage dynamics by the dc link between the VSCs. Its control is based on an ac current loop employing a PI controller as shown in Figure 5.3(b). The dc voltage outer loop is not represented in the WT VSC model since its dynamic response is slow; *i.e.* there is sufficient bandwidth separation with the inner current loop [19], [55]. This ensures that there are no interactions between harmonic resonances and the outer loops, which are not of interest in this thesis. Therefore, the control action based on a PI controller is expressed as:

$$\mathbf{v}_{\text{vsc}}^w = F_{PI,c}(\mathbf{i}_r - \mathbf{i}_{\text{wt}}) + j\omega_1 L_f^w \mathbf{i}_{\text{wt}} + H_v \mathbf{v}_{\text{wt}} \quad (5.6)$$

$$F_{PI,c} = k_{p,c} + \frac{k_{i,c}}{s}; H_v = \frac{\alpha_f}{s + \alpha_f} \quad (5.7)$$

where  $\mathbf{v}_{vsc}^w$  is the reference voltage for the WT converter,  $\mathbf{i}_r$  is the control reference current,  $\mathbf{i}_{wt}$  is the current from the WT VSC,  $L_f^w$  is the coupling inductance,  $\mathbf{v}_{wt}$  is the voltage after the coupling filter,  $F_{PI,c}$  is the PI controller of the current loop,  $H_v$  is the low pass filter of the voltage feed-forward term and  $\alpha_f$  the bandwidth of  $H_v$ . The PI design is based on [153], [155], with proportional and integral gains given as  $k_{p,c} = \alpha_c L_f^w$  and  $k_{i,c} = \alpha_c R_f^w$ , where  $\alpha_c$  is the bandwidth of the current control and  $R_f^w$  is the equivalent resistance of the coupling inductance.

The dynamics across the coupling filter of the WT converter are expressed as:

$$\mathbf{v}_{vsc}^w = \mathbf{v}_{wt} + \mathbf{i}_{wt}(R_f^w + sL_f^w + j\omega_1 L_f^w) \quad (5.8)$$

A Norton equivalent of the WT converter (see Figure 5.2) is obtained combining (5.6) and (5.8):

$$\mathbf{i}_{wt} = \mathbf{i}_r \cdot G_c^w - \mathbf{v}_{wt} \cdot Y_c^w \quad (5.9)$$

$$G_c^w = \frac{F_{PI,c}}{R_f^w + sL_f^w + F_{PI,c}}; Y_c^w = \frac{1 - H_v}{R_f^w + sL_f^w + F_{PI,c}} \quad (5.10)$$

where  $G_c^w$  is the current source transfer function and  $Y_c^w$  is the input-admittance of the VSC.

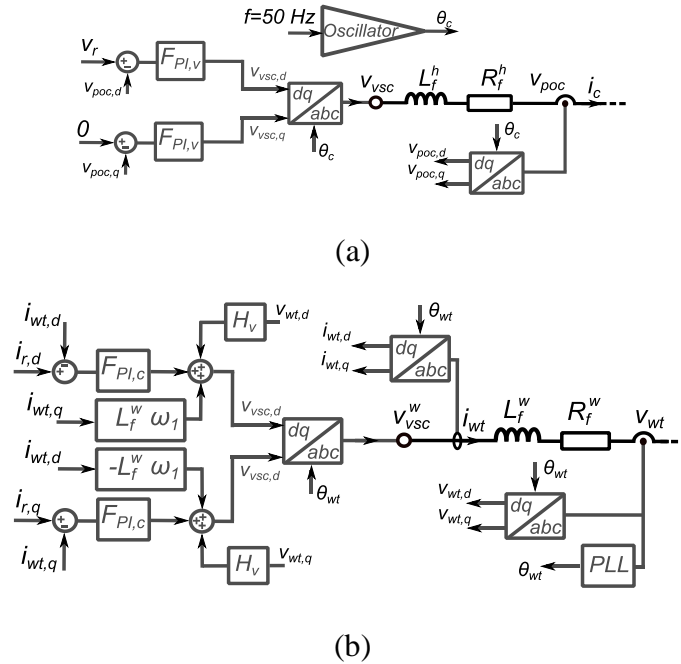


Figure 5.3: Control structures: (a) Offshore HVDC converter and (b) WT grid side converter.

## 5.4 STABILITY ANALYSIS OF HVDC-CONNECTED OWPPS

The stability analysis considers the impedance-based circuit presented in Figure 5.4 where the offshore grid is modelled with an equivalent circuit (further explained in Section 5.5). A similar representation can be found in [51].

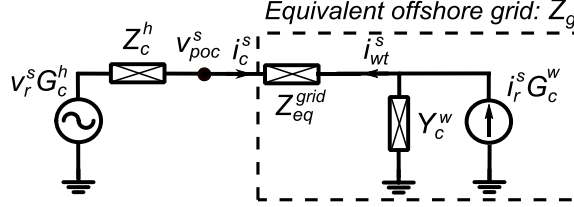


Figure 5.4: Equivalent impedance-based circuit of an HVDC-connected OWPP with representation of offshore grid circuit.

The impedances are expressed in the stationary  $\alpha\beta$  frame [156], [157], which is denoted in boldface letters for voltages and currents as  $\mathbf{v}^s = v_\alpha + jv_\beta$  and  $\mathbf{i}^s = i_\alpha + ji_\beta$ . The current in the stationary  $\alpha\beta$  frame and the Laplace  $s$ -domain is given as:

$$\mathbf{i}_c^s = (\mathbf{v}_r^s G_c^h - \mathbf{i}_r^s G_c^w Z_c^w) \frac{\overbrace{1/Z_g}^{T_h}}{1 + Z_c^h/Z_g} \quad (5.11)$$

where  $Z_g = Z_{eq}^{grid} + 1/Y_c^w$  is the equivalent impedance of the OWPP from the offshore VSC and  $T_h$  is the VSC closed loop transfer function, which can be also expressed as:

$$T_h(s) = \frac{M(s)}{1 + M(s)N(s)} = \frac{M(s)}{1 + L(s)} \quad (5.12)$$

where  $M(s) = 1/Z_g$  is the open loop transfer function,  $N(s) = Z_c^h$  is the feedback transfer function and  $L(s)$  is the loop transfer function.

Assuming that the voltage and current sources in ( 5.11 ) are stable when they are not connected to any load [151], the stability of the OWPP can be studied in the following ways:

- By analysing the poles of  $T_h$  or the roots of  $Z_g + Z_c^h = 0$ .
- By applying the Nyquist stability criterion of  $Z_c^h/Z_g$  [151].
- By considering the passivity of  $T_h$  [156], [157].

In addition to the previous alternatives, a variation to the positive-net-damping criterion given in [58], [150] is here employed instead to analyse system stability. The criterion has been reformulated to evaluate electrical resonance stability as explained in Section 5.4.2.

### 5.4.1 Passivity

A linear and continuous-time system  $F(s)$  is passive if [157]:

- $F(s)$  is stable and,
- $\text{Re}\{F(j\omega)\} > 0 \forall \omega$ , which is expressed in terms of the phase as  $-\frac{\pi}{2} \leq \arg\{F(j\omega)\} \leq -\frac{\pi}{2}$ . This condition corresponds to a non-negative equivalent resistance in electrical circuits.

Passivity can be applied to determine the stability of closed loop systems [156], [157]. A system represented by the closed loop transfer function in ( 5.12 ) is stable if  $M(s)$  and  $N(s)$  are passive since  $-\pi \leq \arg\{L(j\omega)\} \leq -\pi \forall \omega$ . This implies that the Nyquist stability criterion for  $L(s)$  is satisfied. Therefore, the OWPP is stable if  $Z_g$  and  $Z_c^h$  are passive. When the HVDC converter is connected to a passive offshore grid,  $Z_g$  is passive and the stability only depends on the passivity conditions of the converter input-impedance,  $Z_c^h$ .

In a no-load operation (*i.e.* when only the passive elements of the OWPP are energised), the passivity of  $Z_g$  is ensured as WTs are assumed to be disconnected from the offshore grid. However, the WTs represent active elements when they are connected to the offshore grid (*i.e.*  $Z_g$  can have a negative resistance), which may compromise the OWPP stability.

### 5.4.2 Positive-net-damping Stability Criterion

The criterion states that a closed loop system is stable if the total damping of the OWPP is positive at the following frequencies: (i) open loop resonances and (ii) low frequencies where the loop gain is greater than 1 [150]. A detailed demonstration of this criterion is presented in Appendix G. This criterion does not provide a clear relation between electrical resonances of the OWPP and system stability, which increases the complexity for analysing the impact that system parameters have on resonance stability.

The criterion presented in [150] has been reformulated to evaluate the net-damping for electrical series resonances. The approach proposed in this chapter is developed from the phase margin condition [51]. If stability is evaluated in terms of the phase margin,  $L(j\omega) = M(j\omega)N(j\omega)$  must satisfy the following conditions at angular frequency  $\omega$ :

$$|M(j\omega)N(j\omega)| = 1 \quad (5.13)$$

$$-\pi \leq \arg\{M(j\omega)N(j\omega)\} \leq -\pi \quad \forall \omega. \quad (5.14)$$

where  $M(j\omega)$  and  $N(j\omega)$  in (5.13) and (5.14) can be expressed in terms of equivalent impedances as:

$$\frac{1}{M(j\omega)} = Z_g(j\omega) = R_g(\omega) + jX_g(\omega) \quad (5.15)$$

$$N(j\omega) = Z_c^h(j\omega) = R_c^h(\omega) + jX_c^h(\omega) \quad (5.16)$$

Also, the equivalent impedance from the voltage source  $\mathbf{v}_r^s G_c^h$  in Figure 5.4 is expressed as:

$$Z_{eq}^h = Z_c^h + Z_g \quad (5.17)$$

Phase margin condition (5.13) is equivalent to:

$$R_c^h(\omega)^2 + X_c^h(\omega)^2 = R_g(\omega)^2 + X_g(\omega)^2 \quad (5.18)$$

The resistive components in HVAC grids and VSCs may be usually neglected compared to the reactive components. Therefore,  $R_g \ll X_g$ ,  $R_c^h \ll X_c^h$  and (5.13) is simplified to:

$$X_c^h(\omega) = \pm X_g(\omega) \quad (5.19)$$

The electrical series resonances observed from the voltage source  $\mathbf{v}_r^s G_c^h$  in Figure 5.4 correspond to frequencies where  $Z_{eq}^h$  in (5.17) has a dip or a local minimum. If the resistive components are neglected, the series resonance condition is reduced to:

$$\text{Im}\{Z_{eq}^h(j\omega_{res})\} \approx 0 \rightarrow X_c^h(\omega_{res}) = -X_g(\omega_{res}) \quad (5.20)$$

It can be observed that ( 5.20 ) is a particular case of ( 5.19 ); *i.e.* the series resonance condition of  $Z_{eq}^h$  coincides with the stability condition  $|M(j\omega)N(j\omega)| = 1$  given by ( 5.13 ).

Phase margin condition ( 5.14 ) can be expressed in terms of the imaginary part of  $L(j\omega)$  as follows:

$$\left\{ \begin{array}{l} \text{If } \frac{d|L(j\omega)|}{d\omega} > 0 : 0 < \arg\{L(j\omega)\} < \pi \rightarrow R_g(\omega)X_c^h(\omega) - R_c^h(\omega)X_g(\omega) > 0 \\ \text{If } \frac{d|L(j\omega)|}{d\omega} < 0 : -\pi < \arg\{L(j\omega)\} < 0 \rightarrow R_g(\omega)X_c^h(\omega) - R_c^h(\omega)X_g(\omega) < 0 \end{array} \right. \quad (5.21)$$

If the resonance condition in ( 5.20 ) is combined with ( 5.21 ):

$$\left\{ \begin{array}{l} \text{If } \frac{d|L(j\omega)|}{d\omega} > 0 : X_c^h(\omega_{res})[R_c^h(\omega_{res}) + R_g(\omega_{res})] > 0 \\ \text{If } \frac{d|L(j\omega)|}{d\omega} < 0 : X_c^h(\omega_{res})[R_c^h(\omega_{res}) + R_g(\omega_{res})] < 0 \end{array} \right. \quad (5.22)$$

It can be shown (see Appendix G) that if the offshore grid is capacitive (*i.e.*  $X_g < 0$ ) and the HVDC converter is inductive (*i.e.*  $X_c^h > 0$ ), then  $\frac{d|L(j\omega)|}{d\omega} > 0$ . On the other hand, if the offshore grid is inductive (*i.e.*  $X_g > 0$ ) and the HVDC converter is capacitive (*i.e.*  $X_c^h < 0$ ), then  $\frac{d|L(j\omega)|}{d\omega} < 0$ . By considering the previous conditions, ( 5.22 ) is simplified to:

$$R_T(\omega_{res}) = R_g(\omega_{res}) + R_c^h(\omega_{res}) > 0 \quad (5.23)$$

where resistance  $R_T$  represents the total damping of the system, resistance  $R_c^h$  the HVDC converter damping and resistance  $R_g$  the offshore grid damping.

The condition in ( 5.23 ) is equivalent to the positive-net-damping criterion in [150], but evaluated for the series resonances of  $Z_{eq}^h$ . Therefore, the offshore HVDC VSC is asymptotically stable if the total damping of the system,  $R_T$ , is positive in the neighbourhood of an electrical series resonance. The advantage of this criterion with respect to the passivity approach is that stability can be ensured even if  $Z_g$  and  $Z_c^h$  are

not passive because the contribution of both terms in the closed loop system are considered.

It should be noted that if the resistive components of the offshore grid and HVDC VSC are large compared to the reactive elements (*e.g.*  $X_g/R_g < 2$  and  $X_c^h/R_c^h < 2$ ), the approximations in ( 5.19 ) and ( 5.20 ) are not valid and this criterion cannot be used. The resistive component of the medium voltage collector cables is significant compared to the reactance. However, it is assumed that the resistive contribution of the collector grid is small compared to the rest of the offshore grid, *i.e.* the high voltage export cables and transformers.

### 5.4.3 Relation Between Total Damping and Poles of the System

The HVDC-connected OWPP is a high order system with several poles. However, the system response is governed by a dominant poorly-damped pole pair. If this pole pair is related to the electrical series resonance, impedances  $Z_g$  and  $Z_c^h$  around this resonance can be approximated as:

$$Z_{c,res}^h(s) \approx R_c^h + sL_c^h; Z_{g,res}(s) \approx R_g + \frac{1}{sC_g} \quad (5.24)$$

where  $C_g$  is the equivalent capacitor of the offshore grid impedance when the frequency is close the resonance. Employing ( 5.20 ), the series resonance reduces to

$$\omega_{res} = 1/\sqrt{L_c^h C_g}.$$

The poles related to the series resonance are obtained from  $1 + Z_{c,res}^h(s)/Z_{g,res}(s) = 0$ , yielding:

$$s = \frac{-(R_c^h + R_g)C_g \pm \sqrt{(R_c^h + R_g)^2 C_g^2 - 4L_c^h C_g}}{2L_c^h C_g} \quad (5.25)$$

Considering that  $(R_c^h + R_g)^2 C_g^2 \ll 4L_c^h C_g$ , equation ( 5.25 ) is approximated to:

$$s \approx -\frac{R_c^h + R_g}{2L_c^h} \pm j \frac{1}{\sqrt{L_c^h C_g}} \quad (5.26)$$

The imaginary part of the closed loop system poles corresponds to the resonant frequency. Also, the real part of the poles is correlated to the total damping,  $R_c^h + R_g$ , as mentioned in [58]. Therefore, there is a pair of poles that represent the series resonance and can be used to identify instabilities.

## 5.5 RESONANCE CHARACTERISATION

In this section, the low frequency series resonances of an OWPP are characterised. It is useful to identify harmonic series resonances in an OWPP since they can destabilise an offshore HVDC converter. To this end, the frequency response of  $Z_{eq}^h(j\omega)$  is here used to identify electrical resonances. Due to the complexity of the VSC and offshore grid equations, simplifications are used to obtain analytical expressions of the resonant frequencies.

### 5.5.1 Simplifications of the OWPP impedance model

Figure 5.5 shows that the frequency response of VSC impedance can be simplified to RL equivalents above 100 Hz. The input-impedance of the VSCs is represented in an  $\alpha\beta$  frame (see Figure 5.4). To achieve this, a reference frame transformation from  $dq$  to  $\alpha\beta$  is performed using the rotation  $s \rightarrow s - j\omega_1$  [156], [158]. For frequencies higher than  $\omega_1$ , the offshore VSC impedance,  $Z_c^h(s - j\omega_1)$ , is approximated to:

$$R_c^h = \frac{R_f^h}{1 + k_{p,v}}; L_c^h = \frac{L_f^h}{1 + k_{p,v}} \quad (5.27)$$

Similarly, the WT VSC impedance,  $Z_c^w(s - j\omega_1) = 1/Y_c^w(s - j\omega_1)$ , is approximated to:

$$R_c^w = R_f^w + (\alpha_f + \alpha_c)L_f^w; L_c^w = L_f^w \quad (5.28)$$

The previous simplifications do not consider the VSCs as active elements since  $R_c^h$  and  $R_c^w$  are positive for all frequencies.

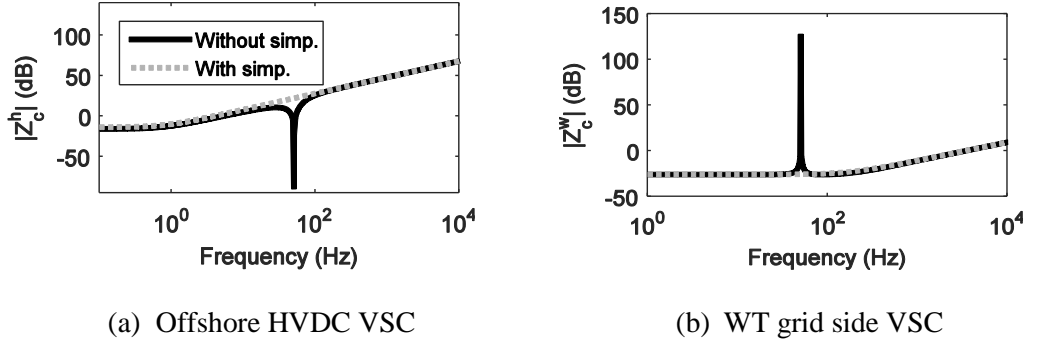


Figure 5.5: Frequency response with and without simplifications (parameters in Appendix H with  $k_{p,v} = 1$ ,  $k_{i,v} = 500$ ).

Figure 5.6 shows the equivalent model of the HVDC-connected OWPP with the simplified VSC and cable models. The capacitor  $C_{ec}$  represents the export cable capacitance. The inductive and resistive components of the export cable are small enough to be combined with the RL equivalent of the transformers and the HVDC converter. Also, the collector cables are removed because their equivalent inductance and capacitance are small and only affect the response at high frequencies, which are not considered in this study.

When collector cables are removed, the aggregation of WTs is reduced to a combination of parallel circuits independent to the collector system topology. Figure 5.7 shows the OWPP model under this scenario, which is equivalent to the model in Figure 5.4. The parameters of the aggregated model are defined as follows:

- $R_{tr}^{CS}$  and  $L_{tr}^{CS}$  are the RL values of the collector transformers.
- $R_{tr,a}^W$  and  $L_{tr,a}^W$  are the RL values of the aggregated WT transformers:

$$R_{tr,a}^W = R_{tr}^W/N; L_{tr,a}^W = L_{tr}^W/N \quad (5.29)$$

where  $N$  is the number of WTs and  $R_{tr}^W$  and  $L_{tr}^W$  are the RL values of one WT transformer.

- $R_{c,a}^W$  and  $L_{c,a}^W$  are the RL values of the aggregated WT converters:

$$R_{c,a}^W = R_c^W/N; L_{c,a}^W = L_c^W/N \quad (5.30)$$

- $C_{f,a}^W$  is the equivalent capacitance of the aggregated WT low pass filters:

$$C_{f,a}^w = C_f^w \cdot N \tag{5.31}$$

where  $C_f^w$  is the capacitance of one WT low pass filter.

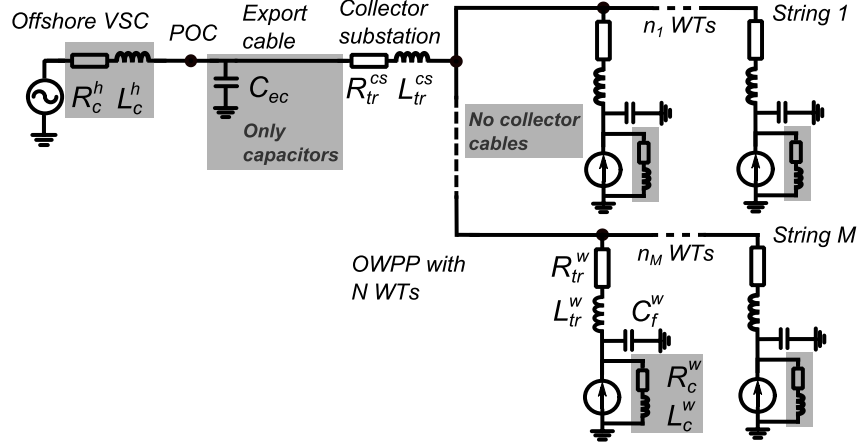


Figure 5.6: Impedance-based model of an HVDC-connected OWPP with simplified VSC and cable models (indicated in grey rectangles)

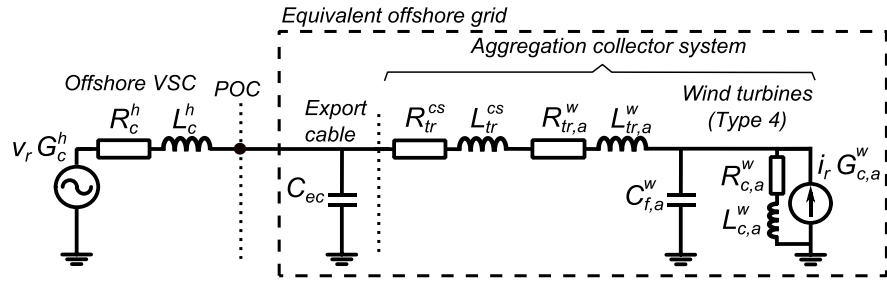
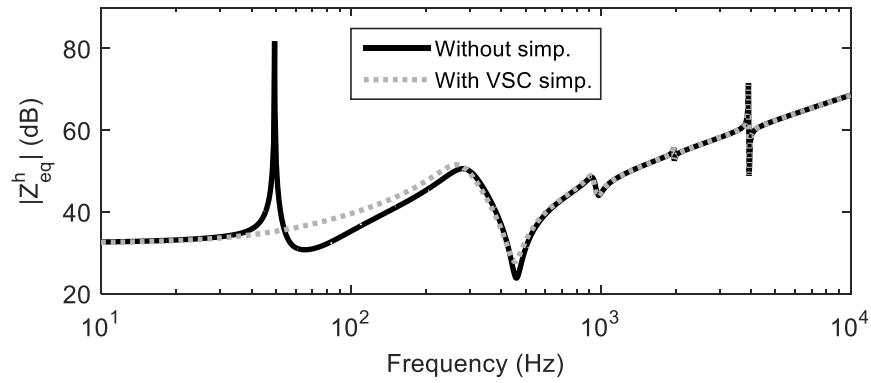
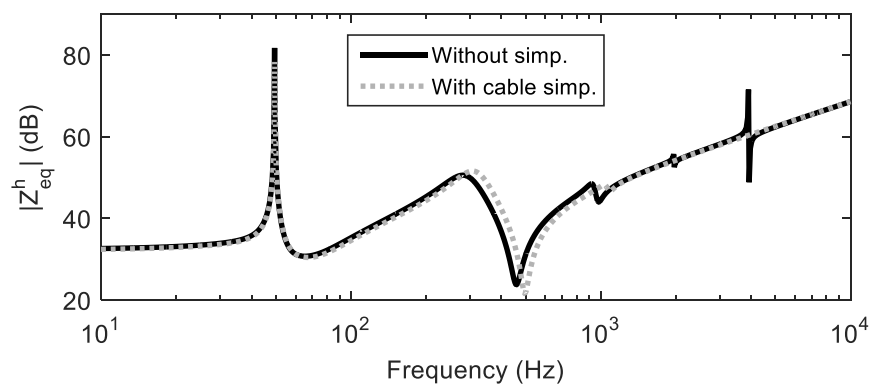


Figure 5.7: Impedance-based model of an HVDC-connected OWPP with aggregation of collector system

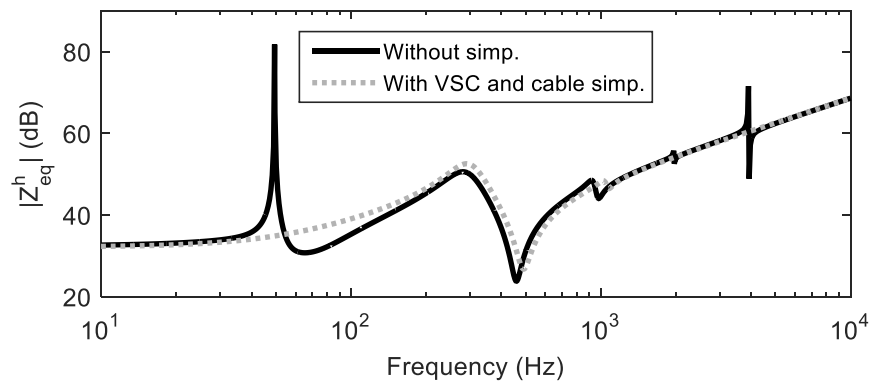
Figure 5.8 shows the frequency response of  $Z_{eq}^h$  with and without simplifications to VSC and cable models. In Figure 5.8a it can be observed that if VSC simplifications are made the 50 Hz resonance of the converter control is not exhibited; however, the frequency response agrees well with that of the un-simplified  $Z_{eq}^h$  over 200 Hz and up to 1 kHz. Additionally, the simplification of the collector cables represent the resonances for frequencies up to 1000 Hz and slightly shifts the series resonance from 459 Hz to 497 Hz as shown in Figure 5.8b. In light of these results, it can be concluded that the simplified frequency response represents a good approximation for harmonic resonances in the range of 200 ~ 1000 Hz.



(a) OWPP impedance with VSC simplifications



(b) OWPP impedance with cable model simplifications



(c) OWPP impedance with VSC and cable model simplifications

Figure 5.8: Frequency response of OWPP impedance without and with VSC and cable model simplifications (parameters in Appendix H with  $k_{p,v} = 1$ ,  $k_{i,v} = 500$ ).

### 5.5.2 Analytical expression for the series resonant frequency

The expression of the lowest series resonant frequency of  $Z_{eq}^h$  is obtained for no-load operation and when WTs are connected. The resistances are neglected as they only have a damping effect on resonance (*i.e.* they barely modify the resonant frequency).

In no-load operation, the WTs are not connected and the contribution of the collector system at low frequencies is negligible. Therefore, the OWPP impedance  $Z_{eq}^h$  in ( 5.17 ) is equivalent to an LC circuit with a resonant frequency:

$$f_{res}^{nload} = \frac{1}{2\pi\sqrt{L_c^h C_{ec}}} \quad (5.32)$$

The lowest series resonant frequency when WTs are connected has been obtained following an algebraic calculation from Figure 5.7:

$$\left\{ \begin{array}{l} f_{res}^{conWT} = \frac{1}{2\pi} \sqrt{\frac{b - \sqrt{b^2 - 4ad}}{2a}} \\ a = C_{ec} L_{c,a}^w (L_{tr}^{cs} + L_{tr,a}^w) L_c^h C_{f,a}^w \\ b = C_{ec} L_c^h (L_{c,a}^w + L_{tr}^{cs} + L_{tr,a}^w) + C_{f,a}^w L_{c,a}^w (L_c^h + L_{tr}^{cs} + L_{tr,a}^w) \\ d = L_c^h + L_{c,a}^w + L_{tr}^{cs} + L_{tr,a}^w \end{array} \right. \quad (5.33)$$

Expressions ( 5.32 ) and ( 5.33 ) may be employed to evaluate the total system damping and to determine stability at series resonances.

## 5.6 VOLTAGE STABILITY ANALYSIS

The modified positive-net-damping criterion is applied to analyse the impact of electrical series resonances in the voltage stability of an HVDC-connected OWPP. The effects of the offshore HVDC converter control and the OWPP configuration are considered in the study. For completeness, the root locus of the system and time-domain simulations in PSCAD/EMTDC are used to confirm the results.

The cable model simplifications considered in the resonance characterisation are used in the stability analysis given that the low frequency response is well-represented and the damping contribution from the cable resistances can be neglected. However, the VSC simplifications in ( 5.27 ) and ( 5.28 ) are not considered, because the

converters are not modelled as active elements. The system is analysed in no-load operation and when WTs are connected based on the OWPP described in Appendix H.

### 5.6.1 No-load operation

In no-load operation, the positive-net-damping stability criterion only includes the damping contribution of the offshore converter,  $R_c^h$ , because the export and collector cables are passive elements with a small resistance compared to the equivalent converter resistance and thus  $R_g$  can be neglected (*i.e.*  $R_g = 0$ ). Therefore, condition ( 5.23 ) is reduced to  $R_c^h(j\omega_{res}) > 0$ , which is equivalent to analysing the passivity of the HVDC converter control at resonant frequencies.

Stability is ensured if the electrical series resonance is located in a frequency region with positive resistance. This region is determined using the zero-crossing frequencies of  $R_c^h$  (*i.e.*  $R_c^h(\omega) = \text{Re}\{Z_c^h(\omega)\} = 0$ ) in ( 5.5 ). The two following solutions are obtained:

$$\left\{ \begin{array}{l} \omega_{cut1} = \omega_1 = 2\pi 50 \\ \omega_{cut2} = \frac{\omega_1}{1 - \frac{k_{i,v} L_f^h}{R_f^h (1 + k_{p,v})}} \end{array} \right. \quad (5.34)$$

When  $\omega_{cut2} < 0$ , the only zero-crossing frequency considered is 50 Hz and  $R_c^h$  is negative for  $\omega > 2\pi 50$ . Therefore, the converter is always unstable for resonant frequencies above 50 Hz. If  $\omega_{cut2} > 0$ , then  $R_c^h$  is negative for  $2\pi 50 < \omega < \omega_{cut2}$  and positive for  $\omega > \omega_{cut2}$  as shown in Figure 5.9. In this case, the converter is stable for frequencies higher than  $\omega_{cut2}$  since the resonance is located in a positive-resistance region. Thus, the offshore HVDC converter is stable when  $R_c^h$  has two zero-crossing frequencies ( $\omega_{cut2} > 0$  and  $\omega_{res} > \omega_{cut2}$ ). The following inequalities are obtained by combining ( 5.32 ) and ( 5.34 ):

$$\left\{ \begin{array}{l} \omega_{cut2} > 0 \rightarrow R_f^h (1 + k_{p,v}) - k_{i,v} L_f^h > 0 \\ \omega_{res} > \omega_{cut2} \rightarrow R_f^{h2} (1 + k_{p,v})^2 - 2R_f^h L_f^h (1 + k_{p,v}) k_{i,v} - \\ \quad - \omega_1^2 R_f^{h2} L_f^h C_{ec} (1 + k_{p,v}) + k_{i,v}^2 L_f^{h2} > 0 \end{array} \right. \quad (5.35)$$

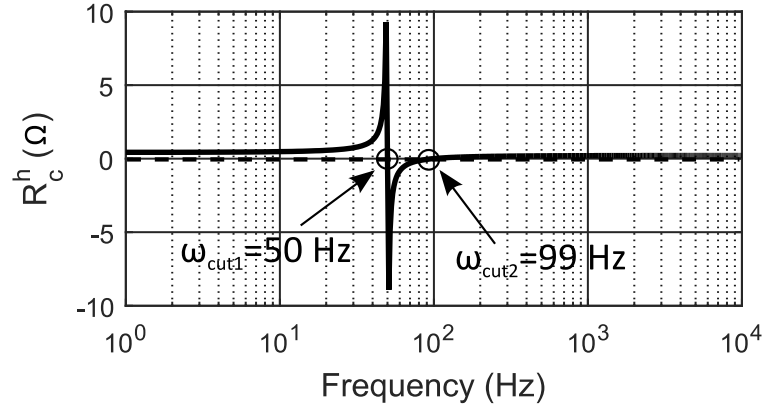


Figure 5.9: Zero-crossing frequencies of  $R_c^h$  when  $k_{p,v} = 0.01, k_{i,v} = 2.5$ .

Figure 5.10 shows the stability area [ $R_c^h(\omega_{res}) > 0$ ] defined by (5.35) as a function of the control parameters of the offshore HVDC converter,  $k_{p,v}$  and  $k_{i,v}$ , and the export cable length,  $l_{cb}$ . It is observed that when the cable length increases the stable area is reduced.

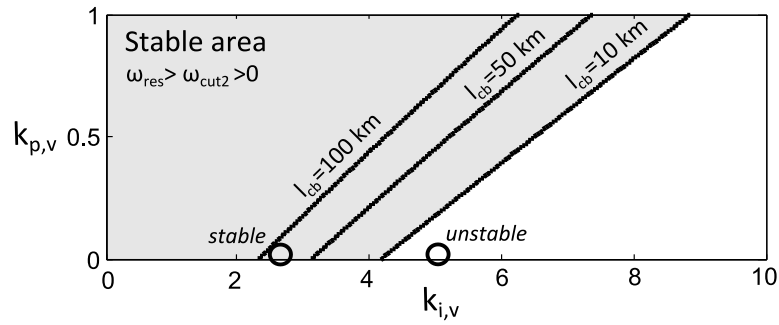
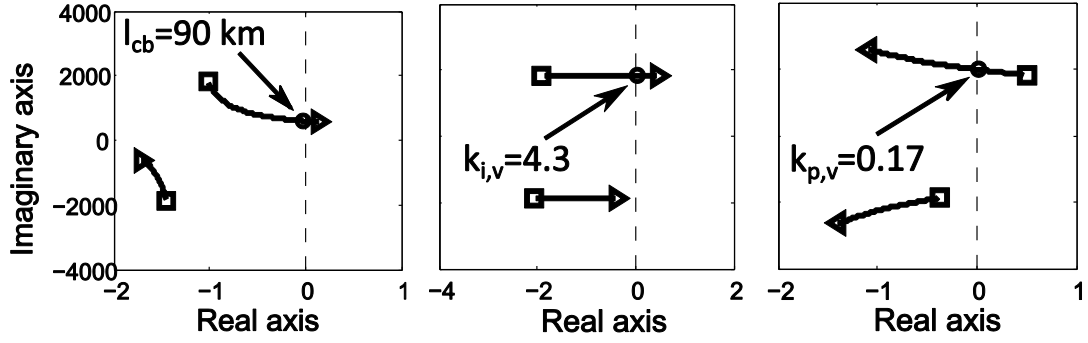


Figure 5.10: Stable area of offshore HVDC converter in no-load operation as function of  $k_{p,v}$ ,  $k_{i,v}$  and  $l_{cb}$  (the stable and unstable examples of Figures 5.12 and 5.13 are marked with circles).

Figure 5.11 shows the root locus of the harmonic resonant poles for parametric variations of  $k_{p,v}$ ,  $k_{i,v}$  and  $l_{cb}$ . It should be emphasised that these poles are not complex conjugates due to the transformation of the VSC input impedance from a synchronous  $dq$  to a stationary  $\alpha\beta$  reference frame, which introduces complex components.

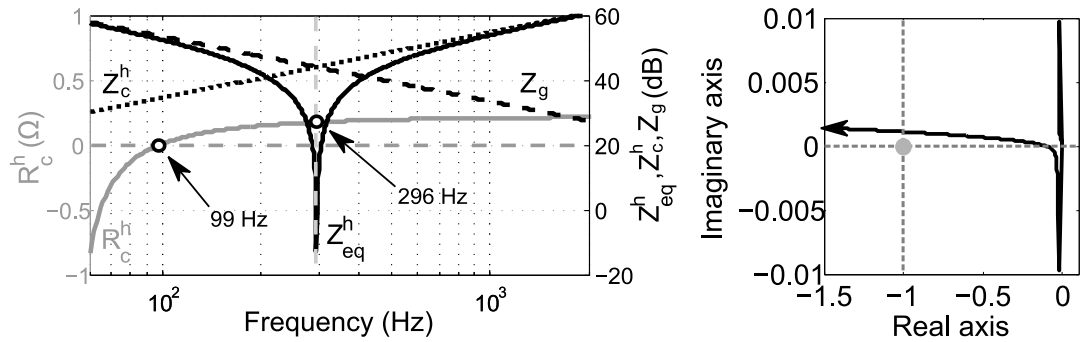


(a) Cable length variation from 1 to 100 km ( $k_{p,v} = 100, k_{i,v} = 1$  to 5). (b) Variation of  $k_{i,v}$  from 1 to 5 ( $k_{p,v} = 100, l_{cb} = 0$  to 10 km). (c) Variation of  $k_{p,v}$  from 0 to 1 ( $k_{i,v} = 5, l_{cb} = 10$  km).

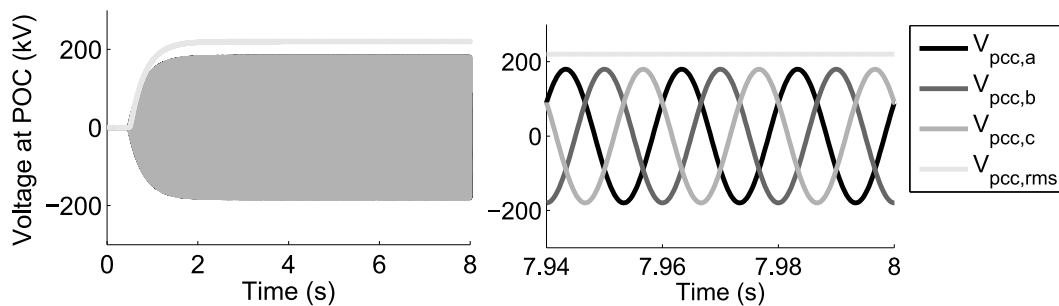
Figure 5.11: Root locus of OWPP in no-load operation for variations of export cable length and ac voltage control parameters.

The increase of cable length moves the resonance to lower frequencies since  $C_{ec}$  increases. As  $k_{p,v}$  increases, the resonance shifts to higher frequencies given that  $L_c^h$  in ( 5.27 ) decreases. Changes in  $k_{i,v}$  do not affect the resonant frequency. The system becomes unstable when one of the resonant poles moves to the positive side of the real axis; this is equivalent to have a negative damping. It can be observed that the stability conditions of the resonant poles agree with the stable areas shown in Figure 5.10.

Figures 5.12 and 5.13 show examples of stable and unstable cases when  $k_{i,v}$  is modified. The intersection between  $Z_c^h$  and  $Z_g$  (i.e.  $1/|M(j\omega)| = |N(j\omega)|$ ) approximately determines the series resonant frequency, as defined in ( 5.20 ). When the system is stable the resonant frequency is located in a positive-resistance region of  $Z_c^h$ , as shown in Figure 5.12a. Also, employing the Nyquist criterion, the Nyquist trajectory encircles  $(-1,0)$  in anti-clockwise direction and the open loop system does not have unstable poles. Therefore, the system is stable as it does not have zeros with positive real part. Although the ac voltage control can be designed to ensure stability, all the poles have a low damping. This slows down the dynamic response, as shown in Figure 5.12c, which is not acceptable for the operation of the offshore converter.

(a) Frequency response:  $R_c^h, Z_{eq}^h, Z_c^h, Z_g^h$ .(b) Nyquist curve of  $Z_c^h/Z_g^h$ 

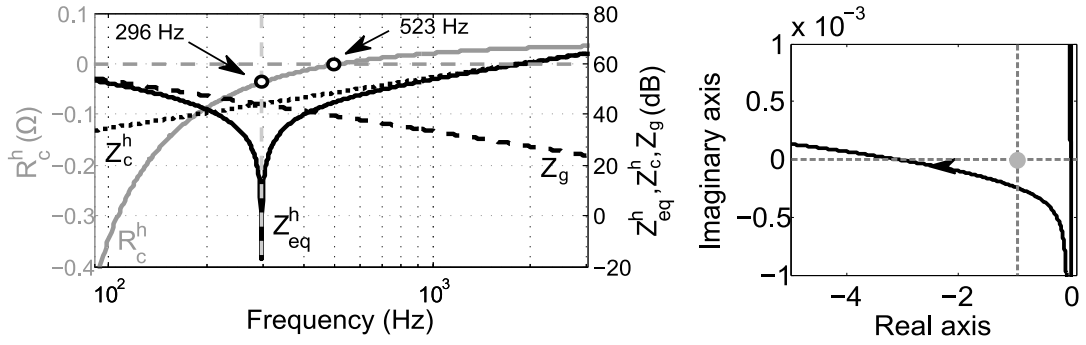
(only positive frequencies)



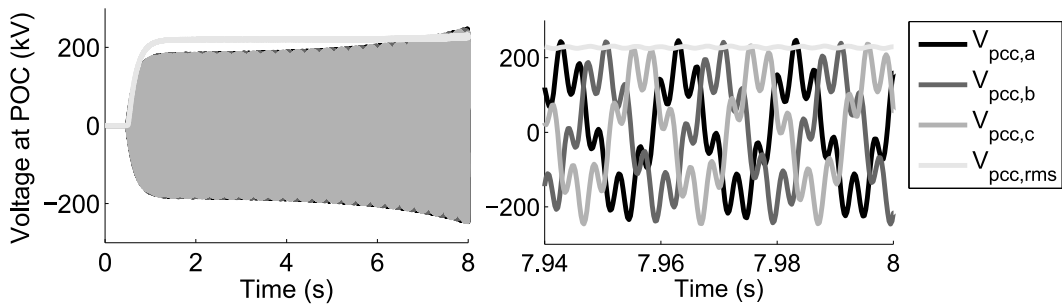
(c) Instantaneous and RMS voltages at POC. Step change is applied at 1 s.

Figure 5.12: Stable example in no-load operation with  $k_{p,v} = 0.01, k_{i,v} = 2.5$  and  $l_{cb} = 10 \text{ km}$ .

When the system is unstable the resonant frequency is located in the negative-resistance region of  $Z_c^h$ , as shown in Figure 5.13a. Following the Nyquist criterion, the Nyquist trajectory encircles  $(-1,0)$  in clockwise direction and the open loop system does not have unstable poles. Therefore, the system is unstable because the total number of zeros with positive real part is 1. In Figure 5.13c, the voltage at the POC shows oscillations at 296 Hz due to the resonance instability identified in Figure 5.13a.

(a) Frequency response:  $R_c^h, Z_{eq}^h, Z_c^h, Z_g^h$ .(b) Nyquist curve of  $Z_c^h/Z_g^h$ 

(only positive frequencies)



(c) Instantaneous and RMS voltages at POC. Step change is applied at 1 s.

Figure 5.13: Unstable example in no-load operation with  $k_{p,v} = 0.01, k_{i,v} = 4.6$  and  $l_{cb} = 10 \text{ km}$ .

## 5.6.2 Connection of Wind Turbines

In this case the WT converters modify the harmonic resonance location and the total damping. The stability conditions are discussed, but the expressions for the zero-crossing frequencies of  $R_T$  are not obtained analytically due to the complexity of the system.

Figure 5.14 shows the stable area defined by  $R_T(\omega_{res}) > 0$ . There is a significant increase of the stable region when the WTs are connected. Therefore, the ac control parameters can be modified for a larger range of values to improve the dynamic response without compromising stability.

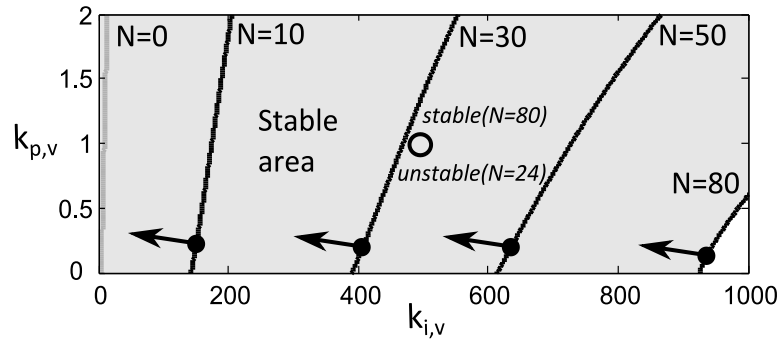
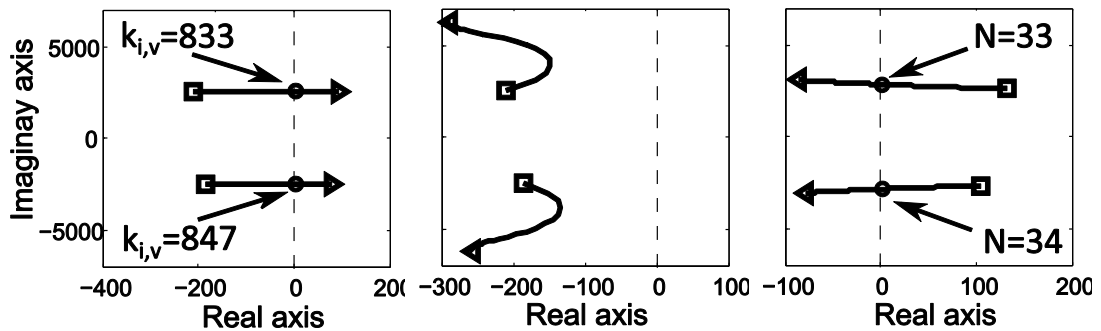


Figure 5.14: Stable area of offshore HVDC converter as a function of  $k_{p,v}$  and  $k_{i,v}$  and the number of connected WTs (the stable and unstable examples of Figures 5.16 and 5.17 are marked with a circle).

Figure 5.15 shows the root locus of the harmonic resonant poles for different ac voltage control parameters and number of WTs. The connection of WTs improves the resonance stability because the associated poles move to the left hand side of the real axis and increase the damping of those harmonic frequency modes. This damping contribution of the WTs is also mentioned in [19]. The stability conditions of the resonant poles agree with the stable area shown in Figure 5.14. Also, the resonance moves to higher frequencies when  $k_{p,v}$  and the number of WTs increases, as shown in Figure 5.15b-c.

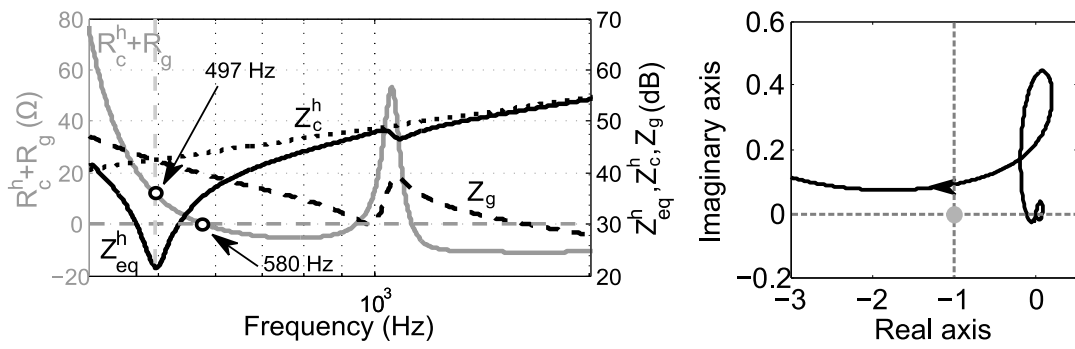


(a) Variation of  $k_{i,v}$  from 1 to 1200 ( $k_{p,v} = 0.01$ ,  $N = 80$ ). (b) Variation of  $k_{p,v}$  from 0 to 100 ( $k_{i,v} = 2.5$ ,  $N = 80$ ). (c) Variation of WTs from 1 to 80 ( $k_{p,v} = 1$ ,  $k_{i,v} = 500$ ).

Figure 5.15: Root locus of OWPP for variations of ac voltage control parameters and number of WTs.

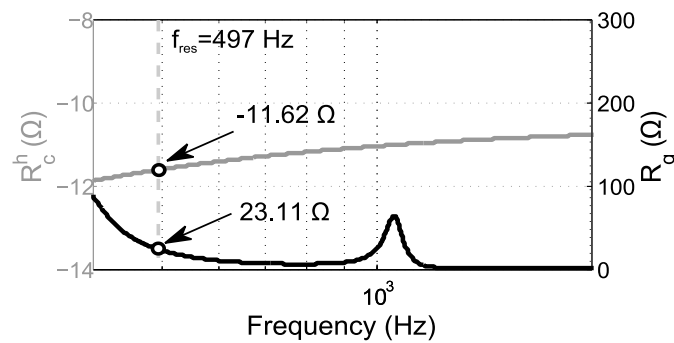
Figures 5.16 - 5.18 describe two situations where the ac voltage control is designed to have a fast dynamic response (e.g.  $k_{p,v} = 1$  and  $k_{i,v} = 500$ ) and the number of WTs decreases from 80 to 24. When all the WTs are connected, the offshore converter is

stable because the resonance is located in a positive-resistance region, as shown in Figure 5.16a. The converter introduces a negative resistance at the resonant frequency, but the total damping is compensated by  $R_g$ , as shown in Figure 5.16c. When the number of WTs reduces to 24 the offshore converter becomes unstable since the resonance lies in the negative-resistance region, as shown in 5.17a. In this case,  $R_g$  cannot compensate  $R_c^h$ , as shown in Figure 5.17c. Also, the Nyquist curve agrees with the positive-net-damping criterion in both situations (Figures 5.16b and 5.17b). In Figure 5.18 the instantaneous voltages at the POC show oscillations at 449 Hz when the number of WTs is reduced at 1 s; this is due to the resonance instability identified in Figure 5.17a.



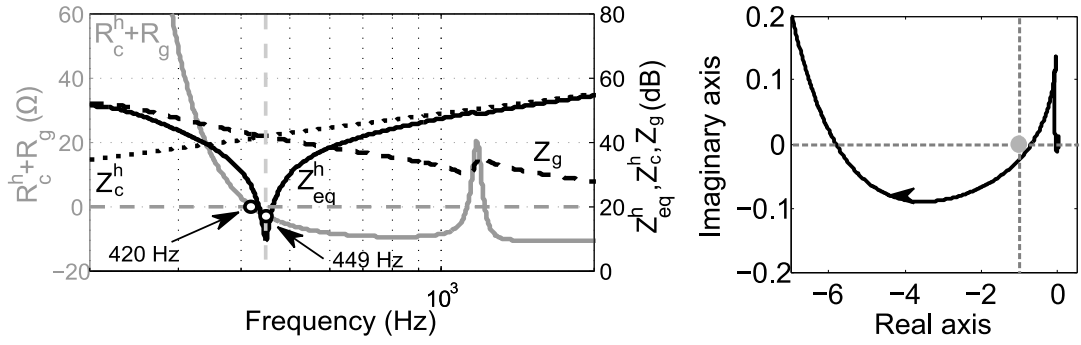
(a) Frequency response of  $R_c^h + R_g$ ,  $Z_{eq}^h$ ,  $Z_c^h$  and  $Z_g$ .

(b) Nyquist curve of  $Z_c^h/Z_g$   
(only positive frequencies)

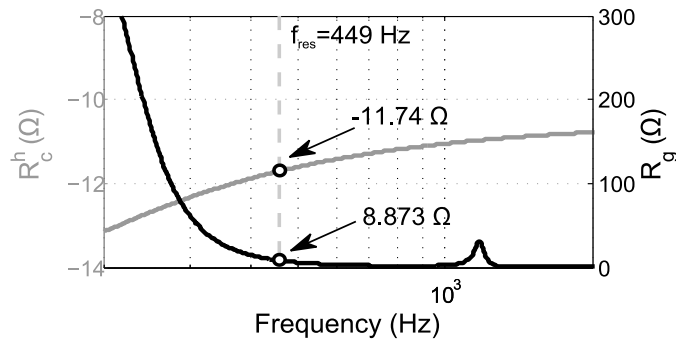


(c) Frequency response of  $R_c^h$  and  $R_g$ .

Figure 5.16: Stable example when all the WTs are connected ( $N = 80$ ),  $k_{p,v} = 1$  and  $k_{i,v} = 500$ .



(a) Frequency response of  $R_c^h + R_g$ ,  $Z_{eq}^h$ ,  $Z_c^h$  and  $Z_g$ . (b) Nyquist curve of  $Z_c^h / Z_g$  (only positive frequencies)



(c) Frequency response of  $R_c^h$  and  $R_g$ .

Figure 5.17: Unstable example when 24 WTs are connected,  $k_{p,v} = 1$  and  $k_{i,v} = 500$ .

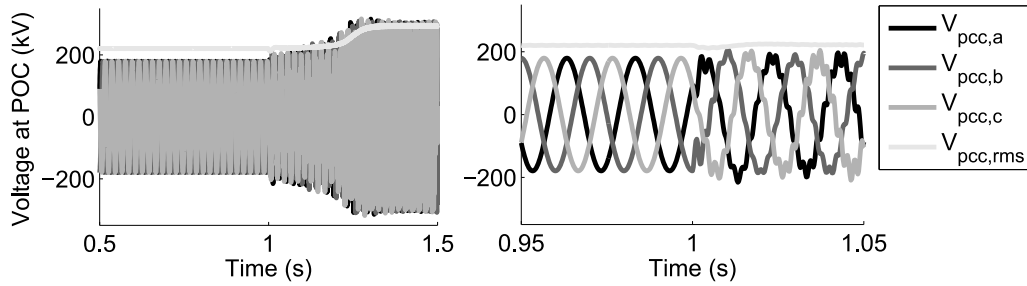


Figure 5.18: Instantaneous and RMS voltages at POC when the number of WTs is reduced from 80 to 24 at 1 s. The ac voltage control parameters are  $k_{p,v} = 1$  and  $k_{i,v} = 500$ .

The variation of connected WTs can be caused by switching configurations during commissioning phases or during outages due to maintenance or contingencies [20]. The offshore converter does not have information of these events and can only provide support based on local measurements. As shown by the previous examples, a sudden reduction in the number of WTs should be carried out with care as this can lead to instability.

## 5.7 SUMMARY

This chapter described the impact of harmonic series resonances in the voltage stability of an HVDC-connected OWPP. The positive-net-damping criterion was reformulated to define the conditions of stability of an HVDC-connected OWPP as a function of the ac voltage control parameters of the HVDC converter and the configuration of the OWPP. The modified criterion was evaluated for electrical series resonances based on the phase margin condition. Expressions of the harmonic resonance were derived from simplified VSC and cable models.

As a result, electrical resonance instabilities were analysed in different operational conditions. The stable area of the system, which represents the area of positive damping at resonant frequencies, was obtained as function of the PI control parameters of the offshore HVDC converter, the export cable length and the number of connected WTs. In no-load operation, the risk of detrimental resonance interaction increases because the resonance has poor damping and is located at the lowest frequency. The system presents resonance instability for high integral gains and low proportional gains of the PI controller. The increase of cable length decreases the resonant frequency and reduces the stable area. The connection of WTs moves the resonance to higher frequencies and increases the total damping. If the HVDC converter control is designed to have a fast dynamic response, the converter reduces the total damping at the resonant frequency.

# CHAPTER 6

## CONCLUSIONS

### 6.1 GENERAL CONCLUSIONS

VSC-HVDC transmission systems are a cost-effective way to connect OWPPs located far from the shore. However, there are still technical challenges that have to be addressed before this solution becomes a mature and reliable technology. This thesis investigated three key areas related to planning, operation and stability issues in HVDC-connected OWPPs.

#### 6.1.1 Contribution of interlinks between Offshore Wind Power Plants

Current HVDC-connected OWPPs are based on point-to-point links. More complex topologies with interlink cables between OWPPs will increase the wind power transfer. Interlink cables between the collector platforms and the offshore HVDC converters were compared according to power loss reduction and increase of energy availability in the transmission system. The following recommendations were concluded to decide the location of interlinks:

- AC interlinks between collector platforms are preferred for short distances between OWPPs (range of 40 - 60 km). This is because interlink cables are located close to the wind generation point and provide more flexible active power sharing between the transmission systems of OWPPs.
- DC interlinks are preferred for long distances between OWPPs, since ac interlinks would require an excessive reactive power compensation that would increase the power losses.

The interlinks were used to exchange active power between the transmission systems of the OWPPs, which resulted in an optimal reduction of power losses up to 10% compared to the case without interlink. This result was comparable to the power loss reduction obtained from an optimal dispatch of reactive power and voltage in the offshore ac grid. However, the final contribution of the interlinks to exchange active

power depends on the wind speed profile in each OWPP and the specifications of the transmission system.

In case of outage, the interlinks were used as alternative supply route, which increased the availability of the transmission system. The maximum availability is obtained when there is enough power capacity and number of alternative routes to transfer all the wind power in case of component failures. Therefore, OWPPs with a low wind capacity factor and transmission system and interlinks with high capacity provided the maximum availability. Also, dc cables were identified as the most sensitive components that affect the availability.

A cost-benefit analysis was carried out to compare the interlink options. The annual savings were mainly from the increase of availability, *i.e.* reduction of wind power curtailment. Also, the results using a dc interlink cable were highly affected by the estimated cost of the dc circuit breakers. The minimum interlink capacity was calculated to ensure that the power losses were minimised and the wind energy availability was maximised for all operational conditions.

### **6.1.2 Provision of Inertia Support**

Inertia emulation is one of the most recent ancillary services required from WPPs with variable speed WTs. Currently, inertia emulation is still at demonstration stage and the requirements must be standardised and agreed between manufacturers and system operators.

Synthetic Inertia and Temporary Overproduction have been defined as two main supplementary control strategies to emulate inertia in WTs. These strategies were discussed and compared according to implementation and simulation results built in MATLAB Simulink. Both strategies provided similar fast frequency containment. However, Temporary Overproduction is more robust against frequency measurement noise and it complies more with system operators' requirements. During the provision of inertia response not all available wind energy was captured due to a reduction of the WT power coefficient. However, it was concluded that the amount of uncaptured wind energy was not significant if the maximum power contribution of the WTs is in the range defined by manufacturers. After the inertia response provision, the WT recovery power caused a second frequency dip. Additional controls at WT level reduced the impact of recovery power. Such controls saturate the recovery power and delay the

recovery period by limiting the rate of change of power or increasing the overproduction time of inertia response. It is recommended to implement inertia emulation as a TO with a saturation of the recovery power.

Emulation of inertia in OWPPs connected through HVDC was demonstrated using a Hardware-in-the-loop test rig formed by scaled-down elements of a simulated system (WT test rig, VSC test rig and dc network cabinet) and a real time simulator interfaced to the rest of the system with a grid simulator. The experimental results had good agreement compared to PSCAD simulation results. The frequency coupling between onshore and offshore grid did not introduce a significant delay compared to the total activation time of inertia emulation.

### **6.1.3 Electrical Resonance Instabilities in Offshore Grids**

Converter control interactions with electrical resonances of the offshore ac grid may cause instability, since offshore ac grids are islanded systems with poorly damped resonances. In agreement with CIGRE Working Groups, harmonic series resonances were identified in the range of a few hundred Hz. These resonances interacted with the ac voltage control of the offshore HVDC converter leading to system instability.

An impedance-based representation was used to identify series resonances of the offshore ac grid and analyse stability. A reformulation of the positive-net-damping criterion was used to define conditions of stability as a function of the ac voltage control parameters of the HVDC converter and the configuration of the OWPP. This criterion is simple to evaluate and provides a practical approach to the stability analysis, because the resonance instability is related to a lack of damping at resonant frequencies. In addition, expressions of the harmonic series resonance were obtained from simplified impedance-based models of VSCs and cables.

Stability was analysed in different operational conditions. A stable area of the system was obtained as function of ac voltage control parameters, export cable length and number of connected WTs. Risk of detrimental resonance interaction increased in no-load operation and when a limited number of WTs were connected. This was caused by the poor damping exhibited by the series resonance of the offshore grid and its location at the lowest frequencies. The design of the ac voltage control to have a fast dynamic response moved the HVDC converter operation close to the unstable area due to a reduction of the total damping at the resonant frequency. External resistors or

active damping control in the VSCs are recommended to compensate the negative damping introduced by the ac voltage control. This will increase the stable area for all possible switching operations and will allow a fast dynamic response of the ac voltage control.

## 6.2 CONTRIBUTIONS

The contributions of this thesis can be summarised as follows:

- Comparison of ac and dc interlink cables between OWPPs in terms of power losses reduction and increase of energy availability of the transmission system.
- Recommendations on the decision of the interlink location between OWPPs and a design procedure to determine the interlink cable capacity.
- Comparison of inertia emulation strategies for wind turbines in terms of control implementation and inertia response performance.
- Experimental validation of inertia response capability of an OWPP connected through an HVDC point-to-point link using a hardware-in-the-loop test rig.
- Implementation of impedance-based models of VSCs to characterise harmonic resonant frequencies in the offshore ac grid and analyse resonance stability.
- Stability criterion to analyse the effect that control parameters of the offshore HVDC converter and OWPP configurations have on the resonance stability of the offshore ac grid.

## 6.3 FUTURE WORK

A summary of potential research questions is outlined in this section.

### 6.3.1 Optimal Interlinks Between Offshore Wind Power Plants

Power losses and reliability were analysed separately. An optimal problem to determine the interlink capacity and choose the best locations could be implemented combining the power loss reduction and increase of availability as energy savings. Also, the minimum number of interlinks between OWPPs could be determined to ensure N-1 or N-2 contingency conditions as in conventional onshore ac grids.

### **6.3.2 Coordination of Wind Turbines for Inertia Emulation**

Inertia emulation was analysed at WT level and an OWPP was represented as an aggregation of a single WT. The wind speed variability modifies significantly the provision of inertia emulation at WT level. However, the inertia response from OWPPs is smoothed due to the geographical distribution of the WTs [118].

An OWPP could be represented as a number of WTs with different wind speeds according to their location. Therefore, the wind speed variability and the wake effect could be included for a more realistic assessment of the inertia response from an OWPP. Also, the impact of the recovery power could be limited with a distributed recovery strategy that coordinates the recovery activation of the WTs.

### **6.3.3 Design of an Active Damping Control**

Instabilities caused by the interaction of converter controls with electrical resonances could be limited if an active damping control is implemented in the offshore HVDC converter. This active damping control would be a virtual resistance that compensates the negative resistance introduced by the ac voltage control of the offshore HVDC converter. The virtual resistance would be designed based on no-load conditions, since this is the case study with the lowest damping at the electrical resonance.

### **6.3.4 Application of Positive-net-damping Criterion in Other Case Studies and Experimental Validation.**

The reformulation of the positive-net-damping criterion could be employed to analyse other resonance instabilities caused by the VSC control, *e.g.* the interaction of outer loops of the VSC control with subsynchronous resonances or supersynchronous resonances close to the synchronous frequency. This stability criterion could be also used in other applications, *e.g.* HVDC grids, traction systems or microgrids. In addition, an experimental platform with scaled-down VSCs would be necessary to validate the stability conditions from the positive-net-damping criterion.

# APPENDIX A

## PUBLICATIONS

### A.1. PUBLICATIONS RELATED TO THIS THESIS

- Journal papers:

M. Cheah-Mane, L. Sainz, J. Liang, N. Jenkins and C.E. Ugalde-Loo, “Electrical Resonance Stability in HVDC-Connected Offshore Wind Power Plants,” *IEEE Transactions on Power Systems* (accepted).

- Conference papers:

M. Cheah-Mane, J. Liang and N. Jenkins, “Permanent magnet synchronous generator for wind turbines: Modelling, control and Inertial Frequency Response,” *2014 49th International Universities Power Engineering Conference (UPEC)*, Cluj-Napoca, 2014, pp. 1-6.

M. Cheah-Mane, Jun Liang, N. Jenkins and L. Sainz, “Electrical resonance instability study in HVDC-connected Offshore Wind Power Plants,” *2016 IEEE Power and Energy Society General Meeting (PESGM)*, Boston, MA, USA, 2016, pp. 1-5.

- Book chapters:

O.D. Adeuyi and M. Cheah-Mane, “Modelling of DC grids using Real Time Digital Simulator and Experimental Platform,” book chapter in *HVDC Grids for Transmission of Electrical Energy: Offshore Grids and a Future Supergrid*, Wiley-IEEE Press Series on Power Engineering, 2016.

### A.2. OTHER PUBLICATIONS DURING THE PHD

- Journals papers:

O. D. Adeuyi, M. Cheah-Mane, J. Liang, L. Livermore and Q. Mu, “Preventing DC Over Voltage in Multi-terminal HVDC Transmission,” *CSEE Journal of Power and Energy Systems*, vol. 1, no. 1, pp. 86-94, March 2015

E. Prieto-Araujo, P. Olivella-Rosell, M. Cheah-Mane, R. Villafafila-Robles, O. Gomis-Bellmunt, "Renewable energy emulation concepts for microgrids," *Renewable and Sustainable Energy Reviews*, vol. 50, pp. 325-345, October 2015.

L. Sainz, L. Monjo, J. Pedra, M. Cheah-Mane, J. Liang and O. Gomis-Bellmunt, "Effect of wind turbine converter control on wind power plant harmonic response and resonances," *IET Electric Power Applications*, September 2016.

O. D. Adeuyi, M. Cheah-Mane, J. Liang and N. Jenkins, "Fast Frequency Response from Offshore Multi-terminal VSC-HVDC Schemes," *IEEE Transactions on Power Delivery*, November 2016.

L. Sainz, M. Cheah-Mane, L. Monjo, J. Liang and O. Gomis-Bellmunt, "Wind power plant resonances," *Journal of Energy Challenges and Mechanics*, vol. 3, no. 4, December 2016.

- Conference papers:

O. D. Adeuyi, M. Cheah-Mane, J. Liang, N. Jenkins, Y. Wu, C. Li, X. Wu, "Frequency support from modular multilevel converter based multi-terminal HVDC schemes," *2015 IEEE Power & Energy Society General Meeting*, Denver, CO, 2015, pp. 1-5.

M. Cheah-Mane, O. D. Adeuyi, J. Liang and N. Jenkins, "A scaling method for a multi-terminal DC experimental test rig," *2015 17th European Conference on Power Electronics and Applications (EPE'15 ECCE-Europe)*, Geneva, 2015, pp. 1-9.

L. Sainz, J. J. Mesas, L. Monjo, J. Pedra and M. Cheah-Mane, "Electrical resonance instability study in wind power plants," *2016 Electric Power Quality and Supply Reliability (PQ)*, Tallinn, 2016, pp. 139-144.

L. Sainz, L. Monjo, J. J. Mesas, J. Pedra and M. Cheah-Mane, "Electrical resonance instability study in traction systems," *2016 Electric Power Quality and Supply Reliability (PQ)*, Tallinn, 2016, pp. 133-138.

M. Cheah-Mane and J. Liang, "Analysis of VSC-HVDC Interconnector for Frequency Containment Reserve between Synchronous Areas," *2016 International High Voltage Direct Current Conference (HVDC 2016)*, Shanghai, 2016, pp. 1-6.

# APPENDIX B

## DETAILS OF POWER LOSS AND AVAILABILITY ANALYSIS

This Appendix presents more details of the OPF formulation and the availability expressions used for the case study of Chapter 3.

### B.1. OBJECTIVE FUNCTION OF OPF ALGORITHM

The objective function of this OPF is to minimise power losses of the transmission system and the VSCs. The expression of the objective function is:

$$p_{losses,T} = p_{loss,ac\_cb} + p_{loss,dc\_cb} + p_{loss,tr} + p_{loss,hvdc\_conv} + p_{loss,wt\_conv} \quad (B.1)$$

where the subscript *ac\_cb* represents ac cables, *dc\_cb* represents dc cables, *tr* represents transformers, *hvdc\_conv* represents HVDC converters and *wt\_conv* represents WT converters.

The power losses of each component can be expressed as follows according to the model defined in Figure 3.5:

$$p_{loss,ac\_cb} = \sum_{i,j=3}^6 i_{off,i-j}^2 r_{off,i-j} + \sum_{i,j=7}^{14} i_{off,i-j}^2 r_{off,i-j} \quad (B.2)$$

$$p_{loss,dc\_db} = \sum_{i,j=1}^4 i_{dc,i-j}^2 r_{i-j} \quad (B.3)$$

$$p_{loss,tr} = \sum_{i,j=1; i \neq 3 \& j \neq 4}^4 i_{off,i-j}^2 r_{off,i-j} + \sum_{i,j=5; i \neq 5 \& j \neq 6}^{10} i_{off,i-j}^2 r_{off,i-j} + \sum_{i,j=11}^{18} i_{off,i-j}^2 r_{off,i-j} + \sum_{i,j=1}^4 i_{on,i-j}^2 r_{on,i-j} \quad (B.4)$$

$$p_{loss,hvdc\_conv} = \sum_{i=1}^2 a_{on} + b_{on}i_{onhvdc\_ac,i} + c_{on}i_{onhvdc\_ac,i}^2 + \quad (B.5)$$

$$+ \sum_{i=1}^2 a_{off} + b_{off}i_{offhvdc\_ac,i} + c_{off}i_{offhvdc\_ac,i}^2$$

$$p_{loss,wt\_conv} = \sum_{i=15}^{18} a_{wt} + b_{wt}i_{wt,i} + c_{wt}i_{wt,i}^2 \quad (B.6)$$

## B.2. VARIABLES OF OPF ALGORITHM

The variables used in the OPF according to the model defined in Figure 3.5 are:

- ac voltage magnitudes and angles in the offshore ac grid,  $v_{off,i}$  and  $\theta_{off,i}$  ( $i=1-18$ ), and the onshore ac grid,  $v_{on,i}$  and  $\theta_{on,i}$  ( $i=1-4$ )
- dc voltage magnitudes in the offshore dc grid,  $v_{dc,1}$  ( $i=1-4$ )
- active and reactive power in the offshore ac grid,  $p_{off,i-j}$  and  $q_{off,i-j}$  ( $i,j=1-18$ ), and the onshore ac grid,  $p_{on,i-j}$  and  $q_{on,i-j}$  ( $i,j=1-4$ )
- active power in the offshore dc grid,  $p_{dc,i-j}$  ( $i,j=1-4$ )
- active and reactive power output from WT converters,  $p_{wt,i}$  and  $q_{wt,i}$  ( $i=15-18$ )
- active power of offshore and onshore HVDC converters at the ac side,  $p_{offhvdc\_ac,i}$  and  $p_{onhvdc\_ac,i}$  ( $i=1,2$ ), and the dc side,  $p_{offhvdc\_dc,i}$  ( $i=3,4$ ) and  $p_{onhvdc\_dc,i}$  ( $i=1,2$ ).
- reactive power outputs of offshore and onshore HVDC converters,  $q_{offhvdc,i}$  and  $q_{onhvdc,i}$  ( $i=1,2$ )

The variables are divided in control and state variables. Control variables, which are represented with the vector  $\mathbf{u}$ , are the variables that can be controlled by the VSCs.

The control variables in this case study are:

- ac voltage magnitudes at the Point of Connection (POC) of each offshore HVDC converter,  $v_{off,3}$  and  $v_{off,4}$
- dc voltages at the onshore HVDC converters,  $v_{dc,1}$  and  $v_{dc,2}$
- reactive power supplied by WT grid-side converters,  $q_{wt,15} - q_{wt,18}$

- reactive power supplied by offshore HVDC converters,  $q_{offhvdc,1}$  and  $q_{offhvdc,2}$
- active power of offshore HVDC converters in the ac side,  $p_{offhvdc\_ac,1}$  and  $p_{offhvdc\_ac,2}$  (only when ac interlinks are used)
- active power of onshore HVDC converters in the dc side,  $p_{onhvdc\_dc,1}$  and  $p_{onhvdc\_dc,2}$  (only when dc interlink is used)

State variables, which are represented with the vector  $\mathbf{x}$ , are the other variables of the system.

### B.3. AVAILABILITY EXPRESSIONS

The availability expressions of S1 - S5 in Figure 3.15b for all states (1 pu, 0.5 pu and 0 pu ) are presented depending on the interlink option. It should be noted that the equivalent availability of S1 is the same as S3 and the equivalent availability of S2 is the same as S4. This is because the two OWPP transmission systems in the case study of Chapter 3 are equal.

#### B.3.1. AC collector interlink

The equivalent availabilities of S1 and S3 are:

$$A_{S1,1pu}^{ac\_col} = A_{S3,1pu}^{ac\_col} = A_{col,1pu} \quad (B.7)$$

$$A_{S1,0.5pu}^{ac\_col} = A_{S3,0.5pu}^{ac\_col} = A_{col,0.5pu} \quad (B.8)$$

$$A_{S1,0pu}^{ac\_col} = A_{S3,0pu}^{ac\_col} = 1 - A_{S1,1pu}^{ac\_col} - A_{S1,0.5pu}^{ac\_col} \quad (B.9)$$

The equivalent availabilities of S2 and S4 are:

$$A_{S2,1pu}^{ac\_col} = A_{S4,1pu}^{ac\_col} = A_{exp\_cb,1pu} \cdot A_{offHVDC,1pu} \cdot A_{trans\_cb,1pu} \cdot A_{onHVDC,1pu} \quad (B.10)$$

$$A_{S2,0.5pu}^{ac\_col} = A_{S4,0.5pu}^{ac\_col} = A_{exp\_cb,1pu} \cdot A_{trans\_cb,1pu} (A_{onHVDC,0.5pu} \cdot A_{offHVDC,1pu} + A_{onHVDC,1pu} \cdot A_{offHVDC,0.5pu} + A_{onHVDC,0.5pu} \cdot A_{offHVDC,0.5pu}) \quad (B.11)$$

$$A_{S2,0pu}^{ac\_col} = A_{S4,0pu}^{ac\_col} = 1 - A_{S2,1pu}^{ac\_col} - A_{S2,0.5pu}^{ac\_col} \quad (B.12)$$

The equivalent availabilities of S5 are:

$$A_{S5,1pu}^{ac\_col} = A_{int\_cb,1pu} \quad (B.13)$$

$$A_{S5,0pu}^{ac\_col} = 1 - A_{S5,1pu}^{ac\_col} \quad (B.14)$$

### B.3.2. AC offshore converter interlink

The equivalent availabilities of S1 and S3 are:

$$A_{S1,1pu}^{ac\_conv} = A_{S3,1pu}^{ac\_conv} = A_{col,1pu} \cdot A_{exp\_cb,1pu} \quad (B.15)$$

$$A_{S1,0.5pu}^{ac\_conv} = A_{S3,0.5pu}^{ac\_conv} = A_{col,0.5pu} \cdot A_{exp\_cb,1pu} \quad (B.16)$$

$$A_{S1,0pu}^{ac\_conv} = A_{S3,0pu}^{ac\_conv} = 1 - A_{S1,1pu}^{ac\_conv} - A_{S1,0.5pu}^{ac\_conv} \quad (B.17)$$

The equivalent availabilities of S2 and S4 are:

$$A_{S2,1pu}^{ac\_conv} = A_{S4,1pu}^{ac\_conv} = A_{offHVDC,1pu} \cdot A_{trans\_cb,1pu} \cdot A_{onHVDC,1pu} \quad (B.18)$$

$$A_{S2,0.5pu}^{ac\_conv} = A_{S4,0.5pu}^{ac\_conv} = A_{trans\_cb,1pu} (A_{onHVDC,0.5pu} \cdot A_{offHVDC,1pu} + A_{onHVDC,1pu} \cdot A_{offHVDC,0.5pu} + A_{onHVDC,0.5pu} \cdot A_{offHVDC,0.5pu}) \quad (B.19)$$

$$A_{S2,0pu}^{ac\_conv} = A_{S4,0pu}^{ac\_conv} = 1 - A_{S2,1pu}^{ac\_conv} - A_{S2,0.5pu}^{ac\_conv} \quad (B.20)$$

The equivalent availabilities of S5 are:

$$A_{S5,1pu}^{ac\_conv} = A_{int\_cb,1pu} \quad (B.21)$$

$$A_{S5,0pu}^{ac\_conv} = 1 - A_{S5,1pu}^{ac\_conv} \quad (B.22)$$

### B.3.3. DC offshore converter interlink

The equivalent availabilities of S1 and S3 are:

$$A_{S1,1pu}^{dc\_conv} = A_{S3,1pu}^{dc\_conv} = A_{exp\_cb,1pu} \cdot A_{col,1pu} \cdot A_{offHVDC,1pu} \quad (B.23)$$

$$A_{S1,0.5pu}^{dc\_conv} = A_{S3,0.5pu}^{dc\_conv} = A_{exp\_cb,1pu} (A_{col,0.5pu} \cdot A_{offHVDC,1pu} + A_{col,1pu} \cdot A_{offHVDC,0.5pu} + A_{col,0.5pu} \cdot A_{offHVDC,0.5pu}) \quad (B.24)$$

$$A_{S1,0pu}^{dc\_conv} = A_{S3,0pu}^{dc\_conv} = 1 - A_{S1,1pu}^{dc\_conv} - A_{S1,0.5pu}^{dc\_conv} \quad (B.25)$$

The equivalent availabilities of S2 and S4 are:

$$A_{S2,1pu}^{dc\_conv} = A_{S4,1pu}^{dc\_conv} = A_{trans\_cb,1pu} \cdot A_{onHVDC,1pu} \quad (B.26)$$

$$A_{S2,0.5pu}^{dc\_conv} = A_{S4,0.5pu}^{dc\_conv} = A_{trans\_cb,1pu} \cdot A_{onHVDC,0.5pu} \quad (B.27)$$

$$A_{S2,0pu}^{dc\_conv} = A_{S4,0pu}^{dc\_conv} = 1 - A_{S2,1pu}^{dc\_conv} - A_{S2,0.5pu}^{dc\_conv} \quad (B.28)$$

The equivalent availabilities of S5 are:

$$A_{S5,1pu}^{dc\_conv} = A_{int\_cb,1pu} \quad (B.29)$$

$$A_{S5,0pu}^{dc\_conv} = 1 - A_{S5,1pu}^{dc\_conv} \quad (B.30)$$

## B.4. OUTAGE COMBINATIONS

Table B.1 represents all the outage combinations of S1 - S5 in Figure 3.15b, when the wind generation is equal to 40% of the OWPP rated power, the transmission system capacity of each OWPP is 100% of the OWPP rated power and the interlink cable capacity is 50% of the OWPP rated power.

Table B.1: Outage combinations of S1-S5 and resulting capacity outage. Capacities of S1-S5 are expressed in per-unit with base power equal to the rated power of an OWPP

S1	S2	S3	S4	S5	Capacity Outage (%)
0	0	0.5	0.5	0	50
0	0	0.5	1	0	50
0	0	1	0.5	0	50
0	0	1	1	0	50
0	0.5	0.5	0.5	0	50
0	0.5	0.5	1	0	50

0	0.5	1	0.5	0	50
0	0.5	1	1	0	50
0	1	0.5	0.5	0	50
0	1	0.5	1	0	50
0	1	1	0.5	0	50
0	1	1	1	0	50
0.5	0	0.5	0.5	0	50
0.5	0	0.5	1	0	50
0.5	0	1	0.5	0	50
0.5	0	1	1	0	50
0.5	0.5	0	0	0	50
0.5	0.5	0	0.5	0	50
0.5	0.5	0	1	0	50
0.5	0.5	0.5	0	0	50
0.5	0.5	0.5	0.5	0	0
0.5	0.5	0.5	1	0	0
0.5	0.5	1	0	0	50
0.5	0.5	1	0.5	0	0
0.5	0.5	1	1	0	0
0.5	1	0	0	0	50
0.5	1	0	0.5	0	50
0.5	1	0	1	0	50
0.5	1	0.5	0	0	50
0.5	1	0.5	0.5	0	0
0.5	1	0.5	1	0	0
0.5	1	1	0	0	50
0.5	1	1	0.5	0	0
0.5	1	1	1	0	0
1	0	0.5	0.5	0	50
1	0	0.5	1	0	50
1	0	1	0.5	0	50
1	0	1	1	0	50
1	0.5	0	0	0	50
1	0.5	0	0.5	0	50
1	0.5	0	1	0	50
1	0.5	0.5	0	0	50
1	0.5	0.5	0.5	0	0
1	0.5	0.5	1	0	0
1	0.5	1	0	0	50
1	0.5	1	0.5	0	0
1	0.5	1	1	0	0

1	1	0	0	0	50
1	1	0	0.5	0	50
1	1	0	1	0	50
1	1	0.5	0	0	50
1	1	0.5	0.5	0	0
1	1	0.5	1	0	0
1	1	1	0	0	50
1	1	1	0.5	0	0
1	1	1	1	0	0
0	0	0.5	0.5	1	50
0	0	0.5	1	1	50
0	0	1	0.5	1	50
0	0	1	1	1	50
0	0.5	0.5	0	1	50
0	0.5	0.5	0.5	1	50
0	0.5	0.5	1	1	50
0	0.5	1	0	1	50
0	0.5	1	0.5	1	50
0	0.5	1	1	1	50
0	1	0.5	0	1	50
0	1	0.5	0.5	1	50
0	1	0.5	1	1	50
0	1	1	0	1	50
0	1	1	0.5	1	50
0	1	1	1	1	50
0.5	0	0	0.5	1	50
0.5	0	0	1	1	50
0.5	0	0.5	0.5	1	37.5
0.5	0	0.5	1	1	0
0.5	0	1	0.5	1	37.5
0.5	0	1	1	1	0
0.5	0.5	0	0	1	50
0.5	0.5	0	0.5	1	50
0.5	0.5	0	1	1	50
0.5	0.5	0.5	0	1	37.5
0.5	0.5	0.5	0.5	1	0
0.5	0.5	0.5	1	1	0
0.5	0.5	1	0	1	37.5
0.5	0.5	1	0.5	1	0
0.5	0.5	1	1	1	0
0.5	1	0	0	1	50

0.5	1	0	0.5	1	50
0.5	1	0	1	1	50
0.5	1	0.5	0	1	0
0.5	1	0.5	0.5	1	0
0.5	1	0.5	1	1	0
0.5	1	1	0	1	0
0.5	1	1	0.5	1	0
0.5	1	1	1	1	0
1	0	0	0.5	1	50
1	0	0	1	1	50
1	0	0.5	0.5	1	37.5
1	0	0.5	1	1	0
1	0	1	0.5	1	37.5
1	0	1	1	1	0
1	0.5	0	0	1	50
1	0.5	0	0.5	1	50
1	0.5	0	1	1	50
1	0.5	0.5	0	1	37.5
1	0.5	0.5	0.5	1	0
1	0.5	0.5	1	1	0
1	0.5	1	0	1	37.5
1	0.5	1	0.5	1	0
1	0.5	1	1	1	0
1	1	0	0	1	50
1	1	0	0.5	1	50
1	1	0	1	1	50
1	1	0.5	0	1	0
1	1	0.5	0.5	1	0
1	1	0.5	1	1	0
1	1	1	0	1	0
1	1	1	0.5	1	0
1	1	1	1	1	0

# APPENDIX C

## MODELLING AND CONTROL OF WIND TURBINE WITH PERMANENT MAGNET SYNCHRONOUS GENERATOR

The WT model used in Chapter 4 is based on a PMSG with FRC. This Appendix presents the WT aerodynamic and mechanical model, the PMSG model and the back-to-back converter control.

### C.1. AERODYNAMIC AND MECHANICAL MODEL

The WT aerodynamic model provides the power generation, which is equal to:

$$P_m = \frac{1}{2} \rho_a A v_w^3 c_p(\lambda, \beta) \quad (\text{C.1})$$

where  $\rho_a$  is the air density,  $A$  is the WT swept area,  $v_w$  is the wind speed,  $c_p$  is the power coefficient,  $\lambda$  is the tip-speed ratio and  $\beta$  is the pitch angle. The power coefficient is expressed as in [160]:

$$c_p(\lambda, \beta) = c_1 \left( \frac{c_2}{\Lambda} - c_3 \beta - c_4 \right) \exp\left(-\frac{c_5}{\Lambda}\right) + c_6 \lambda \quad (\text{C.2})$$

$$\frac{1}{\Lambda} = \frac{1}{\lambda + 0.08\beta} - \frac{0.035}{\beta^3 + 1} \quad (\text{C.3})$$

where  $c_1 - c_6$  are the coefficients of the model.

The WT mechanical dynamics are represented with a single-mass model, which is expressed as:

$$J_{wt} \frac{d\omega_r}{dt} = T_m - r_g T_e \quad (\text{C.4})$$

where  $J_{wt}$  is the WT equivalent inertia,  $\omega_r$  is the rotor speed,  $T_m$  is the mechanical torque,  $r_g$  is the gear ratio and  $T_e$  is the electrical torque.

## C.2. GENERATOR MODEL

The PMSG model is represented with the following voltage and flux equations:

$$\mathbf{v}_s^{\text{abc}} = r_s \mathbf{i}_s^{\text{abc}} + \frac{d}{dt} \boldsymbol{\lambda}_s^{\text{abc}} \quad (\text{C.5})$$

$$\boldsymbol{\lambda}_s^{\text{abc}} = L_s \mathbf{i}_s^{\text{abc}} + \boldsymbol{\lambda}_m \quad (\text{C.6})$$

where  $\mathbf{v}_s^{\text{abc}}$  and  $\mathbf{i}_s^{\text{abc}}$  are the voltages and currents in the stator windings,  $r_s$  and  $L_s$  are the resistance and inductance associated with the stator windings,  $\boldsymbol{\lambda}_s^{\text{abc}}$  is the magnetic flux in the stator and  $\boldsymbol{\lambda}_m$  is the magnetic flux of the permanent magnet.

The dynamic model is usually represented in a synchronous  $dq$  frame considering the rotor speed,  $\omega_r$ , as a reference for the Park transformation:

$$\begin{cases} v_{qs} = r_s i_{qs} + \frac{d\lambda_{qs}}{dt} + \lambda_{qs} \omega_r \\ v_{ds} = r_s i_{ds} + \frac{d\lambda_{ds}}{dt} + \lambda_{ds} \omega_r \end{cases} \quad (\text{C.7})$$

$$\begin{cases} \lambda_{qs} = L_q i_{qs} \\ \lambda_{ds} = L_d i_{ds} + \lambda_m \end{cases} \quad (\text{C.8})$$

where  $L_q$  and  $L_d$  are the inductances associated with d and q axis. The elements related to the homopolar axis have been neglected assuming a symmetric and balanced three-phase system. Combining (C.9) and (C.10):

$$\begin{cases} v_{qs} = r_s i_{qs} + L_q \frac{di_{qs}}{dt} + \omega_r L_d i_{ds} + \omega_r \lambda_m \\ v_{ds} = r_s i_{ds} + L_d \frac{di_{ds}}{dt} + \omega_r L_q i_{qs} \end{cases} \quad (\text{C.9})$$

$$T_m = \frac{3}{2} p (\lambda_m i_{qs} + (L_d - L_q) i_{qs} i_{sd}) \quad (\text{C.10})$$

where  $p$  is the number of pole pairs. It is observed that whether  $i_{sd} = 0$  or the machine has surface mounted magnets ( $L_d = L_q$ ), the torque will have a direct relationship with  $i_{qs}$ . More details about the modelling can be found in [161].



# APPENDIX D

## LOW ORDER SYSTEM FREQUENCY RESPONSE MODEL

The frequency response of an ac system can be modelled with a low order system described in [162]. Figure D.1 shows the diagram of the low order system model, where the power imbalance and the contribution from an OWPP are included as injections of power.

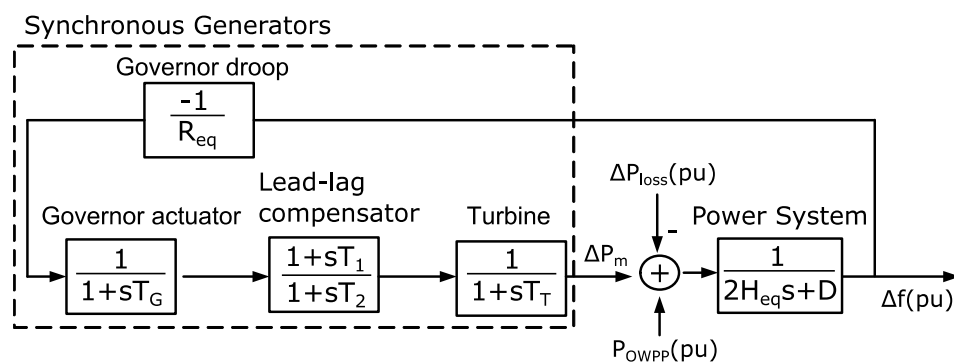


Figure D.1: Block diagram of low order system frequency response model.

This model represents the frequency response of a power system with conventional synchronous generators. The power system is modelled as a first order transfer function with an equivalent inertia,  $H_{eq}$ , and damping,  $D$ , also called self-load regulation effect of a power system. The synchronous generators are represented as reheat steam turbine units with governor. The dynamic response of a reheat steam turbine is modelled with a lead-lag compensator with time constants  $T_1$  and  $T_2$  and a first order system with mechanical time constant,  $T_T$ . The governor is represented with a droop gain,  $1/R_{eq}$  and an actuator modelled as a first order system with time constant,  $T_G$ .

# APPENDIX E

## SPECIFICATIONS OF EXPERIMENTAL TEST RIG

Tables E.1 - E.5 show the details of the experimental test rig used in Chapter 4.

Table E.1: Specifications of wind turbine test rig

Device	Specifications	Equipment rating	Operating rating
Voltage Source Converters (2 units)	Topology	Two-level, three-phase without neutral wire, IGBT switcher	
	Manufacturer	CINERGIA	
	Rated power	10 kW	700 W
	Rated ac voltage	415 V	100 V
	Rated dc voltage	800 V	300 V
	DC capacitors	1020 $\mu$ F	
	Coupling inductor	3.5 mH	
Motor-generator unit	Topology	Permanent Magnet Synchronous Machines	
	Manufacturer	Emerson	
	Rated power	1.2 kW	700 W
	Rated speed	3000 rpm	2050 rpm
	Rated ac voltage	400 V	100 V
	Pole number	6	
Embedded computer (dSPACE)	DS1005		
Unidrive inverter	Control Technique SP2403		

Table E.2: Specifications of VSC test rig

<b>Device</b>	<b>Specifications</b>	<b>Equipment rating</b>	<b>Operating rating</b>
Voltage Source Converters (3 units)	Topology	Two-level, three-phase without neutral wire, IGBT switcher	
	Manufacturer	CINERGIA	
	Rated power	10 kW	2 kW
	Rated ac voltage	415 V	140 V
	Rated dc voltage	800 V	250 V
	DC capacitors	1020 $\mu$ F	
	Coupling inductor	2.2 mH	
Embedded computer (dSPACE)	DS1005		

Table E.3: Specifications of dc network cabinet

<b>Element</b>	<b>Description</b>
DC inductors	3 pairs of 2.4 mH, 2 pairs of 3.4 mH and 1 pair of 9.4 mH
DC capacitors	8 units of 4.7 $\mu$ F
DC cables as distributed $\pi$ sections	Several combinations of $\pi$ sections with 30 inductors of 0.5 mH and 38 capacitors of 200 $\mu$ F
Current flow controller	Two IGBT-controlled variable resistors
DC short-circuit generator	Shunt branch with diode in parallel that is connected through an IGBT. The rated current is 30 A.

Table E.4: Specifications of real time simulator

<b>Specifications</b>	<b>Description</b>
Manufacturer	RTDS technologies
Racks	2 units
Cards	1 GTWIF, 4 GPC (2 IBM PPC750GX 1 GHz), 1 GTIRC, 1 GTDI, 1 GTDO, 1 GTAI, 1 GTAQ, 1 GTNET.

Table E.5: Specifications of grid simulator

<b>Specifications</b>	<b>Description</b>	
Manufacturer	Spitzenberger	
Topology	4-quadrant amplifier	
Rated power	1 kVA (continuous); 2 kVA (short-time)	
Rated ac voltage	270 V	
Rated dc voltage	$\pm 382$ V	
Input signals	Voltage limits	$\pm 5$ V
	Impedance	$\approx 8$ k $\Omega$
	Slew rate	$> 52$ V/ $\mu$ s
Power supply	230 V	
Protection	16 A	

# APPENDIX F

## COMPLEX TRANSFER FUNCTIONS

In this Appendix, complex transfer functions are presented to model three-phase dynamic systems, *e.g.* grid-connected VSCs. This representation was employed in Chapter 5 to obtain an impedance-based model of an HVDC-connected OWPP.

Complex transfer functions are used to model symmetric systems. Balanced three-phase systems are symmetric, *e.g.* RLC components or transformers [163]. The dynamics of VSCs are represented as a symmetric system if the converter control only includes an inner loop.

Three-phase quantities in a stationary  $abc$  frame can be expressed as equivalent two-phase quantities in a stationary  $\alpha\beta$  frame or a synchronous  $dq$  frame. Such two-phase quantities are called space vectors. Complex space vectors are the representation of space vectors with a complex number, where the real and imaginary parts are the components of the vector. The complex space vector associated to a three-phase variable  $\{u_a, u_b, u_c\}$  is expressed in a stationary  $\alpha\beta$  frame as:

$$\mathbf{u}^s = u_\alpha + ju_\beta = \frac{2}{3}(u_a + e^{j2\pi/3}u_b + e^{-j2\pi/3}u_c) \quad (\text{F.1})$$

where the scaling constant is chosen as  $2/3$  to keep the same peak value in both frames. The same complex space vector in a synchronous  $dq$  frame is expressed as:

$$\mathbf{u} = u_d + ju_q = e^{-j\omega_1 t} \mathbf{u}^s \quad (\text{F.2})$$

where  $\omega_1$  is the fundamental frequency of the three-phase variable. It is observed that the  $dq$  transformation is a translation of the frequency response as  $\omega \rightarrow \omega - \omega_1$ .

A linear continuous-time system with input signal  $u$  and output signal  $y$  is expressed in the Laplace  $s$  domain as:

$$y = G(s)u \quad (\text{F.3})$$

where  $G(s)$  is the transfer function. If the signals are represented as space vectors in  $dq$  frame, the input and output signals are denoted as  $u = [u_d, u_q]$  and  $y = [y_d, y_q]$  and  $G(s)$  is a transfer matrix equal to:

$$G(s) = \begin{bmatrix} G_{dd}(s) & G_{qd}(s) \\ G_{dq}(s) & G_{qq}(s) \end{bmatrix} \quad (\text{F.4})$$

When  $G_{dd}(s) = G_{qq}(s) = G_d(s)$  and  $G_{dq}(s) = -G_{qd}(s) = G_q(s)$ ,  $G(s)$  in ( F.4 ) is expressed as:

$$G(s) = \begin{bmatrix} G_d(s) & -G_q(s) \\ G_q(s) & G_d(s) \end{bmatrix} \quad (\text{F.5})$$

The relationship between input and output signals using complex space vectors is the same as using space vectors in ( F.3 ), but denoted with boldface letters:

$$\mathbf{y} = \mathbf{G}(s)\mathbf{u} \quad (\text{F.6})$$

where  $\mathbf{G}(s) = G_d(s) + jG_q(s)$  is the complex transfer function. It can be observed that the transfer matrix  $G(s)$  represents a symmetric system, but for convenience with the complex number notation of  $\mathbf{G}(s)$ , the component (1,2) is negative.

The relationship between input and output signals in ( F.6 ) can be expressed in stationary  $\alpha\beta$  frame if the complex transfer function in  $dq$  frame introduces a rotation such that  $s \rightarrow s - j\omega_1$ :

$$\mathbf{y}^s = \mathbf{G}(s - j\omega_1)\mathbf{u}^s = \mathbf{G}^s(s)\mathbf{u}^s \quad (\text{F.7})$$

# APPENDIX G

## DEMONSTRATION OF POSITIVE-NET-DAMPING STABILITY CRITERIA

This Appendix presents a detailed demonstration of the positive-net-damping criterion proposed in [150] and the alternative positive-net-damping criterion presented in Chapter 5.

### G.1. IMPEDANCE-BASED MODELS

The positive-net-damping criteria analyse a system represented with an impedance-based model. The system under study is divided into a source and a load subsystem. The source is modelled as a Thévenin or Norton equivalent circuit. The load subsystem is represented by an impedance or another Thévenin or Norton equivalent. Figure G.1 shows the equivalent impedance-based circuits when the load subsystem is an impedance. The impedances, currents and voltages are expressed in the stationary  $\alpha\beta$  frame and the Laplace  $s$ -domain.



(a) Source as Thévenin equivalent

(b) Source as Norton equivalent

Figure G.1: Equivalent impedance-based circuit with load subsystem as an impedance.

If the source is a Thévenin equivalent, the current flowing from the source to the load in Figure G.1a is equal to:

$$\mathbf{i}^s = \frac{\mathbf{v}_s^s}{Z_l + Z_s} = \mathbf{v}_s^s \frac{\overbrace{1/Z_l}^{T_v}}{1 + Z_s/Z_l} \quad (\text{G.1})$$

where  $T_v$  is the closed loop transfer function, which can be also expressed as:

$$T_v(s) = \frac{M(s)}{1 + M(s)N(s)} = \frac{M(s)}{1 + L(s)} \quad (\text{G.2})$$

where  $M(s) = 1/Z_l$  is the open loop transfer function,  $N(s) = Z_s$  is the feedback transfer function and  $L(s)$  is the loop transfer function. The stability can be analysed from the loop transfer function, which represents the ratio of impedances  $Z_s/Z_l$ .

If the source is a Norton equivalent, the voltage at the load connection point in Figure G.1b is equal to:

$$\mathbf{v}^s = \frac{\mathbf{i}_s^s}{Y_l + Y_s} = \mathbf{i}_s^s \frac{\overbrace{1/Y_l}^{T_i}}{1 + Y_s/Y_l} \quad (\text{G.3})$$

where  $T_i$  is the closed loop transfer function. In this case, the stability can be analysed from the ratio of admittances  $Y_s/Y_l$ .

If the load subsystem is represented as a Thévenin or Norton equivalent circuit, the ratio of impedances or admittances is also valid to analyse stability. As an example, Figure G.2 shows the impedance-based circuits when the source is a Thévenin equivalent and the load subsystem is a Thévenin or Norton equivalent.

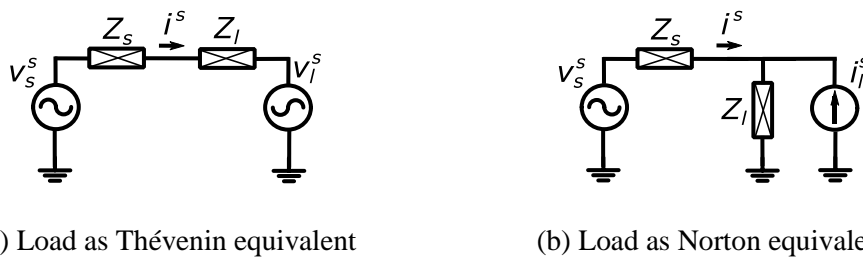


Figure G.2: Equivalent impedance-based circuit with source as a Thévenin equivalent and load as Thévenin or Norton equivalents.

The currents flowing from the source to the load are:

$$\mathbf{i}_{\text{Thev}}^s = (\mathbf{v}_s^s - \mathbf{v}_l^s) \frac{\overbrace{1/Z_l}^{T_{v,\text{Thev}}}}{1 + Z_s/Z_l} \quad (\text{G.4})$$

$$\mathbf{i}_{\text{Nort}}^s = (\mathbf{v}_s^s - Z_l \mathbf{i}_l^s) \frac{\overbrace{1/Z_l}^{T_{v,\text{Nort}}}}{1 + Z_s/Z_l} \quad (\text{G.5})$$

where the close loop transfer functions,  $T_{v,Thev}$  and  $T_{v,Nort}$ , are the same as in ( G.1 ), *i.e.*  $T_v = T_{v,Thev} = T_{v,Nort}$ .

## G.2. POSITIVE-NET-DAMPING STABILITY CRITERIA

The positive-net-damping criteria are based on the evaluation of the total damping, *i.e.* the damping of the source and the load subsystems, at specific frequencies that depend on the criterion definition. In this section, the positive-net-damping stability criteria are demonstrated considering an impedance-based model with a source represented as a Thévenin equivalent, but the same conclusions are valid if the source is a Norton equivalent.

The positive-net-damping criteria are derived from applying the Nyquist criterion to the ratio of impedances. Considering that  $M(s)$  and  $N(s)$  are stable, the closed loop system  $T_v$  in ( G.1 ), ( G.4 ) and ( G.5 ) is asymptotically stable if the Nyquist trajectory of the loop transfer function  $L(s) = M(s)N(s) = Z_s/Z_l$  does not encircle  $(-1,0)$  in clockwise direction. The positive-net-damping criterion presented in [150] is demonstrated from the evaluation of the gain margin condition in the Nyquist trajectory. The alternative approach of the positive-net-damping criterion presented in Chapter 5 is based on the evaluation of the phase margin condition. Figure G.3 shows a representation of the gain and phase margin conditions in the Nyquist trajectory when the system is stable and unstable.

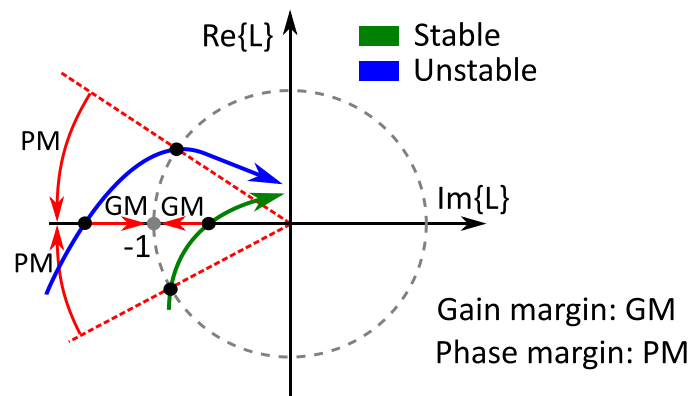


Figure G.3: Nyquist trajectories for stable and unstable systems.

### G.2.1. Positive-net-damping Criterion from the Gain Margin

This criterion states that a closed loop system is stable if the total damping of the system is positive at the following frequencies: (i) open loop resonant frequencies and

(ii) low frequencies where the loop gain is greater than 1 [150]. If stability is evaluated in terms of the gain margin,  $L(j\omega) = M(j\omega)N(j\omega)$  must satisfy the following conditions at angular frequency  $\omega$ :

$$\text{Im}\{M(j\omega)N(j\omega)\} = 0, \quad (\text{G.6})$$

$$M(j\omega)N(j\omega) > -1 \quad (\text{G.7})$$

where  $M(j\omega)$  and  $N(j\omega)$  in ( 5.13 ) and ( 5.14 ) can be expressed in terms of equivalent impedances as:

$$\frac{1}{M(j\omega)} = Z_l(j\omega) = R_l(\omega) + jX_l(\omega) \quad (\text{G.8})$$

$$N(j\omega) = Z_s(j\omega) = R_s(\omega) + jX_s(\omega) \quad (\text{G.9})$$

Combining ( G.8 ) and ( G.9 ) with  $L(j\omega)$ :

$$\begin{aligned} L(j\omega) = M(j\omega)N(j\omega) &= \frac{R_s(\omega) + jX_s(\omega)}{R_l(\omega) + jX_l(\omega)} = \\ &= \frac{R_s(\omega)R_l(\omega) + X_s(\omega)X_l(\omega)}{R_l^2(\omega) + X_l^2(\omega)} + j \frac{R_l(\omega)X_s(\omega) - R_s(\omega)X_l(\omega)}{R_l^2(\omega) + X_l^2(\omega)} \end{aligned} \quad (\text{G.10})$$

If gain margin condition ( 5.13 ) is applied to ( G.10 ) the following condition is obtained:

$$\frac{R_l(\omega)X_s(\omega) - R_s(\omega)X_l(\omega)}{R_l^2(\omega) + X_l^2(\omega)} = 0 \rightarrow \frac{R_s(\omega)}{R_l(\omega)} = \frac{X_s(\omega)}{X_l(\omega)} \quad (\text{G.11})$$

Substituting ( G.11 ) into ( G.10 ) gives,

$$L(j\omega) = \frac{R_s(\omega)}{R_l(\omega)} \quad (\text{G.12})$$

If gain margin condition ( 5.14 ) is combined with ( G.12 ), the following condition is obtained:

$$\frac{R_s(\omega)}{R_l(\omega)} > -1 \rightarrow R_s(\omega) + R_l(\omega) > 0 \quad (\text{G.13})$$

This condition defines the theorem proposed in [150], which states that a system is stable if the total damping (or in this case resistance) is positive for angular frequencies where  $\text{Im}\{M(j\omega)N(j\omega)\} = 0$ , *i.e.* frequencies where the Nyquist trajectory intersects the real axis. These frequencies correspond to resonances in the loop gain  $|M(j\omega)N(j\omega)|$ . Due to the complexity to calculate the frequencies where the Nyquist trajectory intersects the real axis, the positive-net-damping stability criterion was derived from the theorem in [150]. This criterion evaluates the total damping at open loop resonances, which approximately correspond to loop resonant frequencies. Also, low frequencies where the loop gain is greater than 1 must be evaluated since it is a strong indication of instability [150]. The demonstration of this criterion is equivalent for sources modelled as a Norton circuit, but  $M(j\omega)$  and  $N(j\omega)$  are represented as admittances.

### G.2.2. Positive-net-damping Criterion from the Phase Margin

This criterion states that a closed loop system is stable if the total damping of the system is positive at closed loop resonant frequencies. If stability is evaluated in terms of the phase margin,  $L(j\omega) = M(j\omega)N(j\omega)$  must satisfy the following conditions at angular frequency  $\omega$ :

$$|M(j\omega)N(j\omega)| = 1 \quad (\text{G.14})$$

$$-\pi \leq \arg\{M(j\omega)N(j\omega)\} \leq -\pi \quad (\text{G.15})$$

where  $M(j\omega)$  and  $N(j\omega)$  are defined as in the previous section.

The loop gain  $|L(j\omega)| = |M(j\omega)N(j\omega)|$  can be expressed as:

$$|M(j\omega)N(j\omega)| = \frac{\sqrt{R_s(\omega)^2 + X_s(\omega)^2}}{\sqrt{R_l(\omega)^2 + X_l(\omega)^2}} \quad (\text{G.16})$$

Phase margin condition ( G.14 ) combined with ( G.16 ) is equivalent to:

$$\frac{\sqrt{R_s(\omega)^2 + X_s(\omega)^2}}{\sqrt{R_l(\omega)^2 + X_l(\omega)^2}} = 1 \rightarrow R_s(\omega)^2 + X_s(\omega)^2 = R_l(\omega)^2 + X_l(\omega)^2 \quad (\text{G.17})$$

If the resistive components are neglected compared to the reactive components,  $R_s \ll X_s, R_l \ll X_l$  and ( G.17 ) is simplified to:

$$X_s(\omega) = \pm X_l(\omega) \quad (\text{G.18})$$

In an impedance-based model with the source represented as a Thévenin equivalent, series resonances of the closed loop system are equivalent to electrical series resonances from the voltage source  $\mathbf{v}_s^s$  in Figure G.1a and Figure G.2. If the resistive components are neglected, series resonance conditions are reduced to:

$$\begin{aligned} \text{Im}\{Z_s(j\omega_{res}) + Z_l(j\omega_{res})\} \approx 0 &\rightarrow X_s(\omega) + X_l(\omega) = 0 \rightarrow \\ &\rightarrow X_s(\omega) = -X_l(\omega) \end{aligned} \quad (\text{G.19})$$

It can be observed that ( G.19 ) is a particular case of ( G.18 ); *i.e.* the series resonance conditions coincide with the phase margin condition ( G.14 ).

Phase margin condition ( G.15 ) can be divided in two different cases depending on the trend of the loop gain  $d|L(j\omega)|/d\omega$  around the angular frequency  $\omega$ :

$$\begin{cases} \text{If } \frac{d|L(j\omega)|}{d\omega} > 0 \text{ (}|L(j\omega)| \text{ is increasing): } & 0 < \arg\{L(j\omega)\} < \pi \\ \text{If } \frac{d|L(j\omega)|}{d\omega} < 0 \text{ (}|L(j\omega)| \text{ is decreasing): } & -\pi < \arg\{L(j\omega)\} < 0 \end{cases} \quad (\text{G.20})$$

The loop phase  $\arg\{L(j\omega)\}$  can provide conditions for the imaginary part of  $L(j\omega)$  as follows:

$$\begin{cases} 0 < \arg\{L(j\omega)\} < \pi \rightarrow \text{Im}\{L(j\omega)\} > 0 \rightarrow R_l(\omega)X_s(\omega) - R_s(\omega)X_l(\omega) > 0 \\ -\pi < \arg\{L(j\omega)\} < 0 \rightarrow \text{Im}\{L(j\omega)\} < 0 \rightarrow R_l(\omega)X_s(\omega) - R_s(\omega)X_l(\omega) < 0 \end{cases} \quad (\text{G.21})$$

Combining ( G.20 ) and ( G.21 ) the two cases of phase margin condition ( G.15 ) are expressed as:

$$\begin{cases} \text{If } \frac{d|L(j\omega)|}{d\omega} > 0 : & 0 < \arg\{L(j\omega)\} < \pi \rightarrow R_l(\omega)X_s(\omega) - R_s(\omega)X_l(\omega) > 0 \\ \text{If } \frac{d|L(j\omega)|}{d\omega} < 0 : & -\pi < \arg\{L(j\omega)\} < 0 \rightarrow R_l(\omega)X_s(\omega) - R_s(\omega)X_l(\omega) < 0 \end{cases} \quad (\text{G.22})$$

If the resonance condition in ( G.19 ) is imposed to ( G.22 ):

$$\begin{cases} \text{If } \frac{d|L(j\omega)|}{d\omega} > 0 : X_s(\omega_{res})[R_l(\omega_{res}) + R_s(\omega_{res})] > 0 \\ \text{If } \frac{d|L(j\omega)|}{d\omega} < 0 : X_s(\omega_{res})[R_l(\omega_{res}) + R_s(\omega_{res})] < 0 \end{cases} \quad (\text{G.23})$$

The trend of the loop gain depends on the sign of the reactive components. If the resistive components are neglected compared to the reactive components, the loop transfer function is approximated as:

$$L(j\omega) \approx \frac{X_s(\omega)}{X_l(\omega)} \quad (\text{G.24})$$

and its derivative as a function of  $\omega$  is:

$$\frac{d|L(j\omega)|}{d\omega} \approx \frac{1}{|X_l(\omega)|^3} \frac{d|X_s(\omega)|}{d\omega} - \frac{|X_s(\omega)|}{|X_l(\omega)|^2} \frac{d|X_l(\omega)|}{d\omega} \quad (\text{G.25})$$

Therefore, the following conditions can be defined for  $d|L(j\omega)|/d\omega$ :

- If the source subsystem is capacitive,  $X_s < 0$ , and the load subsystem is inductive  $X_l > 0$ :

$$\frac{d|X_s(\omega)|}{d\omega} < 0 \text{ and } \frac{d|X_l(\omega)|}{d\omega} > 0 \rightarrow \frac{d|L(j\omega)|}{d\omega} < 0 \quad (\text{G.26})$$

- If the source subsystem is inductive,  $X_s > 0$ , and the load subsystem is capacitive  $X_l < 0$ :

$$\frac{d|X_s(\omega)|}{d\omega} > 0 \text{ and } \frac{d|X_l(\omega)|}{d\omega} < 0 \rightarrow \frac{d|L(j\omega)|}{d\omega} > 0 \quad (\text{G.27})$$

By considering the previous conditions for  $d|L(j\omega)|/d\omega$ , ( G.23 ) is simplified to:

$$R_l(\omega_{res}) + R_s(\omega_{res}) > 0 \quad (\text{G.28})$$

This equation defines the alternative approach of the positive-net-damping criterion, which states that a system is stable if the total damping (or in this case resistance) is positive at closed loop resonances (or in this case electrical series resonances). The demonstration of this criterion is equivalent for sources modelled as a Norton circuit. However,  $M(j\omega)$  and  $N(j\omega)$  are represented as admittances and the resonance condition in ( G.19 ) corresponds to electrical parallel resonances.

# APPENDIX H

## DETAILS OF CASE STUDIES

### H.1. CASE STUDY IN CHAPTER 3

Tables H.1 and H.2 show the details of the HVDC-connected OWPPs used in the case study of Chapter 3. The interlink cables are supposed to have the same characteristics as the dc transmission cables and the ac export cables.

Table H.1: Parameters of Wind Turbines, HVDC converters and transformers.

Element	Parameter	Value
HVDC converters	Rated power	492 MVA
HVDC transformers (2 units in parallel)	Rated power	246 MVA
	Rated voltages	350/220 kV
	Leakage reactance	0.18 pu
	Load losses	0.005 pu
	No load losses	0.0005 pu
Wind Turbine	Number per each OWPP	82
	Rated power	6 MVA
Wind Turbine transformer	Nominal power	6 MVA
	Nominal voltages	33/0.9 kV
	Leakage reactance	0.06 pu
	Load losses	0.009 pu
	No load losses	0.0009 pu
Collector platform transformers (3-winding type and 2 units in parallel)	Nominal power	280 MVA
	Nominal voltages	220/33/33 kV
	Leakage reactance 1-2	0.15 pu
	Leakage reactance 1-3	0.15 pu
	Leakage reactance 2-3	0.30 pu
	Load losses	0.005 pu
	No load losses	0.0005 pu

Table H.2: Cable parameters.

Element	Parameter	Value
DC transmission cables	Nominal voltage	320 kV
	Resistance	0.0192 $\Omega$ /km
	Inductance	0.24 mH/km
	Capacitance	0.152 $\mu$ F/km
AC export cables (2 cables in parallel)	Nominal voltage	220 kV
	Resistance	0.0323 $\Omega$ /km
	Inductance	0.4 mH/km
	Capacitance	0.17 $\mu$ F/km
AC collector cables (240 mm <sup>2</sup> )	Nominal voltage	33 kV
	Resistance	0.098 $\Omega$ /km
	Inductance	0.36 mH/km
	Capacitance	0.23 uF/km
AC collector cables (630 mm <sup>2</sup> )	Nominal voltage	33 kV
	Resistance	0.041 $\Omega$ /km
	Inductance	0.31 mH/km
	Capacitance	0.34 uF/km

The OWPPs are formed by two wind farm clusters of 41 WTs. These clusters are represented as aggregated single WTs in series to an impedance with equivalent power losses to the detailed collector grid [100]. The equivalent impedance of a string (see Figure 3.8 ) is calculated as:

$$Z_{str,i} = \frac{\sum_1^{N_{wt}} Z_{wt} + \sum_1^{N_{wt}} j \cdot Z_{cb,j}}{N_{wt}^2} \quad (\text{H.1})$$

where  $N_{wt}$  is the number of WTs in the string,  $Z_{wt}$  is the WT impedance and  $Z_{cb,j}$  is the impedance of the cable  $j$ . The equivalent impedance of a wind farm cluster with  $N_{str}$  strings is:

$$Z_{clust} = \frac{\sum_1^{N_{str}} Z_{str,i}}{N_{str}^2} \quad (\text{H.2})$$

Figure H.2 shows the layout of a wind farm cluster, which is partially based on the *Fecamp* project [99], and Table H.3 provides the cable lengths between WTs.

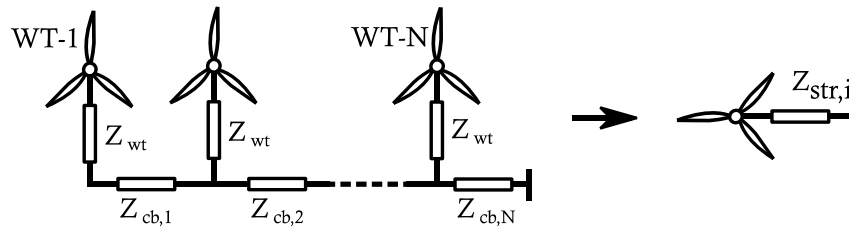


Figure H.1: Equivalent impedance of a string with N WTs.

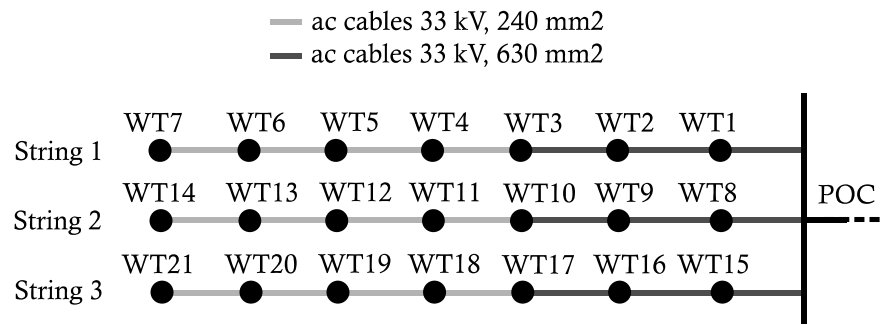


Figure H.2: Wind farm cluster layout.

Table H.3: Cable lengths of wind farm cluster in Figure H.2.

Cables	Length
WT1- POC	5.755 km
WT8- POC	4.684 km
WT15- POC	3.615 km
Others	1.169 km

Table H.4 shows the MTTF and MTTR of different components to calculate availability of the interconnected topologies in Chapter 3.

Table H.4: MTTF and MTTR of transmission system components [102], [103].

Components	MTTF	MTTR (onshore)	MTTR (offshore)
GIS (200 - 300 kV)	250 yrs	120 hrs	184 hrs
GIS (300 - 500 kV)	100 yrs	120 hrs	184 hrs
Transformer	95 yrs	1008 hrs	1512 hrs
Converter reactor	7 yrs	24 hrs	192 hrs
VSC-MMC	1.9 yrs	12 hrs	60 hrs
Control system of converter	1.6 yrs	3 hrs	17 hrs
DC switchyard	4.02 yrs	26.06 hrs	98.06 hrs
HVDC breaker	66.67 yrs	192 hrs	360 hrs
Submarine ac cable	14.29 yrs /100km	-	1440 hrs
Submarine dc cable	14.29 yrs /100km	-	1440 hrs

## H.2. CASE STUDY IN CHAPTER 4

Tables H.5– H10 describe the specifications of the WT model, the HVDC point-to-point transmission system and the onshore ac grid used in Chapter 4.

### H.2.1. Wind Turbine

The WT model is described in Appendix C and the WT specifications are detailed in Tables H.5–H.7.

Table H.5: Parameters of PMSG.

Parameter	Value
Nominal Power	6 MVA
Nominal Voltage	0.6 kV
Nominal rotor speed, $\omega_{g,n}$	1485 rpm
$q$ -axis unsaturated inductance, $L_q$	$8.91 \cdot 10^{-4}$ pu
$d$ -axis unsaturated inductance, $L_d$	$8.91 \cdot 10^{-4}$ pu
Stator winding resistance, $r_s$	0.01 pu
Magnetic flux, $\lambda_m$	1.04
Number of pole pairs, $p$	12

Table H.6: Aerodynamic and mechanical characteristic of WT.

Element	Parameter	Value
Aerodynamic characteristics	Rated wind speed, $v_{w,n}$	12.5 m/s
	Cut-in wind speed, $v_{w,cutin}$	4 m/s
	Cut-off wind speed, $v_{w,cutoff}$	25 m/s
	$c_1$	0.5176
	$c_2$	116
	$c_3$	0.4
	$c_4$	5
	$c_5$	21
	$c_6$	0.0068
Mechanical characteristics	Rotor diameter, $D_{wt}$	116 m
	Gear ratio, $r_g$	10
	WT inertia, $H_{wt}$	4.8 s
	Nominal rotor speed, $\omega_{r,n}$	148.5 rpm
	Minimum rotor speed, $\omega_{r,min}$	45.1 rpm

Table H.7: Specifications and control parameters of WT back-to-back converter.

Element	Parameter	Value
Generator-side VSC	Rated power	6 MVA
	Rated voltages: $V_{ac,n}$ , $V_{dc,n}$	0.6 kV, 1.2 kV
	Equivalent dc capacitor	10 mF
	Coupling inductance	0.105 $\mu$ H
	Coupling resistance	0.1 m $\Omega$
	PI current control: $k_p$ , $k_i$	0.9, 6
Grid-side VSC	Rated power	6 MVA
	Rated voltages: $V_{ac,n}$ , $V_{dc,n}$	0.6 kV, 1.2 kV
	Equivalent dc capacitor	10 mF
	Coupling inductance	0.105 mH
	Coupling resistance	0.1 m $\Omega$
	PI - current control: $k_p$ , $k_i$	0.105, 0.1
	PI - dc voltage control: $k_{p,dc}$ , $k_{i,dc}$	5.97, 111.48
PI - PLL : $k_{p,pll}$ , $k_{i,pll}$	$10^3$ , $10^5$	

## H.2.2. HVDC Point-to-point System

The general control strategies of the onshore and offshore VSCs are described in Chapter 2 and the supplementary droop controls to create a frequency coupling between onshore and offshore ac grids are described in Chapter 4. The offshore VSC control ac voltage based on an amplitude control. Tables H.8–H.9 show the specifications of the HVDC converters and the dc cables.

Table H.8: Specifications and control parameters of dc cables.

Parameter	Value
Nominal Voltage	320 kV
Resistance	0.1646 $\Omega$
Inductance	8.78 mH
Capacitance	6.54 $\mu\text{F}$

Table H.9: Specifications and control parameters of HVDC converters.

Element	Parameter	Value
Offshore VSC	Rated Power	1200 MVA
	Rated voltages: $V_{ac,n}, V_{dc,n}$	380 kV, $\pm 320$ kV
	Equivalent dc capacitor	0.222 mF
	Coupling inductance	11.35 mH
	Coupling resistance	0.5 $\Omega$
	PI - ac voltage control: $k_{p,voff}, k_{i,voff}$	1, 100
	$V_{dc} - f_{off}$ droop gain, $k_f$	0.0125
Onshore VSC	Rated power	1200 MVA
	Rated voltages: $V_{ac,n}, V_{dc,n}$	380 kV, $\pm 320$ kV
	Equivalent dc capacitor	0.222 mF
	Coupling inductance	11.35 mH
	Coupling resistance	0.5 $\Omega$
	PI - current control: $k_{p,c}, k_{i,c}$	11.35, 500
	PI - dc voltage control: $k_{p,vdc}, k_{i,vdc}$	0.1493, 2.786
	PI - PLL : $k_{p,pll}, k_{i,pll}$	10, 1000
	$f_{on} - V_{dc}$ droop gain, $k_v$	80

### H.2.3. Onshore ac Grid

The onshore ac grid model is described in Appendix D and the specifications are detailed in Table H.10.

Table H.10: Specifications of ac grid model.

Parameter	Value
Base power	5 GW
Inertia constant, $H_{eq}$	4.4 s
Self-regulating effect of load, $D$	1
Droop gain, $R_{eq}$	11
Lead-lag time constants: $T_1, T_2$	2 s, 12 s
Governor actuator time constant, $T_G$	0.2 s
Turbine time constant, $T_T$	0.3 s

### H.3. CHAPTER 5

Tables H.11– H.13 show the details of the HVDC-connected OWPP used in the case study of Chapter 5.

Table H.11: Specifications of offshore HVDC converter and HVDC transformer.

Element	Parameter	Value
Offshore HVDC converter (MMC)	Rated power	560 MVA
	Rated ac voltage	350 kV
	Arm inductance, $L_{arm}$	183.7 mH
HVDC transformer (2 units in parallel)	Nominal power	280 MVA
	Nominal voltages	350/220 kV
	Leakage reactance	0.18 pu
	Load losses	0.005 pu
	No load losses	0.0005 pu

Table H.12: Specifications of WT grid-side converter and WT transformer.

Element	Parameter	Value
WT grid-side converter (2-level VSC)	Rated power	6.7 MVA
	Rated voltages	0.9 kV
	Coupling inductance, $L_f^w$	50 $\mu$ H
	Equivalent resistance of coupling inductance, $R_f^w$	0.02 m $\Omega$
	Equivalent capacitance of high frequency filter, $C_f^w$	1 mF
	Low pass filter bandwidth, $\alpha_f$	50
	Current control bandwidth, $\alpha_c$	1000
WT transformer	Nominal power	6.7 MVA
	Nominal voltages	33/0.9 kV
	Leakage reactance	0.06 pu
	Load losses	0.009 pu
	No load losses	0.0009 pu

Table H.13: Specifications of ac export cables and collector transformers.

Element	Parameter	Value
AC export cable (2 cables in parallel)	Nominal voltage	220 kV
	Initial length	10 km
	Resistance	0.0323 $\Omega$ /km
	Inductance	0.4 mH/km
	Capacitance	0.17 $\mu$ F/km
Collector transformer (4 units in parallel)	Nominal power	140 MVA
	Nominal voltages	220/33 kV
	Leakage reactance	0.15 pu
	Load losses	0.005 pu
	No load losses	0.0005 pu

## REFERENCES

- [1] REN21, “Renewables 2016 - Global Status Report,” 2016.
- [2] M. D. Esteban, J. J. Diez, J. S. López, and V. Negro, “Why offshore wind energy?,” *Renew. Energy*, vol. 36, no. 2, pp. 444–450, 2011.
- [3] Global Wind Energy Council, “Offshore Wind,” 2015.
- [4] EWEA, “Wind energy scenarios for 2020,” 2014.
- [5] EWEA, “Wind energy scenarios for 2030,” 2015.
- [6] EWEA, “The European offshore wind industry - key 2015 trends and statistics,” 2016.
- [7] D. Van Hertem and M. Ghandhari, “Multi-terminal VSC HVDC for the European supergrid: Obstacles,” *Renew. Sustain. Energy Rev.*, vol. 14, no. 9, pp. 3156–3163, Dec. 2010.
- [8] P. Bresesti, W. L. Kling, R. L. Hendriks, and R. Vailati, “HVDC Connection of Offshore Wind Farms to the Transmission System,” *IEEE Trans. Energy Convers.*, vol. 22, no. 1, pp. 37–43, Mar. 2007.
- [9] TenneT, “BorWin1.” [Online]. Available: <http://www.tennet.eu/our-grid/offshore-projects-germany/borwin1/>. [Accessed: 14-Oct-2016].
- [10] R. Irnawan, F. da Silva, C. L. Bak, and T. C. Bregnhøj, “An Initial Topology of Multi-terminal HVDC Transmission System in Europe : A Case Study of the North-Sea Region,” in *IEEE International Energy Conference (ENERGYCON) 2016*, 2016, no. 1, pp. 1–6.
- [11] Working Group B4.55, “HVDC Connection of Offshore Wind Power Plants,” 2015.
- [12] O. Daniel Adeuyi, N. Jenkins, and J. Wu, “Topologies of the North Sea Supergrid,” *2013 48th Int. Univ. Power Eng. Conf.*, pp. 1–6, Sep. 2013.
- [13] D. Lane, “Round 3 Offshore wind farm connection study,” 2011.
- [14] “Atlantic Wind Connection Project.” [Online]. Available: <http://www.atlanticwindconnection.com/awc-projects/atlantic-wind-connection>. [Accessed: 25-Nov-2016].

- 
- [15] J. Lin, “Integrating the First HVDC-Based Offshore Wind Power into PJM System—A Real Project Case Study,” *IEEE Trans. Ind. Appl.*, vol. 52, no. 3, pp. 1970–1978, May 2016.
- [16] TenneT, “About offshore projects Germany.” [Online]. Available: <http://www.tennet.eu/our-grid/offshore-projects-germany/about-offshore-projects-in-germany/>. [Accessed: 12-Sep-2016].
- [17] K. R. W. Bell, L. Xu, and T. Houghton, “Considerations in design of an offshore network,” in *CIGRE session 2014*, 2014, pp. 1–14.
- [18] ENTSO-E, “Network Code on High Voltage Direct Current Connections,” 2016.
- [19] C. Buchhagen, C. Rauscher, A. Menze, and J. Jung, “BorWin1 - First Experiences with harmonic interactions in converter dominated grids,” in *International ETG Congress 2015; Die Energiewende - Blueprints for the new energy age*, 2015, pp. 1–7.
- [20] Working Group B3.36, “Special Considerations for AC Collector Systems and Substations Associated with HVDC - Connected Wind Power Plants,” 2015.
- [21] H. Polinder, “Overview of and trends in wind turbine generator systems,” in *2011 IEEE Power and Energy Society General Meeting*, 2011, pp. 1–8.
- [22] H. Polinder, J. A. Ferreira, B. B. Jensen, A. B. Abrahamsen, K. Atallah, and R. A. McMahon, “Trends in Wind Turbine Generator Systems,” *IEEE J. Emerg. Sel. Top. Power Electron.*, vol. 1, no. 3, pp. 174–185, Sep. 2013.
- [23] A. Madariaga, J. L. Martín, I. Zamora, I. Martínez de Alegría, and S. Ceballos, “Technological trends in electric topologies for offshore wind power plants,” *Renew. Sustain. Energy Rev.*, vol. 24, pp. 32–44, Aug. 2013.
- [24] A. Gustafsson, M. Saltzer, A. Farkas, H. Ghorbani, T. Quist, and M. Jeroense, “The new 525 kV extruded HVDC cable system,” 2014.
- [25] S. Wang, J. Liang, and J. Ekanayake, “Optimised topology design and comparison for offshore transmission,” in *2012 47th International Universities Power Engineering Conference (UPEC)*, 2012, pp. 1–6.
- [26] C. MacIver, K. R. W. Bell, and D. P. Nedic, “A Reliability Evaluation of

- Offshore HVDC Grid Configuration Options,” *IEEE Trans. Power Deliv.*, vol. 31, no. 2, pp. 810–819, Apr. 2016.
- [27] H. Ergun, S. Member, D. Van Hertem, S. Member, and R. Belmans, “Transmission System Topology Optimization for Large-Scale Offshore Wind Integration HE European Union has set ambitious goals regarding,” vol. 3, no. 4, pp. 908–917, 2012.
- [28] A. Hassanpoor, S. Norrga, and A. Nami, “Loss evaluation for modular multilevel converters with different switching strategies,” in *ICPE 2015-ECCE Asia*, 2015, no. June, pp. 1558–1563.
- [29] M. Raza, C. Collados, and O. Gomis-Bellmunt, “Reactive power management in an offshore AC network having multiple voltage source converters,” in *2016 IEEE 16th International Conference on Environment and Electrical Engineering (EEEIC)*, 2016, pp. 1–7.
- [30] J. Cao, W. Du, H. F. Wang, and S. Q. Bu, “Minimization of Transmission Loss in Meshed AC/DC Grids With VSC-MTDC Networks,” *IEEE Trans. Power Syst.*, vol. 28, no. 3, pp. 3047–3055, Aug. 2013.
- [31] M. Aragüés-Peñalba, A. Egea-Àlvarez, S. G. Arellano, and O. Gomis-Bellmunt, “Droop control for loss minimization in HVDC multi-terminal transmission systems for large offshore wind farms,” *Electr. Power Syst. Res.*, vol. 112, pp. 48–55, Jul. 2014.
- [32] G. W. Ault, K. R. W. Bell, and S. J. Galloway, “Calculation of economic transmission connection capacity for wind power generation,” *IET Renew. Power Gener.*, vol. 1, no. 1, p. 61, 2007.
- [33] KPMG LLP, “Offshore Transmission : An Investor Perspective,” 2012.
- [34] TenneT, “Requirements for Offshore Grid Connections in the Grid of TenneT TSO GmbH,” 2012.
- [35] J. De Decker and P. Kreutzkamp, “Offshore Electricity Grid Infrastructure in Europe,” 2011.
- [36] National Grid, “Offshore Development Information Statement 2010,” 2010.
- [37] Friends of the Supergrid, “Position Paper on the EC Communication for a

- European Infrastructure Package.” p. 17, 2010.
- [38] L. Tang and B.-T. Ooi, “Locating and Isolating DC Faults in Multi-Terminal DC Systems,” *IEEE Trans. Power Deliv.*, vol. 22, no. 3, pp. 1877–1884, Jul. 2007.
- [39] M. Abedrabbo, C. Petino, and A. Schnettler, “Analysis of the behavior of HVDC converter based on full-bridge submodules during DC fault conditions,” in *2016 IEEE International Energy Conference (ENERGYCON)*, 2016, pp. 1–6.
- [40] X. Li, Z. Yuan, J. Fu, Y. Wang, T. Liu, and Z. Zhu, “Nanao multi-terminal VSC-HVDC project for integrating large-scale wind generation,” in *2014 IEEE PES General Meeting / Conference & Exposition*, 2014, pp. 1–5.
- [41] G. Tang, Z. He, H. Pang, X. Huang, and X. Zhang, “Basic topology and key devices of the five-terminal DC grid,” *CSEE J. Power Energy Syst.*, vol. 1, no. 2, pp. 22–35, Jun. 2015.
- [42] S. Bernal-Perez, S. Ano-Villalba, R. Blasco-Gimenez, and J. Rodriguez-D’Derlee, “Off-shore wind farm grid connection using a novel diode-rectifier and VSC-inverter based HVDC transmission link,” in *IECON 2011 - 37th Annual Conference of the IEEE Industrial Electronics Society*, 2011, pp. 3186–3191.
- [43] P. Lakshmanan, J. Liang, and N. Jenkins, “Assessment of collection systems for HVDC connected offshore wind farms,” *Electr. Power Syst. Res.*, vol. 129, pp. 75–82, 2015.
- [44] J. Pan, S. Bala, M. Callavik, and P. Sandeberg, “DC Connection of Offshore Wind Power Plants without Platform,” in *13th Wind Integration Workshop*, 2014, no. November, pp. 1–6.
- [45] Y. Pipelzadeh, “Inertial response from remote offshore wind farms connected through VSC-HVDC links: a communication-less scheme,” *Power Energy Soc. Gen. Meet. 2012 IEEE*, pp. 1–6, 2012.
- [46] Y. Phulpin, “Communication-Free Inertia and Frequency Control for Wind Generators Connected by an HVDC-Link,” *IEEE Trans. Power Syst.*, vol. 27, no. 2, pp. 1136–1137, May 2012.

- [47] A. D. Hansen, M. Altin, and N. A. Cutululis, “Modelling of Wind Power Plant Controller, Wind Speed Time Series , Aggregation and Sample Results,” 2015.
- [48] C. Dierckxsens, K. Srivastava, M. Reza, S. Cole, J. Beerten, and R. Belmans, “A distributed DC voltage control method for VSC MTDC systems,” *Electr. Power Syst. Res.*, vol. 82, no. 1, pp. 54–58, 2012.
- [49] J. N. Sakamuri, Z. H. Rather, J. Rimez, M. Altin, O. Goksu, and N. A. Cutululis, “Coordinated Voltage Control in Offshore HVDC Connected Cluster of Wind Power Plants,” *IEEE Trans. Sustain. Energy*, vol. 7, no. 4, pp. 1592–1601, Oct. 2016.
- [50] M. Raza and O. Gomis-Bellmunt, “Control System of Voltage Source Converter to Interconnect Offshore AC Hub with Multiple Onshore Grids,” in *2015 International Conference on Renewable Energy Research and Applications (ICRERA)*, 2015, pp. 677–682.
- [51] H. Liu and J. Sun, “Voltage Stability and Control of Offshore Wind Farms With AC Collection and HVDC Transmission,” *IEEE J. Emerg. Sel. Top. Power Electron.*, vol. 2, no. 4, pp. 1181–1189, Dec. 2014.
- [52] L. Xu and B. R. Andersen, “Grid connection of large offshore wind farms using HVDC,” *Wind Energy*, vol. 9, no. 4, pp. 371–382, Jul. 2006.
- [53] L. Zeni, B. Hesselbaek, P. E. Sorensen, A. D. Hansen, and P. C. Kjaer, “Control of VSC-HVDC in offshore AC islands with wind power plants: Comparison of two alternatives,” in *2015 IEEE Eindhoven PowerTech*, 2015, pp. 1–6.
- [54] X. Hu, J. Liang, D. Rogers, and Y. Li, “Power Flow and Power Reduction Control Using Variable Frequency of Offshore AC Grids,” vol. 28, no. 4, pp. 3897–3905, 2013.
- [55] L. Harnefors, X. Wang, A. G. Yepes, and F. Blaabjerg, “Passivity-Based Stability Assessment of Grid-Connected VSCs—An Overview,” *IEEE J. Emerg. Sel. Top. Power Electron.*, vol. 4, no. 1, pp. 116–125, Mar. 2016.
- [56] D. Schwartzberg, I. A. Aristi, J. Holbøll, W. Z. El-Khatib, and L. Zeni, “Transients in VSC-HVDC connected offshore wind power plant,” in *11th IET International Conference on AC and DC Power Transmission*, 2015, p. 101 (6 .)-101 (6 .).

- [57] L. Harnefors, "Analysis of Subsynchronous Torsional Interaction With Power Electronic Converters," *IEEE Trans. Power Syst.*, vol. 22, no. 1, pp. 305–313, Feb. 2007.
- [58] G. Stamatiou and M. Bongiorno, "Stability Analysis of Two-Terminal VSC-HVDC Systems using the Net-Damping Criterion," *IEEE Trans. Power Deliv.*, pp. 1–1, 2016.
- [59] G. Pinares and M. Bongiorno, "Modeling and Analysis of VSC-Based HVDC Systems for DC Network Stability Studies," *IEEE Trans. Power Deliv.*, vol. 31, no. 2, pp. 848–856, Apr. 2016.
- [60] L. P. Kunjumammed, B. C. Pal, C. Oates, and K. J. Dyke, "Electrical Oscillations in Wind Farm Systems: Analysis and Insight Based on Detailed Modeling," *IEEE Trans. Sustain. Energy*, vol. PP, no. 99, pp. 1–12, 2015.
- [61] National Grid, "The grid code," no. 5, p. 632, 2016.
- [62] H. Liu and Z. Chen, "Contribution of VSC-HVDC to Frequency Regulation of Power Systems With Offshore Wind Generation," *IEEE Trans. Energy Convers.*, vol. 30, no. 3, pp. 918–926, Sep. 2015.
- [63] J. F. Conroy and R. Watson, "Frequency Response Capability of Full Converter Wind Turbine Generators in Comparison to Conventional Generation," *IEEE Trans. Power Syst.*, vol. 23, no. 2, pp. 649–656, May 2008.
- [64] F. Díaz-González, M. Hau, A. Sumper, and O. Gomis-Bellmunt, "Participation of wind power plants in system frequency control: Review of grid code requirements and control methods," *Renew. Sustain. Energy Rev.*, vol. 34, pp. 551–564, Jun. 2014.
- [65] EirGrid, "EirGrid Grid Code - Version 6.0," 2015.
- [66] O. D. Adeuyi, M. Cheah-Mane, J. Liang, N. Jenkins, Y. Wu, C. Li, and X. Wu, "Frequency support from modular multilevel converter based multi-terminal HVDC schemes," in *IEEE Power and Energy Society General Meeting*, 2015, vol. 2015–Sept.
- [67] A. Junyent Ferre, Y. Pipelzadeh, and T. C. Green, "Blending HVDC-Link Energy Storage and Offshore Wind Turbine Inertia for Fast Frequency Response," *IEEE Trans. Sustain. Energy*, pp. 1–8, 2014.

- [68] C. E. Spallarossa, M. M. C. Merlin, and T. C. Green, “Augmented inertial response of Multi-Level Converters using internal energy storage,” in *2016 IEEE International Energy Conference (ENERGYCON)*, 2016, pp. 1–6.
- [69] Y. Li, Z. Zhang, Y. Yang, Y. Li, H. Chen, and Z. Xu, “Coordinated control of wind farm and VSC–HVDC system using capacitor energy and kinetic energy to improve inertia level of power systems,” *Int. J. Electr. Power Energy Syst.*, vol. 59, pp. 79–92, Jul. 2014.
- [70] Y. Li, Z. Xu, and K. P. Wong, “Advanced Control Strategies of PMSG-Based Wind Turbines for System Inertia Support,” *IEEE Trans. Power Syst.*, pp. 1–1, 2016.
- [71] J. Zhu, C. D. Booth, G. P. Adam, A. J. Roscoe, and C. G. Bright, “Inertia emulation control strategy for VSC-HVDC transmission systems,” *IEEE Trans. Power Syst.*, vol. 28, no. 2, pp. 1277–1287, May 2013.
- [72] M. Suwan and I. Erlich, “Frequency control by HVDC connected offshore wind farms for overfrequency limitation,” in *2016 IEEE International Energy Conference (ENERGYCON)*, 2016, pp. 1–6.
- [73] Hydro-Quebec TransÉnergie, “Transmission Provider Technical Requirements for the Connection of Power Plants To the Hydro-Québec,” 2009.
- [74] IESO, “LRP I RFP Backgrounder -Connection.” pp. 1–18, 2015.
- [75] ANEEL, “Anexo 14 - Requisitos Técnicos Mínimos para Conexão de Centrais Geradoras Eólicas.” 2015.
- [76] National Grid, “System Operability Framework 2015,” no. November, p. 34, 2015.
- [77] National Grid, “Enhanced Frequency Response - Frequency Asked Questions.” pp. 1–29, 2016.
- [78] C. Nentwig, J. Haubrock, R. H. Renner, and D. Van Hertem, “Application of DC choppers in HVDC grids,” in *2016 IEEE International Energy Conference (ENERGYCON)*, 2016, pp. 1–5.
- [79] C. C. Davidson and R. A. Mukhedkar, “A comparison of different types of Dynamic Braking System for HVDC systems for offshore wind power,” in

- CIGRE Innovation for Secure and Efficient Transmission Grids*, 2014, p. 8.
- [80] O. D. Adeuyi, M. Cheah-Mane, J. Liang, L. Livermore, and Q. Mu, "Preventing DC over-voltage in multi-terminal HVDC transmission," *CSEE J. Power Energy Syst.*, vol. 1, no. 1, pp. 86–94, Mar. 2015.
- [81] A. Abdalrahman and E. Isabegovic, "DolWin1 - Challenges of connecting offshore wind farms," in *2016 IEEE International Energy Conference (ENERGYCON)*, 2016, pp. 1–10.
- [82] C. Moreira and B. Silva, "Operation and control of multiterminal HVDC grids for AC Fault Ride Through compatibility," *Energy Conf. (ENERGYCON), 2014 IEEE Int.*, pp. 287–294, 2014.
- [83] G. Ramtharan, a. Arulampalam, J. B. Ekanayake, F. M. Hughes, and N. Jenkins, "Fault ride through of fully rated converter wind turbines with AC and DC transmission systems," *IET Renew. Power Gener.*, vol. 3, no. 4, p. 426, 2009.
- [84] M. Tsili and S. Papathanassiou, "A review of grid code technical requirements for wind farms," *IET Renew. Power Gener.*, vol. 3, no. 3, p. 308, 2009.
- [85] H. Liu and Z. Chen, "Fault ride-through and grid support of permanent magnet synchronous generator-based wind farms with HVAC and VSC-HVDC transmission systems," *2012 IEEE Int. Energy Conf. Exhib.*, pp. 769–773, Sep. 2012.
- [86] A. Junyent Ferré, "Control of power electronic converters for the operation of wind generation," Universitat Politècnica de Catalunya, 2011.
- [87] Y. Jiang-Hafner, M. Hyttinen, and B. Paajarvi, "On the short circuit current contribution of HVDC Light," in *IEEE/PES Transmission and Distribution Conference and Exhibition*, 2002, vol. 3, pp. 1926–1932.
- [88] M. Ndreko, M. A. M. M. van der Meijden, and M. Popov, "Short Circuit Current Contribution from MTdc Grids to the ac Power System under ac System Faulted Conditions," in *11th IET International Conference on AC and DC Power Transmission*, 2015, pp. 1–8.
- [89] Y. Pipelzadeh, N. R. Chaudhuri, B. Chaudhuri, and T. C. Green, "Coordinated Control of Offshore Wind Farm and Onshore HVDC Converter for Effective

- Power Oscillation Damping,” *IEEE Trans. Power Syst.*, pp. 1–1, 2016.
- [90] Lingling Fan, Haiping Yin, and Zhixin Miao, “On Active/Reactive Power Modulation of DFIG-Based Wind Generation for Interarea Oscillation Damping,” *IEEE Trans. Energy Convers.*, vol. 26, no. 2, pp. 513–521, Jun. 2011.
- [91] J. L. Domínguez-García, O. Gomis-Bellmunt, F. D. Bianchi, and A. Sumper, “Power oscillation damping supported by wind power: A review,” *Renew. Sustain. Energy Rev.*, vol. 16, no. 7, pp. 4994–5006, 2012.
- [92] L. Zeni, R. Eriksson, S. Goumalatsos, M. Altin, P. Sorensen, A. Hansen, P. Kjaer, and B. Hesselbaek, “Power Oscillation Damping From VSC–HVDC Connected Offshore Wind Power Plants,” *IEEE Trans. Power Deliv.*, vol. 31, no. 2, pp. 829–838, Apr. 2016.
- [93] A. Beddard and M. Barnes, “Availability analysis of VSC-HVDC schemes for offshore windfarms,” in *6th IET International Conference on Power Electronics, Machines and Drives (PEMD 2012)*, 2012, pp. E13–E13.
- [94] K. Nieradzinska, C. MacIver, S. Gill, G. A. Agnew, O. Anaya-Lara, and K. R. W. Bell, “Optioneering analysis for connecting Dogger Bank offshore wind farms to the GB electricity network,” *Renew. Energy*, vol. 91, pp. 120–129, Jun. 2016.
- [95] H. Polinder, F. F. A. Van Der Pijl, G.-J. De Vilder, and P. J. Tavner, “Comparison of Direct-Drive and Geared Generator Concepts for Wind Turbines,” *IEEE Trans. Energy Convers.*, vol. 21, no. 3, pp. 725–733, Sep. 2006.
- [96] G. Daelemans and K. Srivastava, “Minimization of steady-state losses in meshed networks using VSC HVDC,” in *Power & Energy Society General Meeting, 2009. PES '09. IEEE*, 2009, pp. 1–5.
- [97] U. N. Gnanarathna, A. M. Gole, A. D. Rajapakse, and S. K. Chaudhary, “Loss Estimation of Modular Multi-Level Converters using Electro-Magnetic Transients Simulation,” in *International Conference on Power Systems Transients*, 2011, pp. 2–7.
- [98] B. Jacobson, P. Karlsson, G. Asplund, L. Harnefors, and T. Jonsson, “VSC-

- HVDC transmission with cascaded two-level converters,” *CIGRE Sess.*, pp. B4–B110, 2010.
- [99] Alstom, “Une énergie d ’ avenir pour votre territoire,” 2015.
- [100] E. Muljadi, C. P. Butterfield, A. Ellis, J. Mechenbier, J. Hochheimer, R. Young, N. Miller, R. Delmerico, R. Zavadil, and J. C. Smith, “Equivalencing the collector system of a large wind power plant,” in *2006 IEEE Power Engineering Society General Meeting*, 2006, p. 9 pp.
- [101] R. Billinton and R. N. Allan, *Reliability Evaluation of Engineering Systems*. Springer, 1992.
- [102] A. J. Beddard, “Factors Affecting the Reliability of VSC-HVDC for the Connection of Offshore Windfarms,” University of Manchester, 2014.
- [103] S. K. Merz, “Calculating Target Availability Figures for HVDC Interconnectors,” 2012.
- [104] The Crown Estate, “Offshore wind - Operational report 2015,” 2015.
- [105] Bundesamt fuer Seeschiffahrt und Hydrographie, “FINO1 - Forschungsplattformen in Nord- und Ostsee Nr. 1.” [Online]. Available: <http://www.fino1.de/en/>. [Accessed: 12-Sep-2016].
- [106] G. Giebel, “On the Benefits of Distributed Generation of Wind Energy in Europe,” Universität Oldenburg, 2000.
- [107] Working Group B4.52, “HVDC Grid Feasibility Study,” 2013.
- [108] National Grid, “Electricity Ten Year Statement 2015 - Appendix E,” 2015.
- [109] Offshore Wind Programme Board, “Transmission Costs for Offshore Wind- Final Report,” 2016.
- [110] ABB, “XLPE Submarine Cable Systems Attachment to XLPE Land Cable Systems - User’s Guide,” 2010.
- [111] J. Morren, J. Pierik, and S. W. H. de Haan, “Inertial response of variable speed wind turbines,” *Electr. Power Syst. Res.*, vol. 76, no. 11, pp. 980–987, Jul. 2006.
- [112] J. Brisebois and N. Aubut, “Wind farm inertia emulation to fulfill Hydro-Québec’s specific need,” in *2011 IEEE Power and Energy Society General Meeting*, 2011, pp. 1–7.

- [113] A. D. Hansen, M. Altin, I. D. Margaritis, F. Iov, and G. C. Tarnowski, "Analysis of the short-term overproduction capability of variable speed wind turbines," *Renew. Energy*, vol. 68, pp. 326–336, 2014.
- [114] F. Hafiz and A. Abdennour, "Optimal use of kinetic energy for the inertial support from variable speed wind turbines," *Renew. Energy*, vol. 80, pp. 629–643, 2015.
- [115] Z.-S. Zhang, Y.-Z. Sun, J. Lin, and G.-J. Li, "Coordinated frequency regulation by doubly fed induction generator-based wind power plants," *IET Renew. Power Gener.*, vol. 6, no. 1, p. 38, 2012.
- [116] H. Ye, W. Pei, and Z. Qi, "Analytical Modeling of Inertial and Droop Responses From a Wind Farm for Short-Term Frequency Regulation in Power Systems," *IEEE Trans. Power Syst.*, pp. 1–10, 2015.
- [117] M. Fischer, A. Mendonca, S. Engelken, and N. Mihov, "Operational experiences with inertial response provided by type 4 wind turbines," *IET Renew. Power Gener.*, vol. 10, no. 1, pp. 17–24, Jan. 2016.
- [118] M. Asmine and C.-É. Langlois, "Field measurements for the assessment of inertial response for wind power plants based on Hydro-Québec TransÉnergie requirements," *IET Renew. Power Gener.*, vol. 10, no. 1, pp. 25–32, Jan. 2016.
- [119] J. Ekanayake and N. Jenkins, "Comparison of the response of doubly fed and fixed-speed induction generator wind turbines to changes in network frequency," *IEEE Trans. Energy Convers.*, vol. 19, no. 4, pp. 800–802, Dec. 2004.
- [120] GE Energy, "WindInertia Control - Fact Sheet." p. 1, 2009.
- [121] K. Clark, N. W. Miller, and J. J. Sanchez-Gasca, "Modeling of GE wind turbine-generators for grid studies," 2010.
- [122] N. W. Miller, K. Clark, and M. Shao, "Frequency responsive wind plant controls: Impacts on grid performance," in *2011 IEEE Power and Energy Society General Meeting*, 2011, pp. 1–8.
- [123] N. W. Miller, K. Clark, and S. Member, "Advanced Controls Enable Wind Plants to Provide Ancillary Services," in *Power and Energy Society General Meeting*, 2010, pp. 1–6.

- 
- [124] ENERCON, “ENERCON Inertia Emulation improves frequency stability,” *WINDBLATT - ENERCON Magazine for wind energy*, p. 16, 2010.
- [125] ENERCON, “ENERCON wind energy converters - Technology & Service.” p. 23, 2015.
- [126] Hydro-Quebec TransÉnergie, “General Validation Test Program for Wind Power Plants Connected to the Hydro-Québec Transmission System,” 2009.
- [127] SEM Committee, “DS3 System Services, Technical Definitions, Decision Paper, SEM-13-098.” p. 20, 2013.
- [128] ENTSO-E, “Future system inertia,” 2015.
- [129] ENTSO-E, “Frequency Stability Evaluation Criteria for the Synchronous Zone of Continental Europe,” 2016.
- [130] G. Ramtharan, N. Jenkins, and J. Ekanayake, “Frequency support from doubly fed induction generator wind turbines,” *IET Renew. Power Gener.*, pp. 3–9, 2007.
- [131] I. Moore, “Inertial Response from Wind Turbines,” Cardiff University, 2012.
- [132] J. Van de Vyver, T. L. Vandoorn, J. D. M. De Kooning, B. Meersman, and L. Vandeveldel, “Energy yield losses due to emulated inertial response with wind turbines,” in *2014 IEEE PES General Meeting | Conference & Exposition*, 2014, pp. 1–5.
- [133] L. Ruttledge and D. Flynn, “Emulated Inertial Response From Wind Turbines: Gain Scheduling and Resource Coordination,” *IEEE Trans. Power Syst.*, vol. 31, no. 5, pp. 3747–3755, Sep. 2016.
- [134] M. Kayikci and J. V. Milanovic, “Dynamic Contribution of DFIG-Based Wind Plants to System Frequency Disturbances,” *IEEE Trans. Power Syst.*, vol. 24, no. 2, pp. 859–867, May 2009.
- [135] J. Van de Vyver, J. D. M. De Kooning, B. Meersman, L. Vandeveldel, and T. L. Vandoorn, “Droop Control as an Alternative Inertial Response Strategy for the Synthetic Inertia on Wind Turbines,” *IEEE Trans. Power Syst.*, vol. PP, no. 99, pp. 1–10, 2015.
- [136] J. Licari and J. Ekanayake, “Coordinated inertia response from permanent

- magnet synchronous generator ( PMSG ) based wind farms,” *J. Natl. Sci. Found. Sri Lanka*, vol. 43, no. 4, 2015.
- [137] J. Morren and S. De Haan, “Ridethrough of wind turbines with doubly-fed induction generator during a voltage dip,” *IEEE Trans. Energy Convers.*, vol. 20, no. 2, pp. 435–441, 2005.
- [138] A. D. Hansen and G. Michalke, “Modelling and control of variable-speed multi-pole permanent magnet synchronous generator wind turbine,” *Wind Energy*, vol. 11, no. 5, pp. 537–554, Sep. 2008.
- [139] S. Temtem and K. Creighton, “Summary of Studies on Rate of Change of Frequency events on the All-Island System August 2012,” 2012.
- [140] Ping-Kwan Keung, Pei Li, H. Banakar, and Boon Teck Ooi, “Kinetic Energy of Wind-Turbine Generators for System Frequency Support,” *IEEE Trans. Power Syst.*, vol. 24, no. 1, pp. 279–287, Feb. 2009.
- [141] I. Martinez Sanz, B. Chaudhuri, and G. Strbac, “Inertial Response From Offshore Wind Farms Connected Through DC Grids,” *IEEE Trans. Power Syst.*, vol. PP, no. 99, pp. 1–10, 2014.
- [142] B. Silva, C. L. Moreira, H. Leite, and J. A. Pecas Lopes, “Control Strategies for AC Fault Ride Through in Multiterminal HVDC Grids,” *IEEE Trans. Power Deliv.*, vol. 29, no. 1, pp. 395–405, Feb. 2014.
- [143] B. Silva, C. L. Moreira, L. Seca, Y. Phulpin, and J. A. Pecas Lopes, “Provision of Inertial and Primary Frequency Control Services Using Offshore Multiterminal HVDC Networks,” *IEEE Trans. Sustain. Energy*, vol. 3, no. 4, pp. 800–808, Oct. 2012.
- [144] S. Akkari, M. Petit, J. Dai, and X. Guillaud, “Interaction between the voltage-droop and the frequency-droop control for multi-terminal HVDC systems,” *IET Gener. Transm. Distrib.*, vol. 10, no. 6, pp. 1345–1352, Apr. 2016.
- [145] X. Guillaud, L. Papangelis, and T. Van Cutsem, “Frequency support among asynchronous AC systems through VSCs emulating power plants,” in *11th IET International Conference on AC and DC Power Transmission*, 2015, p. 008 (9 .)-008 (9 .).
- [146] O. Daniel Adeuyi, “Grid Connection of Offshore Wind Farms through Multi-

- Terminal High Voltage Direct Current Networks,” Cardiff Univeristy, 2016.
- [147] M. Cheah-Mane, J. Liang, and N. Jenkins, “Permanent magnet synchronous generator for wind turbines: Modelling, control and Inertial Frequency Response,” in *2014 49th International Universities Power Engineering Conference (UPEC)*, 2014, pp. 1–6.
- [148] T. Thomas, “Troubleshooting continues,” *Offshore Wind Industry*, 2014. [Online]. Available: <http://www.offshorewindindustry.com/news/troubleshooting-continues>. [Accessed: 31-Oct-2015].
- [149] M. Bradt, B. Badrzadeh, E. Camm, D. Mueller, J. Schoene, T. Siebert, T. Smith, M. Starke, and R. Walling, “Harmonics and resonance issues in wind power plants,” in *2011 IEEE Power and Energy Society General Meeting*, 2011, pp. 1–8.
- [150] L. Harnefors, “Proof and Application of the Positive-Net-Damping Stability Criterion,” *IEEE Trans. Power Syst.*, vol. 26, no. 1, pp. 481–482, Feb. 2011.
- [151] J. Sun, “Impedance-Based Stability Criterion for Grid-Connected Inverters,” *IEEE Trans. Power Electron.*, vol. 26, no. 11, pp. 3075–3078, Nov. 2011.
- [152] X. Wang, F. Blaabjerg, and W. Wu, “Modeling and Analysis of Harmonic Stability in an AC Power-Electronics-Based Power System,” *IEEE Trans. Power Electron.*, vol. 29, no. 12, pp. 6421–6432, Dec. 2014.
- [153] L. Harnefors, M. Bongiorno, and S. Lundberg, “Input-Admittance Calculation and Shaping for Controlled Voltage-Source Converters,” *IEEE Trans. Ind. Electron.*, vol. 54, no. 6, pp. 3323–3334, Dec. 2007.
- [154] J. Lyu, X. Cai, and M. Molinas, “Frequency Domain Stability Analysis of MMC-Based HVdc for Wind Farm Integration,” *IEEE J. Emerg. Sel. Top. Power Electron.*, vol. 4, no. 1, pp. 141–151, Mar. 2016.
- [155] A. Yazdani and R. Iravani, *Voltage-Sourced Converters in Power Systems: Modeling, Control, and Applications*. Wiley, 2010.
- [156] L. Harnefors, A. G. Yepes, A. Vidal, and J. Doval-Gandoy, “Passivity-Based Controller Design of Grid-Connected VSCs for Prevention of Electrical Resonance Instability,” *IEEE Trans. Ind. Electron.*, vol. 62, no. 2, pp. 702–710, Feb. 2015.

- 
- [157] L. Harnefors, L. Zhang, and M. Bongiorno, "Frequency-domain passivity-based current controller design," *IET Power Electron.*, vol. 1, no. 4, p. 455, 2008.
- [158] M. Cespedes and J. Sun, "Modeling and mitigation of harmonic resonance between wind turbines and the grid," in *2011 IEEE Energy Conversion Congress and Exposition*, 2011, pp. 2109–2116.
- [159] J. Rimez, "Optimal operation of hybrid AC / DC meshed grids," KU Leuven.
- [160] S. Heier, *Grid Integration of Wind Energy Conversion Systems*. Wiley, 2006.
- [161] P. C. Krause, O. Wasynczuk, S. D. Sudhoff, and I. P. E. Society, *Analysis of electric machinery and drive systems*. IEEE Press, 2002.
- [162] P. Kundur, *Power System Stability and Control*. McGraw-Hill Education, 1994.
- [163] L. Harnefors, "Modeling of Three-Phase Dynamic Systems Using Complex Transfer Functions and Transfer Matrices," *IEEE Trans. Ind. Electron.*, vol. 54, no. 4, pp. 2239–2248, Aug. 2007.